# Tailored Metal Nanoparticles for Selective Catalysis

Christine V. Gaskell

Submitted for the degree of Doctor of Philosophy

Cardiff University
School of Chemistry

September 2012

# Abstract

The development of clean, sustainable chemical processes is a key priority towards meeting the growing demand for synthetic functional chemicals, while balancing rapidly depleting natural resources. The selective oxidation (selox) of crotyl alcohol to crotonaldehyde and the selective hydrogenation of benzyl cyanide to phenylethylamine are two specific systems for which, it is proposed, new heterogeneous catalysts and deeper mechanistic insight will improve. In this thesis the rational design of palladium catalysts is investigated for these systems, via synthesis of palladium nanoparticles with tailored morphology and palladium-gold nanoparticles with tuneable surface composition. Pd icosahedra, nanorods and nanocubes were synthesised and characterised extensively to confirm the size and morphology of the nanoparticles. Pd icosahedra are revealed to be three times more active for crotyl alcohol selox than the nanocubes, and ten times faster than the nanorods, while maintaining good selectivity. An Au-shell, Pd-core structure was synthesised, progressively annealed to induce alloying and characterised using various *in situ* spectroscopies. Surface Au was found to enhance crotyl alcohol selox activity and selectivity towards crotonaldehyde, in accordance with model predictions. An optimum crotonaldehyde yield was obtained for an $Au_{40}Pd_{60}$ surface alloy.

By employing *in situ* and time-resolved spectroscopies the active site of Pd selox catalysts is examined, and the role of oxygen in this system and the catalyst's kinetic behaviour is defined. Reversible redox cycling of the catalyst dependent on its environment was observed, and it was possible to identify $PdO_x$ as the active catalytic species responsible for selectively oxidising crotyl alcohol to crotonaldehyde, with high temperatures suppressing catalytic selectivity. Systematic characterisation of an industrial carbon supported Pd catalyst, used in nitrile hydrogenation, reveals potential sources of deactivation including surface poisoning by CN species. Solutions to improve catalyst performance are proposed using the knowledge acquired from the nanoparticle catalysts' studies.

# Acknowledgements

First, I would like to thank my supervisors Professor Adam F. Lee and Dr Karen Wilson for all their suggestions, help, guidance, advice and patience throughout the last four years, without which this thesis would never have happened. Thank you for the opportunity. I am also very grateful to Dr Colin Brennan and Dr Martin Bowden at Syngenta for all their assistance, advice and many helpful and interesting discussions.

I would like to thank those in Cardiff Surface, Materials and Catalysis group and previously those in York Surface Chemistry and Catalysis group, particularly Chris Parlett, Dr Lee Dingwall, Dr Jean-Philippe Dacquin and Dr Simon Hackett in assisting me with catalyst synthesis, instrumentation and general motivation. Also all those in Cardiff Catalysis Institute that helped to make the move to Cardiff a smooth transition – Dr Simon Kondrat, Dr Dave Sellick and Ewa Nowicka, J.P. Dacquin and Julie Chochoy for moving me down, Paul Creasey and Julia Woodford for bringing my things!

Thank you to all the stores and workshop staff at York and Cardiff, especially to Alun Davies and Steve Morris for all their patient and ever-cheerful assistance, and to Tricia Wilson and Steve Rogers particularly for helping with arrangements for the beam-time sessions. Many thanks, Dr Nicole Hondow and Dr Teck Lim for the comprehensive microscopy sessions and Dr Mark Newton for all the support and contributions towards the XAS analysis in this thesis.

Finally I would like to thank all those friends and family who have put up with me over the last four years and encouraged me to keep going. Thank you Jenny, Mum and Dad for all your comments and time taken in proof reading, it was a huge help. Thanks for all the teas, chats and for listening, Julia, Andreia and Gwen. Thank you Mum, Dad and Mark for all your love and support. Thank you John, for being there, loving me and not letting me give up. ‘O give thanks unto the Lord; for he is good: for his mercy endureth for ever.’ Ps 136:1

In loving memory of Oma, Opa and Uncle Colin who all gave me so much encouragement and were so excited when I first started this thesis.

# Table of Contents

# Chapter 1

# Introduction

# 1.1 Selective Catalysis

## 1.1.1 Green Chemistry and heterogeneous catalysis

The need for clean processes in the industrial production of fine and commodity chemicals is becoming increasingly urgent and is reflected in the attention this subject receives from the media, government policy and commercially funded research.[1-3] Anastas and Warner's 12 points of Green Chemistry address specific criteria that must be developed in order to attain a clean, sustainable industry whilst continuing to meet with the chemical demands of a growing population.[4] Heterogeneous catalysts remove the necessity for using stoichiometric reagents and, if selectivity can be appropriately controlled, significantly reduce waste, meeting some important criteria in the principles of green chemistry.[5] These terms are briefly defined in the paragraphs below.

The rate at which a reaction occurs is determined by the activation energy of the rate determining step. By providing an alternative reaction pathway with a lower energy barrier, a catalyst can be used to enhance reaction rate. If there are several products and several reaction barriers, catalysts may also direct the formation of one product over another because the reaction path is easier; the catalyst drives the reaction selectivity towards a particular product. This is illustrated in *Figure 1.1*.[6]

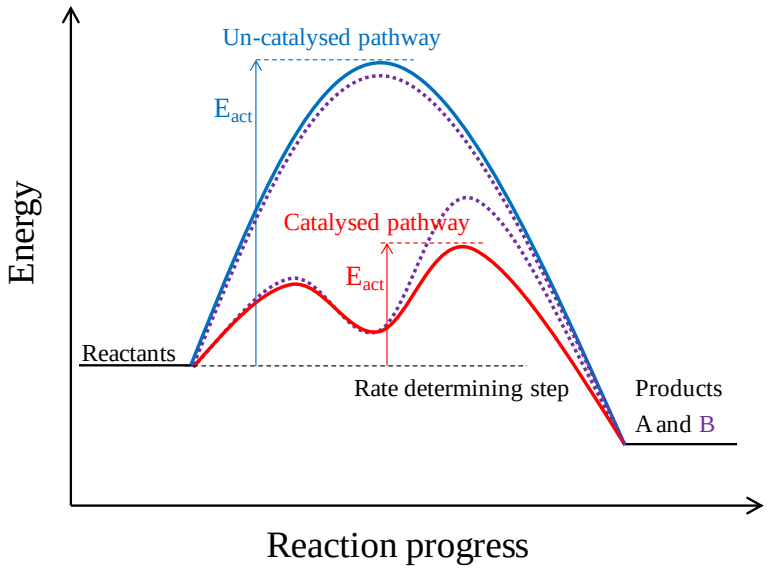


**Figure 1.1 – Catalysts in driving reaction rate and selectivity: a catalyst provides an alternative reaction pathway that has a lower energy barrier so that the reaction rate is enhanced (red and blue solid lines, reaction pathways for product A formation). The catalyst may also alter the reaction pathways for different products changing the reaction selectivity (dotted purple lines leading to product B formation). In this case the catalytic pathway is more selective to product A**

If the catalyst is in the same phase as the reaction mixture it is defined as a homogeneous catalyst, if the two phases are different it is a heterogeneous catalyst. The active site of homogeneous catalysts is more clearly defined, thus advances in catalyst design for more complex reactions, particularly in the fine chemicals and pharmaceutical industries, have generally centred on homogeneous catalysis.[7] However, there are disadvantages to using homogeneous catalysts: they are often more corrosive, more harmful and more expensive than heterogeneous catalysts, and they are difficult and costly to separate from the product reaction mixture.[8] Heterogeneous catalysts overcome many of the issues outlined, although the active site is poorly understood.[9] The catalyst surface is complex and the industrial reactor environment is a system in which many variables will influence the surface properties, and thus the catalyst reactivity, during reaction. Deactivation of the catalyst is also a major issue in the employment of these materials in industry. Consequentially, advances in heterogeneous catalyst design and improved understanding of the active site is crucial to the development of clean industrial technologies.[10-13]

A number of methodologies towards the improved understanding of the heterogeneous catalyst active site and development of catalyst design have been adopted and are reviewed in the subsequent sections of this chapter. The model reaction of the selective oxidation (selox) of crotyl alcohol to crotonaldehyde over tailored palladium catalysts, shown in *Scheme 1.1*, is considered to explore structure-reactivity relations of the catalyst surface under operating conditions and in a realistic environment. Additionally, the selective hydrogenation of benzyl cyanide to 2-phenylethylamine (PEA) using an industrial carbon supported palladium catalyst (Pd/C), outlined in *Scheme 1.2*, is discussed. This is as an example of a catalyst where a detailed understanding of the active site, and the ability to design a catalyst which could perform better, is key to creating a sustainable process.

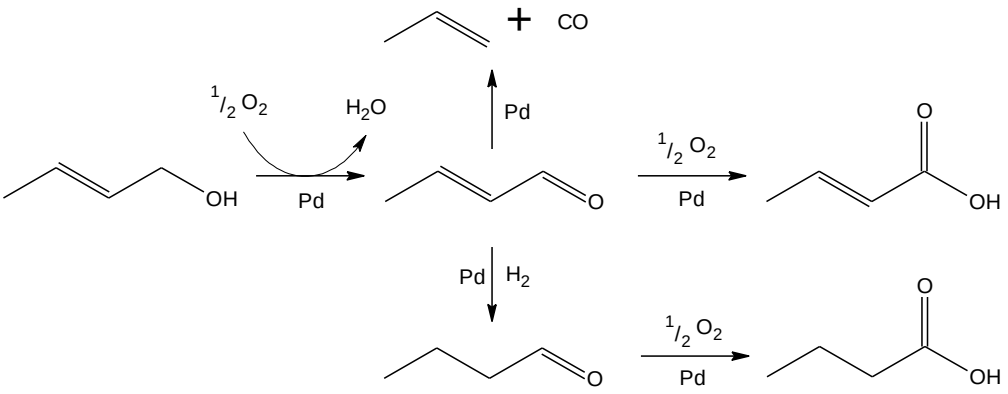


**Scheme 1.1 – Crotyl alcohol selective oxidation reaction pathway**

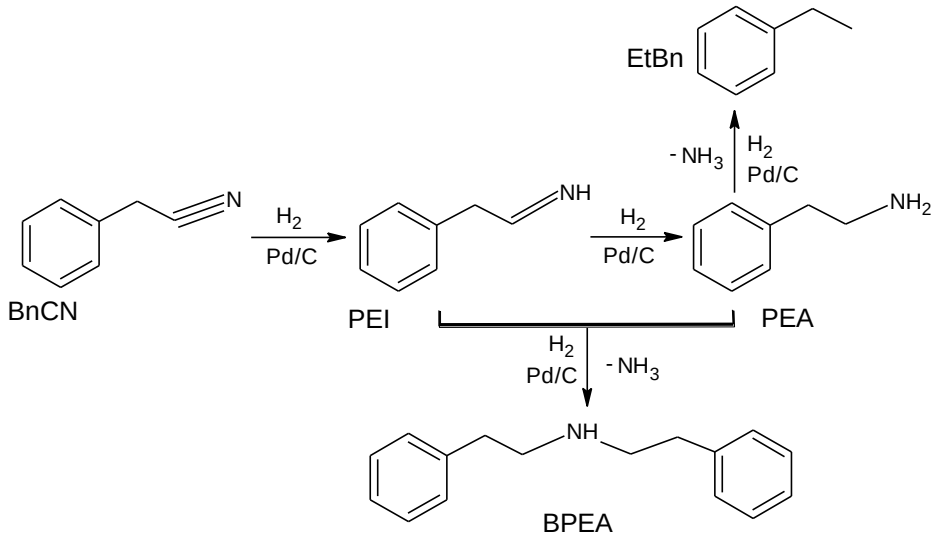


**Scheme 1.2 – Proposed reaction scheme of benzyl cyanide hydrogenation to 2-phenylethylamine (PEA) via phenylethylimine (PEI) and dimerising to bis-(2-phenylethyl)amine (BPEA)**

## 1.1.2 Selective oxidation reactions of allylic alcohols

### 1.1.2.1 General introduction to catalytic selective oxidation chemistry

Selox reactions are fundamental in the synthesis of many chemicals in industry, such as the formation of allylic aldehydes from alcohols which are used in the fine chemicals industry in flavourings and fragrances.[14] Traditionally, stoichiometric reagents such as chromates and permanganates have been used, but these are toxic to the environment and generate a large amount of waste.[15] These harmful reagents can be replaced by using a catalyst with oxygen, air or $H_2O_2$ oxidants, resulting in a more

benign procedure and leading to the formation of water as the only waste product for a selective process.[16]

A wide range of catalysts have been employed for allylic alcohol selective oxidation, which has been reviewed extensively.[10, 17, 18] Typical homogeneous catalysts include using palladium and ruthenium complexes and considerable research into the application of the stable TEMPO (2,2,6,6-tetramethyl-piperidin-1-yl)oxyl radical (see *Figure 1.2*) as a co-catalyst.[19-24] The group of R. A. Sheldon developed a highly selective $RuCl_2(PPh)_3$/TEMPO system, and more recently J. M. Hoover et al. reported an efficient Cu(I)/TEMPO catalyst for selox of a range of alcohols including allylic alcohols.[25, 26] Of more interest to the research outlined in this thesis is the application of heterogeneous catalysts in alcohol selox. Metal and metal oxide catalysts have been explored including (but not limited to) palladium[27-30], silver[31-34] and gold[35, 36] supported on a wide range of tailored materials including alumina, titania and carbon.[28, 37-39]

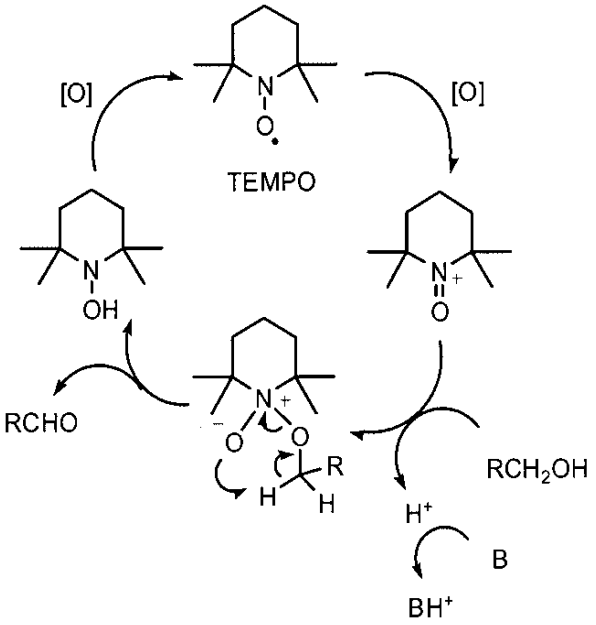


**Figure 1.2 – Mechanism under basic conditions (B) employing the TEMPO radical. Reproduced from reference 24**

In addition to the choice of metal, research relating to the catalyst support[27, 37], the use of promoters[40-43] and the reaction system (e.g. solvents)[44] is vital in developing understanding of the active site. The influence of the catalyst support and reaction conditions in selective alcohol oxidation is not explored in this thesis, although it is important to bear in mind the significant effect all the components and conditions of the

catalyst system have on catalyst performance. Work exploring the use of green solvents, such as supercritical $CO_2$, water or solvent free conditions, has received much attention in recent years.[39, 44-46] However, utilising these solvents is more complicated than traditional organic solvents due to reactant and catalyst miscibility and ease of analysis. Thus, for simplicity, the reactions carried out in this thesis were conducted in toluene, a common and relatively benign solvent for alcohol selox.

Research into palladium and gold catalysts is by far the most extensive and makes them excellent candidates for further research into the mechanism and improvement of such selox catalysts. In particular their application as bimetallic catalysts has seen much attention in recent years (an example of such a catalyst that is discussed later in this chapter is shown in *Figure 1.3*). The use of gold as an active catalyst of superior performance was initiated on the separate discoveries by G. Hutchings in hydrochlorination and M. Haruta in CO oxidation in the mid 1980s.[47, 48] A striking effect of particle size on Au reactivity has been noted by these authors and others, and is one aspect of the investigation of the active site of gold catalysis.[49] G. Schmid outlines the significant consequences of quantum size effects on the properties of gold nanoparticles.[50] Although small clusters (< ~2.5 nm) do not behave as individual molecules, the discrete electronic structure of particles in this size range give them measureable properties that are distinct from the bulk, as Schmid shows.[50, 51] There is, however, still further ongoing debate as to the nature of the active site in gold catalysis, and includes the importance of metal oxidation state, particle size and shape (and hence coordination number) and the influence of strong metal support interactions (SMSI).[49, 52-54] Many observations are reaction dependent, for example in hydrochlorination synthesis Hutchings emphasises the importance of a cationic Au site, although in their studies on CO adsorption on Au M. Boronat and co-workers highlight the key requirement of low metal coordination number as determined by particle size and shape.[53, 55]

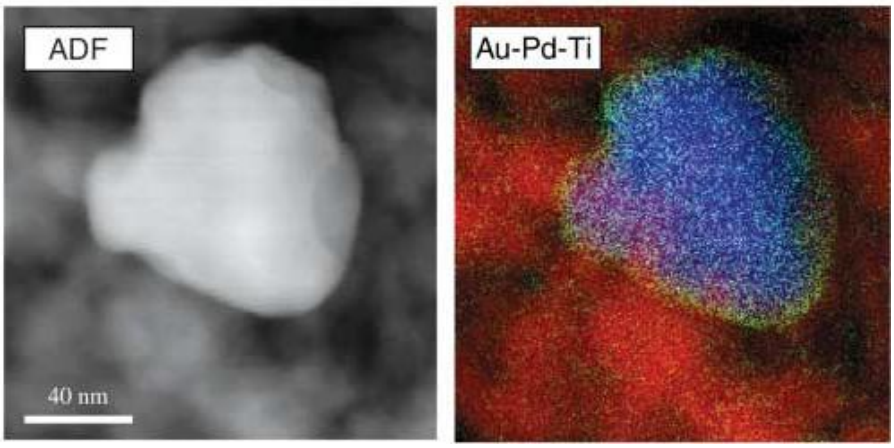


**Figure 1.3 – Angular Dark Field Scanning transmission electron microscope image of an Au-Pd bimetallic nanoparticle supported on $TiO_2$ (left). The core-shell structure of the particle can be seen from the Energy dispersive X-ray analysis map on the right. Reproduced from reference 56**

In addition to monometallic gold catalysis, there has been much focus on its application as a promoter, and the development of bimetallic gold catalysts has resulted in materials with promising catalytic properties.[56-58] Au/Pd catalysts for allylic alcohol oxidation have consistently proven to display excellent reactivity, superior to that of the monometallic counterparts.[59-62] Further details of palladium and gold as bimetallic catalysts for these reactions will be considered in detail in later sections of this chapter and the specific case of palladium as a catalyst for crotyl alcohol selective oxidation is discussed in the next section.

### 1.1.2.2 The selective oxidation of crotyl alcohol

Crotyl alcohol selox to crotonaldehyde, a precursor to the food preservative sorbic acid,[63] is an excellent, relevant reaction to provide a detailed understanding of the properties of the catalyst and which elements of the catalyst are important to engineer for use in a particular reaction.[64] Selectivity must be controlled such that decarbonylation degradation products, oxidation to the carboxylic acid or hydrogenation of the olefin bond do not occur.[29] These steps are outlined in *Scheme 1.1* and the detailed understanding of this reaction already compiled make it an ideal candidate as a model reaction for the development of novel tailored catalysts.

Spectroscopic and theoretical investigation of the adsorption mode of crotyl alcohol on Pd(111) reveals that it adopts a planar orientation and is chemisorbed to the metal surface through both the olefin and alcohol functionalities.[29, 65] This model is

shown in *Figure 1.4*. Consequentially, the adsorption of crotyl alcohol on Pd is strong and both alcohol and allyl functionalities are activated for reaction.

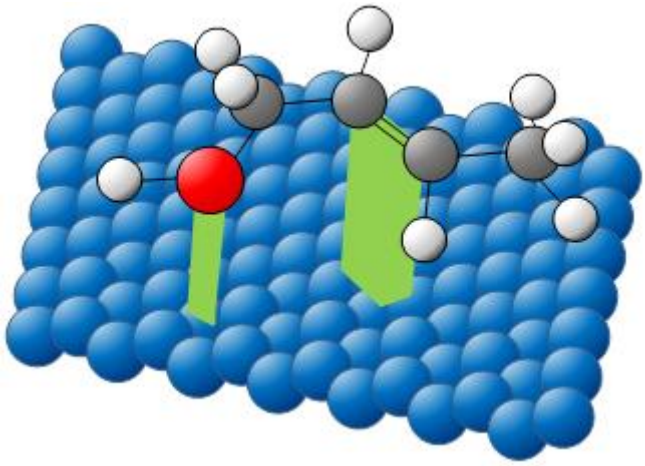

**Figure 1.4 – The adsorption mode of crotyl alcohol on Pd(111): the molecule adsorbs in a planar orientation through the O atom and C $\pi$ bond. See reference 29**

On heating crotyl alcohol over clean Pd(111), time-resolved investigation using X-ray spectroscopic techniques, by Lee et al., reveals the formation of aldehyde on the surface accompanied by CO and propene from subsequent decarbonylation. Significant levels of carbonaceous species remain on the surface after reaction. The temperature programmed desorption (TPD) trace from mass spectrometry (MS) from this experiment is shown in *Figure 1.5*. It is worth noting here the impact of co-adsorbed $O_2$ on this process: crotyl alcohol reactivity remains the same, but some crotonaldehyde desorbs, improving selectivity towards crotonaldehyde formation. Even so, adsorbed aldehyde undergoes decarbonylation and the build up of CO on the surface is still an issue.[29]

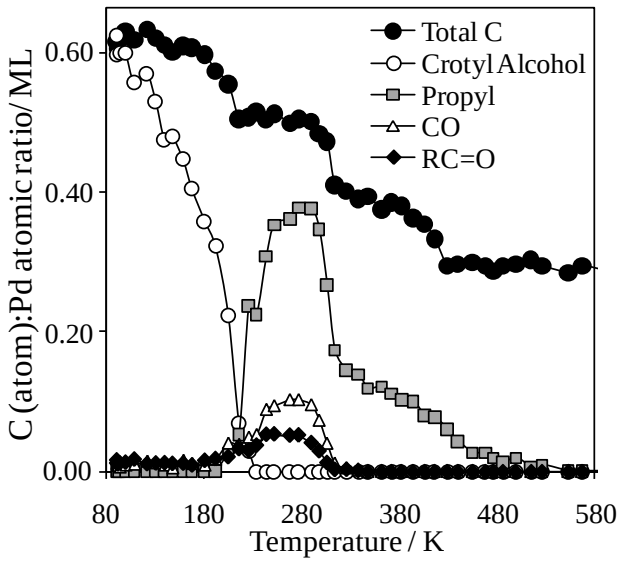


**Figure 1.5 – Temperature programmed desorption traces from the adsorption of crotyl alcohol on Pd(111). Reproduced from reference 29**

The nature of the active site for crotyl alcohol and other allylic alcohol oxidation reactions has been the subject of much debate: both a metallic active site and an oxidic active site have been proposed as the more active phase in contrasting work.[28, 64, 66-68] For example, using hard X-ray techniques such as X-ray absorption spectroscopy (XAS) and X-ray photoelectron spectroscopy (XPS) (see *Chapter 2* for details), A. F. Lee and co-workers identify surface oxide as key to high catalytic activity.[64] XAS is a technique that can detect bulk oxidation state changes. Application of *in situ* XAS by J. D. Grundwalt et al. revealed metallic palladium as the active phase for benzyl alcohol selox.[68] Further debate regarding the role of oxygen in causing or preventing the deactivation of Pd selox catalysts has arisen, and this is discussed in more detail in *Section 1.2.2*. It is clear that understanding the true nature of the active site under operating conditions is necessary for optimising catalyst design.

## 1.1.3 Selective hydrogenation reactions of nitriles

### 1.1.3.1 General introduction to amine production

Amongst the urgent challenges outlined by national and international initiatives, such as material sustainability and energy supply, food security is a priority, which highlights the necessity of developing suitable technologies and stratagems for meeting ever increasing demand.[69, 70] The World Bank stresses that by 2030 cereal production

will have to increase by almost 50 % to satisfy predicted requirements.[71] Crop protection plays a crucial role in meeting these needs: a study by E. -C. Oerke and collaborators reveal the high proportion of crops that could be lost without such protection, even as much as 80 % in some cases.[72]

Primary amines are key intermediates in the synthesis of agrochemicals that provide the valuable protection outlined above. Conventional syntheses use toxic stoichiometric reagents involving several steps, and catalytic methods that have been employed, such as reductive amination with ammonia (see *Scheme 1.3*), or preparation from alcohols with ammonia, are encumbered by harsh reaction conditions and poor selectivity.[73] A promising industrial route to a one-pot, relatively mild, selective synthesis of primary amines utilises the heterogeneous catalytic hydrogenation of nitriles.[74] Unfortunately, nitrile hydrogenation catalysts are widely known to be prone to deactivation, and directing the selectivity of nitrile hydrogenation to the desired primary amine is a challenging task.[75, 76]

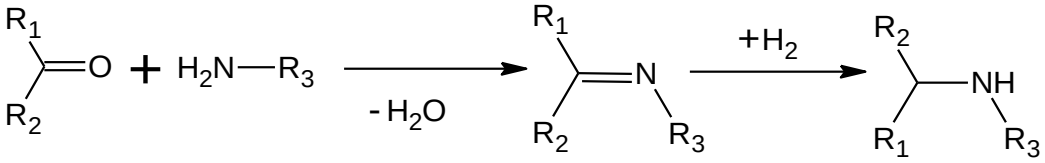


**Scheme 1.3– Reductive amination used in the synthesis of amines**

In order to design nitrile hydrogenation catalysts with superior performance there are thus two areas that warrant investigation: the relationship between the catalyst active site and reactants that drive the reaction to the desired product, and the source of catalyst deactivation. The performance of an industrial Pd/C catalyst in the partial hydrogenation of benzyl cyanide to 2-phenylethylamine is investigated, with particular attention paid to the mechanism of deactivation. Solutions to the catalyst recyclability can then be considered using the principles developed in the previous studies of tailored catalysts used in crotyl alcohol selective oxidation.

### 1.1.3.2 Reaction mechanism and selectivity

The nature of the metal used and presence and nature of dopants is the predominant factor, discussed throughout the literature on selective nitrile hydrogenations, which influences the outcome of the reaction. Generally, for model

studies over simple nitrile molecules such as butyronitrile, rhodium and ruthenium catalysts are the most selective towards primary amine products and palladium and platinum catalysts are more selective towards secondary amine products.[74] Cobalt, especially Co-Raney®, catalysts have been found to be particularly effective for this type of reaction. P. Kukula and co-workers note that chromium doping Co-Raney® has a positive effect on the selectivity to primary amine products.[76] The generally accepted mechanism for nitrile hydrogenation reactions is that outlined by J. B. Senderens in 1905 involving an imine intermediate *(Scheme 1.4)*.[77] In most cases, however, the primary amine product formed from this hydrogenation step undergoes a condensation reaction to form higher amines whilst liberating ammonia.

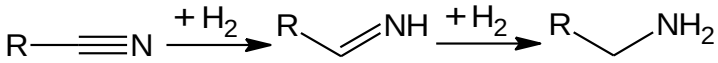


**Scheme 1.4 – The direct formation of nitriles through catalytic hydrogenation as proposed by P. Sabatier (see reference 74)**

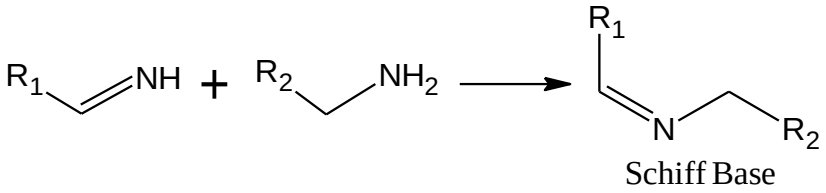


**Scheme 1.5 – The Schiff base, leading to formation of a secondary amine (see reference 74)**

W. M. H. Sachtler and Y. Y. Yuang have studied this reaction in some detail, with a view to determining the identity of the reaction intermediates, establishing the mechanism and finding out the influence of the surface on this step of the reaction.[74] It is worth emphasising the following key points from their studies: first, the mechanism towards higher amines tends to go through a Schiff base intermediate *(Scheme 1.5)* and the catalyst surface is involved in both this step and the hydrogenation step of the reaction; secondly solvent effects are generally limited, but seem to assist product desorption somewhat; thirdly, spiking with amine impurity improves selectivity to the primary amine slightly, but more significantly suppresses the reaction; and finally, from a study using deuterated amines, the group suggest that amine desorption is instigated through hydrogen transfer from an adsorbed nitrile molecule.[78] This work accentuates the importance and difficulty of removing the primary amine product from the surface

in order to achieve desired selectivity and prevent site blocking, and thus catalyst deactivation.

Further to this mechanistic study, it is also useful to consider the nature of the adsorption of the nitrile molecule to the catalyst surface. In their hydrogen transfer study, Sachtler and Yuang indicate that both the carbon and nitrogen atom in the CN bond is chemisorbed to the surface.[78] G. D. Yadav et al. also briefly discuss the adsorption of the nitrile group and compare it with the interaction of C=O to a metal surface or atom: increased metal backbonding to the nitrile LUMO will weaken the CN bond and so a high electron density at the active site will favour hydrogenation.[79]

#### 1.1.3.3 Benzyl cyanide hydrogenation

The selective hydrogenation of benzyl cyanide has not been extensively studied, although L. Hegadus and co-workers have investigated the reaction over Pd/C.[80] There are a number of points that it is worth noting regarding this system. First of all, this reaction is generally undertaken in the presence of acid, commonly sulphuric acid, in order to remove primary amine product from the surface and prevent conversion to higher amines. In this study, the most effective combination of solvent and acid, out of those investigated, is deemed to be $NaH_2PO_4$ and dichloromethane. Also of note is that the authors further consider the thermodynamics of the adsorbed products and geometric arrangement of 2-phenylethylimine. They deduce that, since the products have a similar Gibbs free energy of formation, it is the arrangement of the imino group in the imine intermediate lying above the plane of the benzene ring that makes it easily accessible to react and form secondary amines.

There is very limited research into the surface chemistry of this species or the reaction on palladium, although there has been research into the adsorption modes of small nitrile molecules such as acetonitrile and butyronitrile. The adsorption of acetonitrile onto Pt, Rh and Au surfaces was proposed to be side on via the π-bond from Fourier transform infra-red (FTIR) and MS studies. Dissociation to adsorbed CN species was subsequently observed.[81] A study of butyronitrile on a Pt surface showed that initial adsorption led to partial hydrogenation to the imine, possibly chemisorbed atop through the nitrogen lone pair.[82] It is clear that strong adsorption through the CN functionality plays an important role in the chemistry of nitrile catalysis, although evidence for the adsorption mode, particularly for larger molecules such as benzyl cyanide, is very limited.

## 1.2 Catalyst deactivation

Deactivation in catalysis is defined by Schlögl as "the collection of effects which reduce the intrinsic activity of a catalyst system" and notes that the classical definition of a catalyst, in which it is recovered unchanged, would imply that the lifetime of all catalysts is infinite.[83] Identifying the sources of catalyst deactivation, and so extending its lifetime and recyclability, are clearly key areas for focus in catalyst design.[84] Although this is the predominant investigation of *Chapter 6*, the preceding chapters all address secondary consequences of poor catalyst design leading to deactivation, particularly with regard to the role of oxygen and self poisoning, discussed at the end of this section.

However, before an analysis of catalyst deactivation can be embarked upon, it is important to outline the possible sources. P. Albers et al. discuss this in their review on palladium catalyst deactivation and include particle growth, changes in valency, chemical poisoning, leaching, and coke deposition.[85] In order to achieve high surface areas small particles are desirable, thus particle growth processes that lead to a reduction in surface area and so activity, such as sintering or Ostwald ripening (see *Figure 1.6*), are prevalent issues in heterogeneous catalysis.[83, 86, 87] Additionally, surface area can be lost through leaching of metal atoms into the reaction solution.[88, 89] Support structure and design plays an important role in reducing deactivation through particle growth.[89, 90]

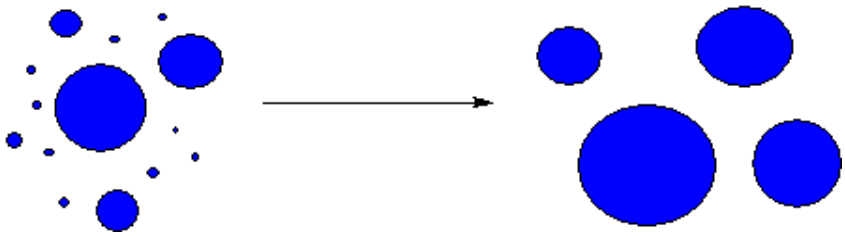

**Figure 1.6 – Ostwald ripening: larger particles grow at the expense of smaller particles**

As outlined in the discussion on the oxidation state of Pd in allylic alcohol selox, valency is an important factor in catalysis and *in situ* changes in oxidation state can render the catalyst ineffective. Often catalysts are "re-activated" and recovered through reduction pre-treatments, which can also remove any reversibly bound poisons on the surface.[91-95] However, irreversibly bound poisons, such as the build up of carbonaceous species through coke deposition, can limit catalyst recyclability.[29]

Since the causes of deactivation for a particular catalyst system can be so varied, understanding the predominant source of deactivation under particular conditions could be key to improving catalyst design. For example, the nitrile hydrogenation reaction considered here is performed under hostile acidic conditions because the amine product is an established catalyst poison (see previous section).[75, 80] If, as a result of these conditions, particle growth is the significant cause of deactivation, then improving how the catalyst is stabilised and supported could inhibit deactivation. Alternatively, if particle growth has minimal effect compared to chemical poisoning, varying electronic and geometric structure of the adsorption surface may improve the catalyst longevity.[96] This is discussed further in *Section 1.4*.

An example where understanding the cause of deactivation has coincided with research into catalyst design is that of allylic alcohol selox over palladium. In *Section 1.1.2.2* it was highlighted that the nature of the active site in these catalysts is debated.[28] The issue is an important one due to the relationship between deactivation and oxygen in the catalytic system. So called over-oxidation has been considered as one cause for the observed deactivation implying that, in order to prevent deactivation, metallic Pd particles must be used and maintained. However, it has also been noted that poisoning by accumulation of CO is an issue on a metallic surface.[68] This has led to detailed investigation into the role of oxygen.

Baiker and collaborators proposed in 2002 that oxygen was involved in removing accumulated CO through oxidation, but stated that pre-adsorbed oxygen (i.e. surface PdO) hinders, rather than promotes, catalytic activity.[66] However, Lee noted that a Pd(111) surface pre-covered with oxygen promoted desorption of crotonaldehyde, thus preventing the accumulation of CO on the catalyst surface in the first place.[29] It was then necessary, after this surface science study, to test the notion that oxidic particles would perform better as a catalyst and not deactivate so rapidly. Since surface oxide is more stable on smaller particles, designing a catalyst in which the metal dispersion would be high should result in small oxidic particles. This has been achieved using a high surface area support that could stabilise the small particles. In fact, highly oxidic Pd supported on mesoporous-alumina was found to be extremely active towards allylic alcohol selox.[28] It is still of interest, however, to consider the performance of these catalyst under *in situ* spectroscopic investigation, in order to assess the role of oxygen in preventing deactivation and driving selectivity.

## 1.3 Catalyst reaction dynamics

The model of a static catalyst surface, driving reaction kinetics continuously under reaction conditions, is unrealistic and this "black box" understanding of catalysis limits the scope of rational design. However, there are countless conditions in the reactor that will influence catalyst structure and reactivity, such that realising catalyst dynamics *in situ* is an immense task. The development of techniques where the physical and chemical properties of catalysts can be studied in real-time, so called "operando" conditions, has much scope for uncovering these complex processes.[43, 67, 97] In the following section some examples are given of experiments utilising XAS, a powerful technique for operando spectroscopy, and the impact of such research is briefly reviewed.

The application of XAS for *in situ* analysis has received considerable attention. Technical details of this technique are discussed in *Chapter 2* but briefly put, XAS is a non-destructive hard X-ray technique that can be used, under ambient conditions and with up to millisecond timescale resolution, to probe catalyst structure and acquire information such as average coordination numbers, oxidation state and bond distances.[97, 98]

Through the application of *in situ* XAS and operando Fourier-Transform Infra-red spectroscopy (FTIR), details of the dynamic active site in Bi-promoted oxidation catalysts, and the effect of sulphur poisoning on Pt have been revealed.[99, 100] B. Kimmerle and co-workers have recently utilised operando XAS and IR thermography in order to spatially resolve changes across a $Pd/Al_2O_3$ catalyst bed.[101]

Integrating operando spectroscopy with XAS is of particular interest in the relationship between catalyst stability, the reaction progress and its outcome. Research on the effects of metal reducibility, primarily elucidated from XAS, has been used to further understand catalyst mechanisms on the promotion effects of metals and metal oxides to the catalyst. The stability of reduced metal sites and the capacity of the catalyst to store oxygen are both revealed to be important factors in driving high activities in a study on Pd doped $Cu/CeO_2$ catalysts and K doped Co catalysts. In both cases the promoter metal leads to a less reducible and more active catalyst.[102, 103] In these, and other examples, support effects were also studied. The mobility of oxygen in a ceria support diminishes the metal reducibility. The redox stability of PdO is reported to be increased in one example of a ceria supported catalyst.[104] A highly reducible

catalyst can thus be advantageous for meeting the requirements of the reaction, or will alternatively be implemental in the catalyst deactivation as a result of its poor stability.

This research has been taken a step further in achieving the real-time observation of catalyst reducibility in a number of studies over rhodium catalysts that have been carried out at the ESRF beamline, ID24, that emphasise the versatility of the technique. Energy dispersive XAS (EDXAS) has been used here to follow oxidation/reduction kinetics of Rh and $Rh_2O_3$ catalysts and to deduce the surface species involved in the formation of $N_2O$ in NO oxidation over Rh.[105, 106] Also, local structure of the surface species in NO and CO oxidation reactions over Rh have been described, where a clear diagram of the experimental setup is illustrated and is also shown here, adapted, in *Chapter 4*.[107] Also in *Chapter 4*, experiments developed using EDXAS at ID24, on a series of palladium catalysts for vapour phase crotyl alcohol selox, are described and further evidence is provided that the catalyst is dynamic and that this influences reactivity.

# 1.4 Catalyst design

## 1.4.1 Tailoring nanoparticle size and shape

### 1.4.1.1 Surface science studies

Model studies, using computational techniques and ultra-high vacuum (UHV) single crystal catalysts, have provided useful information on the interaction of alcohols and nitriles with solid surfaces, but only under pristine environments unrepresentative of practical catalysts operating at pressure and temperature in the liquid phase.[13, 29] This work aims to bridge the pressure and material gaps between such fundamental research and commercial processes, through the use of size- and shape-controlled metal nanoparticles and powerful analytical tools to study 'working catalysts in action'. Designing metal nanoparticles that exhibit controlled morphology make it possible to tune factors such as the type of exposed facet (see *Figure 1.7*).

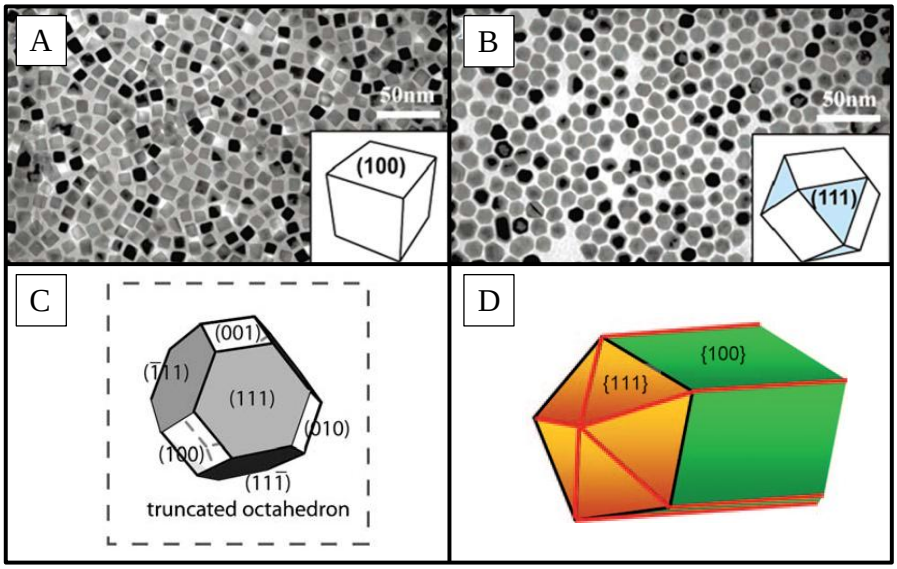


**Figure 1.7 – Controlling nanoparticle shape can be used to tune the exposed facets: Pt nanocubes exposing (100) facets (A) and Pt cuboctahedra (B) reproduced from reference 136; the facets of a truncated octahedron (C) reproduced from reference 122 and a fivefold twinned rod (D) reproduced from reference 135**

Palladium metal has a face-centred cubic (fcc) crystal structure, with a bulk average coordination number of 12 (i.e. each Pd atom has 12 nearest neighbours) and the lowest index facets increase in energy from Pd(111) < Pd(100) < Pd(110).[108, 109] The thermodynamically stable shape the Pd nanoparticle will adopt is a cuboctahedron, comprising Pd(111) and Pd(100) facets.[110, 111] The fcc crystal structure and cuboctahedron shape are shown in *Figure 1.8*. If the conditions when synthesising the nanoparticles are controlled, it is possible to form Pd icosahedra or octahedra, entirely terminated by Pd(111) facets, or Pd cubes enclosed solely by Pd(100) facets.[112, 113] The effect of these properties on a reaction can then be assessed and compared with information already acquired from UHV studies, thus providing a bridge between low pressure catalyst models and understanding of the catalyst in environments more similar to those in the plant.

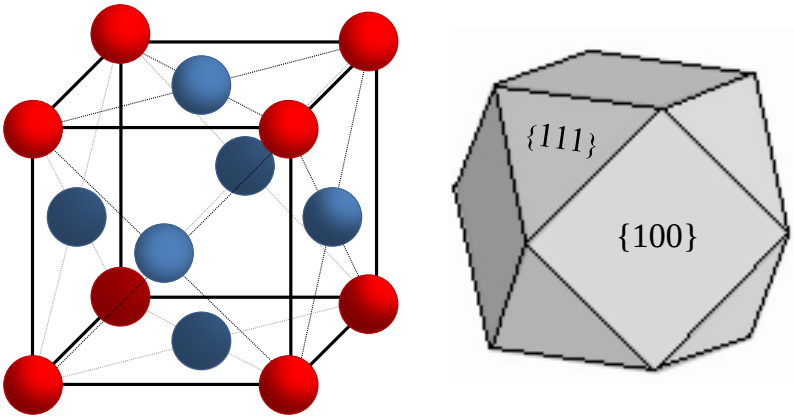


**Figure 1.8 – The face-centred-cubic unit cell (left) and the facets and geometry of a cuboctahedron (right)**

Before considering the synthesis of such novel metal nanoparticles, surface science studies that demonstrate surface structure sensitivity over low index facets is outlined. In previous sections crotyl alcohol selox over a Pd(111) surface has been described, although there has been no explanation of this reaction over the other low index palladium facets, Pd(110) and Pd(100).[29] Surface science studies of reactions over the three low-index facets of Pd show differences in reactivity that are structure sensitive. E. D. Wang et al. studied ethanol oxidation using DFT and found that Pd(100) catalyses ethanol dehydrogenation most efficiently.[114] Investigation into the structure sensitivity of methane combustion reveals that adsorption energies of reactants and intermediates differ for low coverages of oxygen and bare metal, but the reaction is independent of structure over oxidic Pd surfaces.[115] Additionally it has been found that Pd(100) is most reactive towards CO oxidation.[116] Further details of oxygen and CO interactions with Pd surfaces are considered in *Chapter 3*. It is clear from this brief introduction that surface structure can potentially influence catalytic reactivity significantly.

### 1.4.1.2 Synthesis

The synthesis of noble metal nanoparticles displaying controlled morphology is a rapidly developing area of research, including applications of such nanoparticles in the study of optical properties, sensor technologies, spectroscopic applications, as well as catalysis.[117-122] The synthesis of nano-cubes,[123-125] nano-polyhedra,[126-128] anisotropic nanoparticle shapes[129-132] and even nanocages[133] has been recorded in recent literature. There are several methods for synthesising nanoparticles that have been developed,

ranging from sol-gel methods, co-precipitation, synthesis through microemulsions and liquid crystal templates, electrochemistry and other related routes.[134] The focus here will be on the relatively undemanding process of synthesising nanoparticle colloids through kinetically controlled reduction of the metal salt precursor.

Even within the past two years there has been an explosion of research into the controlled synthesis of metal nanoparticles and further examples can be found in various reviews on the subject.[122, 135, 136] However, despite the many varied methods for developing different nanoparticle shapes, there are very few examples where synthesis has been attempted on > mg scale. One of the most recent examples of shape control on Pd particles at the time of writing, an extremely shape selective synthesis of Pt-Pd nanoicosahedra, used only 0.015 mmol of each metal salt, resulting in a maximum yield of around 4.5 mg of metal.[137] Achieving the control required and obtaining shape and size monodispersity on a large scale, is still a relatively overlooked challenge.

A. R. Tao et al., have reviewed some of the successful syntheses of various noble metal nanoparticles displaying shape control, including those methods developed by his own group (see *Figure 1.9*).[122] The examples outlined in the following paragraphs highlight some of the synthetic considerations required in achieving controlled nanoparticle synthesis. Following this, an interesting recent study using small angle X-ray scattering (SAXS) is described in which the nucleation and growth process for nanoparticle synthesis is explored.

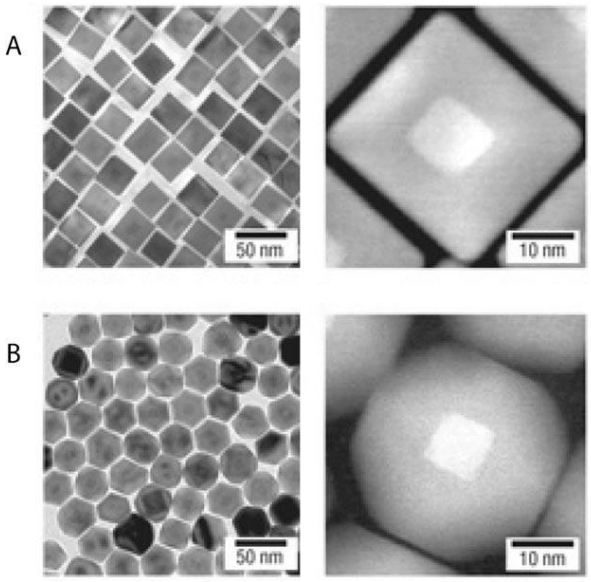


**Figure 1.9 – Cubic Pt seeds used to control the morphology of a Pd shell, showing cubes (A) and cuboctahedra (B). Reproduced from reference 122**

If a lot of energy is put into the synthesis, for example through using a relatively high temperature or a strong reductant, the thermodynamically stable nanoparticles will form. These tend to be larger, so that the surface area is reduced, and cuboctahedron in shape. This shape is the most stable as it contains only low energy facets, and for the fcc structure of metals such as Pd, Pt and Au, it is the least strained polyhedron shape. [135, 138, 139] Thus, to achieve size and shape control, kinetic control of the reaction is required. Fundamentally, this means employing mild reductants and temperatures: reducing agents such as citric acid, water and ethylene glycol are often used. However, there are many other conditions that must be monitored and that will affect the particle shape, including the reaction time, reductant and precursor concentration, the nature of the capping agent, the stirring rate and the addition rate. In their review, Tao and collaborators also discuss how these reaction conditions affect particle growth. The rate of addition is of particular importance as it governs the instantaneous relative precursor and reductant concentrations. This can control the rate of the nucleation process; only if this rate is kept constant is it possible to form a monodisperse colloid.[122] Y. Xia et al. also discuss the importance of precursor concentration in their review and this is illustrated in *Figure 1.10*.[135]

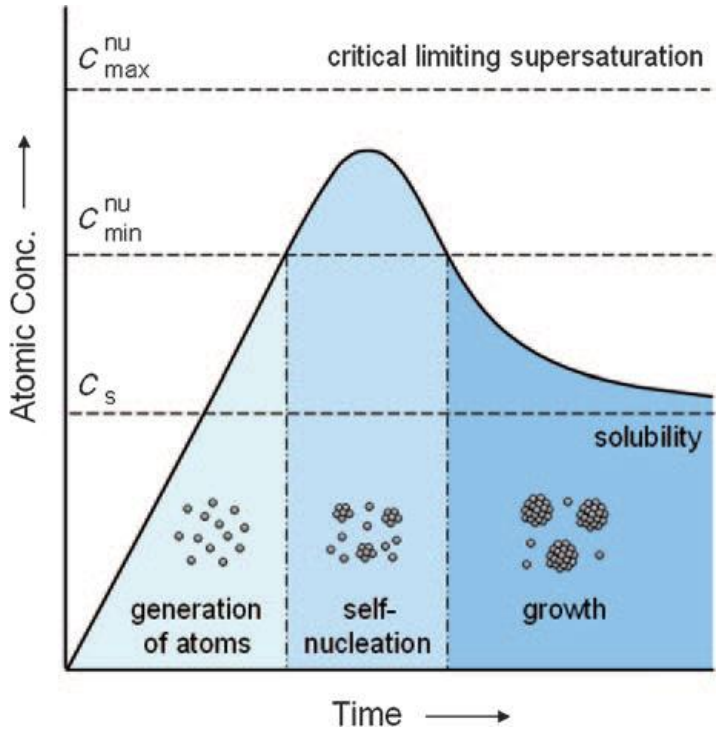


**Figure 1.10 – Metal concentration and the critical concentrations required for nucleation and growth as described by Y. Xia and collaborators in reference 135**

M. M. Koebel et al. achieved size tuneable platinum nanoparticles through controlling the precursor concentration.[140] Nucleation was induced using NaOH to form seeds and, by ensuring the precursor concentration was kept low, growth of the seeds would occur in preference to further nucleation. Another group successfully attained size control on Au nanoparticles through temperature variation by using N,N-dimethylacetoacteamide as both a reductant and stabiliser.[141] This molecule forms a keto-enolate structure that is able to displace the $Cl^-$ ions from the $HAuCl_4$ precursor and forms a chelated gold ion, shown in *Figure 1.11*. This slows down the reduction rate, ensuring kinetic control of the reaction.

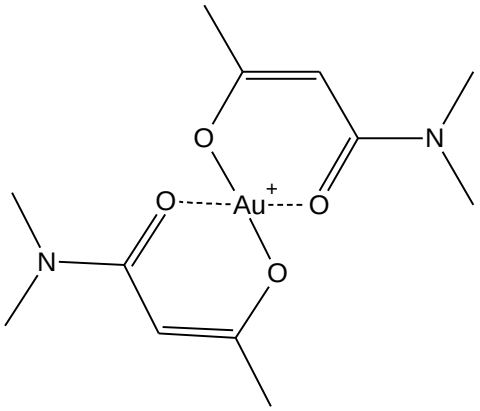


**Figure 1.11 – β-diketonate structure formed on displacement of $Cl^-$ ions from $HAuCl_4$ precursor reacting with N,N-dimethylacetoacetamide**

The formation of size tuneable gold nano-octahedra is another interesting example (*Figure 1.12*). C. Li et al. used poly(dialkyl dimethylammonium) chloride (PDDA) as a stabiliser in the formation of these nanoparticles.[126] This adsorbs to the {111} planes preferentially, increasing the growth rate in the <100> direction. Ethylene glycol contributes to the stepwise reduction of $AuCl_4^-$ via $AuCl_2^-$ to $Au^0$, which provides the kinetic control required to make these strained polyhedra. By adjusting the pH of the reaction, size control was possible: a lower pH decreases the reduction rate allowing more time for the nanoparticles to grow.

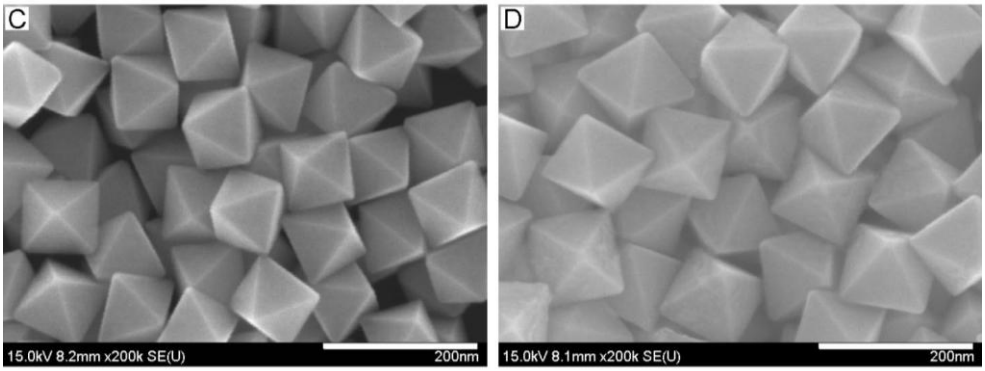


**Figure 1.12 – Scanning electron microscopy images of Au octahedra with edge lengths of 95 nm (A) and 110 nm (B). Reproduced from reference 126**

The final three examples of shape control that will be discussed here have been attempted and adapted later on in this project for applications in catalysis. The first example concerns the synthesis of palladium icosahedra (*Figure 1.13*). Reaction time and temperature were used to control size, although it was noted that a change in temperature affected the monodispersity of the sample. Citric acid was used as a reductant, which is thought to block the oxidative etching process that is attributed in this work to be responsible for the growth of (100) facets. It is proposed by Xia that oxidation on the surface ordinarily promotes growth in certain directions so that structures that are less strained, such as the cuboctahedron, preferentially form. Citric acid, however, binds strongly to the surface and the authors suggest it competes with oxygen adsorption. So oxidative etching does not occur, and under a slow growth regime, a multiply twinned particle with 20 (111) faces is formed.[113]

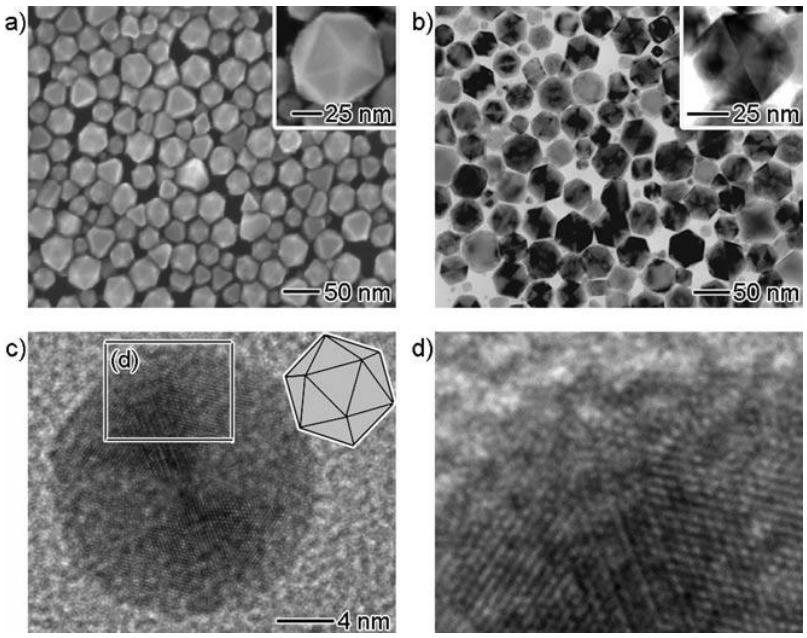


**Figure 1.13 – SEM (A), TEM (B) and HRTEM (C and D) micropgraphs of Pd icosahedra as synthesised by Y. Xiong et al. Reproduced from reference 113**

The next example involves the synthesis of palladium nanorods and nanobars displayed in *Figure 1.14*. In this case oxidative etching is promoted by adding KBr to the reaction mixture. The precursor, KBr and the stabiliser are slowly and simultaneously added to ethylene glycol and water to control the nucleation of seeds, followed by controlled anisotropic growth as a result of the presence of KBr. In this case the respective concentrations of ethylene glycol and water control the reduction rate and thus the size and shape, as water is a weaker reductant.[111]

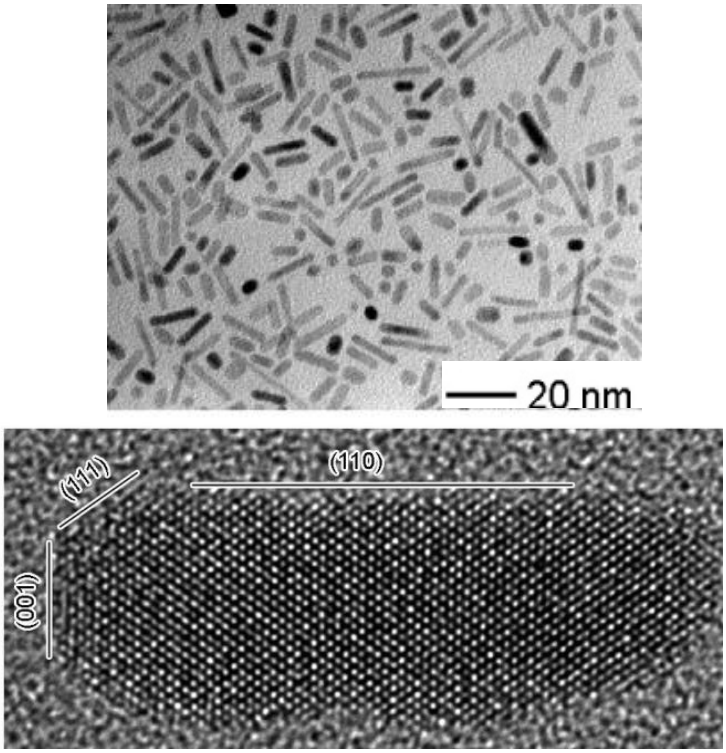


**Figure 1.14 – TEM micrograph of Pd nanorods (top) and HRTEM image of a single nanorod recorded along [110] as synthesis by Y. Xiong et al. (bottom) Reproduced from reference 111**

The final example that will be considered is that of the synthesis of Pd nanocubes, shown in *Figure 1.15*. F. R. Fan et al. report the synthesis of Pd nanocubes and Pd nanodendrites, controlling the morphology between the two species by varying the concentration of halide salt. Two procedures are used which result in particles of different size. Although in the first example the CTAB stabiliser and $Na_2PdCl_4$ precursor are mixed before addition, and in the second example the two components are kept separate and added simultaneously, it is likely that size differences are due to the different addition rates and methods adopted for the two procedures. The authors suggest that nanoparticles form through an intermediate complex produced from CTAB and $Na_2PdCl_4$, and it is at this stage that further halide concentration influences particle shape.[123]

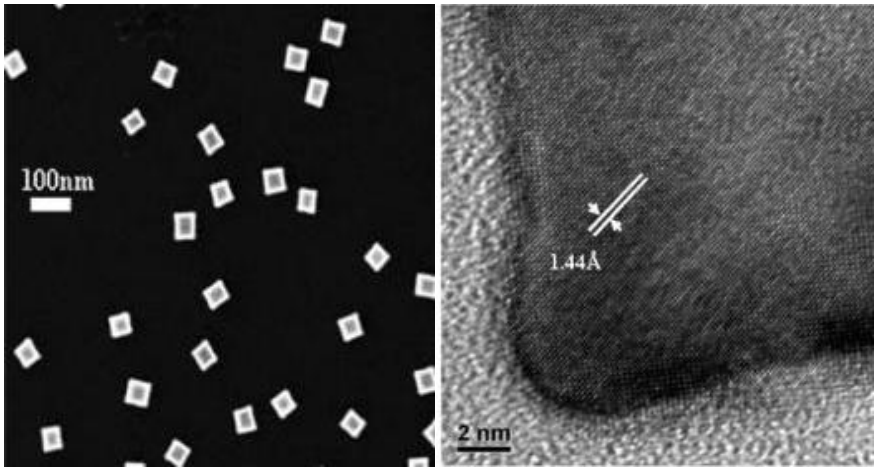


**Figure 1.15 – SEM image of Pd nanocubes (left) and HRTEM image of a single cube (right) as prepared by F. R. Fan et al. Reproduced from reference 123**

The delicate control required in nanoparticle synthesis, and the very limited understanding in how morphology control is achieved, make it a very unpredictable science and factors as diverse as geographical location* and glassware have been known to affect the outcome of a particular synthesis.[142] Jorg Polte and collaborators have developed a technique for studying the poorly understood nucleation and growth process of metal nanoparticle synthesis. By using combined small angle X-ray scattering (SAXS) and X-ray absorption near edge spectroscopy (XANES), they have followed both the classic synthesis of Au nanoparticles using citrate stabiliser and the rapid synthesis of small Au nanoparticles using $NaBH_4$ reductant in the absence of stabiliser. In the first study, the authors propose a four stage model for nanoparticle formation and growth: rapid nucleation, coalescence of the reduced particles accompanied by slow reduction of further precursor, further growth by diffusion of reduced particles and finally rapid reduction and growth from the remainder of the precursor once the particles are greater than approximately 5 nm. The second study confirms the significance of the initial reduction of precursor and nucleation followed by coalescence of the existing reduced particles.[143, 144]

* In her talk entitled "Colloidal inorganic nanocrystals: shape and evolution" at the 240th ACS national Meeting, Boston, C. Murphy remarked that on moving laboratory from South Carolina to Illinois, the same student, using the same apparatus and the same procedure consistently synthesised different nanoparticles in the new location.

### 1.4.1.3 Reactions using morphology controlled nanoparticles

Within the field of catalysis there has been significant progress towards testing and understanding nanoparticle size effects, notably on the dramatic effect of gold nanoparticle size on catalytic activity, but also more generally throughout heterogeneous catalysis.[145-148] Investigation into the influence of nanoparticle shape on catalytic reactivity is considerably rarer; challenges in achieving shape control for application in catalysis have only been met in the last few years.[136]

Significant work has been carried out by R. Narayanan and co-workers on a comparison of Pt tetrahedra, cubes and spheres in the activity of the electron-transfer reaction. Catalysis was found to be shape dependent, although shape changes were observed *in situ* which correlated with changes in reactivity. For these small (< 10 nm) particles, the variation in catalytic activity was attributed to the proportion of corner and edge sites and not the exposed facets.[149, 150] Further studies on the shape-dependence of Pt catalysed reactions have been carried out by X. Gong et al. using branched and polyhedral nanoparticles for methanol oxidation, whereby an enhancement in activity is observed for the more defective branched particles.[151]

The above examples illustrate that Pt is an attractive metal to study because it has been found to be one of the easiest metals for which size and shape can be manipulated. Also, the exposed facets of Pt are clearly distinct in electrochemistry studies, and catalytic activity can be tested on minimal quantities of sample in relatively simple experiments. However, the wide range of applications of palladium as a catalyst, mean that comparable research on morphology dependence is underway.[136] In citral and cyclohexene hydrogenation, Pd multipods and tetrahedra were found to be more active than Pd spheres (*Figure 1.16*).[152] Dendritic Pd nanowires exhibited different electro-activity and increased resistance to poisoning.[153]

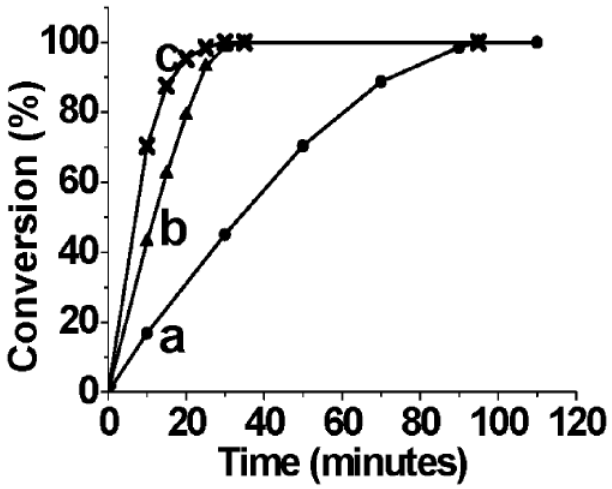


**Figure 1.16 – Example reaction profile showing morphology dependence of Pd spheres (a), Pd tetrahedra (b) and Pd multipods (c) on cyclohexene hydrogenation. Reproduced from reference 152**

In the examples so far, the variation in reactivity has been ascribed to differences in the number of defects, edge and corner sites. However, controlling particle size does not only affect the number of low-coordination sites, and particularly for reactions that occur on terraces, the atomic arrangement may be crucial in governing catalytic activity and selectivity. To this end, there have been many model studies that use simulations and single crystals, introduced in *Section 1.1.2.2*. For larger polyhedral nanoparticles, where the terrace sites are a more dominant feature, it is possible that shape controlled synthesis, where cubic structures expose (100) fcc facets and tetrahedral structures expose (111) fcc facets, could be used to translate the model studies to ambient gas-phase, and especially liquid phase, conditions. This type of study has been carried out by J.C. Serrano-Ruiz et al. using carbon-supported Pt(111) and Pt(100) approx. 10 nm particles on the selective hydrogenation of crotonaldehyde and cinnamaldehyde. After carefully characterising the exposed facets, and accounting for differences in average coordination number to confirm the importance of the terrace sites over the edges and corners, the authors show that consistently for both molecules Pt(100) is more active than Pt(111). The latter is more selective towards the unsaturated alcohol, however. This difference in selectivity is explained due to the planar orientation of the aldehyde unsaturated C=C bond on Pt(100) such that the π-bond is weakened and more prone to hydrogenation. This orientation is less favourable on Pt(111).[154]

In addition, an electrochemical approach over bimetallic Pd-Pt(111) tetrahedra and (100) cubes reveals that the reactive pathways of the (100) and (111) faces in

methanol oxidation are different. The (111) facet is found to be more resistant to poisoning and the (100) facet is more active.[155] By using a larger particle size range to minimize the effect of defect sites, L. Piccolo and co-workers observe that the activity of butadiene hydrogenation under UHV conditions over α-alumina supported Pd nanoparticles decreases with decreasing Pd(111) sites.[156]

Thus, the synthesis of shape controlled Pd nanoparticles provides the opportunity to consider the effect of different facets on reaction activity/selectivity under realistic conditions. In this work, the shape dependence of liquid phase, aerobic crotyl alcohol selox to crotonaldehyde (*Scheme 1.1*), a precursor to the food preservative sorbic acid, over a series of Pd icosahedra (111), rods (110) and cubes (100) is shown.

## 1.4.2 Bimetallic catalysts

### 1.4.2.1 Surface science studies

As with the controlled design of nanoparticles of different morphology and their application in catalytic chemistry, there has been a wealth of recent research into designing bimetallic catalysts with improved performance. This was introduced in the first sections of this chapter, and here a consideration of the surface chemistry of Au/Pd bimetallic catalysts will be discussed.

The catalysis of gold and palladium as monometallic species has already been outlined, and as a bimetallic system these metal have both exhibited excellent catalytic activity for numerous reactions and make an interesting system to study the effect of alloying on catalysis.[157] Au and Pd are completely miscible, very similar in size with only a slight lattice mismatch, and have similar surface energies (Pd 2.05 J $m^{-2}$; Au 1.63 J $m^{-2}$).[158] Thus it is possible to tune alloy composition, and examine the influence of increasing gold concentration in a palladium catalyst.

An interest in understanding the structure and reactivity of alloyed catalysts is reported as early as the 1950s.[159] Both electronic and geometric effects were considered relevant to the understanding of catalytic reactions, and with the onset of powerful research tools such as computational modelling, these theories can be explored with increasing depth to aid understanding of catalyst structure-reactivity relations. M. Neurock et al. use density functional theory (DFT) calculations and Monte Carlo

simulations to examine the two factors that will lead to changes in the catalyst surface. Namely these are the geometry of the active site (i.e. preferentially isolating Pd single sites or dimers) and the local electronic structure, whereby the charge density of the Pd d band is slightly reduced or increased through charge transfer. In their study, they show that the electronic effect is negligible, that sites required for hydrogen activation are deactivated by gold diminishing non-selective ethylidyne formation during ethylene hydrogenation.[96] This is illustrated in *Figure 1.17*.

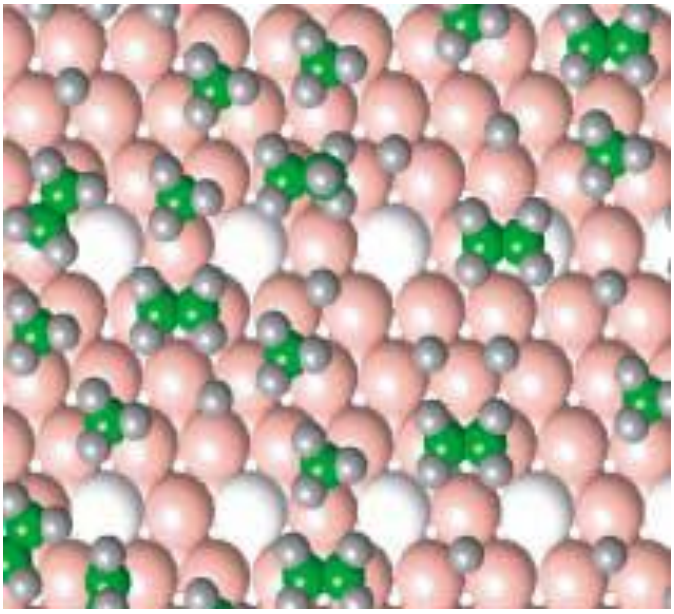

**Figure 1.17 – Snapshot of DFT calculation for ethylene hydrogenation over a $Pd_{87.5\ \%}$ (pink) – $Au_{12.5\ \%}$ (white) surface. Ethylidyne and hydrogen both adsorb on Pd 3-fold hollow sites. Reproduced from reference 96**

In a high throughput study on the effect of gold composition in a Pd/Au alloy surface, for the hydrogen evolution and hydrogen oxidation reactions, it is revealed that particular palladium ensembles display varying reactivity. The authors report that Pd monomer sites, which are dominant when concentrations of Au are high, cannot activate $H_2$ and so hinder the hydrogen oxidation reaction. These are, however, a source of increased activity for the reverse hydrogen evolution reaction. This is another example of a study in which the geometric effects of alloying Pd and Au can tune catalysis.[160]

Alloying palladium catalysts with gold offer the ability to tune surface reactivity, direct selectivity and develop catalysts less susceptible to deactivation. Further to the study of the Pd(111) surface, Lee and collaborators considered the reactivity of crotyl alcohol over Au/Pd(111) leading to improved selectivity to

crotonaldehyde. This study is considered in some detail in *Chapter 5*, as a comparison between tuning model conditions and tuning a liquid phase core-shell nanoparticle catalyst. In addition to this work, the interaction of crotonaldehyde and propene with Au/Pd(111) was explored.[161] In the absence of any Au, crotonaldehyde was found to undergo decarbonylation at room temperature and at elevated temperatures dehydrogenation of propene occurred. Although crotonaldehyde desorption was found to be enhanced at low Au concentrations, it was only at high concentrations that both secondary pathways no longer ensued – concentrations at which alcohol oxidation would not occur. Thus it would appear that Au composition is fundamental to achieving optimum catalytic performance in this case: too much and activity will suffer, too little and selectivity and longevity will be compromised.

#### 1.4.2.2 Gold-palladium bimetallic nanoparticles

Further to the discussion in *Section 1.4.1.2*, the formation of core-shell structured Au/Pd bimetallic colloids will be considered. Early studies mainly consisted of palladium shell, gold core structures, where a standard gold sodium citrate sol is made up in dilute conditions using or adapting the method developed by Turkevich et al. in the 1950s.[162] In fact, Turkevich and G. Kim developed this method themselves for the formation of core-shell colloid synthesis in 1970 by carefully controlling the pH and addition rate of the palladium acid added to the gold sol.[163] J. B. Michel and J. T. Schwartz used this same procedure to synthesise gold coated palladium colloids, and G. Schmid developed the same method to form Au/Pd core shell colloids stabilised with $P(m\text{-}C_6H_4SO_3Na)_3$ surfactant instead of just sodium citrate.[164, 165] Schmid further discusses the synthesis of these nanoparticles in a review on the synthesis of metal clusters and colloids in 1992.[166]

There are two more recent, interesting examples of the synthesis of core-shell structures that will be addressed here. In the first example, the authors successfully controlled particle size and the thickness of the Pd shell. They prepared Au seeds of varying sizes and, after making dilute solutions of these seeds, added a range of known concentrations of $H_2PdCl_4$. This was slowly reduced by the controlled addition of ascorbic acid using a syringe pump. A low temperature was used so that there would be no intermixing of the two metals. The reaction mixture was stabilised using sodium citrate.[167] The other example used well defined faceted cubic Pt seeds to direct the growth of a Pd overlayer to form shape controlled core-shell Pd/Pt structures (see

*Figure 1.9*). Ascorbic acid was once again used as the reductant for $K_2PdCl_4$ with tetradecyltrimethylammonium bromide (TTAB) surfactant. Oxidative etching was once again utilised to direct growth and control the shell shape: $NO_2$ is thought to deposit adsorbed oxygen onto the surface resulting in a more active surface for growth.[168]

There have been many developments in the controlled synthesis of metal nanoparticles, although there are fewer studies in the synthesis of shape controlled core-shell nanoparticles. There are also still limitations in the synthesis of the core-shell structures since the majority of the methods discussed above only produce small amounts of product from dilute conditions on the litre scale. Thus, preparing sufficient product for characterisation and further applications in catalysis is still a difficult task, particularly if monodisperse nanoparticles are required.

#### 1.4.2.3 Reactions using Au/Pd bimetallic nanoparticles

Reactions that use bimetallic catalysts have been investigated for numerous systems for a number of decades, although the specific application of gold as a promoter metal has seen considerably more attention recently with the discovery of gold as an active catalyst (see *Section 1.1.2.1*).[53, 56, 159, 169] Gold has been found to improve catalyst activity, selectivity and longevity in various cases, and as a result the Pd-Au bimetallic system has been tested for a wide range of reactions.

The effect of metal composition for bimetallic Au-Pd structures has been tested for reactions from CO oxidation[170-172] and $H_2O_2$ synthesis[173-176], to cross-coupling reactions[177, 178], alcohol oxidations[57, 61, 179, 180] and organic block chemical synthesis[56]. It has been noted in many of these studies that the surface composition is not a homogeneous alloy, but that a core-shell structure with a palladium rich shell forms.[180, 181] Thus, it is important to assess surface composition, not just bulk composition, in the study of bimetallic catalyst reactivity. A theoretical study by J. Zhang et al. predicts that for CO oxidation, a gold rich shell will be more active because of the adsorption properties of the two metals. The CO adsorption site on pure Pd is reported to dominate over fcc hollow sites, whereas this changes to atop sites on increased Au concentration.[172] There have been few experimental studies using Au rich shells: it has generally been found that without using sequential steps in the synthesis that stabilises the Pd core, a Pd rich shell will form. This is thought to be a result of the stabilising nature of adsorbates on the Pd surface.[181]

Of specific interest here are the reasons outlined as to why the promoter effects of Au are seen. This is discussed briefly in *Section 1.4.2.1*, but here a number of examples relating to the bimetallic catalyst reactivity are outlined. S. Marx et al. consider the selective oxidation of benzyl alcohol over Au-Pd bimetallic catalysts and study the catalyst using XPS and XANES to analyse changes in the electronic structure.[182] The most selective catalyst contains Au and Pd metals in a ratio of 1:9. In this combination the electronic configuration of the metals is distorted. The Au 5d band is more filled in this alloyed composition than as pure metal, the authors explain that this would increase the density of states near the Fermi level and, therefore, adsorbate strength will be higher. W. Hou and collaborators, on their study of the same reaction, talk of the Au atoms withdrawing electron density from the Pd atoms.[61] They quote an Au:Pd ratio of 1:3 with the highest TOF for benzyl alcohol selox. These experiments isolate the electronic structures of the mono and bimetallic catalysts, and show that there may be a relationship between fine tuning the catalyst electronic structure and reactivity. However, *operando* investigation, which correlates holistically all the variables in the bimetallic catalyst, is imperative to further understanding in this field. Experiments, such as those introduced in *Section 1.3* and described in *Chapter 4*, can be developed to uncover the specific properties of gold that lead to such a significant enhancement in catalyst performance for so many systems.

## 1.5 Conclusion

The potential of selective heterogeneous catalysis, for meeting the demands of future sustainable chemical production, is evident from the examples outlined in this introduction. However, the current limitations in catalyst performance and synthesis towards highly active, selective, recyclable and economically viable systems are also clear. Thus, detailed understanding of catalyst structure-reactivity relations and routes of rational catalyst design are crucial developments required in this field.

Two specific reactions have been considered here: crotyl alcohol selective oxidation and benzyl cyanide hydrogenation. The surface chemistry and mechanism of crotyl alcohol selox have been outlined in some detail. This reaction was chosen as it is relatively simple, while still offering selective pathways and exhibiting deactivation. It has also already been extensively studied. There has been limited investigation into the

catalysis of benzyl cyanide hydrogenation however, and this reaction is considered in this thesis as an example of a problematic, industrially relevant system that requires rational catalyst design to improve primary amine production.

Catalyst deactivation is a significant problem and has many potential sources. In order to tailor a catalyst to overcome these issues, the sources of deactivation need to be identified. Following the catalyst performance *in situ*, under *operando* conditions, can also be used to detect the components of the catalyst structure that direct reactivity or lead to deactivation, so that these components can be tuned in designing the catalyst.

This thesis focuses on tailoring the metal structure and composition; support considerations are generally ignored. Electronic and geometric properties of the catalyst can be tuned by changing the metal size, shape and bimetallic composition. Surface science studies have provided significant fundamental information, but these studies have their limitations. A number of examples have been highlighted that utilise tailored nanoparticles for reactions under ambient conditions and under more hostile reaction conditions, showing that these electronic and geometric factors do influence catalyst performance.

So, the effect of catalyst morphology and Au promotion for Pd reactivity in crotyl alcohol selox is studied systematically in this thesis, alongside model data already obtained for this reaction. Crotyl alcohol selox over a series of further Pd catalysts are studied using operando spectroscopy in order to isolate time-resolved structure-reactivity relations. Finally, the reaction of benzyl cyanide hydrogenation over Pd/C is extensively characterised and the key sources of deactivation are identified. This system is considered in light of the structure-reactivity investigations of the tailored catalysts.

## 1.6 References


1. K. Sanderson, *Nature*, 2011, **469**, 18.
2. C. Stanier and J. Hutchinson, *A Sustainable Global Society*, Chemical Sciences and Society Summit (CS3), 2011.
3. *BBC News, Nottingham University to get 'green' chemistry lab - 30/11/2010*, http://www.bbc.co.uk/news/uk-england-nottinghamshire-11875584, Accessed 17/02/2012.
4. P. T. Anastas and J. C. Warner, *Green Chemistry: Theory and Practice*, Oxford University Press, Oxford, 2000.
5. R. A. Sheldon, *Pure Appl. Chem.*, 2000, **72**, 1233.
6. P. Atkins and H. de Paula, *Elements of Physical Chemistry*, Fourth edn., Oxford University Press, Oxford, 2005.

7. G. Rothenberg, *Catalysis: Concepts and Green Applications*, Wiley-VCH, Weinheim, 2008.
8. G. J. Hutchings, *J. Mater. Chem.*, 2009, **19**, 1222.
9. J. M. Thomas, *J. Chem. Phys.*, 2008, **128**, 19.
10. C. P. Vinod, K. Wilson and A. F. Lee, *J. Chem. Technol. Biotechnol.*, 2011, **86**, 161.
11. J. C. Bertolini, *Catal. Today*, 2008, **138**, 84.
12. J. Durand, E. Teuma and M. Gomez, *Eur. J. Inorg. Chem.*, 2008, 3577.
13. G. A. Somorjai and C. J. Kliewer, *React. Kinet. Catal. Lett.*, 2009, **96**, 191.
14. C. Chapuis and D. Jacoby, *Appl. Catal. A-Gen.*, 2001, **221**, 93.
15. R. A. Sheldon, *Pure Appl. Chem.*, 1998, **72**, 1233.
16. J. Rostrup-Nielsen, *Catal. Today*, 2006, **111**, 4.
17. T. Mallat and A. Baiker, *Chem. Rev.*, 2004, **104**, 3037.
18. T. Punniyamurthy, S. Velusamy and J. Iqbal, *Chem. Rev.*, 2005, **105**, 2329.
19. P. Gamez, I. Arends, R. A. Sheldon and J. Reedijk, *Adv. Synth. Catal.*, 2004, **346**, 805.
20. K. M. Gligorich and M. S. Sigman, *Chem. Commun.*, 2009, 3854.
21. R. A. Sheldon and I. Arends, *Adv. Synth. Catal.*, 2004, **346**, 1051.
22. H. J. Guo, W. D. Liu and G. C. Yin, *Applied Organomet. Chem.*, 2011, **25**, 836.
23. N. Zotova, K. Hellgardt, G. H. Kelsall, A. S. Jessiman and K. K. Hii, *Green Chem.*, 2010, **12**, 2157.
24. M. Angelin, M. Hermansson, H. Dong and O. Ramstrom, *Eur. J. Org. Chem.*, 2006, 4323.
25. A. Dijksman, A. Marino-Gonzalez, A. M. I. Payeras, I. Arends and R. A. Sheldon, *J. Am. Chem. Soc*, 2001, **123**, 6826.
26. J. M. Hoover and S. S. Stahl, *J. Am. Chem. Soc.*, 2011, **133**, 16901.
27. C. M. A. Parlett, D. W. Bruce, N. S. Hondow, A. F. Lee and K. Wilson, *ACS Catalysis*, 2011, **1**, 636.
28. S. F. J. Hackett, R. M. Brydson, M. H. Gass, I. Harvey, A. D. Newman, K. Wilson and A. F. Lee, *Angew. Chem.-Int. Edit.*, 2007, **46**, 8593.
29. A. F. Lee, Z. Chang, P. Ellis, S. F. J. Hackett and K. Wilson, *J. Phys. Chem. C*, 2007, **111**, 18844.
30. T. Harada, S. Ikeda, F. Hashimoto, T. Sakata, K. Ikeue, T. Torimoto and M. Matsumura, *Langmuir*, 2010, **26**, 17720.
31. M. J. Beier, T. W. Hansen and J.-D. Grunwaldt, *J. Catal.*, 2009, **266**, 320.
32. L. Jia, S. Zhang, F. Gu, Y. Ping, X. Guo, Z. Zhong and F. Su, *Microporous Mesoporous Mater.*, 2012, **149**, 158.
33. T. Mitsudome, Y. Mikami, H. Funai, T. Mizugaki, K. Jitsukawa and K. Kaneda, *Angew. Chem.-Int. Edit.*, 2008, **47**, 138.
34. Z. Yang, J. Li, X. G. Yang, X. F. Xie and Y. Wu, *J. Mol. Catal. A: Chem.*, 2005, **241**, 15.
35. A. Abad, A. Corma and H. Garcia, *Pure Appl. Chem.*, 2007, **79**, 1847.
36. C. Della Pina, E. Falletta and M. Rossi, *Chem. Soc. Rev.*, 2012, **41**, 350.
37. K. Kaneda, K. Ebitani, T. Mizugaki and K. Mori, *Bull. Chem. Soc. Jpn.*, 2006, **79**, 981.
38. C. L. Bianchi, S. Biella, A. Gervasini, L. Prati and M. Rossi, *Catal. Lett.*, 2003, **85**, 91.
39. S. E. Dapurkar, Z. Shervani, T. Yokoyama, Y. Ikushima and H. Kawanami, *Catal. Lett.*, 2009, **130**, 42.
40. N. Lopez and C. Vargas-Fuentes, *Chem. Commun.*, 2012, **48**, 1379.

41. C. Mondelli, J.-D. Grunwaldt, D. Ferri and A. Baiker, *Phys. Chem. Chem. Phys.*, 2010, **12**, 5307.
42. F. Wang and G. Lv, *Progress in Chemistry*, 2010, **22**, 1538.
43. A. F. Lee, J. J. Gee and H. J. Theyers, *Green Chem.*, 2000, **2**, 279.
44. T. Mallat and A. Baiker, *Catal. Sci. Technol.*, 2011, **1**, 1572.
45. A. O. Chapman, G. R. Akien, N. J. Arrowsmith, P. Licence and M. Poliakoff, *Green Chem.*, 2010, **12**, 310.
46. T. Mallat and A. Baiker, *Catal. Today*, 1994, **19**, 247.
47. G. J. Hutchings, *J. Catal.*, 1985, **96**, 292.
48. M. Haruta, T. Kobayashi, H. Sano and N. Yamada, *Chem. Lett.*, 1987, 405.
49. C. Lemire, R. Meyer, S. Shaikhutdinov and H. J. Freund, *Angew. Chem.-Int. Edit.*, 2004, **43**, 118.
50. G. Schmid and B. Corain, *Eur. J. Inorg. Chem.*, 2003, 3081.
51. J. Kleis, J. Greeley, N. A. Romero, V. A. Morozov, H. Falsig, A. H. Larsen, J. Lu, J. J. Mortensen, M. Dulak, K. S. Thygesen, J. K. Norskov and K. W. Jacobsen, *Catal. Lett.*, 2011, **141**, 1067.
52. J. J. Delgado, J. M. Cies, M. Lopez-Haro, E. del Rio, J. J. Calvino and S. Bernal, *Chem. Lett.*, 2011, **40**, 1210.
53. G. J. Hutchings, *Gold Bull.*, 2009, **42**, 260.
54. A. Chiorino, M. Manzoli, F. Menegazzo, M. Signoretto, F. Vindigni, F. Pinna and F. Boccuzzi, *J. Catal.*, 2009, **262**, 169.
55. M. Boronat, P. Concepcion and A. Corma, *J. Phys. Chem. C*, 2009, **113**, 16772.
56. E. Falletta, C. Della Pina, M. Rossi, Q. He, C. J. Kiely and G. J. Hutchings, *Faraday Discuss.*, 2011, **152**, 367.
57. N. Dimitratos, A. Villa, D. Wang, F. Porta, D. S. Su and L. Prati, *J. Catal.*, 2006, **244**, 113.
58. L. Prati, F. Porta, D. Wang and A. Villa, *Catal. Sci. Technol.*, 2011, **1**, 1624.
59. D. I. Enache, J. K. Edwards, P. Landon, B. Solsona-Espriu, A. F. Carley, A. A. Herzing, M. Watanabe, C. J. Kiely, D. W. Knight and G. J. Hutchings, *Science*, 2006, **311**, 362.
60. P. G. N. Mertens, P. Vandezande, X. Ye, H. Poelman, D. E. De Vos and I. F. J. Vankelecom, *Adv. Synth. Catal.*, 2008, **350**, 1241.
61. W. B. Hou, N. A. Dehm and R. W. J. Scott, *J. Catal.*, 2008, **253**, 22.
62. P. Miedziak, M. Sankar, N. Dimitratos, J. A. Lopez-Sanchez, A. F. Carley, D. W. Knight, S. H. Taylor, C. J. Kiely and G. J. Hutchings, *Catal. Today*, 2011, **164**, 315.
63. *USA Pat.*, US 6794540, 2004.
64. A. F. Lee, S. F. J. Hackett, J. S. J. Hargreaves and K. Wilson, *Green Chem.*, 2006, **8**, 549.
65. J. Naughton, A. Pratt, C. W. Woffinden, C. Eames, S. P. Tear, S. M. Thompson, A. F. Lee and K. Wilson, *J. Phys. Chem. C*, 2011, **115**, 25290.
66. C. Keresszegi, T. Burgi, T. Mallat and A. Baiker, *J. Catal.*, 2002, **211**, 244.
67. A. F. Lee and K. Wilson, *Green Chem.*, 2004, **6**, 37.
68. J. D. Grunwaldt, M. Caravati and A. Baiker, *J. Phys. Chem. B*, 2006, **110**, 25586.
69. *Stragetic Framework 2010-2019*, Food and Agriculture Organisation of the United Nations, 2009.
70. *Food Matters: Towards a Strategy for the 21st Century*, Cabinet Office Strategy Unit, July 2008.

71. *World Development Report: Agriculture for Development*, The World Bank, 2008.
72. E. C. Oerke and H. W. Dehne, *Crop Prot.*, 2004, **23**, 275.
73. C. Gunanathan and D. Milstein, *Angew. Chem.-Int. Edit.*, 2008, **47**, 8661.
74. Y. Y. Huang and W. M. H. Sachtler, *Appl. Catal. A-Gen.*, 1999, **182**, 365.
75. M. W. Duch and A. M. Allgeier, *Appl. Catal. A-Gen.*, 2007, **318**, 190.
76. P. Kukula and K. Koprivova, *J. Catal.*, 2005, **234**, 161.
77. P. Sabatier and J. B. Senderens, *C. R. Hebd. Seances Acad. Sci.*, 1905, **140**, 482.
78. Y. Y. Huang and W. M. H. Sachtler, *J. Catal.*, 2000, **190**, 69.
79. G. D. Yadav and M. R. Kharkara, *Appl. Catal., A.*, 1995, **126**, 115.
80. L. Hegedus, T. Mathe and T. Karpati, *Appl. Catal., A.*, 2008, **349**, 40.
81. J. Rasko and J. Kiss, *Appl. Catal., A.*, 2006, **298**, 115.
82. I. Ortiz-Hernandez and C. T. Williams, *Langmuir*, 2007, **23**, 3172.
83. R. Schlögl, ed., *Catalysis from A to Z: a concise encyclopaedia "Deactivation"*, Second, Completely Revised and Enlarged edn., Wiley-VCH, Weinheim, 2003.
84. M. Besson and P. Gallezot, *Catal. Today*, 2003, **81**, 547.
85. P. Albers, J. Pietsch and S. F. Parker, *J. Mol. Catal. A: Chem.*, 2001, **173**, 275.
86. I. H. Leubner, *Curr. Opin. Colloid Interface Sci.*, 2000, **5**, 151.
87. S. B. Simonsen, I. Chorkendorff, S. Dahl, M. Skoglundh, J. Sehested and S. Helveg, *J. Catal.*, 2011, **281**, 147.
88. M. Besson and P. Gallezot, *Catal. Today*, 2000, **57**, 127.
89. J. Panpranot, K. Pattamakomsan and P. Praserthdam, *React. Kinet. Catal. Lett.*, 2005, **86**, 141.
90. S. Abate, S. Perathoner and G. Centi, *Catal. Today*, 2012, **179**, 170.
91. P. Castellazzi, G. Groppi, P. Forzatti, A. Baylet, P. Marecot and D. Duprez, *Catal. Today*, 2010, **155**, 18.
92. N. C. Concibido, T. Okuda, W. Nishijima and M. Okada, *Appl. Catal., B*, 2007, **71**, 64.
93. N. Hickey, P. Fornasiero, R. Di Monte, J. Kaspar, J. R. Gonzalez-Velasco, M. A. Gutierrez-Ortiz, M. P. Gonzalez-Marcos, J. M. Gatica and S. Bernal, *Chem. Commun.*, 2004, 196.
94. J. H. J. Kluytmans, A. P. Markusse, B. F. M. Kuster, G. B. Marin and J. C. Schouten, *Catal. Today*, 2000, **57**, 143.
95. F. Trabelsi, F. Stuber, K. Abaroudi, M. A. Larrayoz, F. Recasens and J. E. Sueiras, *Ind. Eng. Chem. Res.*, 2000, **39**, 3666.
96. M. Neurock and D. H. Mei, *Top. Catal.*, 2002, **20**, 5.
97. M. A. Newton, *Chem. Soc. Rev.*, 2008, **37**, 2644.
98. J. M. Hollas, *Modern Spectroscopy*, 4th edn., John Wiley and Sons, Chichester, 2004.
99. G. L. Chiarello, J. D. Grunwaldt, D. Ferri, R. Krumeich, C. Oliva, L. Forni and A. Baiker, *J. Catal.*, 2007, **252**, 127.
100. F. J. Gracia, S. Guerrero, E. E. Wolf, J. T. Miller and A. Kropf, *J. Catal.*, 2005, **233**, 372.
101. B. Kimmerle, A. Baiker and J. D. Grunwaldt, *Phys. Chem. Chem. Phys.*, 2010, **12**, 2288.
102. E. B. Fox, A. F. Lee, K. Wilson and C. S. Song, *Top. Catal.*, 2008, **49**, 89.
103. G. P. Huffman, N. Shah, J. M. Zhao, F. E. Huggins, T. E. Hoost, S. Halvorsen and J. G. Goodwin, *J. Catal.*, 1995, **151**, 17.
104. I. E. Beck, V. V. Kriventsov, B. N. Novgorodov, E. P. Yakimchuk, D. I. Kochubey, V. I. Zaikovsky, I. Y. Pakharukov, N. Y. Kozitsyna, M. N. Vargaftik

and V. I. Bukhtiyarov, *Nucl. Instrum. Methods Phys. Res., Sect. A*, 2009, **603**, 178.
105. M. A. Newton, C. Belver-Coldeira, A. Martinez-Arias and M. Fernandez-Garcia, *Angew. Chem.-Int. Edit.*, 2007, **46**, 8629.
106. M. A. Newton, S. G. Fiddy, G. Guilera, B. Jyoti and J. Evans, *Chem. Commun.*, 2005, 118.
107. M. A. Newton, *Top. Catal.*, 2009, **52**, 1410.
108. B. Fu, W. Liu and Z. Li, *Appl. Surf. Sci.*, 2010, **256**, 6899.
109. N. E. Singh-Miller and N. Marzari, *Phys. Rev. B*, 2009, **80**, 235407.
110. I. V. Yudanov, A. Genest and N. Rosch, *J. Clust. Sci.*, 2011, **22**, 433.
111. Y. J. Xiong, H. Cal, B. J. Wiley, J. Wang, M. J. Kim and Y. N. Xia, *J. Am. Chem. Soc.*, 2007, **129**, 3665.
112. F. R. Fan, A. Attia, U. K. Sur, J. B. Chen, Z. X. Xie, J. F. Li, B. Ren and Z. Q. Tian, *Cryst. Growth Des.*, 2009, **9**, 2335.
113. Y. J. Xiong, J. M. McLellan, Y. D. Yin and Y. N. Xia, *Angew. Chem.-Int. Edit.*, 2007, **46**, 790.
114. E. D. Wang, J. B. Xu and T. S. Zhao, *J. Phys. Chem. C*, 2010, **114**, 10489.
115. C.-Q. Lv, K.-C. Ling and G.-C. Wang, *J. Chem. Phys.*, 2009, **131**, 144704.
116. M. Jin, H. Liu, H. Zhang, Z. Xie, J. Liu and Y. Xia, *Nano Res.*, 2011, **4**, 83.
117. V. Mazumder, Y. Lee and S. H. Sun, *Adv. Funct. Mater.*, 2010, **20**, 1224.
118. H. J. Chen, G. Wei, A. Ispas, S. G. Hickey and A. Eychmuller, *J. Phys. Chem. C*, 2010, **114**, 21976.
119. M. Slouf, E. Pavlova, M. Bhardwaj, J. Plestil, H. Onderkova, A. A. Philimonenko and P. Hozak, *Mater. Lett.*, 2011, **65**, 1197.
120. Y. L. Wang, H. J. Chen and E. K. Wang, *Nanotechnology*, 2008, **19**, 105604.
121. C.-J. Jia and F. Schueth, *Phys. Chem. Chem. Phys.*, 2011, **13**, 2457.
122. A. R. Tao, S. Habas and P. D. Yang, *Small*, 2008, **4**, 310.
123. F. R. Fan, A. Attia, U. K. Sur, J. B. Chen, Z. X. Xie, J. F. Li, B. Ren and Z. Q. Tian, *Cryst. Growth Des.*, 2009, **9**, 2335.
124. F. R. Fan, D. Y. Liu, Y. F. Wu, S. Duan, Z. X. Xie, Z. Y. Jiang and Z. Q. Tian, *J. Am. Chem. Soc.*, 2008, **130**, 6949.
125. W. X. Niu, Z. Y. Li, L. H. Shi, X. Q. Liu, H. J. Li, S. Han, J. Chen and G. B. Xu, *Cryst. Growth Des.*, 2008, **8**, 4440.
126. C. Li, K. L. Shuford, M. Chen, E. J. Lee and S. O. Cho, *ACS Nano*, 2008, **2**, 1760.
127. B. Lim, M. J. Jiang, J. Tao, P. H. C. Camargo, Y. M. Zhu and Y. N. Xia, *Adv. Funct. Mater.*, 2009, **19**, 189.
128. T. Ming, W. Feng, Q. Tang, F. Wang, L. Sun, J. Wang and C. Yan, *J. Am. Chem. Soc.*, 2009, **131**, 16350.
129. L. Bisson, C. Boissiere, L. Nicole, D. Grosso, J. P. Jolivet, C. Thomazeau, D. Uzio, G. Berhault and C. Sanchez, *Chem. Mater.*, 2009, **21**, 2668.
130. E. Carbo-Argibay, B. Rodriguez-Gonzalez, J. Pacifico, I. Pastoriza-Santos, J. Perez-Juste and L. M. Liz-Marzan, *Angew. Chem.-Int. Edit.*, 2007, **46**, 8983.
131. S. J. Guo, L. Wang, W. Wang, Y. X. Fang and E. K. Wang, *J. Colloid Interface Sci.*, 2007, **315**, 363.
132. B. P. Khanal and E. R. Zubarev, *Angew. Chem.-Int. Edit.*, 2009, **48**, 6888.
133. J. Zeng, Q. Zhang, J. Chen and Y. Xia, *Nano Lett.*, 2009, **10**, 30.
134. B. L. Cushing, V. L. Kolesnichenko and C. J. O'Connor, *Chem. Rev.*, 2004, **104**, 3893.

135. Y. Xia, Y. J. Xiong, B. Lim and S. E. Skrabalak, *Angew. Chem.-Int. Edit.*, 2009, **48**, 60.
136. Y. Li, Q. Y. Liu and W. J. Shen, *Dalton Trans.*, 2011, **40**, 5811.
137. A.-X. Yin, X.-Q. Min, W. Zhu, H.-S. Wu, Y.-W. Zhang and C.-H. Yan, *Chem. Commun.*, 2012, **48**, 543.
138. C. Barreteau, M. C. Desjonqueres and D. Spanjaard, *Eur. Phys. J. D*, 2000, **11**, 395.
139. A. Zuttel, C. Nutzenadel, G. Schmid, C. Emmenegger, P. Sudan and L. Schlapbach, *Appl. Surf. Sci.*, 2000, **162**, 571.
140. M. M. Koebel, L. C. Jones and G. A. Somorjai, *J. Nanopart. Res.*, 2008, **10**, 1063.
141. J. H. Song, Y. J. Kim and J. S. Kim, *Curr. Appl. Phys.*, 2006, **6**, 216.
142. C. J. Murphy, *Abstr. Paper Am. Chem. Soc.*, 2010, **240**, 158-COLL.
143. J. Polte, T. T. Ahner, F. Delissen, S. Sokolov, F. Emmerling, A. F. Thunemann and R. Kraehnert, *J. Am. Chem. Soc.*, 2010, **132**, 1296.
144. J. Polte, R. Erler, A. F. Thunemann, S. Sokolov, T. T. Ahner, K. Rademann, F. Emmerling and R. Kraehnert, *ACS Nano*, 2010, **4**, 1076.
145. S. Bhattacharjee, D. M. Dotzauer and M. L. Bruening, *J. Am. Chem. Soc.*, 2009, **131**, 3601.
146. G. C. Bond, *Surf. Sci.*, 1985, **156**, 966.
147. J. Chen, Q. H. Zhang, Y. Wang and H. L. Wan, *Adv. Synth. Catal.*, 2008, **350**, 453.
148. J. A. van Bokhoven and J. T. Miller, in *X-Ray Absorption Fine Structure-XAFS13*, eds. B. Hedman and P. Painetta, Editon edn., 2007, vol. 882, pp. 582-584.
149. R. Narayanan and M. A. El-Sayed, *J. Am. Chem. Soc.*, 2004, **126**, 7194.
150. R. Narayanan and M. A. El-Sayed, *Nano Lett.*, 2004, **4**, 1343.
151. X. Gong, Y. Yang, L. Zhang, C. Zou, P. Cai, G. Chen and S. Huang, *J. Colloid Interface Sci.*, 2010, **352**, 379.
152. B. J. Hu, K. L. Ding, T. B. Wu, X. S. Zhou, H. L. Fan, T. Jiang, Q. A. Wang and B. X. Han, *Chem. Commun.*, 2010, **46**, 8552.
153. B. K. Jena, S. C. Sahu, B. Satpati, R. K. Sahu, D. Behera and S. Mohanty, *Chem. Commun.*, 2011, **47**, 3796.
154. J. C. Serrano-Ruiz, A. Lopez-Cudero, J. Solla-Gullon, A. Sepulveda-Escribano, A. Aldaz and F. Rodriguez-Reinoso, *J. Catal.*, 2008, **253**, 159.
155. A. X. Yin, X. Q. Min, Y. W. Zhang and C. H. Yan, *J. Am. Chem. Soc.*, 2011, **133**, 3816.
156. L. Piccolo, A. Valcarcel, M. Bausach, C. Thomazeau, D. Uziob and G. Berhault, *Phys. Chem. Chem. Phys.*, 2008, **10**, 5504.
157. C. J. Baddeley, R. M. Ormerod, A. W. Stephenson and R. M. Lambert, *J. Phys. Chem.* , 1995, **99**, 5146.
158. J. A. Boscoboinik, C. Plaisance, M. Neurock and W. T. Tysoe, *Phys. Rev. B*, 2008, **77**, 045422.
159. D. A. Dowden and P. W. Reynolds, *Discuss. Faraday Soc.*, 1950, 184.
160. F. A. Al-Odail, A. Anastasopoulos and B. E. Hayden, *Phys. Chem. Chem. Phys.*, 2010, **12**, 11398.
161. J. Naughton, A. F. Lee, S. Thompson, C. P. Vinod and K. Wilson, *Phys. Chem. Chem. Phys.*, 2010, **12**, 2670.
162. J. Turkevich, P. C. Stevenson and J. Hillier, *Discuss. Faraday Soc.*, 1951, 55-&.
163. J. Turkevich and G. Kim, *Science*, 1970, **169**, 873.

164. G. Schmid, A. Lehnert, J.-O. Malm and J.-O. Bovin, *Angew. Chem.-Int. Edit.*, 1991, **30**, 874.
165. J. B. Michel and J. T. Schwartz, *Stud. Surf. Sci. Catal.*, 1987, **31**, 669.
166. G. Schmid, *Chem. Rev.*, 1992, **92**, 1709.
167. J. W. Hu, J. F. Li, B. Ren, D. Y. Wu, S. G. Sun and Z. Q. Tian, *J. Phys. Chem. C*, 2007, **111**, 1105.
168. S. E. Habas, H. Lee, V. Velimir Radmilovic and G. A. Somorjai, *Nat. Mater.*, 2007, **6**, 692.
169. L. Kesavan, R. Tiruvalam, M. H. Ab Rahim, M. I. bin Saiman, D. I. Enache, R. L. Jenkins, N. Dimitratos, J. A. Lopez-Sanchez, S. H. Taylor, D. W. Knight, C. J. Kiely and G. J. Hutchings, *Science*, 2011, **331**, 195.
170. V. Celorrio, M. G. M. de Oca, D. Plana, R. Moliner, M. J. Lazaro and D. J. Fermin, *J. Phys. Chem. C*, 2012, **116**, 6275.
171. D. W. Yuan and Z. R. Liu, *Phys. Lett. A*, 2011, **375**, 2405.
172. J. Zhang, H. Jin, M. B. Sullivan, F. Chiang, H. Lim and P. Wu, *Phys. Chem. Chem. Phys.*, 2009, **11**, 1441.
173. J. A. Lopez-Sanchez, N. Dimitratos, N. Glanville, L. Kesavan, C. Hammond, J. K. Edwards, A. F. Carley, C. J. Kiely and G. J. Hutchings, *Appl. Catal., A.*, 2011, **391**, 400-406.
174. J. K. Edwards, B. E. Solsona, P. Landon, A. F. Carley, A. Herzing, C. J. Kiely and G. J. Hutchings, *J. Catal.*, 2005, **236**, 69.
175. T. Ishihara, R. Nakashima and Y. Nomura, *Catal. Sci. Technol.*, 2012, **2**, 961.
176. E. N. Ntainjua, M. Piccinini, S. J. Freakley, J. C. Pritchard, J. K. Edwards, A. F. Carley and G. J. Hutchings, *Green Chem.*, 2012, **14**, 170.
177. C.-W. Yang, K. Chanda, P.-H. Lin, Y.-N. Wang, C.-W. Liao and M. H. Huang, *J. Am. Chem. Soc.*, 2011, **133**, 19993.
178. T. S. A. Heugebaert, S. De Corte, T. Sabbe, T. Hennebel, W. Verstraete, N. Boon and C. V. Stevens, *Tetrahedron Lett.*, 2012, **53**, 1410.
179. T. Balcha, J. R. Strobl, C. Fowler, P. Dash and R. W. J. Scott, *ACS Catalysis*, 2011, **1**, 425.
180. D. I. Enache, D. Barker, J. K. Edwards, S. H. Taylor, D. W. Knight, A. F. Carley and G. J. Hutchings, *Catal. Today*, 2007, **122**, 407.
181. S. Alayoglu, F. Tao, V. Altoe, C. Specht, Z. Zhu, F. Aksoy, D. R. Butcher, R. J. Renzas, Z. Liu and G. A. Somorjai, *Catal. Lett.*, 2011, **141**, 633.
182. S. Marx and A. Baiker, *J. Phys. Chem. C*, 2009, **113**, 6191.

# Chapter 2

# Experimental

## 2.1 Catalyst synthesis

### 2.1.1 Materials

Tetraaminepalladium (II) nitrate solution, sodium palladium chloride, poly(vinylpyrrolidone) (PVP), potassium bromide, Pluronic P123, Pluronic P127, tetramethyl orthosilicate, lauric acid, aluminium *sec*-butoxide and 1-propanol were supplied by Sigma Aldrich. Ethylene glycol (EG), citric acid and hydrochloric acid (37.5 %) were purchased from Fisher Scientific. Ascorbic acid and cetyltrimethylammonium bromide (CTAB) were obtained from Sigma Aldrich. Deionised water was used in all cases. The 5 wt% Pd/C (50 % wet paste) catalyst tested in *Chapter 6* was supplied by Syngenta and originated from Heraeus.

### 2.1.2 Supported catalyst synthesis

#### 2.1.2.1 Mesoporous alumina supported catalysts

Mesoporous alumina (referred to as meso-alumina or meso-$Al_2O_3$ in this thesis) supports were prepared by Simon Hackett and Christopher Parlett using the method described by Davis and co-workers.[1] Aluminum *sec*-butoxide (43.8 g) was reacted with deionized water (10.3 g) in 1-propanol (275 g) to form an aluminium hydroxide suspension. Lauric acid (10.8 g) was added after 60 minutes of stirring. The reaction mixture was aged under static conditions for 24 hours at room temperature. It was then held at 110 °C for 48 hours. The solid was filtered, washed with ethanol, and dried at room temperature. The product was calcined in air at 550 °C for 5 hours. The catalyst used in *Chapter 4* was synthesised by Justin Cerff under the supervision of Simon Hackett and the catalyst used in *Chapter 3* was synthesised by the author with assistance from Christopher Parlett. Both catalysts were prepared using the incipient wet impregnation technique. Just sufficient volume of aqueous tetraaminepalladium (II) nitrate solution (4.16 % Pd, 5 ml) of equivalent concentration for 2.5 wt% was added to 1 g mesoporous alumina. This was covered, stirred at 400 rpm for 24 hours, then uncovered and heated to 50 °C to dryness. The sample was calcined at 500 °C for 2 hours in air (ramp rate 10 °C $min^{-1}$) prior to reduction at 100 °C for 2 hours (ramp rate 10 °C $min^{-1}$) under flowing hydrogen (10 $cm^3$ $min^{-1}$). Further details of these catalysts are given in Hackett's thesis and papers.[2, 3]

#### 2.1.2.2 SBA-15 supported catalysts

SBA-15 supports were synthesised by Christopher Parlett following the procedure of G. D. Stucky.[4, 5] In a typical synthesis Pluronic P123 (20 g) was dissolved in water (149 ml) and hydrochloric acid (2 M, 583 ml) with stirring at 35 °C. Tetramethyl orthosilicate (31 ml) was added with stirring at 35 °C and left for 20 hours with agitation. The resulting gel was aged for 24 hours at 80 °C without agitation. The precipitate was filtered and washed with water (1000 ml). The product was air dried at room temperature and calcined at 500 °C for 6 hours in air (ramp rate 10 °C $min^{-1}$). SBA-15 was impregnated using insipient wet impregnation. Just sufficient aqueous tetraaminepalladium (II) nitrate solution (4.16 % Pd made up to 12 ml with dilution for metal loadings of 5 and 2.5 wt%) was added to SBA-15 (1.5 g). The slurry was stirred for 18 hours at room temperature before heating to 50 °C and left to dryness. The powder was calcined at 500 °C for 2 hours in air (ramp rate 10 °C $min^{-1}$) prior to reduction at 400 °C for 2 hours (ramp rate 10 °C $min^{-1}$) under flowing hydrogen (10 $cm^3$ $min^{-1}$). Further details of these catalysts are given in Parlett's thesis and papers.[4, 6]

### 2.1.3 Nanoparticle synthesis

#### 2.1.3.1 Palladium icosahedra synthesis

The synthesis of Pd nano-icosahedra was adapted from the procedure described by Y. Xia and co-workers.[7] PVP (0.534 g, 55,000 $M_w$) and citric acid (0.900 g, 4.68 mmol) were dissolved in 120 ml water at room temperature, with good mechanical stirring. A reflux condenser was set up and the reagents were heated to 90 °C in air. $Na_2PdCl_4$ (0.282 g, 0.96 mmol) was dissolved in 45 ml water at room temperature and added to the reaction mixture using a syringe pump at a rate of 85 ml $min^{-1}$. After a further 5 hours, the volume was reduced using a rotary evaporator and the colloid was collected under centrifugation at 4000 rpm, washed once with acetone and three times with ethanol. Variations on this method for size control, described in *Section 3.2.3* involved extending the reaction time to 8 hours, 21 hours and 24 hours. All other aspects of the procedure remained the same.

### 2.1.3.2 Palladium nanorod synthesis

The synthesis of Pd nanorods was adapted from another method developed by Xia's group.[8] EG (30 ml) was heated to 100 °C in a flask fitted with a reflux condenser under good mechanical stirring. A solution of $Na_2PdCl_4$ (0.292g, 0.99 mmol) was prepared in 18 ml water at room temperature and a second solution of PVP (0.550g, 55,000 $M_w$) was prepared in 18 ml EG also at room temperature. These solutions were added simultaneously to the heated EG using a dual channel syringe pump and flow rate of 45 ml $hour^{-1}$. The reaction mixture was heated for one hour further before collection under centrifugation as in the previous procedure.

A variation on this procedure was attempted in order to achieve size control, described in *Section 3.2.2*. The concentration of EG in water was varied by changing the volume of EG and water used in preparing the PVP and $KBr/Na_2PdCl_4$ solutions. These conditions are given in *Table 2.1*.

| Concentration EG / % | Vol water syringe 1 / ml | Vol water syringe 2 / ml | Vol water flask / ml |
|---|---|---|---|
| 0 | 18 | 18 | 30 |
| 45.5 | 18 | 18 | 0 |
| 72.7 | 18 | 0 | 0 |
| 85.0 | 10 | 0 | 0 |

**Table 2.1 – Distribution of water used to vary the concentration of ethylene glycol (EG) during the synthesis of Pd nanorods. Syringe 1 contained $Na_2PdCl_4$ and KBr, syringe 2 contained PVP each with a total of 18 ml liquid where the remainder was made up with EG. The flask contained 30 ml liquid in all cases.**

### 2.1.3.3 Palladium nanocubes synthesis

Pd nanocubes were synthesised using an adapted procedure from F. R. Fan et al.[9] 100 ml aqueous solutions of $Na_2PdCl_4$ (0.294 g, 10 mM) and CTAB (0.365 g, 10 mM), and a 250 ml solution of ascorbic acid (1.10 g, 25 mM) were prepared at room temperature. 200 ml ascorbic acid was stirred vigorously at room temperature in a 2 litre reactor. Using a peristaltic pump (Watson Marlow PVC double manifold tubing 0.8 mm bore size, 981.0142.000), 50 ml $Na_2PdCl_4$ and 50 ml CTAB were added simultaneously at a rate of 10 rpm. Once all the solutions were added, the reaction was left stirring for a

further 30 minutes. At this stage PVP (0.44 g) was dissolved in water (20 ml) and added to the reaction mixture using the peristaltic pump at a rate of 20 rpm. The reaction was left stirring for a further 15 minutes. Product was collected under centrifugation at 12,000 rpm for 20 minutes, washed with water and centrifuged for a further 20 minutes, then washed with ethanol and collected under a final 20 minutes of centrifugation.

### 2.1.4 Nanoparticle impregnation

Both the Pd icosahedra and Pd nanorods were impregnated using the incipient wet impregnation technique. Equivalent mass of sample for 5 wt% was dispersed in a minimal volume of ethanol (5 ml). This was stirred for 24 hours and then dried at 50 °C, as previously described. These samples were not calcined or reduced, as this step is rendered unnecessary due to the initial controlled reduction synthesis of the nanoparticles.

### 2.1.5 Synthesis of Au-shell, Pd-core titania supported catalysts

The synthesis of the fresh particles was carried out by Adam Lee[10], based on a procedure by Gunter Schmidt.[11] $H_2PdCl_4$ solution (16 ml, 2.68 g $l^{-1}$ of Pd) and water (1600 ml) were heated to boiling and treated with a 1 % sodium citrate solution (80 ml) using good mechanical stirring. After refluxing for 1 hour, the resulting palladium nanoparticle product was dark grey. This was diluted with 6000 ml of water, and over the course of 8 hours, $HAuCl_4$ solution (1.9 ml, 7.44 g $l^{-1}$ of Au) and hydroxylamine hydrochloride solution (5 ml, 10 g $l^{-1}$) were added at room temperature while stirring, during which time the solution lightened. Stirring was continued for a further 48 hours, and then p-$NH_2C_6H_4SO_3Na$ (0.2 g) was added. The reaction mixture was reduced by evaporation until the bimetallic nanoparticles began to coagulate. Centrifugation (5000 rpm) yielded a pale grey powder, which was subsequently solubilised in water, dispersed onto P25 titania (Degussa) and evaporated to dryness. Samples for reactor testing were subsequently heated to temperature (5 °C $min^{-1}$) within a tube furnace under flowing $N_2$ (20 ml $min^{-1}$) and held for 30 minutes, then cooled under inert before screening.

## 2.2 Catalyst characterisation

### 2.2.1 Microscopy and elemental analysis

#### 2.2.1.1 Transmission electron microscopy

Transmission electron microscopy (TEM) is an ideal instrument for study of nanometre sized metal particles. An electron beam is generated through a high voltage electron gun, usually operating between 80 kV to 200 kV, although on some instruments, including one used in this thesis, voltages as high as 400 kV are possible. Operating at higher voltage improves contrast and the penetration of the beam, particularly useful for polymer capped nanoparticles or nanoparticles on relatively dense supports. This is, however, at the expense of optimum resolution, thus it is important to consider the minimum voltage required to study a sample in order to attain maximum quality images. Alignment of the electron gun is an important step in TEM operation.

A simplified description of the microscope operation under bright field imaging, used in this thesis, is described in the following paragraph and shown in *Figure 2.1*. The beam is focused using electromagnetic fields through the condenser lens onto the specimen, all operating under vacuum conditions. The beam passes through the specimen and is focused onto a fluorescent screen through the objective lens setup. Electrons that pass straight through the specimen appear bright on the screen. Electrons that are scattered by the specimen are not detected, thus these areas appear darker. Condenser and objective apertures are used to limit the detection of scattered electrons and improve the image quality, through reducing the beam intensity and removal of high angle scattered electrons from diffraction interaction with the specimen.[12]

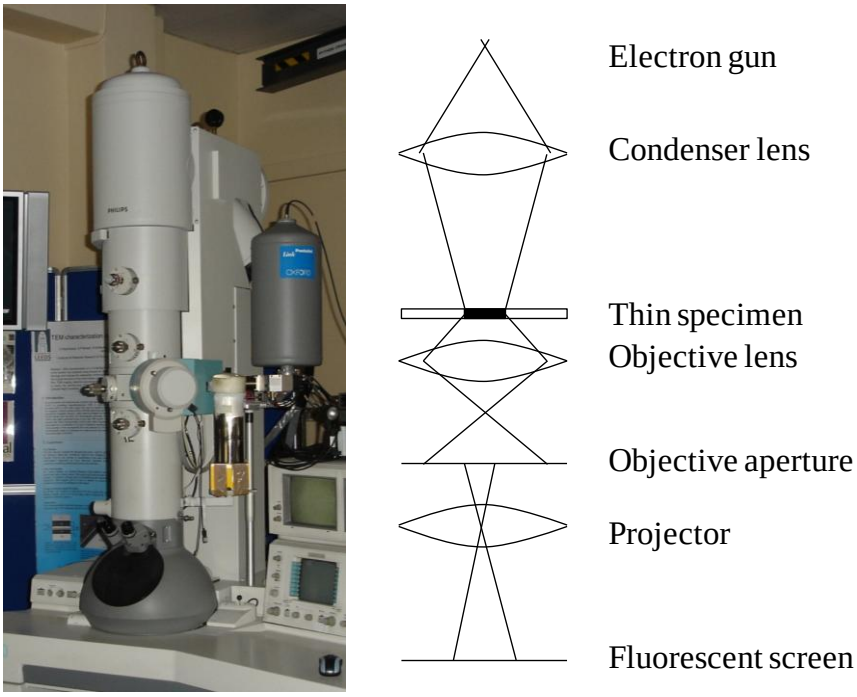


**Figure 2.1 – The FEI CM200 TEM in the LENNF facility at the University of Leeds (left) and the basic components of a TEM adapted from reference 12 (right). An aperture component is also often available for the condenser lens**

Particle and support morphology were confirmed using high resolution transmission electron microscopy (HRTEM). Dilute suspensions of the samples were made up in ethanol and dispersed on holey carbon film 300 mesh copper grids (supplied by Agar Scientific S147-3H). Images for the Pd nanorods, the Pd-Au core-shell nanoparticle and Pd/C (Heraeus) catalyst were taken at the LENNF facility in Leeds using an FEI CM200 TEM operating at 197 kV, fitted with an Oxford Instruments energy dispersive X-ray (EDX) analyser and a Gatan imaging filter by Nicole Hondow (see *Figure 2.1*). Pd icosahedra and Pd nanocube images were obtained using a JEOL JEM-4000EX HREM instrument at Oxford Materials under the EPSRC equipment access scheme operating at 400 kV by Teck Lim. Lower magnification images were additionally used for particle size analysis.

Average particle sizes from TEM for the Pd nanorods and Pd icosahedra were calculated by measuring the length of the major axis of the nearest ellipse to fit the particle using ImageJ software. The mean size was calculated for > 200 particles. The Pd nanocubes, Au-Pd/$TiO_2$ catalyst and Pd/C catalyst particles were more dispersed on the TEM grid, so the lengths of individual particles were measured, once again using

the ImajeJ software. In these cases approximately 50 particles were measured across three different regions of the TEM grid.

#### 2.2.1.2 Energy dispersive X-ray spectroscopy

For many electron microscopy techniques (scanning electron microscopy, TEM, scanning transmission electron microscopy) it is possible to include an X-ray detector which can be used in bulk elemental analysis. The electron beam is sufficient to excite the specimen core electrons. The resulting hole is filled by a higher energy electron and X-rays are generated in the process. The wavelengths of these X-rays are characteristic to the element which generates them, and from this quantitative elemental analysis is possible.[13]

EDX analysis was performed on the instrument described in the previous section for Au-Pd/$TiO_2$ nanoparticles by Nicole Hondow. The Pd/C (Heraeus) catalyst used in *Chapter 6* was characterised by using the EDX detector attached to a Carl Zeiss Evo-40 SEM electron microscope at Cardiff University.

#### 2.2.1.3 Inductively coupled plasma – optical emission spectrometry

Elemental analysis for both the Au-Pd/$TiO_2$ nanoparticles and the Pd/C catalyst was also performed using inductively coupled plasma – optical emission spectrometry (ICP-OES). Palladium weight loadings for the SBA-15 supported catalysts were also assessed using this technique. Plasma (typically argon) is created through electromagnetic induction into which the aqueous sample is injected. The atoms in the sample will emit radiation of characteristic wavelength upon ionisation in the plasma, which can be quantitatively assessed for elemental analysis. All ICP-OES analysis for these catalysts was completed by MEDAC UK using a Varian Vista MPX ICP-OES system. For further information on this technique refer to reference 14.[14]

#### 2.2.1.4 Atomic absorption spectroscopy

Elemental analysis of the Pd/meso-alumina catalyst, undertaken by Simon Hackett, and the tailored Pd nanoparticles, carried out by the author, was established using a Hitachi Z-5300 polarised Zeeman atomic absorption spectrometer (AAS). The catalysts were digested in 1 M aqueous nitric acid for 48 hours prior to analysis. The principle of AAS is similar to that of ICP-OES: the sample is vaporised into an acetylene/air flame. Emitted EM radiation is detected using a cathode lamp of fixed

wavelength to the element that is being detected.[15] For Pd samples analysed here a lamp of 244 nm was used. Calibration solutions using 1020 mg $l^{-1}$ Pd in 5 % HCl AAS solution (Aldrich) of 1 ppm, 5 ppm, 10 ppm 20 ppm and 40 ppm were made up for quantitative analysis.

## 2.2.2 Titrations and thermal analysis

### 2.2.2.1 Thermogravimetric analysis

Thermal analysis techniques can be used to assess a range of material properties, including the analysis of adsorbates, thermal stability, phase transitions and other energy releasing and consuming processes. Thermogravimetric analysis (TGA) has been used here to qualitatively consider the stability of components and adsorbates in the initial catalyst synthesis and spent catalyst characterisation. The sample is placed on a sensitive balance, and under flowing inert gas the mass loss is measured as a function of temperature. Differential thermal analysis (DTA), a measure of heat change in relation to a reference sample, can be measured simultaneously and energy fluctuations due to phase changes that will not be detected by mass lost can be detected using DTA.[16]

Thermogravimetric analysis was carried out using a Stanton Redcroft STA-780 series thermal analyser. Approximately 10 mg of catalyst was accurately weighed into an alumina crucible and heated to 700 °C at 10 °C $min^{-1}$ under 20 ml $min^{-1}$ helium flow. An equivalent mass of alumina was used as a reference.

### 2.2.2.2 Carbon monoxide pulse chemisorption

The dispersion of a catalyst is defined as the number of available metal surface atoms ($M_{surf}$) as a percentage of the total number of metal atoms ($M_{tot}$). CO selectively adsorbs on the metal surface and not the support, and hence is a good titrant for metal surface area measurements. The reported stoichiometry for Pd supported on silicas and aluminas is generally between 1 and 2, increasing towards 2 as particle size increases.[17-19] It is noted in single crystal studies that, unless only isolated Pd sites are available, such as for a bimetallic particle, CO preferentially adsorbs bridging over Pd surfaces.[20] Thus an average stoichiometry of 2 has been used in all dispersion calculations. If a known volume of CO is titrated onto the surface of a Pd catalyst, it is possible to calculate the dispersion. $M_{tot}$ can be determined from the metal weight loading and

catalyst mass used as in *Equation 2.1*. $M_{surf}$ is deduced from the volume of CO adsorbed per gram of catalyst and multiplying the resulting number of atoms by 2, since each CO molecule will adsorb to two Pd atoms. This is shown in *Equation 2.2*.

$$M_{tot} = n_{Pd} \times N_A$$

**Equation 2.1 – The total number of metal atoms $M_{tot}$ can be calculated from the number of moles of Pd in the catalyst determined from the catalyst mass and scaled to the catalyst weight loading. $N_A$ is Avogadro's number**

$$M_{surf} = 2\left[\frac{\left(V_{CO} \diagup V_m N_A\right)}{w_{cat}}\right]$$

**Equation 2.2 – The number of surface atoms is determined from the number of moles of CO adsorbed where $V_{CO}$ is the volume of CO, $V_m$ is the molar volume and $w_{cat}$ is the catalyst mass use. A stoichiometry of 2 surface atoms per CO molecule has been assumed.**

Metal dispersions were measured by pulse chemisorption using a Quantachrome Chembet 3000 and analysis using TPRWin software. Approximately 50 mg sample was accurately weighed into the sample tube. Each catalyst was out-gassed at 100 °C for 2 hours under 2 bar helium at 20 ml $min^{-1}$. The catalyst was then reduced under 1 bar $H_2$ (20 ml $min^{-1}$) for 1 hour at 100 °C. The catalyst sample was loaded with 50 µl pulses of 1 bar carbon monoxide (5 ml $min^{-1}$) until the size of three consecutive pulses were the same. This is illustrated in *Figure 2.2*.

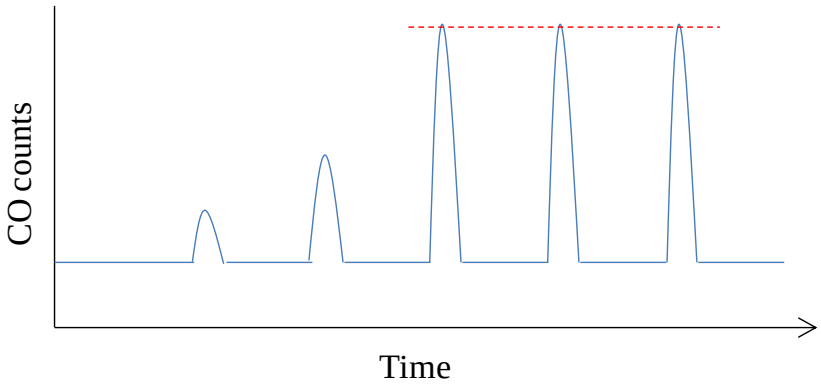


**Figure 2.2 – Illustration of raw data collected during a CO chemisorption experiment. As the surface becomes saturated more CO is detected until it is no longer adsorbed and three consecutive peaks have reached a maximum (red line)**

### 2.2.2.3 Diffuse reflectance infra-red Fourier transform spectroscopy

Diffuse reflectance infra-red Fourier transform spectroscopy (DRIFTS) is a surface sensitive infra-red spectroscopic technique. The absorption of infra-red radiation excites the vibrational modes of bonding moieties in molecular species. IR radiation that is not absorbed by the sample reaches a detector, and the functionalities in the sample can be identified.[21]

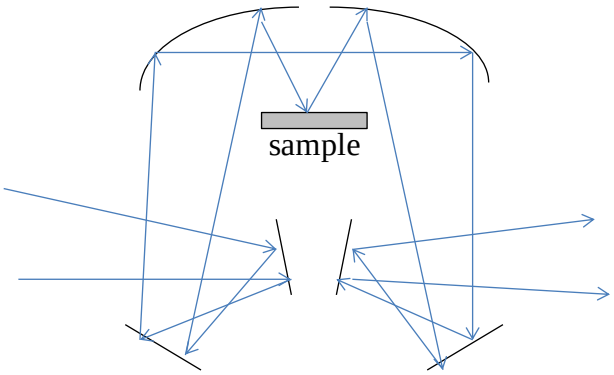


**Figure 2.3 – The sample compartment in diffuse reflectance IR. A parabolic mirror directs radiation towards the rough sample surface then to the detector. Reproduced from reference 21**

Solid powders and rough surfaces can be analysed using DRIFTS: the reflected IR beam is directed to the detector through a parabolic mirror (see *Figure 2.3*).[21] This technique is particularly useful for identifying chemisorbed species on a catalyst surface after reaction, but it is also possible to use a suitable titrant to examine the properties of the metal surface directly. As described in the previous section, CO is an excellent

titrant molecule on Pd surfaces due to its selective, strong adsorption to the metal. The adsorption mode of CO affects the vibrational frequency of the C=O bond and is thus sensitive to the surface geometry and the presence of Au promoters. This is illustrated in *Figure 3.8.*[22-24] Further details of CO adsorption are discussed in *Chapter 3*.

DRIFTS measurements were collected on a Nicolet Avatar 370 MCT with SmartCollector accessory and using a gold coated *in situ* cell with temperature control and a gas manifold. Background spectra were collected over dried KBr under flowing nitrogen (10 ml $min^{-1}$). Ex-situ measurements of the Pd/C catalyst were diluted with KBr to 0.5 wt%. These were collected using OMINC software and processed using OPUS 6 software: all spectra of treated samples and spent catalyst were subtracted from the fresh catalyst spectrum. *In situ* measurements on all other samples were performed neat.

*In situ* measurements of the tailored Pd catalysts were collected at room temperature. The cell was purged with nitrogen (1.5 bar, 10 ml $min^{-1}$) for 5 minutes, and a spectrum was collected. Subsequently, the cell was dosed with CO (1 bar, 10 ml $min^{-1}$) for a further 5 minutes and a spectrum was measured. The cell was then further purged with nitrogen and spectra were collected every 10 minutes until free CO was no longer visible.

CO titration measurements of the Au-Pd/$TiO_2$ catalysts were also collected at room temperature after *in situ* annealing. Samples were heated to temperature (100 °C, 150 °C, 200 °C, 300 °C, 400 °C and 500 °C) at 10 °C $min^{-1}$ under flowing nitrogen (20 ml $min^{-1}$) and held at temperature for 10 minutes. They were then cooled to room temperature, and then exposed to 5 % CO/He (20 ml $min^{-1}$) for 5 minutes. Spectra were measured prior to CO exposure, during exposure and after purging with nitrogen.

#### 2.2.2.4 Nitrogen porosimetry

Nitrogen porosimetry is conducted using gas adsorption manometry setup. A simple outline of the apparatus is described here. The temperature of the sample is kept constant by cooling in liquid nitrogen. A calibrated sample tube of known volume containing a catalyst of known mass is loaded on to the instrument. A specified volume of nitrogen is dosed into the sample tube and a transducer detects the changes in pressure until equilibrium pressure is maintained. This is used to calculate the amount of adsorbed gas.[25] The porosity and surface area of the Pd/C catalyst in *Chapter 6* was determined using nitrogen porosimetry. The nitrogen adsorption and desorption

isotherms were recorded on a Quantachrome Nova 1200 at 77 K. Approximately 50 mg of catalyst was accurately weighed into the sample tube and then was out-gassed under vacuum at 120 °C for 24 hours.

Surface areas were calculated using the Brunauer, Emmett and Teller (BET) isotherm. This isotherm is an extension of the Langmuir isotherm to multilayer adsorption. In BET theory, the first layer of molecules acts as adsorption sites for the next layer and so on to infinite layers. It is assumed that the adsorption behaviour of all subsequent layers after adsorption to the initial monolayer (amount of adsorbed gas for monolayer coverage given by $n_m$) is the same. Thus, the total amount of adsorbed gas n is related to the equilibrium pressure p as in *Equation 2.3*. The constant C is approximately related to the energy of adsorption in the first layer $E_1$ and subsequent layers $E_L$ as in *Equation 2.4*. The specific surface area is determined from the linear region of the BET plot, in this case measured between $p/p^0$ = 0.03-0.19 and is related to n through the adsorbate cross section, σ, taken as 0.162 $nm^2$ for $N_2$ at 77 K (*Equation 2.5*).[25]

$$\frac{p}{n\left(p^0 - p\right)} = \frac{1}{n_m C} + \frac{C-1}{n_m C} \times \frac{p}{p^0}$$

**Equation 2.3 – The linear form of the BET isotherm where $p/p^0$ is the relative pressure, n is the amount of adsorbed gas and $n_m$ is the amount of adsorbed gas for monolayer coverage, and C is a constant defined below**

$$C \approx \exp\left(\frac{E_1 - E_L}{RT}\right)$$

**Equation 2.4 – An approximate definition for the constant C used in the BET isotherm where $E_1$ is the adsorption energy of the first layer and $E_L$ is the adsorption energy of subsequent layers, R is the gas constant and T is the operation temperature**

$$a(BET) = n_m N_A \sigma$$

**Equation 2.5 – Calculation of the BET specific surface area a(BET) from the monolayer capacity $n_m$ and cross sectional area of the adorptive gas σ. $N_A$ is Avogadro's number**

Pore diameters were determined from the desorption branch of the isotherm using the Barrett, Joyner and Halenda (BJH) method. This method uses an adaptation of

the Kelvin equation to calculate the pore volume and pore radius of mesopores. The Kelvin equation is given in *Equation 2.6*, where $\ln(p/p^0)$ represents the change in gas pressure as a function of $r_k$, the Kelvin radius, or the average curvature of the meniscus of the condensed gas; $\gamma$ is the surface tension and $\nu$ is the molar volume of the liquid. The adaptation of this model for mesopore calculations assumes that pores are filled through a capillary condensation process: after initial filling, the pores are spontaneously filled through capillary action. This means that it becomes easier to fill the pores and more difficult to empty them. There are also two opposing effects; loss of surface area reduces adsorption even though capillary action increases it. This is accounted for in the Kelvin equation by including two radii for curvature with opposite signs relating to the opposing processes.[25]

$$\ln \frac{p}{p^0} = \frac{-2\gamma\upsilon}{r_k RT}$$

**Equation 2.6 – The Kelvin equation relating the change in relative pressure $p/p^0$ to the average curvature of the meniscus $r_k$. This is adapted to account for capillary condensation in mesopore analysis as described in the text. $\gamma$ is the surface tension, $\nu$ is the molar volume of liquid, R is the gas constant and T is the operation temperature**

Micropore volumes were determined using the t-plot method developed by de Boer. This method uses the surface area calculated from the BET isotherm. The amount of adsorbed gas n is plotted as a function of the multilayer thickness t. The gradient of the linear part of the t-plot, before capillary condensation occurs, equates to the external surface area, and is compared with a standard reference. In this case $p/p_0$ over the range 0.25-0.49 was used for t-plot micropore analysis. Deviation from the reference is indicative of micropore filling. Multilayer adsorption will not occur in micropores, thus the micropore volume can be calculated from subtracting the external surface area from the total surface area obtained from the BET method.[25]

## 2.2.3 X-ray techniques

### 2.2.3.1 X-ray diffraction

An ordered crystal structure, such as metal particles, will diffract X-rays due to the similarity in the distance between atoms and X-ray wavelengths. This principle is

used in X-ray diffraction to characterise crystal structure. The angle at which the X-ray beam is diffracted is dependent on the wavelength of the X-ray source and the distance between lattice planes, as given by the Bragg equation in *Equation 2.7*.[26]

$$\lambda = 2d \sin\theta$$

**Equation 2.7 – The Bragg law, where λ is the wavelength of the incident X-rays, d is the distance between lattice planes and θ is the glancing angle between the incident X-ray and the lattice plane**

Palladium and gold both have face-centred cubic structures, shown in *Figure 2.4*.[27] In *Chapter 1* the low index exposed facets of Pd were referred to as (111), (100) and (110). This notation is derived from a set of coordinates that is used to describe 3-dimensional crystal structure where the Miller indices, or coordinates (h k l) refer to the location of the nearest atoms of a repeating unit cell. In depth discussion of Miller indices can be found elsewhere[26], although the notation is important to raise here in determination of the lattice parameters (size of the unit cell). For a cubic lattice such as fcc Pd, lattice parameters are all equal and indicated in the figure. The lattice parameter can be calculated using the distance between planes determined from the Bragg law by applying *Equation 2.8*.[26]

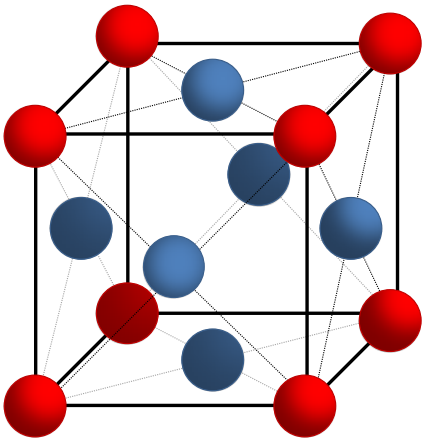

**Figure 2.4 – The fcc crystal structure**

$$d = \frac{a}{\sqrt{h^2 + k^2 + l^2}}$$

**Equation 2.8 – Relationship between the distance between lattice planes and the lattice parameter for a cubic unit cell. h, k and l are Miller indices**

XRD is also used in this thesis for particle size determination. Nanoparticle crystal structure is finite, and this affects the angle at which the X-rays are diffracted resulting in line broadening that can be picked up in the spectrum. The Scherrer equation can be applied to estimate particle size based on the extent of broadening. This is described in further detail in *Chapter 3*.[28]

Catalysts were characterised using powder X-ray diffraction. All ex-situ experiments were performed on a PANalytical X'pertPro X-ray diffractometer fitted with an X'celerator detector and Cu Kα (1.54 Å) radiation source. The *in situ* analysis for Au-Pd/$TiO_2$ nanoparticles and the unsupported Pd nanorods was carried out on a Bruker D8 Advance diffractometer fitted with a Lynxeye high speed strip detector and Cu Kα (1.54 Å) radiation source with an Anton Paar HTK 1200 high-temperature cell and were heated under vacuum to temperature, held for 10 minutes before cooling to 50 °C for data collection. The Au-Pd/$TiO_2$ nanoparticle measurements were collected over 2θ = 20-90° with a step of 0.02° and with a heating rate of 10 °C $min^{-1}$, and the Pd nanorods measurements were collected over 30-55° with a step of 0.016° and a heating rate of 20 °C $min^{-1}$. The *in situ* experiment on sol-immobilised Pd cubes on alumina, were performed on the PANalytical instrument, and heated under nitrogen (1 bar, 20 ml $min^{-1}$) as the instrument was not set up for analysis under vacuum. This data was also collected over 30-55° with a step of 0.016° and a heating rate of 20 °C $min^{-1}$ was used.

#### 2.2.3.2 X-ray photoelectron spectroscopy

X-ray photoelectron spectroscopy (XPS) is a surface sensitive technique that can be used both in elemental analysis and to explore the chemical environment of the sample in question. Core electrons have a binding energy equivalent to the X-ray region, thus by exposing the sample to an incident photon in excess of the core binding energy a photoelectron is ejected leaving behind a core hole (see *Figure 2.5*). This creates an excited ionic state, which then relaxes into the final ground state as outer electrons fill the core holes.[29]

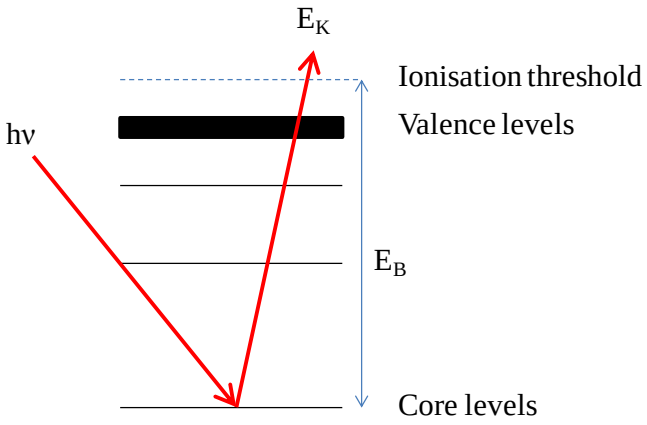


**Figure 2.5 – Generation of a core level photoelectron with kinetic energy $E_K$ by an incident X-ray photon with energy hν where h is Planck's constant and ν is the incident wavelength. $E_B$ is the binding energy**

The kinetic energy of the ejected photoelectron is detected in XPS. It is related to the binding energy of the electron through the photon energy as shown in *Equation 2.9*. This energy is characteristic of the corresponding atom, and so can be used in elemental analysis. Chemical bonding and changes in oxidation state affect the binding energy of the core electron leading to a chemical shift in the detected photoelectron kinetic energy. Simplistically, if the positive charge on the atom is increased through electron withdrawing species bound to the surface or increased oxidation state, the binding energy of the core electron is also increased.[30]

$$E_B = h\nu - E_K$$

**Equation 2.9 – Binding energy $E_B$ can be determined from the kinetic energy of the ejected photoelectron $E_K$ and is dependent on the incident photon energy hν**

Relaxation of the excited ionic state to fill the core hole can lead to two final states due to spin-orbit coupling shown in *Equation 2.10*. For one unpaired electron, s = ±½ and the orbital angular momentum l = 0, 1, 2, 3... corresponding to s, p, d, f... orbitals. Hence for a state where l > 0 and there is one unpaired electron, a doublet peak will be observed. For example, analysis of the Pd 3d state will result in doublet peaks corresponding to $3d_{5/2}$ and $3d_{3/2}$ states.[30]

$$j = l + s$$

**Equation 2.10 – total angular momentum j is given by the vector sum of the orbital and spin components l and s respectively. This gives rise to spin-orbit coupling and doublet peaks in the XP spectra corresponding to states where l > 1 and s is ± ½**

XPS measurements were performed on a Kratos AXIS HSi instrument equipped with a charge neutraliser, Mg $K_\alpha$ source (1253 eV) and a monochromated Al $K_\alpha$ (1486.6 eV) source. Spectra for the Pd catalysts used in *Chapter 3* and the Pd/C catalyst measurements in *Chapter 6* were collected using the Al monochromated X-ray source only and recorded at normal emission using an analyser pass energy of 40 eV and X-ray power of 156 W. *In situ* measurements for the Au-Pd/$TiO_2$ catalysts were carried out by Karen Wilson and were also recorded at normal emission, but using an analyser pass energy of 80 eV. Samples were heated in the main chamber (5 °C $min^{-1}$) whilst maintained at a pressure of 1 x $10^{-9}$ Torr, equilibrated for 30 minutes and cooled down to room temperature before measurements were taken. Spectra were processed using CasaXPS version 2.3.15. All spectra were Shirley background subtracted and were charge corrected to adventitious carbon at 285 eV. Metal lineshapes were fitted using an asymmetric Doniach Sunjic profile and all other spectra were fitted using a symmetric Gaussian–Lorentzian profile. A Doublet separation of 5.27 eV was used for all Pd 3d spectra and of 3.7 eV for the Au 4f spectra. Further fitting parameters are described where relevant in the text.

### 2.2.3.3 X-ray absorption spectroscopy

X-ray absorption spectroscopy (XAS) utilises monochromatic high energy X-rays generated by a synchrotron radiation source in order to follow the extent of X-ray absorption with increasing photon energy. An example XAS spectrum for Pd is shown in *Figure 2.6*. As stated in the previous section, core electrons have equivalent energy to be excited by an X-ray photon and this energy is unique for each element. Thus, XAS experiments are set up for study of the element in question in the sample being studied. Once the incident photon energy is sufficient to excite core electrons an absorption edge is observed in the spectrum. The core electron edge to be studied (using the notation K, $L_I$, $L_{II}$, $L_{III}$... corresponding to 1s, 2s, $2p_{1/2}$, $2p_{3/2}$...) must be selected carefully to avoid overlap with another absorption edge. Analysis of the part of the spectrum immediately after the absorption edge, referred to as the X-ray absorption near edge structure

(XANES) indicated on the figure, is useful for identifying the valency of the analysed species. The intensity of the spectrum here is effectively dependent on the availability of unoccupied states. Thus, an oxidic species that has fewer valence electrons, and so more unoccupied states, will have a more intense peak at lower energy than a reduced species. This is described in further detail in *Chapter 4*.[29, 31]

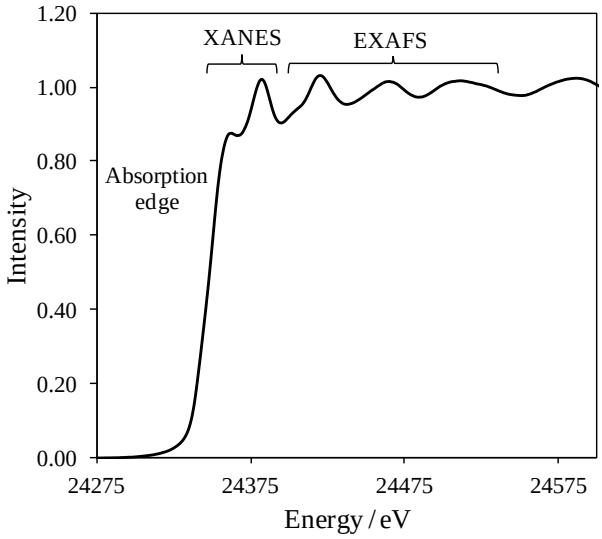


**Figure 2.6 – Example EXAFS spectrum for the Pd K-edge (24350 eV)**

X-ray absorption for photon energies above the absorption edge gradually decays. Across this part of the spectrum oscillations, or modulations in the spectrum are observed. This is the extended X-ray absorption fine structure (EXAFS) and arises due to interference between the emitted photon and neighbouring atoms that lead to scattering of that photon. Constructive and destructive interference with these scattering atoms result in periodic changes in the amplitude of the EXAFS spectrum. The EXAFS spectrum is plotted in 'k-space' and fit to a suitable model using a range of parameters that can provide further information about the atom environment, such as the coordination number and scattering distance between nearest neighbours.[29] This is considered in some more detail in *Chapter 5*. For further details of EXAFS processing see reference 32.[32]

XAS measurements for the experiments in *Chapter 4* are described in *Section 2.3.2*. XAS analysis on Au-Pd/$TiO_2$ catalysts was carried out by Adam Lee and Karen Wilson at Station 9.3 at the Daresbury SRS facility. Fluorescence mode measurements of the Au $L_{III}$ (11.92 keV) and Pd K-edge (24.35 keV) were collected. A Si(220)

double-crystal monochromator with a beam current/energy of 150 mA/2 GeV and 9-channel Ortec germanium solid-state detector was used. Samples were mounted neat within a silica cell under flowing He and were heated at 10 °C $min^{-1}$ to 500 °C for 20 min. Spectra were recorded before heating and after cooling back down to room temperature. Spectra were processed by Adam Lee, using Athena and Artemis from the IFEFFIT Open Source software suite for background subtraction, and phaseshift determination and fitting were performed using Daresbury Excurv98.

## 2.3 Catalyst testing

### 2.3.1 Crotyl alcohol selective oxidation

A stock solution containing crotyl alcohol (6.036 g, 83.9 mmol), mesitylene (1 ml) and toluene (100 ml) was prepared. A reaction was set up using Radley's apparatus containing 10 ml stock solution heated to 60 °C for each catalyst, so that each tube was charged with 8.4 mmol crotyl alcohol. A simultaneous reaction was set up as a control containing 0.34 wt% Pd on amorphous alumina, which had previously been tested on this reaction. A t=0 minutes measurement was taken of the stock solution. Then, 50 mg of each catalyst was added to the respective reaction mixture and a 250 µl sample was removed and filtered for analysis after 6 minutes, 12 minutes, 20 minutes, 30 minutes, 1 hour, 1.5 hours, 2 hours, 3 hours 4 hours and 24 hours. Percentage conversion of crotyl alcohol was measured using gas chromatography (GC) fitted with an FID detector and a CP-Sil 5 CB 15 x 0.25 cm column. A split/splitless injection mode with a split ratio of 90 was applied, an injection temperature of 260 °C and an injection volume of 3 µl. The column oven temperatures and ramp rates are summarised in *Table 2.2* and a carrier flow of 2 ml $min^{-1}$ was used.

| Temperature / °C | Rate / °C $min^{-1}$ | Hold / min | Total / min |
|---|---|---|---|
| 35 | initial | 2 | 2 |
| 90 | 20 | 0 | 4.75 |
| 290 | 40 | 2 | 11.75 |

**Table 2.2 – GC column oven method for the analysis of crotyl alcohol selective oxidation**

The sample is injected into a carrier gas flow (the mobile phase) at high temperature onto the stationary phase immobilised on a long inert metal column. The polarity of the stationary phase, temperature and heating rate of the column oven in particular are used to control separation. In general, more volatile species will be removed from the column first, although species with similar boiling temperatures may have very different retention times depending on their polarity.

### 2.3.2 *In situ* vapour phase crotyl alcohol selective oxidation

1 wt% Pd/meso-$Al_2O_3$, 5 wt% Pd icosahedra/meso-$Al_2O_3$, 5 wt% Pd nanorods/meso-$Al_2O_3$, 2 wt% Pd/SBA-15 and 4 wt% Pd/SBA-15 (40 mg alumina catalysts, 14 mg SBA-15 catalysts) were packed into the sample bed of an *in situ* cell, described in detail in reference 33 and shown in *Figure 4.1*.[33] This was heated to a range of fixed temperatures between 80 °C and 250 °C. Crotyl alcohol was pumped into heated lines (80 °C) at a flow rate of 2 ml $h^{-1}$ (0.4 mmol $min^{-1}$) under 80 ml $min^{-1}$ He carrier flow. Analysis at temperatures below 80 °C was not possible due to condensation of crotyl alcohol on the reactor system. Simultaneously, $O_2$ (80 ml $min^{-1}$, 5 mmol $min^{-1}$) was pumped into a separate line, whilst 4 port valves regularly switched between the two reactants (approximately 0.006 Hz). Surface species were then monitored by DRIFTS using a Bruker IFS66 spectrometer with a high sensitivity MCT detector and 4 $cm^{-1}$ resolution. Desorbed products were followed with mass spectrometry (MS) on a Pfeiffer Omnistar quadrupole mass spectrometer with a heated capillary held at 80 °C. The sample is ionized at a high temperature under vacuum so that charged gas phase molecules and fragments can be passed through a magnetised chamber and collected in terms of their mass/charge ratio. The sample can be ionized either through electron ionization or chemical ionization. Catalyst physical properties were analysed using energy dispersive XAS (EDXAS), described below. Details of data processing are given in *Chapter 4*.

Unlike conventional XAS, energy dispersive techniques can be applied on an extremely fast (ms) timescale, such that it is possible to observe subtle changes to the catalyst structure during reaction.[34] A fixed number of snapshot spectra (1000) for a designated energy window around the Pd K edge (24.35 keV) were collected using beamline ID24 at the European Synchrotron and Radiation Facility (ESRF) in Grenoble. Software and methodology for processing XAS data is not ideally suited for analysis of

dispersive results, and this is currently a limiting factor in the application of this powerful experimental tool. The method adopted for processing data collected in this thesis using the ATHENA package of the IFEFFIT Open Source software suite is described in *Chapter 4.* All X-ray measurements were taken using a symmetric Si [311] polychromator in Bragg configuration with a Frelon X-ray transmittance detector and vertical defocusing of the X-ray beam. A second "reference sample" was also used for normalising out scattering due to support materials. This reference was mounted at the same focal length as the sample. The X-ray pathlength was 5 mm.

## 2.3.3 Benzyl cyanide hydrogenation

### 2.3.3.1 Catalyst pre-treatments

A series of pre-treatments using product adsorption and acid exposure under reaction conditions was executed on the Pd/C catalyst studied in *Chapter 6* carried out by Amy Kidner under the supervision of the author. In all cases approximately 2.5 g of catalyst was added to a Radley's reactor tube charged with the treatment solution in methanol (total 10 ml). Treatment conditions are listed in *Table 2.3* and were undertaken with and without hydrogen (2 bar, 20 $ml^{-1}$). All experiments were carried out at room temperature, under vigorous mechanical stirring for 5 hours. The reaction mixture was then washed with methanol and deionised water, centrifuged at 4,000 rpm and dried under vacuum at 40 °C overnight.

| Pretreatment | $H_2$ pressure / bar | PEA / mmol | $H_2SO_4$ / mmol |
|---|---|---|---|
| Fresh catalysts | 0 | 0 | 0 |
| Blank treatment | 2 | 0 | 0 |
| Product adsorption | 0 | 8.4 | 0 |
| Product adsorption | 2 | 8.4 | 0 |
| Promoter effects | 0 | 0 | 1 |
| Promoter effects | 0 | 0 | 5 |
| Promoter effects | 0 | 0 | 10 |
| Promoter effects | 0 | 8.4 | 1 |

**Table 2.3 – Pretreatment conditions used by Amy Kidner to assess the effect of phenylethylamine (PEA) product adsorption and $H_2SO_4$ as a promoter to the properties of 5 wt% Pd/C (2.5 g)**

### 2.3.3.2 Reactor setup

Reaction measurements were also carried out in a Radley's tube reactor. A stock solution containing benzyl cyanide (9.84 g, 84 mmol), mesitylene (1 ml) and methanol (100 ml) was prepared. A reaction was set up once again using Radley's tube reactor, and the apparatus was heated to the appropriate temperature and purged with $H_2$ at the specified pressure (20 ml $min^{-1}$) through a dip tube. A needle was inserted into the reactor lid for the experiment exhaust, which passed through a bleach scrubber. For each experiment, the reactor was charged with 10 ml stock solution to which 5 wt% Pd/C catalyst (200 mg) was added. A t=0 minutes measurement was taken of the stock solution. Then a 250 μl sample was removed and filtered for analysis after 10 minutes, 20 minutes, 30 minutes, 1 hour, 2 hours, 3 hours and 6 hours. The catalyst was recovered through centrifugation (4,000 rpm) and washing with methanol and deionised water. Percentage conversion of benzyl cyanide was measured using gas chromatography-mass spectrometry (GC-MS).

Once the sample has been separated on the GC column it is detected by on-line MS. GCMS was carried out on a Varian 450-GC and Varian 240-MS using electron ionisation. The GC column was a VF-5ms 30 m x 0.25 mm column, injector (1177) and detector temperatures of 250 °C and valve temperature of 280 °C. A split ratio of 90 was used and injection volume of 1 μl. The column method used is outlined in *Table 2.4*. Centroid acquisition was applied for MS detection covering a mass range between m/z 70 to m/z 400 with a scan time of 0.43 s $scan^{-1}$. A filament delay was applied for 3 minutes to by-pass detection of the solvent. Tune type DFTPP was used with an emission current of 25 μA.

| Temperature / °C | Rate / °C $min^{-1}$ | Hold / min | Total / min |
|---|---|---|---|
| 80 | initial | 2 | 2 |
| 300 | 30 | 2 | 11.33 |

**Table 2.4 – GCMS column oven method for the analysis of benzyl cyanide hydrogenation**

## 2.4 References


1. F. Vaundry, S. Khodabandeh and M. E. Davis, *Chem. Mater.*, 1996, **8**, 1451.
2. S. F. J. Hackett, University of York (PhD), 2008.

3. S. F. J. Hackett, R. M. Brydson, M. H. Gass, I. Harvey, A. D. Newman, K. Wilson and A. F. Lee, *Angew. Chem.-Int. Edit.*, 2007, **46**, 8593.
4. C. M. A. Parlett, D. W. Bruce, N. S. Hondow, A. F. Lee and K. Wilson, *ACS Catalysis*, 2011, **1**, 636.
5. D. Zhao, Q. Huo, J. Feng, B. F. Chmelka and G. D. Stucky, *J. Am. Chem. Soc.*, 1997, **120**, 6024.
6. C. M. A. Parlett, Cardiff University (PhD), Submitted 2012.
7. Y. J. Xiong, J. M. McLellan, Y. D. Yin and Y. N. Xia, *Angew. Chem.-Int. Edit.*, 2007, **46**, 790.
8. Y. J. Xiong, H. Cal, B. J. Wiley, J. Wang, M. J. Kim and Y. N. Xia, *J. Am. Chem. Soc.*, 2007, **129**, 3665.
9. F. R. Fan, A. Attia, U. K. Sur, J. B. Chen, Z. X. Xie, J. F. Li, B. Ren and Z. Q. Tian, *Cryst. Growth Des.*, 2009, **9**, 2335.
10. A. F. Lee, C. V. Ellis, K. Wilson and N. S. Hondow, *Catal. Today*, 2010, **157**, 243.
11. G. Schmid, A. Lehnert, J.-O. Malm and J.-O. Bovin, *Angew. Chem.-Int. Edit.*, 1991, **30**, 874.
12. D. Chescoe and P. J. Goodhew, *The operation of the transmission electron microscope*, Oxford University Press, Oxford, 1984.
13. R. J. Keyse, A. J. Garrett-Reed, P. J. Goodhew and G. W. Lorimer, *Intorduction to Scanning Transmission Electron Microscopy*, BIOS Scientific Publishers, Oxford, 1998.
14. M. Thompson and J. N. Walsh, *Handbook of Inductively Coupled Plasma Spectrometry*, 2nd edn., Blackie Academic & Professional, Glasgow, 1989.
15. M. Slavin, *Atomic Absorption Spectroscopy*, 2nd edn., John Wiley and Sons, 1978.
16. M. E. Brown, *Introduction to thermal analysis: techniques and applications*, Chapman and Hall, Cambridge, 1988.
17. R. S. Monteiro, L. C. Dieguez and M. Schmal, *Catal. Today*, 2001, **65**, 77.
18. C. L. M. Joyal and J. B. Butt, *J. Chem. Soc. Faraday Trans. 1*, 1987, **83**, 2757.
19. S. Devarajan, P. Bera and S. Sampath, *J. Colloid Interface Sci.*, 2005, **290**, 117.
20. H. Conrad, G. Ertl, J. Koch and E. E. Latta, *Surf. Sci.*, 1974, **43**, 462.
21. H. Gunzler and H.-U. Gremlich, *IR Spectroscopy: An Introduction*, Wiley-VCH, Weinheim, 2002.
22. A. Guerrero-Ruiz, S. W. Yang, Q. Xin, A. Maroto-Valiente, M. Benito-Gonzalez and I. Rodriguez-Ramos, *Langmuir*, 2000, **16**, 8100.
23. Z. J. Li, F. Gao, Y. L. Wang, F. Calaza, L. Burkholder and W. T. Tysoe, *Surface Science*, 2007, **601**, 1898.
24. I. V. Yudanov, R. Sahnoun, K. M. Neyman, N. Rosch, J. Hoffmann, S. Schauermann, V. Johanek, H. Unterhalt, G. Rupprechter, J. Libuda and H. J. Freund, *J. Phys. Chem. B*, 2003, **107**, 255
25. F. Rouquerol, J. Rouquerol and K. Sing, *Adsorption by Powders and Porous Solids: Principles, Methodology and Applications*, Academic Press, London, 1999.
26. P. Atkins and J. de Paula, *Atkins' Physical Chemistry*, 7th edn., Oxford University Press, Oxford, 2002.
27. B. Fu, W. Liu and Z. Li, *Appl. Surf. Sci.*, 2010, **256**, 6899.
28. P. Scherrer, *Math.-Physik.*, 1918, **2**, 98.
29. J. F. Watts, in *Surface Science Techniques*, eds. J. M. Walls and R. Smith, Elsevier, Oxford, Editon edn., 1994.

30. K. Kolasinski, *Surface Science: Foundations of Catalysis and Nanoscience*, John Wiley & Sons, Chichester, 2002.
31. J. M. Hollas, *Modern Spectroscopy*, 4th edn., John Wiley and Sons, Chichester, 2004.
32. B. Ravel and M. Newville, *J. Synchrot. Radiat.*, 2005, **12**, 537-541.
33. M. A. Newton, *Top. Catal.*, 2009, **52**, 1410.
34. M. A. Newton, *J. Synchrot. Radiat.*, 2007, **14**, 372.

# Chapter 3

# The effect of palladium nanoparticle morphology on crotyl alcohol selective oxidation

## 3.1 Introduction

Selective oxidation (selox) is a key process employed for the synthesis of important fine and specialty chemicals utilised within the fragrances and flavourings industries.[1] These transformations are currently performed via hazardous stoichiometric reagents or expensive homogeneous catalysts, hence alternative clean technologies employing heterogeneous catalysts and benign oxidants are urgently sought.[2] However, the development of such alternative solid catalysts is hindered by a poor understanding of the active site responsible for selox chemistry.[3] Recent advances in simple, wet chemical approaches to monodisperse nanoparticle synthesis have resulted in a wealth of literature directed towards developing metal nanoparticles of well defined size and shape, through which the catalyst active site can potentially be tuned.[4, 5] In *Chapter 1* the synthesis of size and shape controlled nanoparticles is reviewed, and the benefits of such systems applied to catalyst design is considered. Although the synthetic methods for morphology controlled monodisperse particles have improved immensely in recent years, understanding of the chemical processes is still limited.[6] Fine control is possible on very dilute small scales, but scale-up, such that there is sufficient product to study extensively, requires further development. As a result, research into the properties of such tailored nanoparticles and their practical application is scarce, although some examples have been addressed in *Chapter 1*.

The aim of this chapter is to assess the shape dependent catalytic properties of suitable Pd nanoparticles on crotyl alcohol selox, in order to aid understanding for catalyst design. Here, the literature procedures of three tailored nanoparticles – Pd icosahedra, Pd nanorods and Pd nanocubes – are adapted for catalytic investigation, extensively characterised and their reactivity is tested. A highly active mesoporous alumina supported Pd catalyst is referred to at points in this chapter as a benchmark to compare the reactivity of the three nanoparticulate shapes.[2, 7]

First, the morphology and nature of the exposed facets is identified using microscopy and various spectroscopic techniques. Conventional platinum group metal (PGM) nanoparticles adopt a cuboctahedron morphology exposing both (111) and (100) facets. The icosahedron is entirely encapsulated with (111) facets and the cube with only (100) facets. The tapered rod shape contains all three low-index facets: the tapered ends are (111), and lengthways (100) and (110) terminated faces are exposed in approximate proportions of 1:5:5 respectively.[4, 8] This is illustrated in *Figure 3.1*.

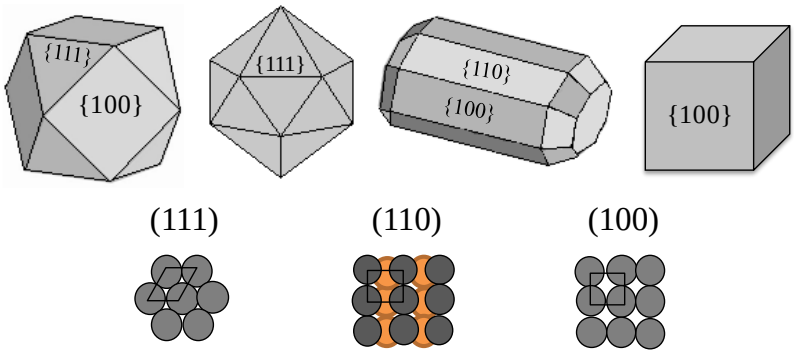


**Figure 3.1 – Nanoparticle shapes expose different facets. From left to right: fcc Pd cuboctahedron, icosahedron, rod and cube**

Three different procedures have been attempted to control the size of the three tailored nanoparticles. In the first two experiments the initial reaction conditions were adapted. Limitations of these methods, and further ways in which reaction conditions can potentially be modified in order to control nanoparticle size, are then discussed. The third method, which led to a study of the thermal properties of the catalysts, involves post-synthesis treatment of the nanoparticles through controlled heating. Although this is unsuccessful here, this procedure is used in controlling surface metal concentration in *Chapter 5*.

Finally, the three tailored catalysts are tested alongside the benchmark alumina supported catalyst for crotyl alcohol selox. The effect of nanoparticle shape on reactivity is illustrated and an explanation for the observed results is proposed.

# 3.2 Results and discussion

## 3.2.1 Synthesis and characterisation of Pd nanoparticles

### 3.2.1.1 Transmission electron microscopy

The syntheses of Pd nanorods, Pd icosahedra and Pd nanocubes are described in *Chapter 2*, based on the procedures developed by Y. J. Xiong et al. and F. R. Fan and co-workers.[8-10] *Figure 3.2* shows the high resolution transmission electron microscope (HRTEM) image of Pd nanorods, alongside an example of one of the lower magnification micrographs that were used for particle size analysis (see *Chapter 2*). The high resolution image confirms the elongated structure of the nanoparticles, made up of (100) and (110) facets, with slightly tapered ends that expose (111) facets. From the size distribution histogram, displayed in *Figure 3.3*, the mean particle size is 9.2 nm. Note

the bimodal distribution: it is not possible to distinguish between shorter particles, and nanoparticles that are imaged end-on. In order to confirm that the bimodal distribution is due to nanoparticle orientation, and not that some smaller particles and some larger particles have formed, the aspect ratio as a function of particle size is considered. There is a positive correlation (*Figure 3.3*) indicative of a singular particle size range. Particle width does not change, but particle length does. The average aspect ratio is 2.8.

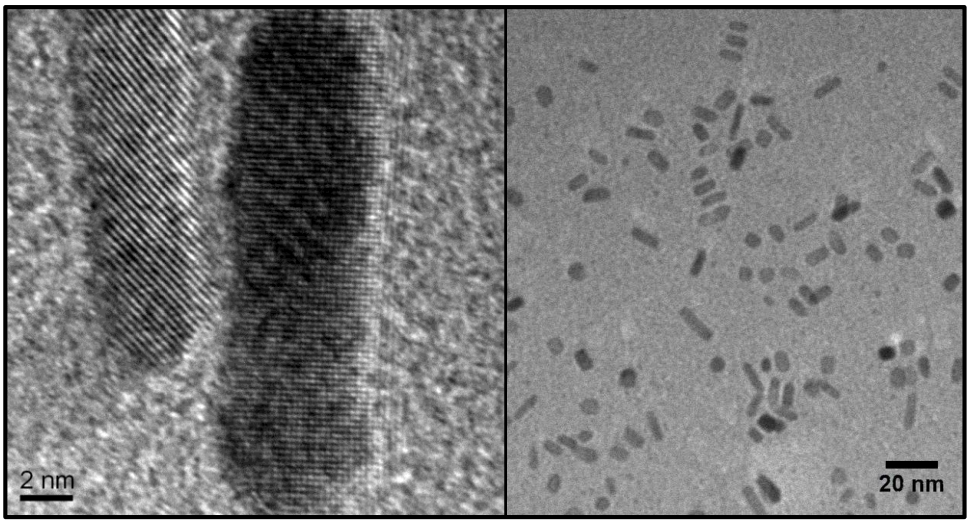


**Figure 3.2 – HRTEM of Pd nanorods (left) and low resolution image of Pd nanorod particles (right)**

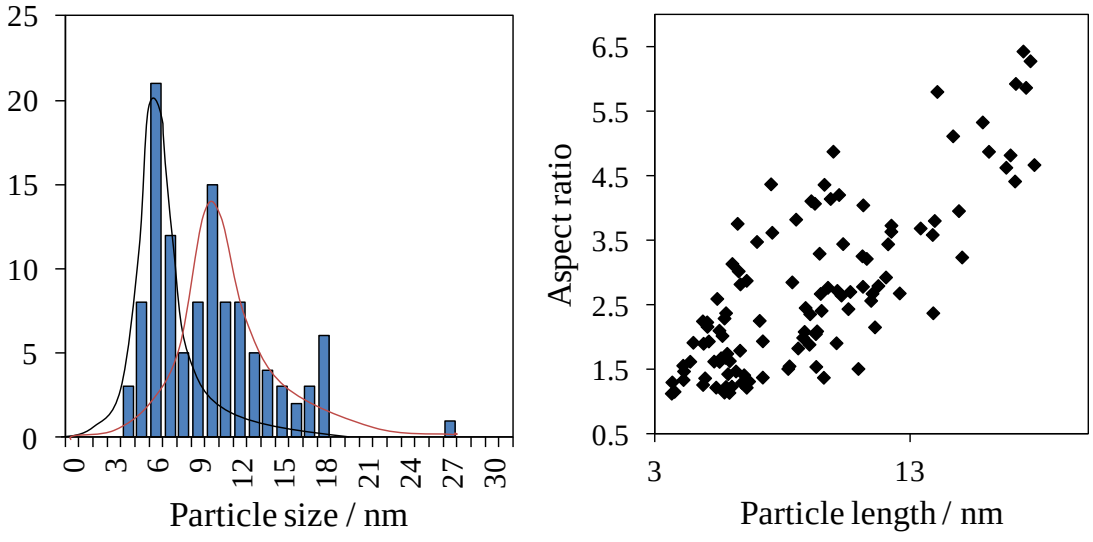


**Figure 3.3 – Size distribution of Pd nanorods (left) and correlation between aspect ratio and particle length (right)**

HRTEM of Pd icosahedra is given in *Figure 3.4*, alongside the lower magnification image and a particle histogram. The morphology can be confirmed from

the image: the 5 fold symmetry of the icosahedron shape is indicated in the figure. This synthesis was scaled up 10 times from the original literature synthesis. Attempts made to increase particle size will be discussed in a later section, but it is worth noting that the larger these strained twinned shapes are, the less stable they are, and triangular sheets or cuboctahedra are more likely to form.[4] The mean particle size in this case was 2.8 nm by TEM.

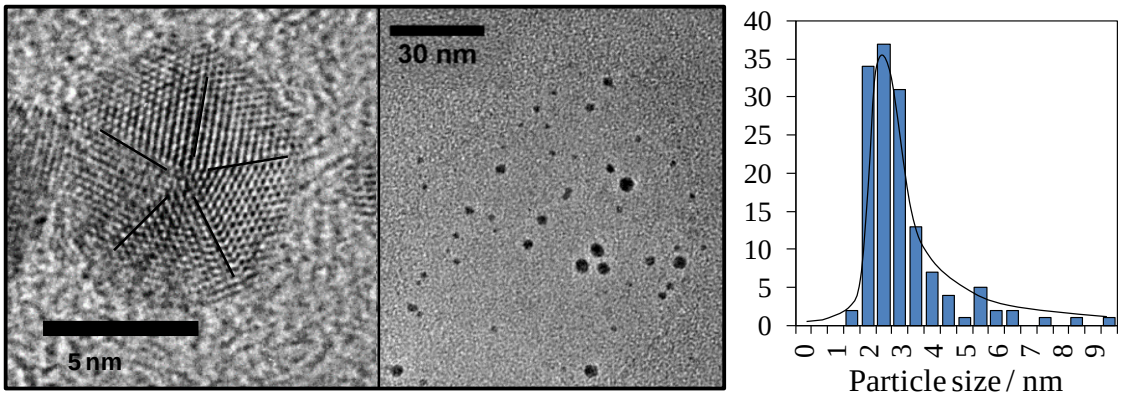


**Figure 3.4 – HRTEM micrograph of Pd icosahedra indicating 5-fold symmetry (left) and one of the low resolution images used to create the particle size histogram (right)**

Finally, an HRTEM micrograph and a particle size histogram of Pd nanocubes are displayed in *Figure 3.5*. Contrary to the Pd icosahedra, the synthesis of Pd nanocubes smaller than approx. 20 nm at the time this research was commenced, had not been achieved. Y. Xia and collaborators have since synthesised sub-10 nm Pd nanocubes and tested their catalytic reactivity on 2-methyl-3-butyn-2-ol.[11] Thus, it will be possible to develop the structure sensitive relations investigated in this thesis further, using these new synthetic strategies. Due to the larger particle size and higher dispersion on the TEM grid, the particle size analysis was compiled using more images containing approx. 5-10 particles (approx. 100 particles in total) and each particle was measured individually. The cube shape is clear from the high resolution image. Some tetrahedra shapes and nanodendrites were present in the sample, but Pd nanocubes were dominant. Mean particle size was determined to be 24.0 nm.

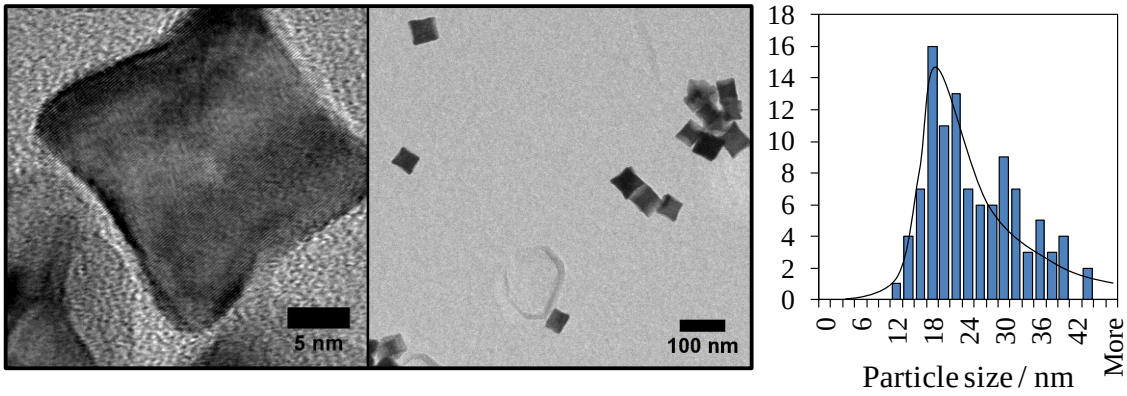


**Figure 3.5 – HRTEM micrograph of Pd nanocubes (left) and one of the low resolution images used to create the particle size histogram (right)**

### 3.2.1.2 Powder X-ray diffraction

Powder X-ray diffraction (XRD) was performed on the three catalyst samples, from which an average particle size could be calculated by applying the Scherrer equation (*Equation 3.1*).[12] The incident wavelength, λ, is 1.54 Å; B is the full width half maximum of the lowest index reflection; S is 0.15, a constant corresponding to diffractometer broadening, determined from the peak width obtained from a quartz standard. The values of the shape factor, k, that correspond to different symmetric shapes recommended by XPert XRD software, are given in *Table 3.1*. The XRD does not, however, discriminate length from width, and so particle size calculated for anisotropic shapes using this method will be an underestimate. A value for k of 1 was used in measuring Pd nanorod particle size.

$$P = \frac{k\lambda}{\sqrt{\left(B^2 - S^2\right)\cos\theta}}$$

**Equation 3.1 – The Scherrer equation for particle size analysis from XRD line broadening. P is the particle size, k is the shape factor, λ the incident wavelength in this case 1.54 Å, B is the full width half maximum of the lowest index peak, S corresponds to the diffractometer line broadening and θ is the lowest index peak position.**

| Particles | k based on FWHM | k used |
|---|---|---|
| Spheres | 0.89 | |
| Cubes | 0.83-0.91 | 0.87 |
| Tetrahedra | 0.73-1.03 | |
| Octahedra | 0.82-0.94 | |
| Rods | | 1.00 |
| Icosahedra | | 0.90 |
| Cuboctahedra | | 0.90 |

**Table 3.1 – Shape factors, k, used to determine particle size from X'pert Data Collector Version 2.2b help file[*]**

In addition, there are a number of limitations which must be raised in the Scherrer formula approach to deducing particle size. In a review on particle size and size distribution measurements by R. J. Matyi et al., it is shown that particle size calculated using the Scherrer formula is likely to be less than the actual particle size. Other contributing factors to line broadening in XRD, such as crystal stacking faults, are not addressed in the Scherrer formula, which may affect the particle size estimate.[13] Size data here will be used to complement size analysis data already calculated by TEM.

The XRD patterns of the three nanoparticles are shown in *Figure 3.6*. The peaks highlighted * in the Pd nanorod pattern are from KBr(220), KBr(311) and KBr(222) reflections, in order of increasing angle.[14] The peaks at 39.8° and 45.6 ° (†) correspond to Pd(111) and Pd(200) respectively. Particle size analysis is as follows: 4.3 nm for Pd nanorods, 2.7 nm for Pd icosahedra and 16.3 nm for Pd nanocubes. As expected, the Pd nanorods size estimate is smaller than the TEM size estimate, but the Pd icosahedra and Pd nanocubes are in excellent agreement with TEM.

[*] X'Pert Data Collector Version 2.2b PANalytical B.V. Almelo The Netherlands 1996-2012

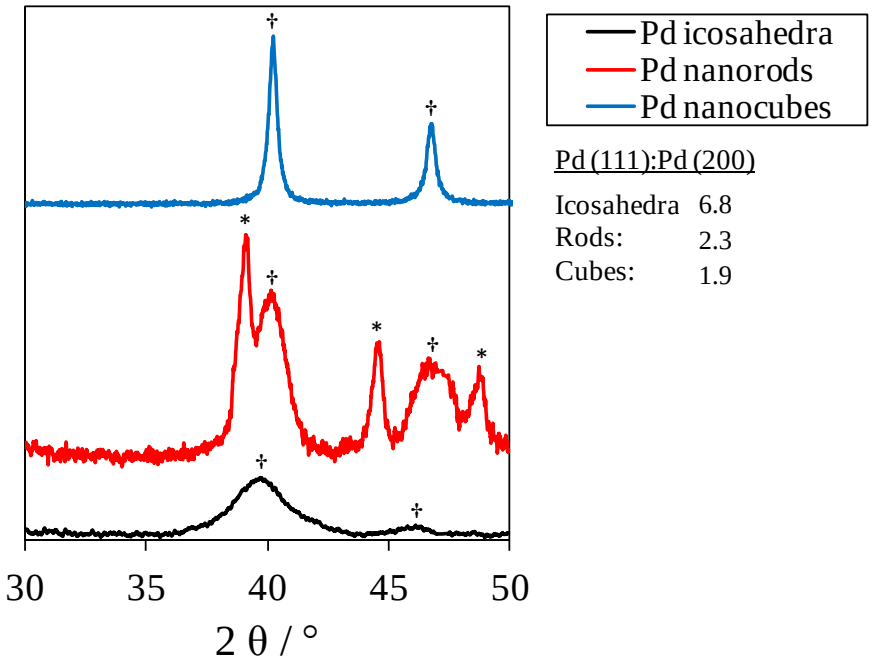


**Figure 3.6 – Powder XRD patterns of Pd icosahedra, Pd nanorods and Pd nanocubes including the ratio of Pd(111):Pd(200) intensity**

In addition to size analysis, it is possible to obtain some information regarding the exposed facets of the nanoparticles from the XRD patterns. Although XRD is a bulk technique, and thus diffraction occurs across all crystal planes, texturing effects, due to the orientation in which the particles will lie, affect the relative intensity of the reflections for each plane.[15] In *Figure 3.6*, the Pd(111) and Pd(200) reflections are apparent. Taking the ratio of the intensity of these two reflections reveals that the Pd (200) reflection is relatively more intense for the (100) enclosed Pd nanocubes than for the (111) encapsulated icosahedra. The values of these ratios are given in the figure.

### 3.2.1.3 *In situ* diffuse reflectance infra-red Fourier transform spectroscopy

A final method, used to investigate the exposed surface terminations of the nanoparticles, involved probing the catalyst surface, after exposure to CO, with diffuse reflectance infra-red Fourier transform spectroscopy (DRIFTS). The molecular orbital diagram of CO is illustrated in *Figure 3.7*. When CO chemisorbs on Pd, the π bond is weakened due to back donation from the Pd HOMO $d_{z^2}$ orbital to the CO π* orbital. The absorption energy is sensitive to the CO adsorption mode such that the relative strength of the CO π bond is dependent on how the CO molecule adsorbs on the surface. Hence

the stretching frequency of the C=O bond is dependent on the surface atomic arrangement.

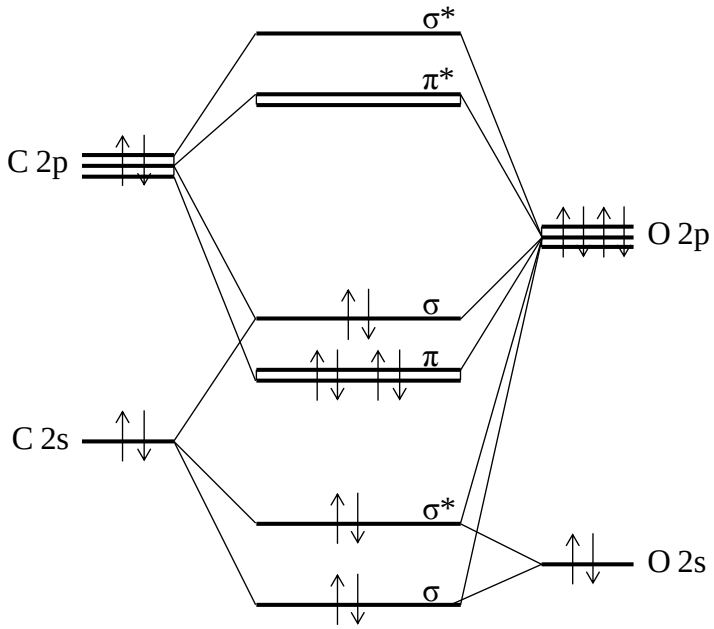


**Figure 3.7 – Carbon monoxide molecular orbital energy level diagram**

A simplified illustration of CO adsorption modes is given in *Figure 3.8*. In particular, it is worth noting the differences in the multi-coordinate sites on the low index facets. Pd(111) has three-fold hollow sites, but no four-fold hollow sites. The situation is the reverse for Pd(100). For Pd(110) there are trough sites that may be adopted. Even if the CO adsorbs bridging on all three surfaces, the stretching frequency will not be the same.

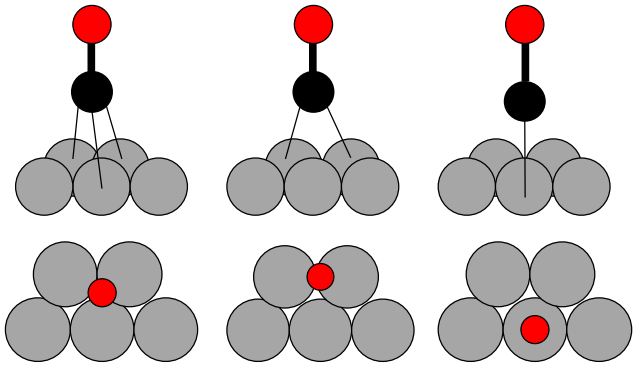

**Figure 3.8 – Schematic representing the adsorption modes of CO on a Pd(111) surface. Although strictly speaking the 'bonds' to the surface may be better represented by band structure, the illustration shows the increasing strength of the Pd-C interaction through π-π * backbonding and the consequential shift to lower energy of the CO vibration**

By exploiting the effects described above, it is possible to investigate qualitatively the Pd nanoparticle shapes and confirm the nature of the exposed facets using an entirely surface sensitive technique. The DRIFT spectra during and after CO exposure for the three catalysts is displayed in *Figure 3.9*. The dotted line in all three spectra was taken before CO exposure.

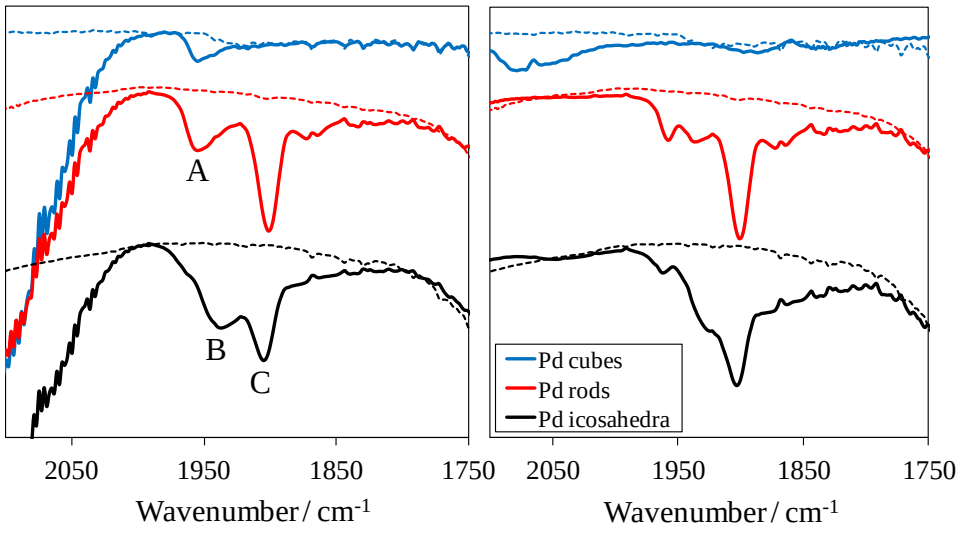


**Figure 3.9 – DRIFT spectra for Pd icosahedra, nanorods and nanocubes during CO exposure (left) and after purging with nitrogen for 40 minutes (right)**

Three adsorption modes for CO on Pd facets have been identified from the literature: CO adsorbed bridging over Pd(100) at 1953 $cm^{-1}$, CO adsorbed bridging over Pd(111) at 1934 $cm^{-1}$ and CO adsorbed multi-coordinate at 1900 $cm^{-1}$ labelled A, B and C, respectively, in the figure.[16] The intensity of adsorption in the nanocubes is considerably less than the nanorods and icosahedra. The lower surface area of the nanocubes is likely to be a significant reason for this. However, the stretching frequency of adsorbed CO is attributable, in this instance, to CO bridging on Pd(100). This provides further evidence that the exposed surfaces in this sample are made up of Pd(100) terminated facets. It is also interesting to note that no multi-coordinate CO is present, although it is dominant in both the nanorods and icosahedra samples. Computational studies by I. V. Yudanov et al. predict that CO adsorption over 4-fold hollows has a lower stretching frequency and would be expected at around 1650-1690 $cm^{-1}$.[17] It was not possible to resolve any features here, due to a large band from PVP.

However, the absence of CO at 1900 $cm^{-1}$ for the Pd nanocubes does confirm that there are no three-fold hollow sites for this sample.

A comparison of the spectra for the Pd icosahedra and Pd nanorods is also useful. Of the bridging adsorption modes, Pd(111) is dominant for the icosahedra. There is only a slight shoulder during CO exposure, which was resolved into a relatively small peak after purging. This has been assigned to CO adsorbed bridging to Pd(100). Thus, the Pd icosahedra catalyst largely comprises Pd(111) facets.

Contrary to this, the dominant bridging feature during CO exposure for the Pd nanorods sample has been identified as CO adsorbed to a Pd(100) surface. However, after purging with nitrogen, it is clear that there is a significant contribution from Pd(111) adsorbed CO. This is consistent with a nanorod model comprising Pd(111) tapered ends and some Pd(100) exposed edges. It has not been possible to identify Pd(110) facets from this technique. Nevertheless, the presence of Pd(111) facets confirms that the particles are rod shaped rather than bar shaped, as the latter would be entirely encapsulated by 6 Pd(100) enclosed faces. It can further be inferred from geometric considerations, described in the literature procedure, that the nanoparticles expose Pd(110) edges as well as Pd(100).[8]

### 3.2.2 Effect of ethylene glycol concentration on Pd nanorods

It has been well documented that particle size influences nanoparticle properties and reaction outcome, particularly below approximately 4 nm.[18-21] As a result, several attempts were made to synthesise a size series of the morphology controlled nanoparticles. Although some progress was made, it soon became clear that this work would require more in depth exploration, in order to achieve the necessary control to compare only size properties of particular nanoparticle facets (i.e. maintain morphology whilst tuning size), on a scale large enough to test the unsupported particles. Further work is necessary in this area, and some ideas on how to proceed are proposed.

It is widely understood that the liquid phase approach to nanoparticle synthesis proceeds via a nucleation and growth mechanism, although the details of this mechanism are still being debated.[22] The fundamental criterion influencing this mechanism is the instantaneous concentration of reduced metal particles at any one time: thus, reducing rate and reductant and precursor concentrations are all crucial. If

the instantaneous concentration of metal particles is high, up to a point before the particles agglomerate, nucleation will occur in preference to further growth and small particles that exhibit more uniform shapes will form. There is also a critical size that the seed must reach in order for particle growth to occur. Other chemical additives and stabilisers play an important role, the extent of which is not understood. However, maintaining these, whilst controlling the properties mentioned will have an effect on the nanoparticle size and shape.[22-25]

Thus, conditions that can be varied include the reductant strength (in all the syntheses described in this thesis, mild reducing agents are used, which slow down the reduction rate), the reductant concentration, the addition rate, the reaction temperature and the reaction time. In this first example, the concentration of ethylene glycol in water was varied to control particle size. This was seen to have an effect for a small scale synthesis in the literature, as ethylene glycol is a slightly stronger reducing agent than water ($pK_a$ of ethylene glycol is 14.8, $pK_a$ of water is 15.7). The greater the ethylene glycol concentration, the faster the reducing process and smaller particles are predicted to form.

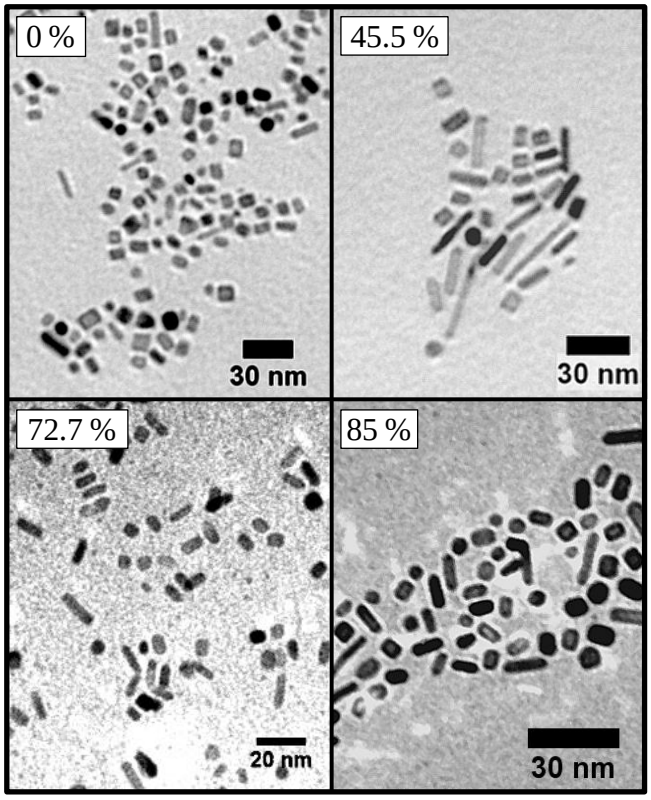


**Figure 3.10 – TEM micrographs of Pd nanorods using different concentrations of ethylene glycol, as indicated on the figure.**

*Figure 3.10* includes TEM micrographs of the nanoparticles synthesised using 0 %, 45.5 %, 72.7 % and 85 % ethylene glycol concentration in water. The Pd nanorods referred to in the rest of this chapter and *Chapter 4* were synthesised using 72.7 % ethylene glycol. Even by eye, it is clear that there is a difference in particle size between the different concentrations. However, the first points to note from these images are the changes to particle shape. In the absence of ethylene glycol, the aspect ratio is near to one, whilst for the lower ethylene glycol concentrations, predominantly nanobars have formed, not nanorods. This is significant: the nanobar shape is entirely enclosed by (100) facets, such that the (110) surface is not exposed. Any further study of how the physical and chemical properties of the nanoparticles vary with size is not possible using this method, as the nature of the exposed facets has already been changed.

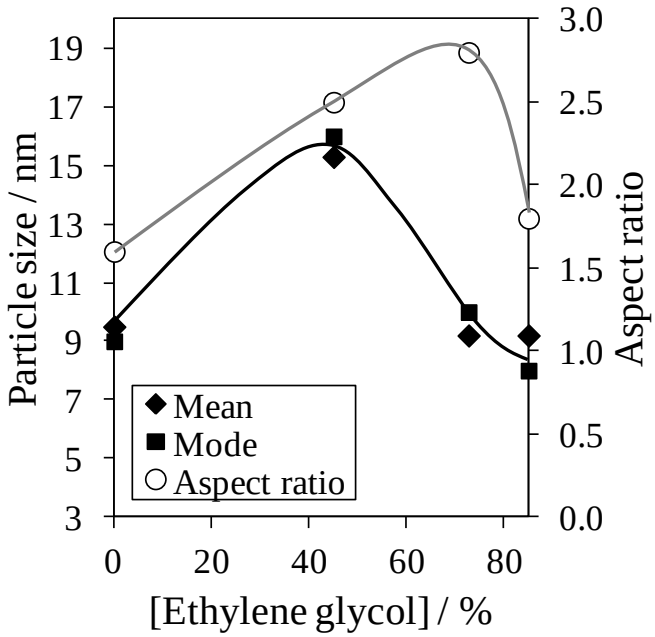


**Figure 3.11 – Average particle size and aspect ratio as a function of ethylene glycol concentration used in Pd nanorods synthesis**

In *Figure 3.11* the mean size, mode size and aspect ratio is plotted against concentration. Interestingly there is no linear relationship: the largest particles were synthesised at 45.5 % ethylene glycol concentration. Towards 50 % concentration the particle size of the nanobars increases, while at a greater than 50 % concentration the size of the nanorods decreases. It would be interesting to investigate further concentrations in both regimes to confirm where the nanorods → nanobars transition occurs and whether the particle size variation is consistent. It is also worth noting that

the aspect ratio increases up to 72.7 % ethylene glycol concentration. It is only at the highest concentration that the aspect ratio begins to drop again. The deviation in particle size growth occurs at the same concentration that nanorods, rather than nanobars are seen.

### 3.2.3 Effect of reaction time on icosahedra

In the literature procedure, Pd icosahedra particle size was successfully controlled by changing the reaction time, and so this was attempted here on a larger scale. *Figure 3.12* shows TEM micrographs for the reaction after 5 hours (used throughout this thesis), 8 hours, 21 hours and 24 hours. In addition, particle size histograms are given in *Figure 3.13*. In this case the reaction time did not influence the average particle size. The particle size distributions are broader for longer reaction times. In order to ascertain if these results were influenced by the scale-up of the procedure from the literature, or another factor in the synthesis, the reaction procedure over 26 hours was copied exactly. Larger Pd icosahedra were formed (*Figure 3.14*), although a number of triangular sheets were also observed. It is likely that increasing reaction time for a larger reaction does not provide the controlled growth necessary to achieve monodispersity. Unlike the other procedures investigated, the icosahedra synthesis uses a very fast addition rate. Mass transport limitations in combination with this fast addition rate on a larger scale will affect the instantaneous concentration in the reaction vessel.

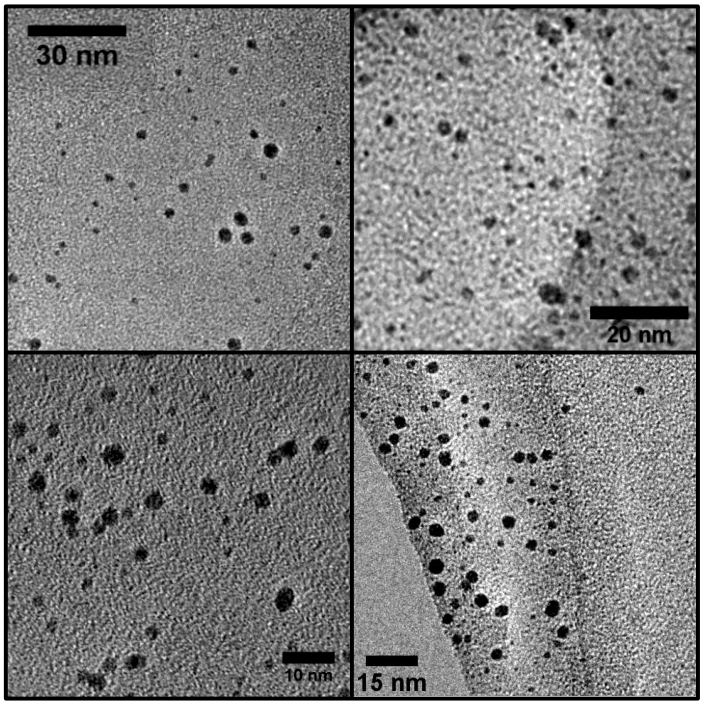


**Figure 3.12 – TEM micrographs of 5 hour, 8 hour, 21 hour and 24 hour syntheses from Pd icosahedra procedure**

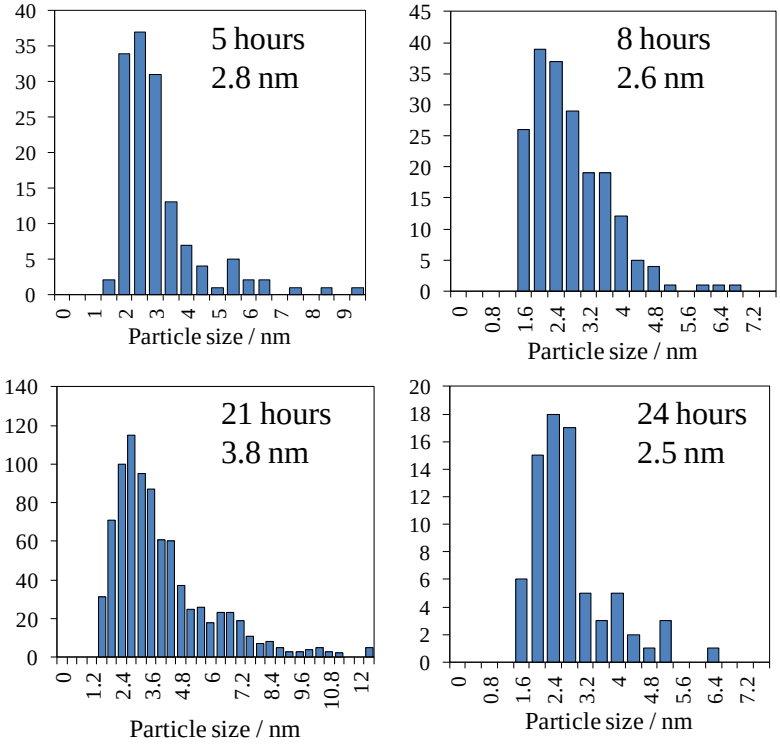


**Figure 3.13 – Size histograms of 5 hour, 8 hour, 21 hour and 24 hour syntheses from Pd icosahedra procedure**

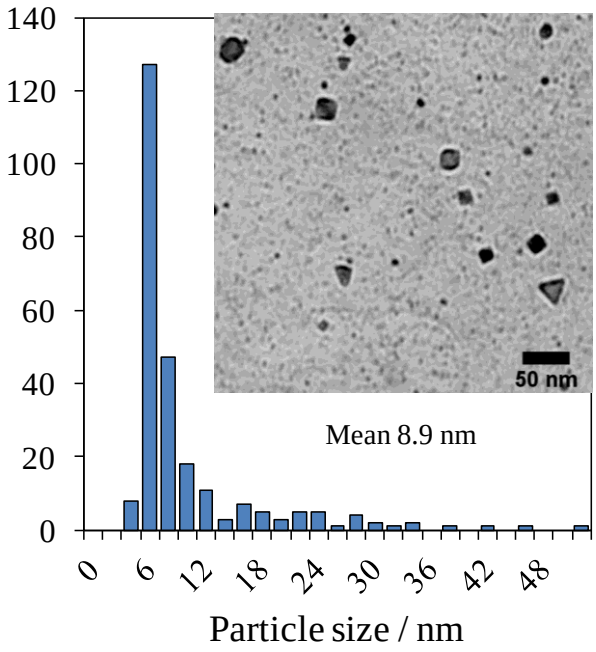


**Figure 3.14 – TEM micrograph and size histograms of 26 hour literature scale synthesis from Pd icosahedra procedure**

Another area that has not been explored and that may be used to influence the size of the nanoparticles is that of addition rate. Synthetic procedures that adopt a slower addition rate exhibit better control on a large scale, since the instantaneous concentration is of such importance. If the conditions of the synthesis were developed, such that particle shape was maintained at slower addition rate, then it may be possible to control particle size. For the icosahedra synthesis, it is proposed that a higher citric acid concentration and slower addition rates would achieve this. As well as increasing reduction rate on higher citric acid concentration, it is suggested in the literature procedure that the presence of citric acid is key to creating the (111) encapsulated morphology.

## 3.2.4 Thermal properties of PVP stabilised Pd nanoparticles

### 3.2.4.1 Thermogravimetric analysis

An investigation into the thermal properties of the Pd nanoparticles studied in this chapter was undertaken in order to establish the temperatures at which morphology and size changes occur. An important consideration is the order in which such changes occur: if the particle size can be tuned up to a point, whilst maintaining particle shape,

this method could be used to create a size series of different nanoparticle shapes, for which the catalyst reactivity can be tested further. The thermal evolution under inert conditions provides a possible route for tuning the nanoparticle size without changing the chemical composition.

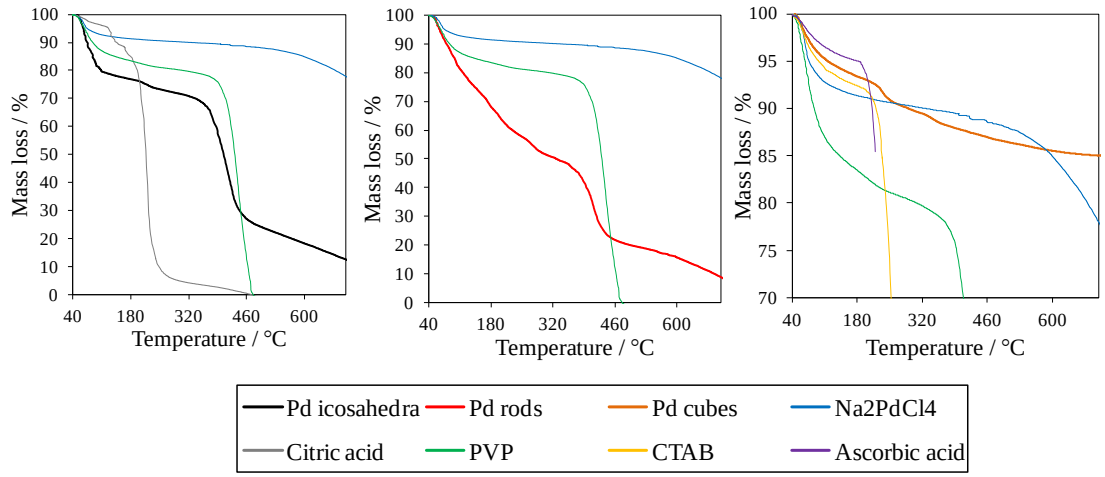


**Figure 3.15 – TGA percentage mass loss for nanoparticle shapes and standards used in synthesis**

TGA was performed on the three unsupported nanoparticles under He up to 700 °C. The results for the three nanoparticles, alongside standards of the stabilisers and precursors used in synthesis, are given in *Figure 3.15*. For both Pd icosahedra and Pd nanorods, the most significant mass loss can be associated with PVP, commencing at 320 °C. There is a small mass loss below this temperature, at around 200 °C for the Pd icosahedra, coinciding with loss of citric acid. Additionally, there is a larger mass loss for the Pd nanorods, most likely associated with water and residual ethylene glycol (boiling point ~196-198 °C). These nanoparticles were extremely hydroscopic and had an increasingly viscous tar-like consistency over a period of months. The importance of these additives, stabilisers and the PVP capping agent, on the stability of particle size and shape after synthesis, can be deduced through further ex-situ TEM and XRD and *in situ* XRD, outlined in the next sections. Changes up to 300 °C can be correlated with factors other than loss of PVP.

The more significant mass loss for the Pd nanocubes is associated with CTAB by 240 °C. These nanoparticles are >70 wt% palladium, hence the smaller overall mass loss, but it is also clear that the PVP capping agent is less significant here than CTAB, so it is expected that size and shape changes will occur at lower temperature.

### 3.2.4.2 Transmission electron microscopy

The three Pd nanoparticle samples were annealed at 250 °C and 350 °C (20 °C $min^{-1}$) under He (20 ml $min^{-1}$) and held at temperature for 30 minutes. TEM images and particle size distributions of the Pd nanoparticles after ex-situ annealing are given in *Figure 3.16*, *Figure 3.17*, and *Figure 3.18*. Tabulated particle size data are displayed in *Table 3.2*.

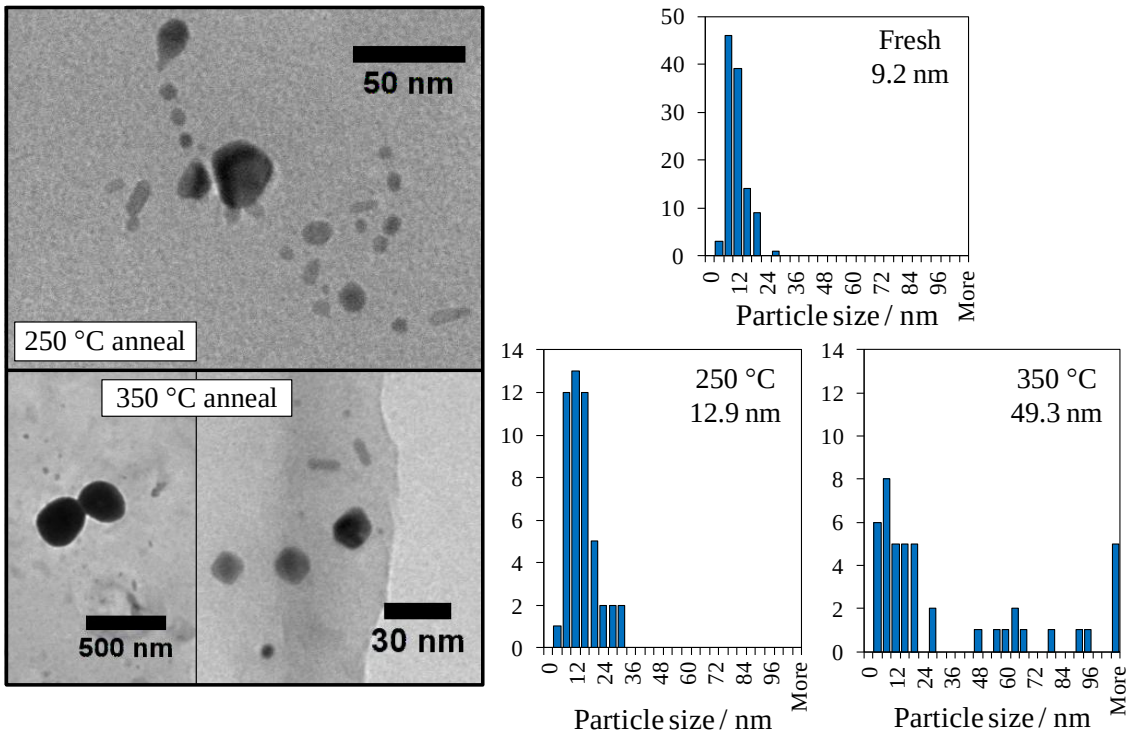


**Figure 3.16 – TEM micrographs and particle size histograms of Pd nanorods after annealing at 250 °C (top) and 350 °C (bottom) under He for 30 minutes**

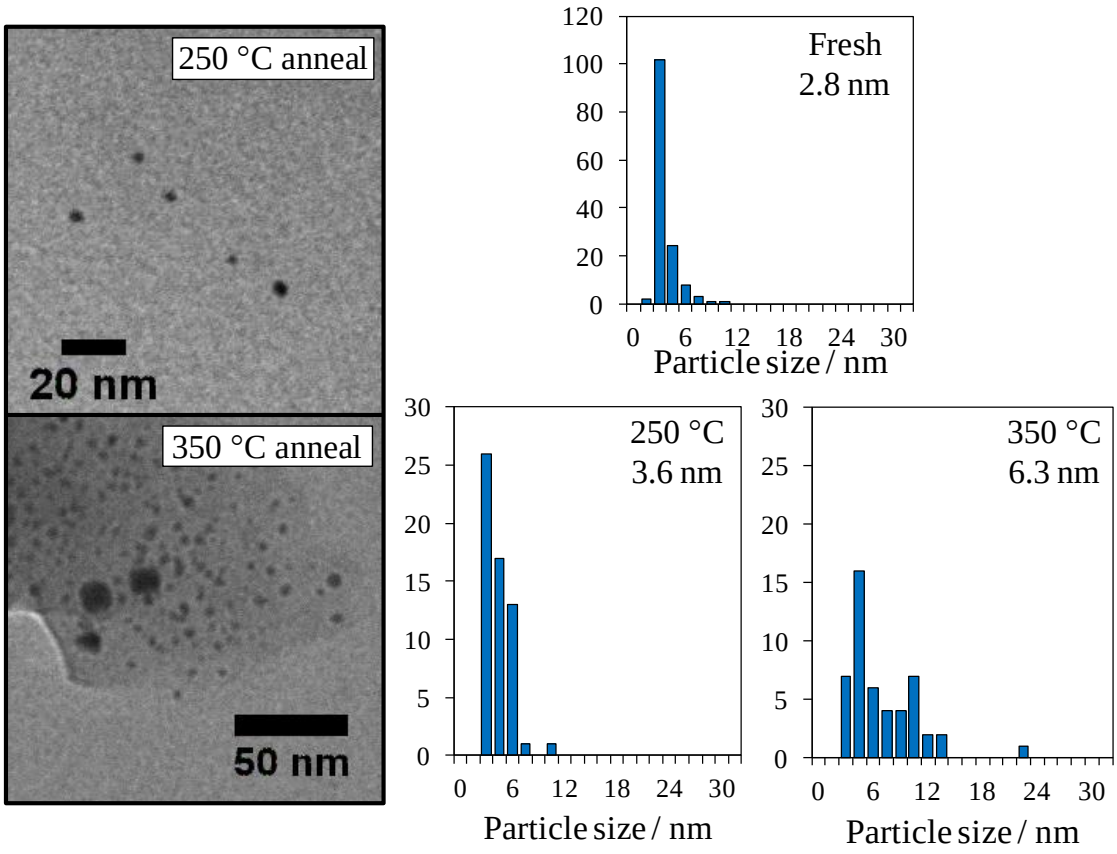


**Figure 3.17 – TEM micrographs and particle size histograms of Pd icosahedra after annealing at 250 °C (top) and 350 °C (bottom) under He for 30 minutes**

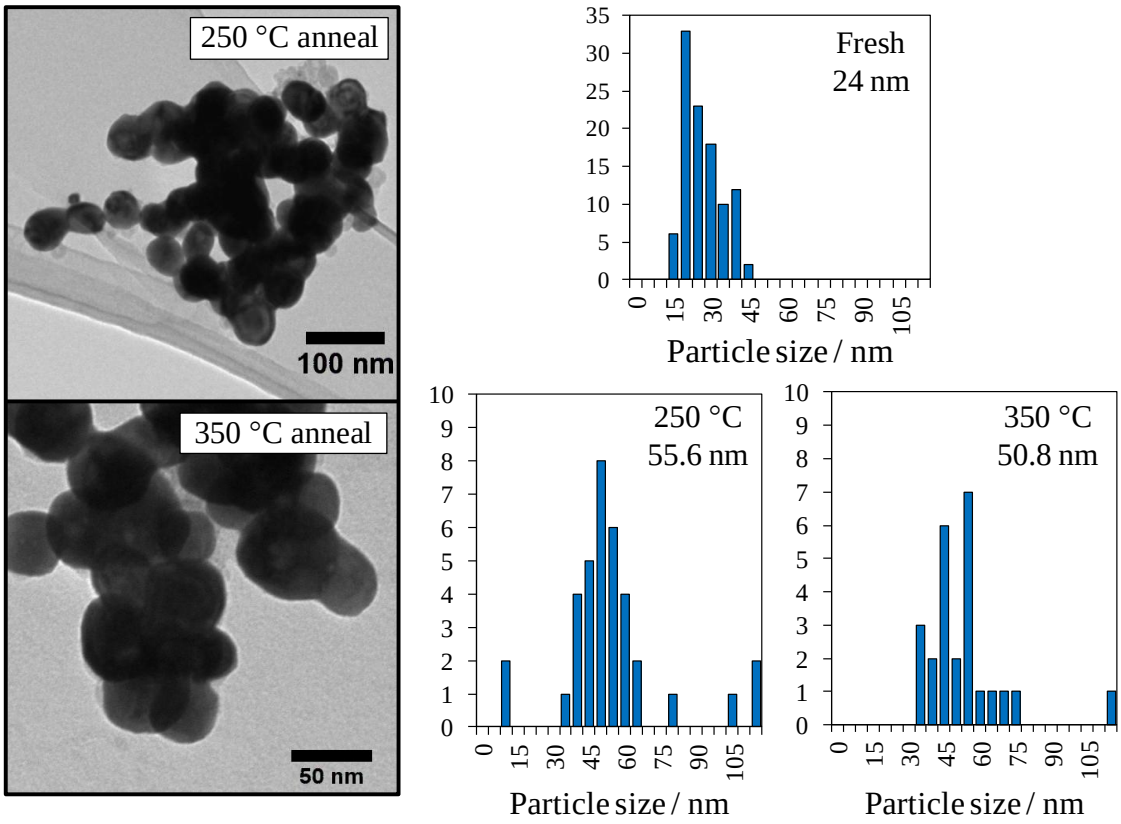


**Figure 3.18 – TEM micrographs and particle size histograms of Pd nanocubes after annealing at 250 °C (top) and 350 °C (bottom) under He for 30 minutes**

| Anneal Temperature / °C | Particle size / nm | | |
|---|---|---|---|
| | Pd icosahedra | Pd nanorods | Pd nanocubes |
| Fresh | 2.8 | 9.2 | 24.0 |
| 250 | 3.6 | 12.9 | 55.6 |
| 350 | 6.3 | 49.3 | 50.8 |

**Table 3.2 – Summary of particle size analysis by TEM on ex-situ anneals of Pd nanoparticle shapes**

There are no significant changes in particle size up to 250 °C for the Pd nanorods and Pd icosahedra. The Pd nanorods particle size does increase by 350 °C and a small increase is observed for the Pd icosahedra. Since PVP stabiliser decomposes between 250 °C and 350 °C, this suggests that PVP is effective in maintaining particle size for these nanoparticles. There is an increase in the particle size of Pd nanocubes and agglomeration has occurred by 250 °C, thus CTAB is more important in stabilising these Pd nanocubes than PVP, since CTAB decomposes below 250 °C by TGA. There is no further increase in particle size of the Pd nanocubes by 350 °C, although further agglomeration is evident.

There are some changes to particle morphology observed by TEM. Particle shape has changed by 250 °C for the Pd nanorods, although some rod shapes that remain unchanged were also observed in the sample. It would appear that PVP only preserves the size of the Pd nanorods; changes in morphology have begun to occur prior to the loss of PVP. In addition to agglomeration, the Pd nanocube structure has become more rounded by 250 °C. This may be due to loss of CTAB stabiliser. No change in particle shape is detected by low resolution TEM for the Pd icosahedra by 250 °C, although by 350 °C particle shape uniformity is lost, as triangular sheets and irregular morphologies are visible.

#### 3.2.4.3 X-ray diffraction

Further characterisation of the thermal stability of the Pd nanoparticles was performed using *in situ* and ex-situ XRD. The onset of changes in average particle size, and some variation in morphology, can be identified using this technique and used to support information obtained from TGA and TEM. Unfortunately, there were a number of limitations with the experiments carried out, such that *in situ* XRD analysis was only successful for Pd nanorods under inert conditions and Pd nanocubes immobilised on alumina. Reasons for this are explained in the appendix. Nevertheless, in conjunction with ex-situ analysis, these results can be used to confirm the onset of particle size and morphology changes.

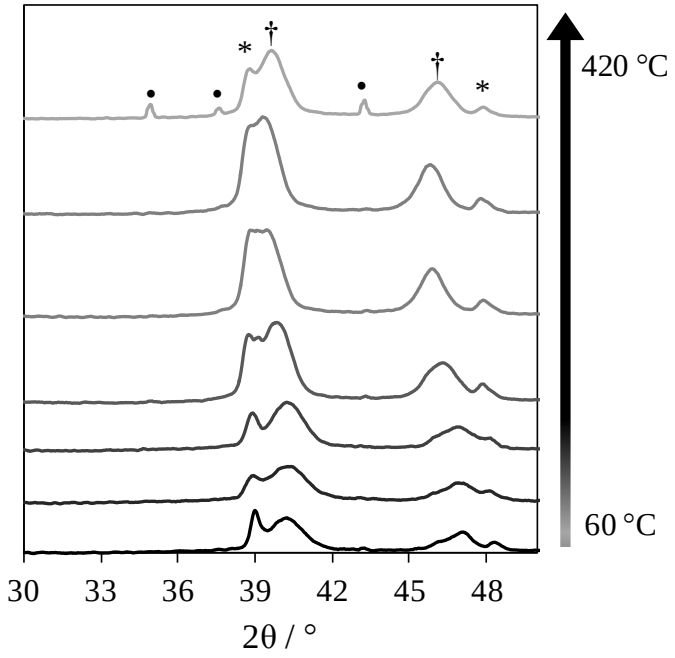


**Figure 3.19 – *In situ* XRD patterns of Pd nanorods under vacuum from 60 °C, then in 60 °C increments to 420 °C. Pd peaks are indicated by † and KBr by *.**

*In situ* XRD of the Pd nanorods under vacuum conditions is shown in *Figure 3.19*. There is a sharpening in the Pd reflections with increasing temperature. Due to an abnormal shift in all the reflections on heating, the spectra have been aligned to KBr. Lattice parameters did not vary consistently with temperature and were measured to be between 0.3881 nm and 0.3971 nm. This variability is likely to be due to polydisperse particle size and shape, which becomes more significant with increased temperature. Additionally, roughening of the sample surface and changes to the physical properties of the sample during analysis could increase error in the data collection. Structural changes to PVP, for example, could disturb the smooth surface prepared when the sample was loaded in to the instrument. Quantitative analysis of this experiment has been further compared with ex-situ analysis later in this section.

There is a pattern of three small peaks that appear above 270 °C. The peaks at 34.7° and 42.8°, indicated by • , could be due to PdO formation. Although the conditions are inert, oxygen from residual ethylene glycol, or from PVP hydroxyl groups, could result in Pd oxidation. This does not explain the presence of the peak at 37.3°. It has been confirmed, however, that these peaks are not due to $PdBr_2$, KBr, precursor Pd salts or NaCl.

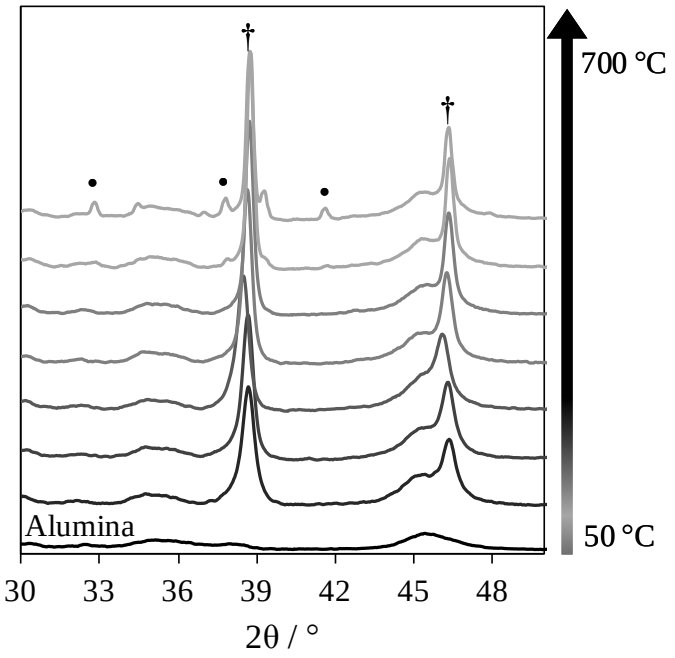


**Figure 3.20 – *In situ* XRD patterns of Pd nanocubes under inert from 50 °C, then 200 °C and in 100 °C increments to 700 °C. Pd peaks are indicated by †. The alumina background is shown at the bottom of the plot.**

The powder patterns for Pd nanocubes immobilised on alumina are given in *Figure 3.20*. Again, all the reflections have shifted with heating and were aligned to the alumina reflection. Lattice parameter measurements ranged from 0.4020 nm to 0.4049 nm, and no trend in this variation was observed. The same pattern of peaks, possibly attributed to PdO formation, is visible at 700 °C in these results as in the Pd nanorods. The Pd reflections once again sharpen and increase in intensity with increasing temperature.

Having qualitatively examined the *in situ* XRD patterns, it is now of use to consider quantitative analysis of particle size and any changes between the Pd(111) and Pd(200) reflections that could indicate morphology evolution. Analysis, using the Scherrer equation and a measure of the ratio in peak areas between the (200) and (111) reflections, is shown in *Figure 3.21*.

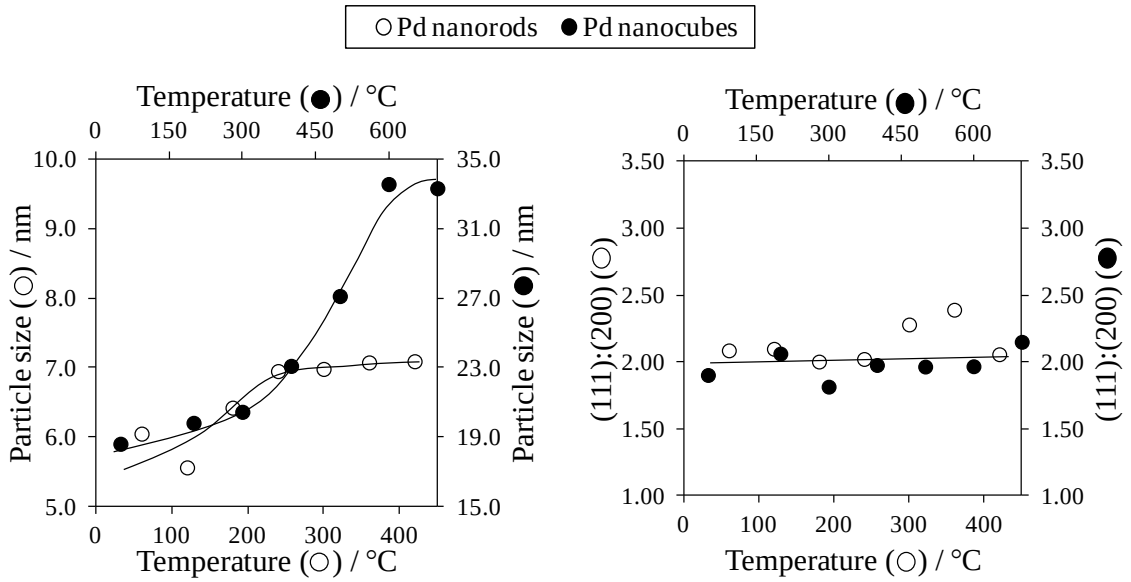


**Figure 3.21 – Quantitative analysis of *in situ* XRD on Pd nanorods and supported Pd nanocubes: particle size from Scherrer analysis (left) and peak area ratios of (111) and (200) reflections (right)**

The unsupported Pd nanorods particle size increases slightly up to 300 °C. The Pd nanocubes show a significant increase in particle size particularly between 300 °C – 600 °C. These observations are consistent with ex-situ TEM analysis on the unsupported nanoparticles. It is interesting that in both cases particle size increases up to a point, and then stabilises. This may be because the most thermodynamically stable shape is reached and more energy is required to increase particle size further than would be gained by reducing surface tension. The ratio of (111):(200) reflections remains approximately constant upon annealing, implying no significant changes in particle morphology for either nanorods or nanocubes, although TEM suggests some melting/rounding of both structures may occur at the highest temperature.

The ex-situ XRD patterns of the annealed catalysts have been recorded. It was also possible to obtain ex-situ XRD data for the icosahedra and unsupported nanocubes. The particle sizes, lattice parameters and peak intensity ratios from these experiments are tabulated in *Table 3.3*.

| Anneal Temperature / °C | Particle size | | | Lattice parameter | | | Pd (111):Pd (200) | | |
|---|---|---|---|---|---|---|---|---|---|
| | Icosahedra | Rods | Cubes | Icosahedra | Rods | Cubes | Icosahedra | Rods | Cubes |
| Fresh | 2.7 | 4.3 | 16.3 | 0.3928 | 0.3913 | 0.3883 | 6.8 | 2.3 | 1.9 |
| 250 | 2.4 | 10.4 | 26.1 | 0.3943 | 0.3878 | 0.3883 | 3.7 | 2.1 | 2.0 |
| 350 | 2.5 | 31.1 | 39.5 | 0.3971 | 0.3898 | 0.3885 | 2.4 | 2.2 | 2.1 |

**Table 3.3 – Quantitative analysis of ex-situ XRD on unsupported Pd shapes: particle size from Scherrer analysis lattice parameters calculated from the Bragg law and ratio of Pd(111):Pd(200) peak areas**

There is an increase in particle size for both the Pd nanorods and the Pd nanocubes, but not for the Pd icosahedra. Although a particle size increase was observed for the Pd icosahedra by TEM, the distribution is still dominated by smaller particles. The increase was by approximately 4 nm instead of > 30 nm observed for the other two shapes. These results together imply that the Pd nanorod and Pd nanocube particles are more prone to particle growth than the Pd icosahedra.

The onset of changes to particle shape have also been assessed from the lattice parameters and ratio of the Pd(111) and Pd(200) peak areas. The lattice parameters of the nanocubes and nanorods show no significant variations with temperature, while their (111):(200) ratios remain essentially constant, in agreement with the preceding *in situ* measurements. The lattice parameter for the Pd icosahedra increases systematically with temperature, in parallel with a decrease in the (111):(200) ratio, suggesting significant changes in morphology (but not size) accompany annealing.

These results show that it is difficult to preserve particle morphology while controlling nanoparticle size through post-synthesis thermal processing.

### 3.2.5 Liquid phase crotyl alcohol selective oxidation

The aerobic selective oxidation of crotyl alcohol has been used to determine the effect of morphology on catalytic activity and selectivity. This is shown in *Scheme 3.1*. A further palladium catalyst, supported on mesoporous alumina, was tested alongside the shape-controlled nanoparticles, as a control.[2, 7] It was only possible to use a relatively small mass of catalyst, due to synthesis scale up limitations, and this combined with low surface areas, mean that reaction conversions were low (final conversion 8 % for Pd nanorods, 5 % for Pd icosahedra and 4 % for Pd nanocubes). It is possible this trend in reactivity is real, but errors of approx. ±2 % from multiple reactions make it impossible to tell. As a result, the total observed product formation has been normalised to catalyst weight loading, determined from elemental analysis, and metal surface area per gram. This does not take into account the formation of any volatile products or adsorbed products that have not been detected by GC, however.

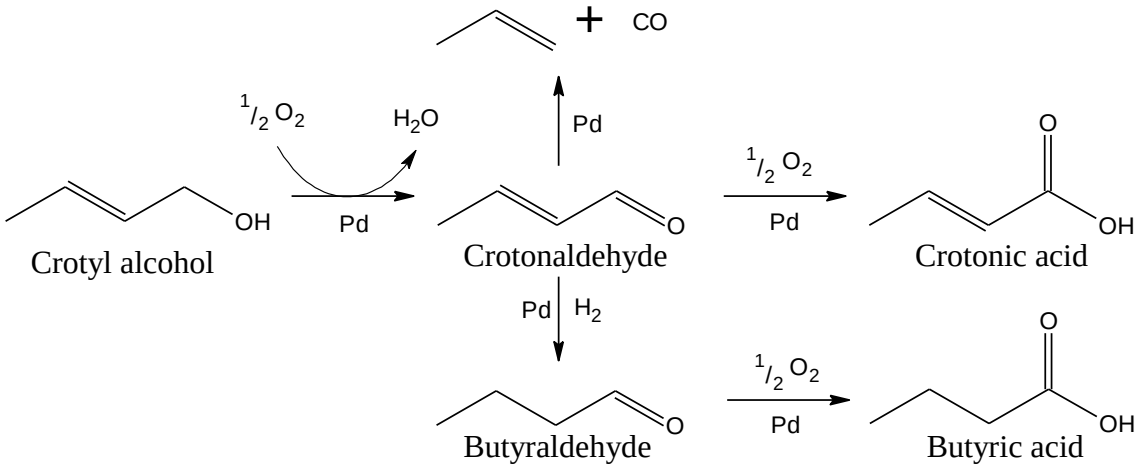


**Scheme 3.1 – Crotyl alcohol selective oxidation reaction pathway**

The metal surface area of the mesoporous alumina supported Pd catalyst was calculated using CO chemisorption (see *Chapter 2*). Chemisorption experiments have been difficult to perform on the tailored nanoparticles due to their physical properties, so dispersion measurements were calculated using the dimensions obtained from TEM data, assuming that the entire surface is available for catalysis. These were compared with chemisorption measurements that were attempted after immobilising the nanoparticle sols on alumina and were found to be in reasonable agreement after consideration of error and instrument limitations. The calculated values were deemed to be more reliable. These are summarised in *Table 3.4*.

| Sample | Dispersion (Chembet) / % | Dispersion (MS) / % | Dispersion (Calc) / % |
|---|---|---|---|
| 0.34 wt% $Pd/Al_2O_3$ | 45 | 42 | 43.6 |
| 5.35 wt% Pd icos | 46.5 | 69 | 32.1 |
| 3.81 wt% Pd rods | 7.5 | 34 | 21.5 |
| 70.54 wt% Pd cubes | 0.5 | 0.3 | 2.3 |

**Table 3.4 – Summary of dispersion measurements for benchmark alumina supported catalyst and nanoparticle shapes**

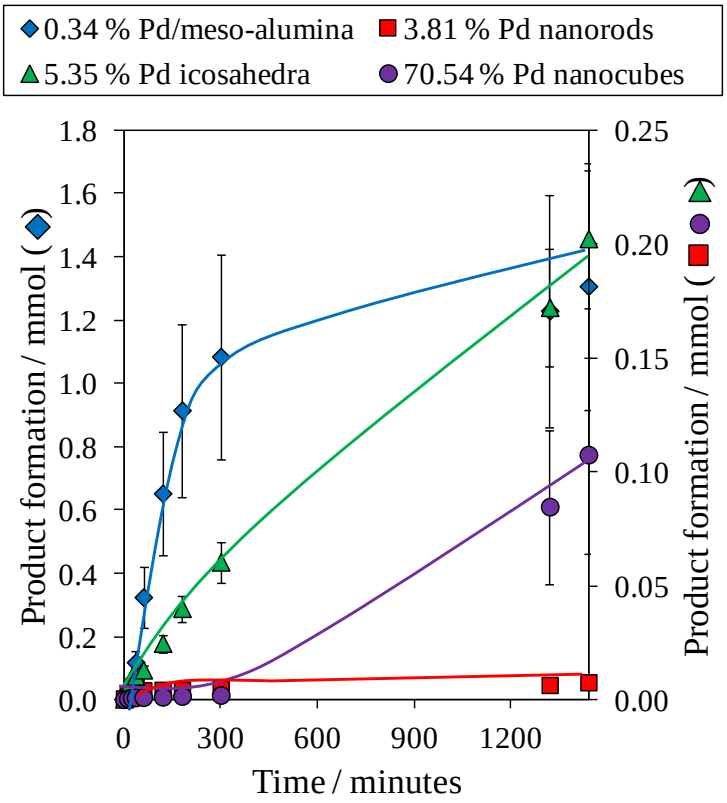


**Figure 3.22 – Product conversion of Pd/meso-alumina benchmark catalyst and Pd shapes, normalised to surface area of Pd with respect to the benchmark**

The reaction profile for the reaction using 8.4 mmol substrate in toluene at 60 °C normalised to the Pd surface area, is given in *Figure 3.22*. The supported benchmark catalyst is clearly most active. Preparation methods, support effects and a very high dispersion may contribute towards this, and will be considered in further detail in the next section. There are two further observations to be noted from *Figure 3.22*: the Pd nanorods rapidly deactivate and the Pd nanocubes exhibit an induction period before displaying an activity similar to that of the Pd icosahedra. This may be accounted for by changes in morphology, chemical poisoning, or even the removal of chemical poisons during reaction that were on the catalyst surface during synthesis. Again, this will be considered in further detail in the next section.

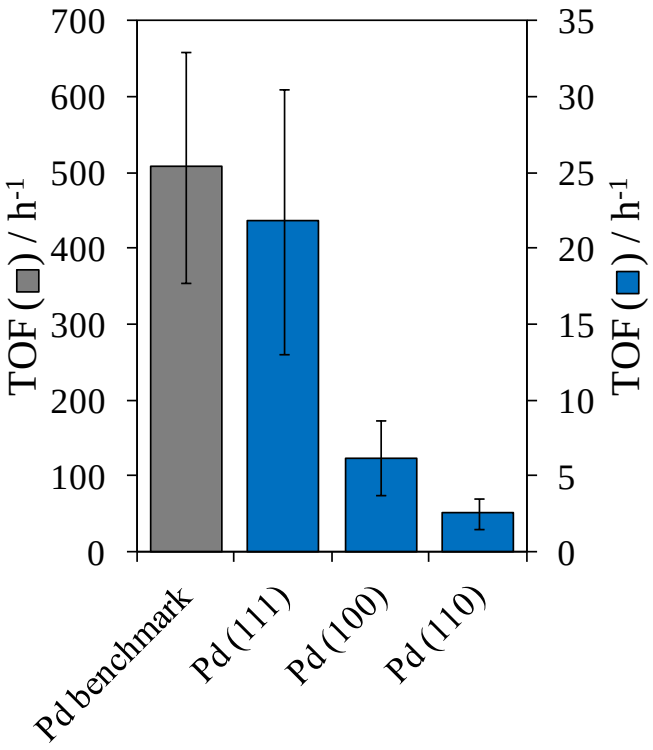


**Figure 3.23 – Turn over frequencies of Pd/meso-alumina benchmark catalyst and Pd shapes. Initial rates were measured over the first 40 minutes of reaction**

*Figure 3.23* shows the turn over frequencies (TOFs) for the four catalysts determined from the initial rate and calculated for the different Pd facets exposed in each catalyst (assuming a proportion of 5:1:1 Pd(111):(100):(110) on the Pd nanorods). Note that the Pd cube TOF was still measured between 0-40 minutes, and thus does not account for the increase in rate observed after 5 hours. Initial inspection of *Figure 3.23* shows that there is a 25 fold rate enhancement between the most active tailored catalyst and the benchmark catalyst. Additionally, the (111) encapsulated icosahedra are four times more active for crotyl alcohol selox than (100) terminated nanocubes, which in turn is twice as active as the (110) facets of Pd nanorods. It has been established, therefore, that all four catalysts behave differently, but it is not clear at this point if this is due to the morphology and, if so, what aspect of the morphology tunes activity.

| Catalyst | Crotonaldehyde / % | Butryaldehyde / % | Crotonic acid / % | Butyric acid / % |
|---|---|---|---|---|
| Pd/meso-$Al_2O_3$ | 90 | 9 | 0.8 | 0.2 |
| Pd (111) | 57 | 40 | 0.5 | 2.5 |
| Pd (100) | 85 | 13.5 | 1 | 0.5 |
| Pd (110) | 62 | 14 | 0 | 24 |

**Table 3.5 – Product selectivities for crotyl alcohol oxidation over benchmark Pd/meso-alumina and Pd nanoparticle shapes**

The catalyst selectivities after 24 hours for the four detected products are recorded in *Table 3.5* and selectivity to crotonaldehyde with time is shown in *Figure 3.24*. The selectivity of the reaction is different for the four catalysts. A reaction scheme is provided in *Scheme 3.1*, where the detected bi-products are included. Mass balances were 90%, 97 % and 96 % after 6 hours of reaction for Pd nanorods, Pd icosahedra and Pd nanocubes respectively. These had all reduced by approximately 20 % after 24 hours, most likely due to evaporation through bubbling oxygen, although formation of CO and propene is also possible.

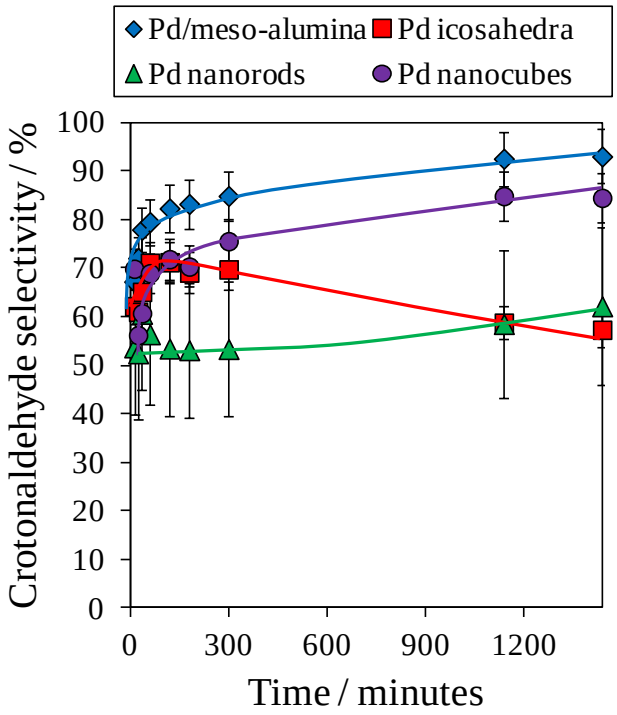


**Figure 3.24 – Selectivity to crotonaldehyde of Pd/meso-alumina benchmark catalyst and Pd shapes**

A different trend is observed for the three catalysts regarding selectivity. After 24 hours Pd(111) is least selective towards crotonaldehyde. Pd(111) forms proportionally the most butyraldehyde. This could occur if hydrogen is not efficiently removed from the surface. The low selectivity may also be due to decarbonylation. Surface science studies over metallic Pd(111) reveal significant decarbonylation of crotonaldehyde to CO.[26]

The Pd(110) terminated nanoparticles form proportionally more butyric acid than any of the other catalysts and are least selective to crotonaldehyde formation for up to 20 hours of the reaction. Also, no crotonic acid formation is observed at all. Thus, C=C hydrogenation would appear to be a significant pathway for this catalyst, including further oxidation to butyric acid. It is surprising that if butyric acid formation is observed, crotonic acid formation is not. Although butyraldehyde formation may occur through hydrogenation of crotonaldehyde, it is also possible that the (110) facet activates the C=C functionality sufficiently that remaining crotonaldehyde is consumed through decarbonylation to CO and propene. This would, in fact, account for the rapid deactivation observed for this catalyst, and may disguise the superior activity of this surface over Pd(111) and Pd(100).

It is clear from the rationale put forward to explain the difference in activity of the four catalysts that an investigation of the surface chemistry is necessary. There are a number of points that require an explanation: why is the benchmark catalyst 25 times more active than any of the Pd shapes; is the difference in reactivity for the tailored catalysts due to their exposed facets, and if so why does the exposed facet lead to these differences? Each facet has a different surface energy, and geometric and electronic factors influence chemisorption of species such as $O_2$ and CO on the surface.[27] Formation of bulk oxide is more facile on Pd(110) than Pd(100), which again is more reactive to $O_2$ than Pd(111). However, surface oxide formation would appear to be more feasible on Pd(111). In fact R. Westerström et al. propose that subsurface oxide does not form on Pd(110): the bulk oxide forms directly from chemisorbed species.[28-32]

CO is found to adsorb less strongly on surface oxide than the bare metal and thicker oxide films. Thus, CO may be a more significant poison if the surface resembles either a bare metal or bulk oxide, for which Pd(110) is more susceptible, than a surface oxide, as expected for Pd(111). The initial adsorption energy of CO increases for Pd(111) < (100) < (110) as does the maximum coverage.[27] This would imply that, not only is decarbonylation more likely to occur over Pd(110), but that CO poisoning may

additionally be a more significant issue. This possibility is considered alongside experimental data in the next section.

## 3.2.6 X-ray photoelectron spectroscopy*

In order to further support or refute this model, and understand these theoretical explanations, the surface chemistry of the nanoparticles will be explored by X-ray photoelectron spectroscopy (XPS). *Table 3.6* shows the % composition by mass of the chemical species listed for the four catalysts. The XPS experiments were conducted in some cases on carbon tape, and as such an exact composition cannot be determined. This was due to the small quantities of material for Pd nanocubes, and difficulties in the physical properties of the nanorods and icosahedra.

| Catalyst | Surface compositions / % | | | | | | | Synthesis |
|---|---|---|---|---|---|---|---|---|
| | Pd 3d | O 1s | N 1s | Cl 2p | Br 3d | K 2p | Al 2p | |
| Pd/m-$Al_2O_3$ | 0.12 | 56.07 | 0.00 | 0.00 | 0.00 | 0.00 | 43.81 | n/a |
| Pd icosahedra | 0.45 | 59.77 | 38.88 | 0.90 | 0.00 | 0.00 | 0.00 | Citric acid/PVP |
| Pd nanorods | 1.18 | 53.98 | 34.21 | 4.04 | 1.07 | 5.53 | 0.00 | EG/PVP/KBr |
| Pd nanocubes | 28.43 | 62.68 | 6.07 | 0.00 | 2.81 | 0.00 | 0.00 | CTAB/AA/PVP |

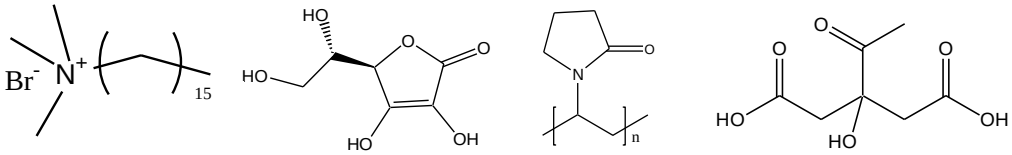


CTAB Ascorbic acid PVP Citric acid

**Table 3.6 – Surface compositions by mass for 4 catalysts tested for crotyl alcohol selox calculated excluding C 1s composition. Stabilisers and additives present from the synthesis of the tailored catalysts included in the last column.**

The compositional data shows that halide is present in all the sol-prepared catalysts, and significant nitrogen is present in the Pd nanorods and icosahedra. Interestingly, there is far less nitrogen present for Pd nanocubes. It is important to note at this point that any nitrogen associated with CTAB is going to relate to approximately 62 times more stabiliser than that of PVP due to the significantly larger chain length of

* Databases used throughout this section: *NIST X-ray Photoelectron Spectroscopy Database*, Version 3.5 (National Institute of Standards and Technology, Gaithersburg, 2003) http://srdata.nist.gov/xps Accessed 30/04/2012; R. Benoit, *La Surface*, http://www.lasurface.com/accueil/index.php, Date accessed: 30/04/2012

the latter molecule. The assignment of the nitrogen observed here to the stabilisers referred to in the last column of *Table 3.6* will be discussed later.

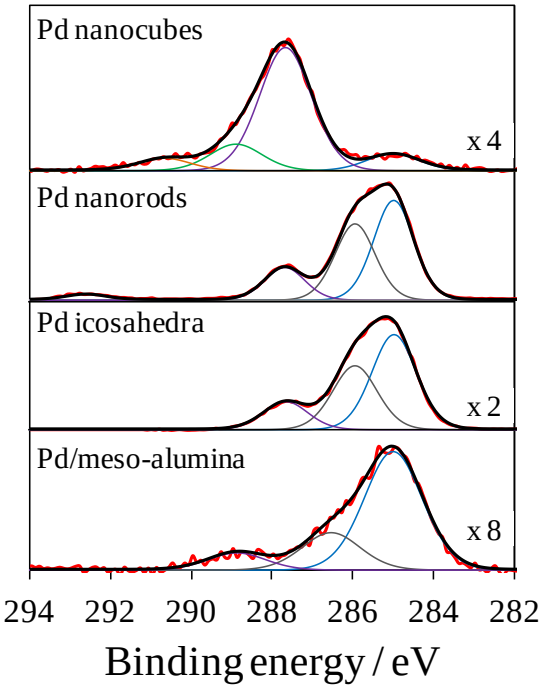


**Figure 3.25 – C 1s XP spectra for shape-controlled and benchmark catalysts tested for crotyl alcohol selox. The spectra have been scaled for clarity as indicated on the figure**

Although experiments were conducted on carbon tape, the C 1s XP spectra are informative, and given in *Figure 3.25*. All XP spectra considered here were charge corrected to adventitious carbon at 285 eV. A reasonable amount of organic residue is expected for these samples due to the nature of their synthesis, thus the most useful information to be gleaned in interpreting these spectra is by comparing the chemical states with those in the organic stabilisers.

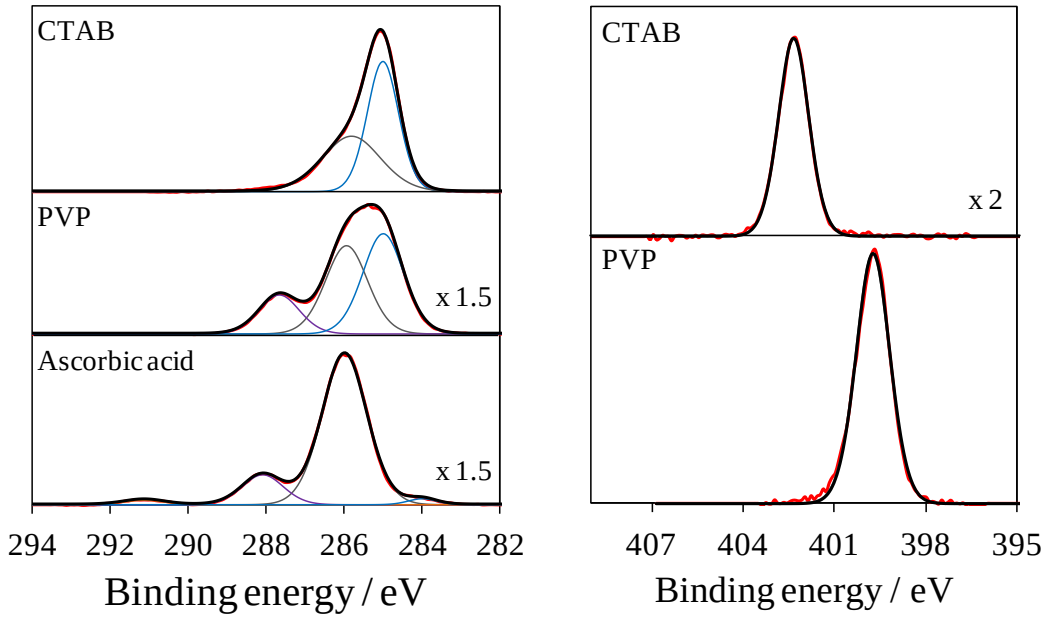


**Figure 3.26 – C 1s (left) and N 1s (right) XP spectra for stabilisers used in the synthesis of the tailored Pd nanoparticles**

The C 1s XP spectra for PVP, CTAB and ascorbic acid are shown in *Figure 3.26* and the corresponding chemical structures are shown in *Table 3.6*. The chemical shifts to 286 eV and 287.8 eV in the PVP spectrum can be assigned to C-N and C=O environments in PVP and these features are identical to that observed in the Pd icosahedra and Pd nanorods spectra. The peaks at 286 eV, 288 eV and 290.9 eV in the ascorbic acid spectrum can be rationalised from the alcohol, ether and acid functionalities. These features compare with the Pd nanocubes spectrum. From these figures it is apparent that the C 1s XPS of the Pd icosahedra and Pd nanorods are dominated by PVP, and that of the Pd nanocubes is dominated by ascorbic acid.

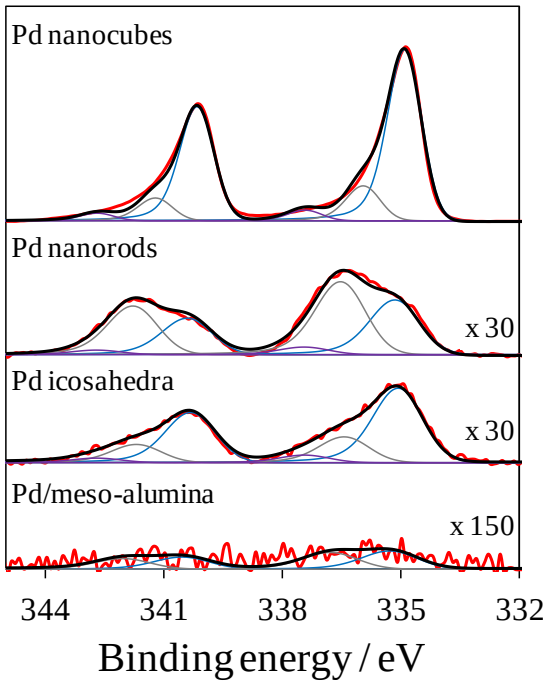


**Figure 3.27 – Pd 3d XP spectra for tailored and benchmark catalysts tested for crotyl alcohol selox. The spectra have been scaled for clarity as indicated on the figure**

The Pd 3d XP spectra for the catalysts, shown in *Figure 3.27*, reveals that there are three distinct states in the spectra of the three nanoparticle shapes, but only two states in that of the more active benchmark catalyst. The dominant peak in all four spectra, at 335.3 eV, is consistent with Pd $3d_{5/2}$ metal.[33] The chemical shift of the peak shifted to higher binding energy, present in all four catalysts at 336.5 eV, is in agreement with that of a PdO surface species.[34] In the three tailored catalysts there is a further state, shifted to even higher binding energy, at 337.6 eV. Preparation methods, which used $Na_2PdCl_4$ precursor in all cases, and used bromide based additives for the Pd nanocubes and Pd nanorods, support the existence of a Pd-halide state at this binding energy.

Further inspection of *Figure 3.27* shows that there is a clear variability in the peak width for the different samples. Sources of line broadening in XPS include inhomogeneity of the sample and the magnitude of the core-hole lifetime.[35] A core hole is formed on ejection of a photoelectron from the atom core after irradiation with an X-ray photon (see *Chapter 2*). The hole is filled by relaxation of a higher level electron, and factors such as the depth of the core-hole (increasing with atomic number) and particle size affect its lifetime. Larger Pd clusters exhibit more metallic properties, and are thus expected to permit faster core-hole screening, resulting in shorter lifetimes.

Since the XPS peak width is inversely proportional to core-hole lifetime (through the Heisenberg Uncertainty principle in *Equation 3.2*), the decreasing particle size from nanocubes > nanorods > icosahedra > 1 wt% $Pd/Al_2O_3$ benchmark may be expected to induce a concomitant increase in peak width, with the largest Pd nanocubes exhibiting the broadest peaks. However, the reverse is observed in *Figure 3.27* suggesting that other more influential final state effects may operate, or that sample inhomogeneity is the controlling factor in regulating peakwidth.[35]

$$\Gamma = \frac{h}{\tau}$$

**Equation 3.2 – The relationship between peak width Γ and core-hole lifetime τ as a consequence of the Heisenberg Uncertainty principle. h is Planck's constant**

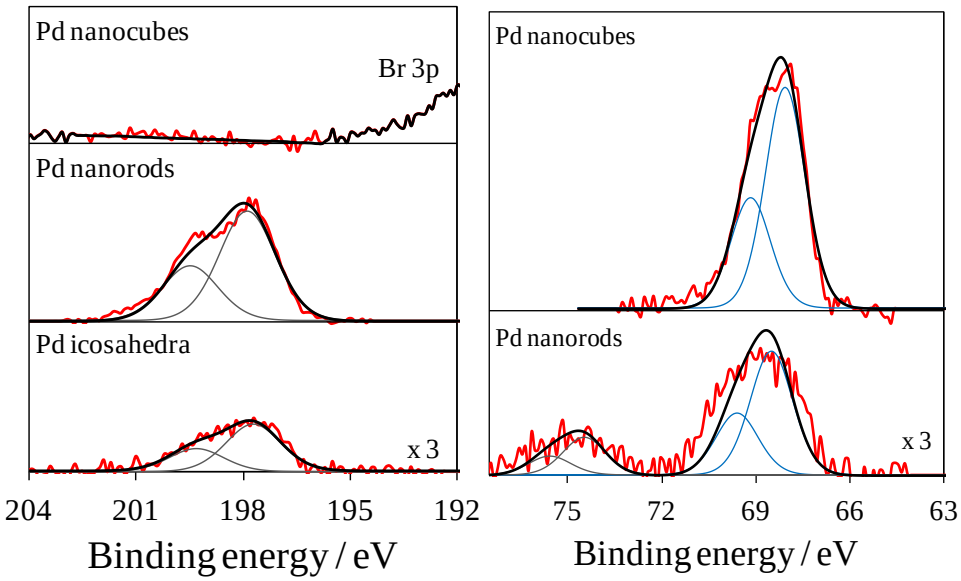


**Figure 3.28 – Cl 2p (left) and Br 3d (right) XP spectra for the tailored catalysts tested for crotyl alcohol selox. The spectra have been scaled for clarity as indicated on the figure**

The presence of a halide state is further confirmed on consideration of the Cl 2p and Br 3d XP spectra given in *Figure 3.28*. Both icosahedra and nanorod samples contain surface chloride with a binding energy for Cl $2p_{3/2}$ centred at 197.8 eV (ΔBE = 1.6 eV between the doublet peaks), in agreement with values corresponding to metal bonded chloride (KCl, $PdCl_2$, RbCl, AgCl all have similar binding energies).[36-38] In

addition, the Pd nanorods and Pd nanocubes show clear evidence for surface bromide. $Br^-$ from CTAB stabiliser is to be expected for Pd nanocubes. The presence of two states in the Pd nanorods sample, with the Br $3d_{5/2}$ binding energies at 68.0 eV and 74.5 eV (ΔBE = 1.1 eV), may be a result of KBr and $PdBr_2$ species proposed in the literature example of this synthesis.[8, 39] The reason for the large shift in binding energy between these two states is not clear: data compiled from the NIST XPS database indicate that the higher binding energy peak is more likely to be attributable to organic bromide species, such as that which would be expected from CTAB stabiliser in the nanocubes sample.[40] There was no evidence of residual sodium from XPS, thus it is unlikely that any of these halide species are a result of NaBr.

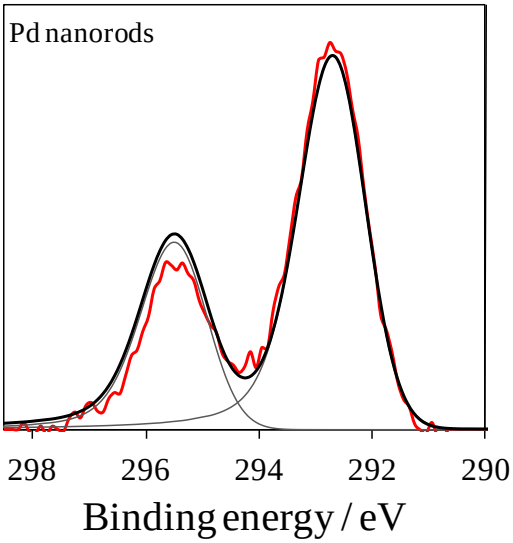


**Figure 3.29 – K 2p XP spectra for Pd nanorods**

Evidence for KBr in the nanorods sample can be further confirmed by consideration of the K 2p XP spectrum, given in *Figure 3.29*, where a clear peak with binding energy for K $2p_{3/2}$ centred at 292.8 eV (ΔBE = 2.8 eV), consistent with KBr, is observed.[38] It is possible that an organic bromide species has formed during synthesis of Pd nanorods, which could explain the large shift in the second bromide state. Furthermore, there is literature evidence for an interaction between PVP and $Br^-$ ions, in particular a study by J. D. Song et al. reveals anionic binding by NMR between the two species.[41-44] If this is the case, the halide peak observed in the Pd 3d XP spectra could be assigned to a $PdCl_2$ species, as in the case of the icosahedra sample. Although the

precise assignments cannot be determined, it is clear from this assessment that halide species are present on the surface of the sol-prepared Pd nanoparticles.

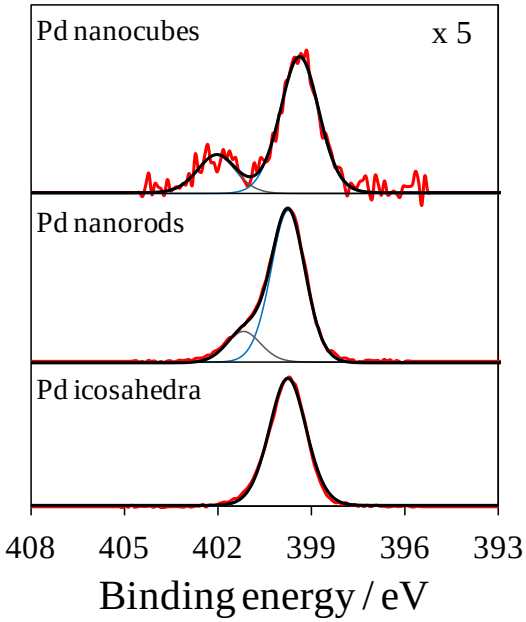


**Figure 3.30 – N 1s XP spectra for the tailored catalysts tested for crotyl alcohol selox. The spectra have been scaled for clarity as indicated on the figure**

Finally, since all three catalysts are stabilised by nitrogen based PVP, and additionally nitrogen containing CTAB in the case of Pd nanocubes, the N 1s XP spectra are displayed in *Figure 3.30*. One state is common to all three catalysts: at 400.0 eV, which agrees with the assignment from PVP (see *Figure 3.26*). Two further distinct states are present in the Pd nanocubes and Pd nanorods. The chemical shift due to coordination with bromide at 402 eV, is to be expected for Pd nanocubes from the presence of CTAB and is confirmed by comparison with the CTAB N 1s spectrum in *Figure 3.26*. A second state in the Pd nanorods sample is a surprise, since the only nitrogen containing species in this synthesis was PVP. This state may be a result of the interaction between Br anions and PVP described earlier. Alternatively, decomposition of PVP under synthesis conditions may have led to the formation of an oxidised N species.

### 3.2.7 Nanoparticle reactivity: discussion

The chemical states that are present in the catalysts have been considered, and further quantitative analysis will now be discussed in relation to the reactivity series proposed in the previous section. *Table 3.7* shows a comparison of the oxide content, halide content, amount of stabiliser present and relative theoretical surface energies of the three surfaces present in the Pd shapes.

| Catalyst | PdX / % | Pd:stabiliser | PdO / % | Metal surface energy |
|---|---|---|---|---|
| Pd/m-$Al_2O_3$ | 0.00 | n/a | 45.83 | Low |
| Pd icosahedra | 6.20 | 0.005 | 24.07 | Low |
| Pd nanorods | 5.46 | 0.012 | 54.90 | High |
| Pd nanocubes | 4.88 | 0.397 | 15.85 | Medium |

**Table 3.7 – Compositions of halide and oxide components of Pd 3d XP spectra and the ratio of Pd to total stabiliser species (excluding C 1s) alongside the relative stability of the different exposed facets for the benchmark and tailored catalysts that were tested for crotyl alcohol selox**

The experimental data were calculated using the compositional information from *Table 3.6*. The observed trend in activity improves over the series (110) < (100) < (111), although this is discounting any products such as gaseous or adsorbed propene and CO. This trend is reverse to that of surface energy, which would predict more active Pd(110).[45, 46] In addition to this reactivity trend, the benchmark catalyst exhibits superior activity to any of the tailored catalysts.

The first possibility, for hindering the predicted reactivity that arises, is the obstruction of surface sites by the organic stabiliser. This could be significant for the difference observed between the benchmark catalysts and the three nanoparticle shapes. It is unclear from literature studies how significant the interaction of PVP with the catalyst surface is on reactivity. It is clear that the polymer solubility and the reaction medium is crucial, and, if chosen poorly, this can affect reactivity (e.g. PVP is insoluble in a completely non-polar medium).[47] However, it has also been reported that PVP does not exhibit a significant reduction in turn over frequency.[48] It is generally agreed that any reduction in activity due to PVP is only a result of fewer available sites.[49] One study on catalysis by gold indicates that electron transfer from PVP enhances Au activity, although it may be that this change in electronic structure to the active site is peculiar to gold and linked to the significant rate enhancement seen for very small Au clusters.[50]

Nevertheless, the Pd icosahedra have almost 2.5 times more stabiliser than Pd nanorods, and yet the former are the most reactive. The Pd nanocubes have dramatically less stabiliser present and are also less reactive than the Pd icosahedra. It is important to raise the possibility of residual reducing agent interfering with selective oxidation for both the Pd nanorods and Pd nanocubes. From XPS, it is clear that ascorbic acid is still present in the Pd nanocubes catalysts. Removal of ascorbic acid during reaction may account for the induction period. From TGA it is apparent that there is some ethylene glycol remaining in the Pd nanorod sample, although this cannot be confirmed by XPS. This may also account for the low activity of the Pd nanorods.

The second factor that must be considered, from the data in *Table 3.7*, is the effect of halide on reactivity. This is more likely to be a source of reduced reactivity in the tailored nanoparticles. Chloride is a well recorded catalyst poison for Pd,[51] and there is sufficient evidence of chemisorbed halide for all three catalysts, to suggest that this is a likely source of the significant reduction in activity between the benchmark and shape-controlled catalysts. However, halide still does not explain the difference in reactivity between the three tailored nanoparticles: approximately the same proportions of PdX are present in all three catalysts, although excess halide in the form of a potassium salt is present in the Pd nanorods, which may contribute towards deactivation. This is discussed further in the next paragraphs.

The remaining column in *Table 3.7* shows the surface PdO content of the four catalysts. Here, unlike previously, there is a difference between values and there is literature evidence that oxide content influences catalyst reactivity.[2, 3] Any trends, however, are not immediately obvious. The Pd icosahedra are more active and have higher surface oxide content than the Pd cubes. This is in agreement with the proposal by Adam Lee that surface PdO is the active site for crotyl alcohol selox, and further evidence for this in *Chapter 4*.[2, 3] Conversely, the Pd nanorods have very high oxide content, by XPS, and are the least reactive. However, it is clear that the Pd nanorods rapidly deactivate, and some source of deactivation may account for this apparent low activity.

Recall that the mass balances for (110) encapsulated Pd nanorods was 7 % lower than for the Pd nanocubes and icosahedra. This could be explained if decarbonylation leads to the formation of small amounts of CO. Although this may only be responsible for a small drop in selectivity compared with butyraldehyde and acid formation, it could explain the significant deactivation observed. This possibility was discussed in *Section*

*3.2.5* with regards to the selectivity of the Pd nanorods: the absence of crotonic acid as a product, when all three other products are observed and crotonic acid is formed for this reaction over the other catalysts, suggests that crotonic acid formation is hindered. Some of this will be accounted for in the formation of butyraldehyde, but decarbonylation may also be occurring. Theoretical evidence discussed in this section also indicates that CO adsorption is expected to be stronger on the Pd(110) surface than the other low energy facets, which may also contribute to this effect. A further source of deactivation that may be of more significance for the Pd nanorods than the other two shapes is the quantity of halide present. There is twice as much halide present in the Pd nanorods proportionally to Pd metal than in the icosahedra, although there is a similar quantity of the PdX state in all three catalysts. The extra halide, present in the form of a potassium salt, may be a source of deactivation during reaction.

In summary, therefore, stabiliser does not appear to affect catalyst reactivity, halide is a likely source of reduced activity for the tailored nanoparticles, and oxidation state, surface energy and deactivation through self-poisoning are all potential contributors to the reactivity of different nanoparticle shapes. One way in which this model can be developed further is to test particle size effects. Quantum size effects for particles < 4 nm, where bulk metal properties are no longer dominant, are known to significantly influence reactivity.[18] Additionally, oxidation state for Pd nanoparticles increases with decreasing particle size, so oxidation state effects that relate directly to particle shape, will only be comparable on particles of equivalent size.[2] Also, if there is little difference in activity per surface site for particles in a size range of 5-20 nm, then this is evidence that the reaction is occurring on the surface and not the edge and corner sites, so the catalysis is sensitive to the surface atom arrangement. This type of study is referred to in a review by J. Durand and collaborators.[52] As outlined in *Chapter 1* and the attempts described in this chapter, the development of synthetic procedures to produce nanoparticles of monodisperse shape over a size range of < 4 nm to 20 nm is still a considerable challenge.

## 3.3 Conclusions

The synthesis of Pd nanoparticles for which the (111), (100) and (110) low index facets can be isolated has been achieved and the nature of the exposed facets

confirmed by extensive characterisation. Attempts to create a size range, with particle morphology preserved, on a sufficiently large scale to fully characterise and test reactivity, has been unsuccessful. However, recent developments in the literature and alternative strategies that could be adopted to control particle size have been proposed to further this work.

Characterisation of the nanoparticles by XPS reveals significant quantities of stabiliser and halide on the tailored nanoparticle surfaces. The catalyst oxidation state decreases in the order Pd nanorods, benchmark Pd/meso-alumina, Pd icosahedra and Pd nanocubes. These surface properties have been considered in conjunction with catalyst reactivity.

Crotyl alcohol selox reveals a trend in activity between Pd icosahedra, Pd nanocubes and Pd nanorods that is the reverse of the trend of increasing surface energy. However, patterns in deactivation of the three catalysts indicate that the Pd nanorods experience rapid deactivation and have a slightly lower mass balance than the Pd nanocubes and Pd icosahedra. Analysis of the surface science literature reveals that CO adsorption is more significant over Pd(110) than Pd(100) and particularly Pd(111). Although surface oxide is thought to diminish decarbonylation of crotonaldehyde to CO, this effect may be different over the higher energy (110) surface. Alternatively, more significant quantities of halide from the precursor salt and KBr additive may be hindering activity. Thus, it is proposed that, although the apparent activity of Pd(110) nanorods is considerably less than Pd(111) icosahedra, the nanorods experience rapid deactivation. Further investigation is necessary in order to confirm this, particularly with regard to particle size. However, due to the nature of the nanoparticle synthetic methods this challenging analysis would require significant development.

## 3.4 References


1. C. Chapuis and D. Jacoby, *Appl. Catal. A-Gen.*, 2001, **221**, 93.
2. S. F. J. Hackett, R. M. Brydson, M. H. Gass, I. Harvey, A. D. Newman, K. Wilson and A. F. Lee, *Angew. Chem.-Int. Edit.*, 2007, **46**, 8593.
3. A. F. Lee, S. F. J. Hackett, J. S. J. Hargreaves and K. Wilson, *Green Chem.*, 2006, **8**, 549.
4. Y. Xia, Y. J. Xiong, B. Lim and S. E. Skrabalak, *Angew. Chem.-Int. Edit.*, 2009, **48**, 60.
5. A. R. Tao, S. Habas and P. D. Yang, *Small*, 2008, **4**, 310.
6. Y. Li, Q. Liu and W. Shen, *Dalton Trans.*, 2011, **40**, 5811.

7. S. F. J. Hackett, University of York (PhD), 2008.
8. Y. J. Xiong, H. Cal, B. J. Wiley, J. Wang, M. J. Kim and Y. N. Xia, *J. Am. Chem. Soc.*, 2007, **129**, 3665.
9. Y. J. Xiong, J. M. McLellan, Y. D. Yin and Y. N. Xia, *Angew. Chem.-Int. Edit.*, 2007, **46**, 790.
10. F. R. Fan, A. Attia, U. K. Sur, J. B. Chen, Z. X. Xie, J. F. Li, B. Ren and Z. Q. Tian, *Cryst. Growth Des.*, 2009, **9**, 2335.
11. M. Crespo-Quesada, A. Yarulin, M. S. Jin, Y. N. Xia and L. Kiwi-Minsker, *J. Am. Chem. Soc.*, 2011, **133**, 12787.
12. P. Scherrer, *Math.-Physik.*, 1918, **2**, 98.
13. R. J. Matyi, L. H. Schwartz and J. B. Butt, *Catal. Rev.*, 1987, **29**, 41.
14. P. Cortona, *Phys. Rev. B*, 1992, **46**, 2008.
15. C. Wang, H. Daimon, T. Onodera, T. Koda and S. H. Sun, *Angew. Chem.-Int. Edit.*, 2008, **47**, 3588.
16. A. Guerrero-Ruiz, S. W. Yang, Q. Xin, A. Maroto-Valiente, M. Benito-Gonzalez and I. Rodriguez-Ramos, *Langmuir*, 2000, **16**, 8100.
17. I. V. Yudanov, R. Sahnoun, K. M. Neyman, N. Rosch, J. Hoffmann, S. Schauermann, V. Johanek, H. Unterhalt, G. Rupprechter, J. Libuda and H. J. Freund, *J. Phys. Chem. B*, 2003, **107**, 255
18. J. A. van Bokhoven and J. T. Miller, in *X-Ray Absorption Fine Structure-XAFS13*, eds. B. Hedman and P. Painetta, Editon edn., 2007, vol. 882, pp. 582-584.
19. J. Chen, Q. H. Zhang, Y. Wang and H. L. Wan, *Adv. Synth. Catal.*, 2008, **350**, 453.
20. G. C. Bond, *Surf. Sci.*, 1985, **156**, 966.
21. S. Bhattacharjee, D. M. Dotzauer and M. L. Bruening, *J. Am. Chem. Soc.*, 2009, **131**, 3601.
22. J. Polte, R. Erler, A. F. Thunemann, S. Sokolov, T. T. Ahner, K. Rademann, F. Emmerling and R. Kraehnert, *ACS Nano*, **4**, 1076.
23. C. Tojo, E. Barroso and A. de Dios, *J. Colloid Interface Sci.*, 2006, **296**, 591.
24. S. Auer and D. Frenkel, *Nature*, 2001, **409**, 1020.
25. F. Baletto and R. Ferrando, *Rev. Mod. Phys.*, 2005, **77**, 371.
26. A. F. Lee, Z. Chang, P. Ellis, S. F. J. Hackett and K. Wilson, *J. Phys. Chem. C*, 2007, **111**, 18844.
27. H. Conrad, G. Ertl, J. Koch and E. E. Latta, *Surf. Sci.*, 1974, **43**, 462.
28. N. Seriani, J. Harl, F. Mittendorfer and G. Kresse, *J. Chem. Phys.*, 2009, **131**.
29. R. Westerstrom, C. J. Weststrate, J. Gustafson, A. Mikkelsen, J. Schnadt, J. N. Andersen, E. Lundgren, N. Seriani, F. Mittendorfer, G. Kresse and A. Stierle, *Phys. Rev. B*, 2009, **80**, 125431.
30. R. Westerstrom, C. J. Weststrate, A. Resta, A. Mikkelsen, J. Schnadt, J. N. Andersen, E. Lundgren, M. Schmid, N. Seriani, J. Harl, F. Mittendorfer and G. Kresse, *Surf. Sci.*, 2008, **602**, 2440
31. G. Zheng and E. I. Altman, *Surf. Sci.*, 2000, **462**, 151
32. G. Zheng and E. I. Altman, *Surf. Sci.*, 2002, **504**, 253
33. K. Kishi, Y. Motoyoshi and S. Ikeda, *Surf. Sci.*, 1981, **105**, 313.
34. K. Noack, H. Zbinden and R. Schlogl, *Catal. Lett.*, 1990, **4**, 145.
35. K. Kolasinski, *Surface Science: Foundations of Catalysis and Nanoscience*, John Wiley & Sons, Chichester, 2002.
36. K. Kishi and S. Ikeda, *J. Phys. Chem.*, 1974, **78**, 107.

37. A. G. Wren, R. W. Phillips and L. U. Tolentino, *J. Colloid Interface Sci.*, 1979, **70**, 544
38. W. E. Morgan, W. J. Stec and J. R. Vanwazer, *J. Am. Chem. Soc.*, 1973, **95**, 751.
39. C. D. Wagner, W. M. Riggs, L. E. Davis, J. F. Moulder and G. E. Muilenberg, *Handbook of X-Ray Photoelectron Spectroscopy*, Perkin-Elmer Corporation, Physical Electronics Division, Eden Prairie, Minn. 55344, 1979.
40. X. L. Zhou, F. Solymosi, P. M. Blass, K. C. Cannon and J. M. White, *Surf. Sci.*, 1989, **219**, 294.
41. A. Dan, S. Ghosh and S. P. Moulik, *J. Phys. Chem. B*, 2008, **112**, 3617.
42. M. V. Murugendrappa, S. Khasim and M. Prasad, *Indian J. Eng. Mater. Sci.*, 2000, **7**, 456.
43. J. D. Song, R. Ryoo and M. S. Jhon, *Macromol.*, 1991, **24**, 1727.
44. C. Umadevi, K. R. Mohan, V. B. S. Achari, A. K. Sharma and V. V. R. N. Rao, *Ionics*, 2010, **16**, 751.
45. B. Fu, W. Liu and Z. Li, *Appl. Surf. Sci.*, 2010, **256**, 6899.
46. N. E. Singh-Miller and N. Marzari, *Phys. Rev. B*, 2009, **80**, 235407.
47. C. Kim and H. Lee, *Catal. Commun.*, 2009, **10**, 1305.
48. J. Y. Park, C. Aliaga, J. R. Renzas, H. Lee and G. A. Somorjai, *Catal. Lett.*, 2009, **129**, 1.
49. J. N. Kuhn, C. K. Tsung, W. Huang and G. A. Somorjai, *J. Catal.*, 2009, **265**, 209.
50. H. Tsunoyama, N. Ichikuni, H. Sakurai and T. Tsukuda, *J. Am. Chem. Soc.*, 2009, **131**, 7086.
51. P. A. Gravil and H. Toulhoat, *Surf. Sci.*, 1999, **430**, 176.
52. J. Durand, E. Teuma and M. Gomez, *Eur. J. Inorg. Chem.*, 2008, 3577.

# Chapter 4

## *In situ* oxidation and reduction dynamics of palladium nanoparticles as catalysts for crotyl alcohol selective oxidation

## 4.1 Introduction

The traditional study of heterogeneous catalysis has often been criticised for its "black box" approach, wherein catalyst properties are characterised before and after reaction, with any attendant differences used to interpret catalytic performance and derive mechanistic insight.[1, 2] Recent so-called "operando" investigations (i.e. under true working temperature, pressure, solvents, practical feedstocks etc.) have revealed the inadequacy of such traditional approaches, which tend to view catalyst behaviour as independent of reaction conditions.[1-4] There has been a consequent explosion of interest surrounding *in situ* techniques able to probe catalyst dynamics during reactions, which have to-date revealed relationships between the reaction environment and, for example, the phase, oxidation state and dispersion of active sites that affect reaction outcomes.[3, 5-8] A number of *in situ* techniques, including those mentioned in the paragraph below, are described in *Chapters 1* and *2*.

Recent examples include an operando FTIR kinetic study of formate decomposition during methanol oxidation over $Au/CeO_2$ catalysts.[9] Scalbert et al. also used operando diffuse reflectance FTIR spectroscopy (DRIFTS), to understand the effects of $CO_2$ on catalyst deactivation, during toluene hydrogenation over $Rh/Al_2O_3$ catalysts versus platinum catalysts.[10] CO and NO oxidation over Rh and Pd have likewise been probed by operando DRIFTS, in parallel with X-ray absorption spectroscopy (XAS) measurements, using the same experimental set-up employed in this chapter.[11-13] These experiments have revealed insight into the surface species involved in each reaction, and the latter studies enable correlations between redox kinetics and active site (re)dispersion.

In this chapter the relationship between the oxidation state of palladium nanoparticles, the associated catalytic activity and selectivity during the vapour phase selective aerobic oxidation (selox) of crotyl alcohol will be explored. Previous liquid phase studies have revealed the importance of Pd(II) species, present on smaller particles which exhibit exceptionally high activity in crotyl alcohol conversion to crotonaldehyde. In this study it is suggested that formation of self-poisoning CO by-product is reduced by the presence of surface oxide.[14] However, the precise link between palladium oxidation state, oxygen concentration and indeed the catalytically active site during reaction, remains controversial.[15, 16] Baiker and co-workers have proposed that Pd metal is responsible for alcohol selox, and that oxygen removes CO

from the surface once it is formed.[17]

The response of Pd catalysts, including the sol-immobilised Pd icosahedra and nanorods on meso-alumina described in *Chapter 3*, a Pd/meso-$Al_2O_3$ and two SBA-15 supported Pd catalysts synthesised by Christopher Parlett will be studied.[14, 18, 19] The effect of different environments will be probed in detail, to determine the influence of particle shape/size and support,[20] and thus identify any common trends in catalyst redox capacity and performance. Using the dynamic pulsing approach adopted in this chapter, it is possible to employ kinetic analysis so that activation barriers and reaction rate constants can be determined, thus providing greater insight into the selox mechanism.

*Figure 4.1* illustrates the reactor setup used throughout this chapter, and this is described further in *Chapter 2*. Catalyst powder was placed in the sample well, and heated to temperatures varying between 80 °C and 250 °C. Lower temperatures were not possible due to crotyl alcohol condensation in the gas lines. Vapour phase operation enabled elimination of bulk mass transport limitations prevalent in liquid phase selox that would compromise analysis of the intrinsic reaction kinetics. Crotyl alcohol and oxygen were alternately admitted to the catalyst bed in a helium carrier stream. Vapour phase reaction products were detected via on-stream mass spectrometry (MS), adsorbates via DRIFTS, and the catalyst oxidation state/structure by energy dispersive X-ray absorption spectroscopy (XAS) at ID24 of the ESRF (Grenoble).

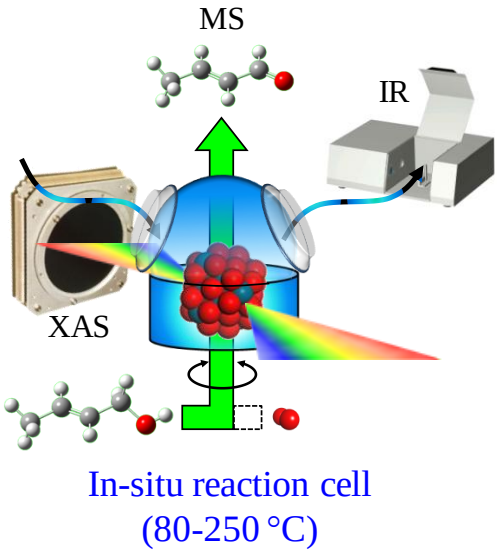


**Figure 4.1 - Schematic of reactor arrangement for synchronous DRIFTS/MS/XAS measurements**

## 4.2 Results and discussion

### 4.2.1 Characterisation

#### 4.2.1.1 On-stream mass spectrometry

Crotyl alcohol/$O_2$ conversion and the evolution of reactively-formed products was followed by on-stream MS. *Table 4.1* indicates the primary mass ions that were tracked for each species, while *Figure 4.2* shows an example reaction profile. Oxygen and alcohol switching was effectively achieved, although some tailing of the alcohol pulse into the oxygen cycle was observed, attributed to its higher mass and stronger adsorption within the gas lines and reaction chamber. This displacement process and residual reactant overlap, was only apparent for temperatures below 120 °C, the boiling point of crotyl alcohol.

| Species | Primary Mass Ion | Rel. Abundance |
|---|---|---|
| Helium | 4 | 100 |
| Oxygen | 16 | 100 |
| Water | 18 | 100 |
| Carbon monoxide | 28 | 100 |
| Propene | 41 | 100 |
| Carbon dioxide | 44 | 100 |
| Crotonaldehyde | 70 | 81.8 |
| Crotyl alcohol | 72 | 25.8 |

**Table 4.1 – Primary mass ions followed for each reaction component, and associated relative abundance of the pure component**

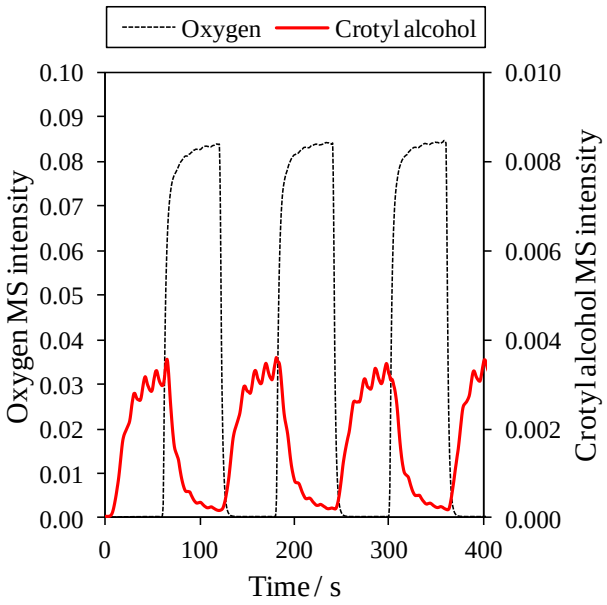


**Figure 4.2 – Example reaction profile for 1 wt% Pd/meso-alumina catalyst at 120 °C. Only first three cycles illustrated**

Relative reactant and product concentrations were calculated by integrating the area under the trace for each mass fragment, after normalising to the He carrier stream, to eliminate pressure fluctuations. Peak areas were averaged over 8 crotyl alcohol/$O_2$ cycles. Mass spectral fragmentation patterns for crotyl alcohol, crotonaldehyde and propene are shown in *Figure 4.3*, highlighting overlap from the crotyl alcohol reactant into the crotonaldehyde, propene (and also CO and $CO_2$) channels. Product quantification thus required subtraction of this crotyl alcohol contribution, and the resulting peak areas were finally normalised to their respective ionisation cross sections, to permit direct comparison of their concentrations.

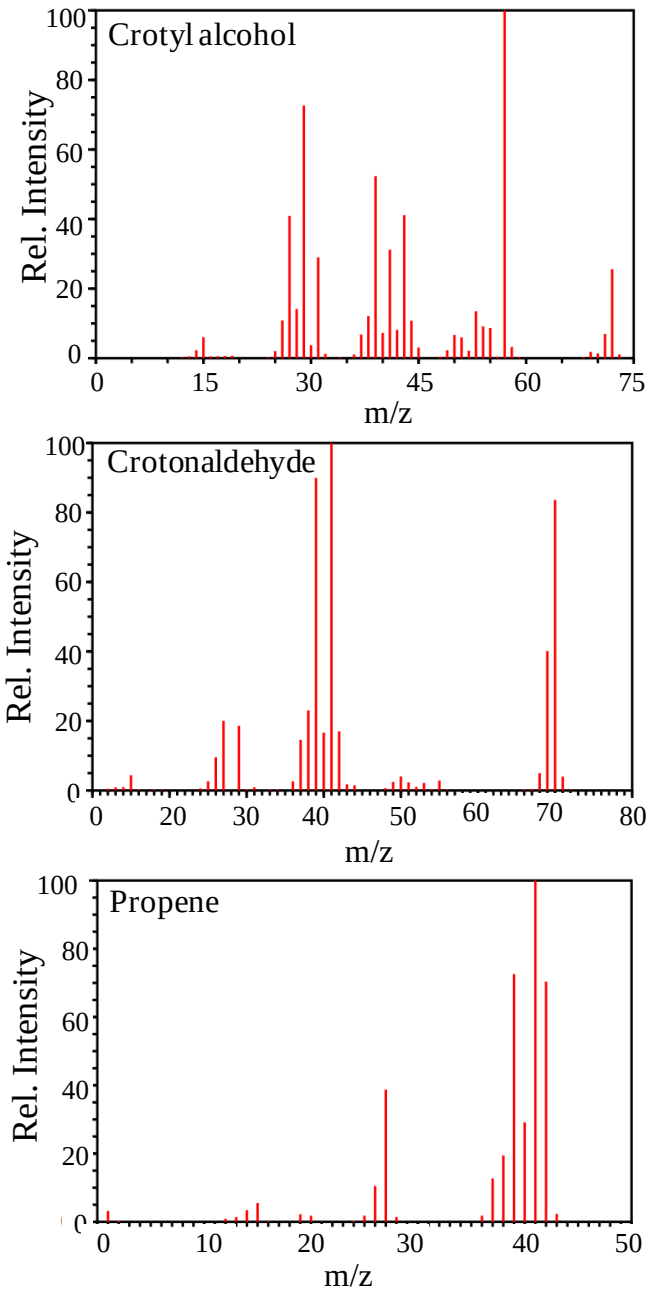


**Figure 4.3 – Electron ionisation mass spectra of crotyl alcohol, crotonaldehyde and propene taken from the NIST Chemistry WebBook (http://webbook.nist.gov/chemistry)**

The resulting product concentrations were summed and then normalised with respect to Pd weight loading, surface area and total catalyst mass, to give a total product yield. Crotyl alcohol conversions were calculated relative to the baseline gas phase alcohol concentration observed over Pd nanorods at 120 °C (which exhibit generally very low reactivity in laboratory measurements), to compensate for any adsorption within the reactor lines at lower temperature. Potential competing reaction pathways and their associated stoichiometries are shown in *Scheme 4.1*.

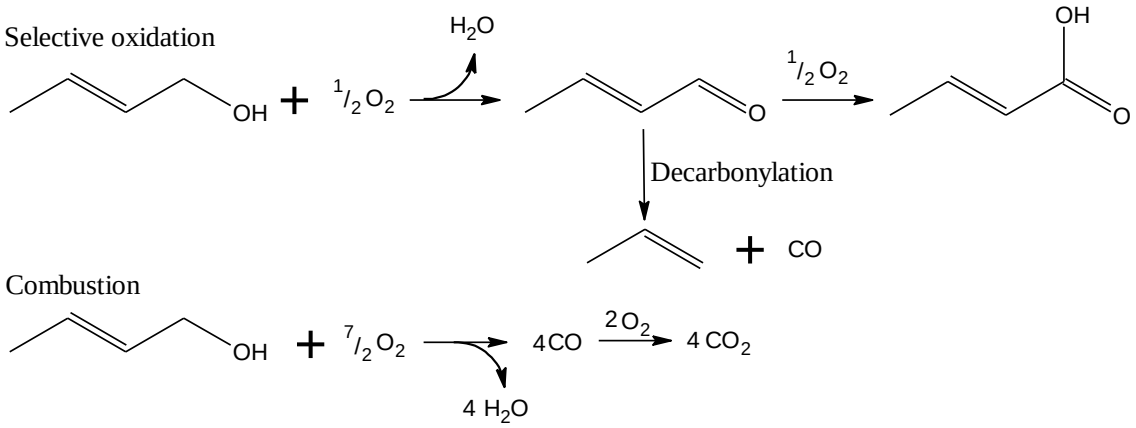


**Scheme 4.1 – Selective oxidation to crotonaldehyde, and competing decarbonylation and combustion pathways**

#### 4.2.1.2 *In situ* energy dispersive X-ray absorption spectroscopy

Structural changes in Pd catalysts were probed by Pd K-edge XAS (24.35 keV). Samples were first thermally equilibrated under He at any given temperature before treatment with reactive gases, during which 1000 spectra were sequentially measured at a rate of 0.803 s.spectrum$^{-1}$ (including 1.6 ms of dead time). Spectra were subsequently normalised and background subtracted using the ATHENA software package in batches of 50, and the resulting X-ray absorption near edge structure (XANES) intensities were quantified for comparison against Pd metal and PdO standards to provide a quantitative measure of oxidation state. *Figure 4.4* shows XAS spectra of the Pd foil and PdO standards. For PdO, comprising electron deficient $Pd^{2+}$ centres, core-shell electron excitation into valence band vacancies results in an intense white line compared with that of $Pd^0$.

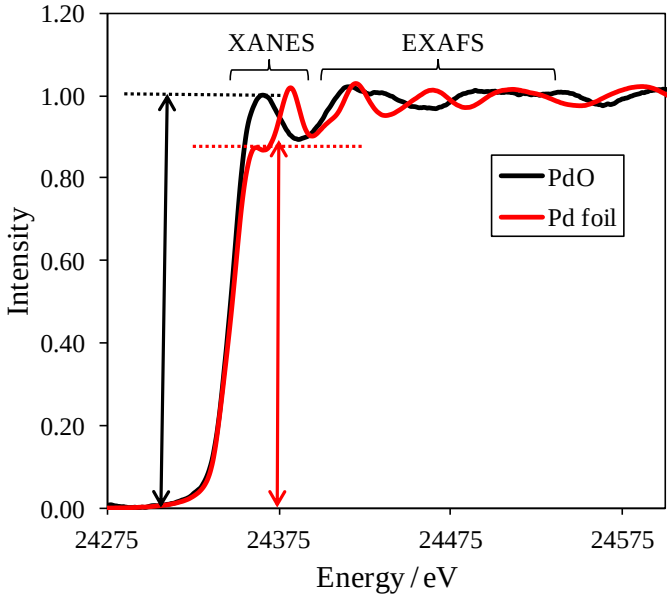


**Figure 4.4 – Pd K-edge XAS spectra of PdO and Pd metal foil standards. Arrows indicate the differing white-line intensities. The XANES and EXAFS regions are indicated**

The maximum XANES absorbance for PdO occurs at 24,362 eV, and that for Pd metal at 24,385 eV. The absorbance of Pd samples at these two energies were used to determine the oxide:metal ratio, and thus %PdO by simple scaling, relative to the corresponding intensities of oxide and metal standards. Oxidation states were calculated at different reaction temperatures, as a function of time, for comparison against synchronous DRIFTS and MS data. Average redox capacities were calculated across several reducing or oxidising cycles.

Time-dependent oxidation state information permits kinetic analysis of Pd oxidation and reduction dynamics, and associated activation barriers, as described in *Section 4.2.4*. The palladium oxidation state was also calculated via the least squares fitting module within Athena, to quantify the relative Pd foil and oxide contributions to spectra over a defined energy window about the edge-jump. An example of the resulting fit is shown for a 1 wt% Pd/meso-$Al_2O_3$ sample at 180 °C during a metallic cycle in *Figure 4.5*. Excellent agreement was found between these two approaches to determining oxidation states, and hence the former (simpler) scaling methodology was generally adopted. The latter method is referred to in *Section 4.2.3*.

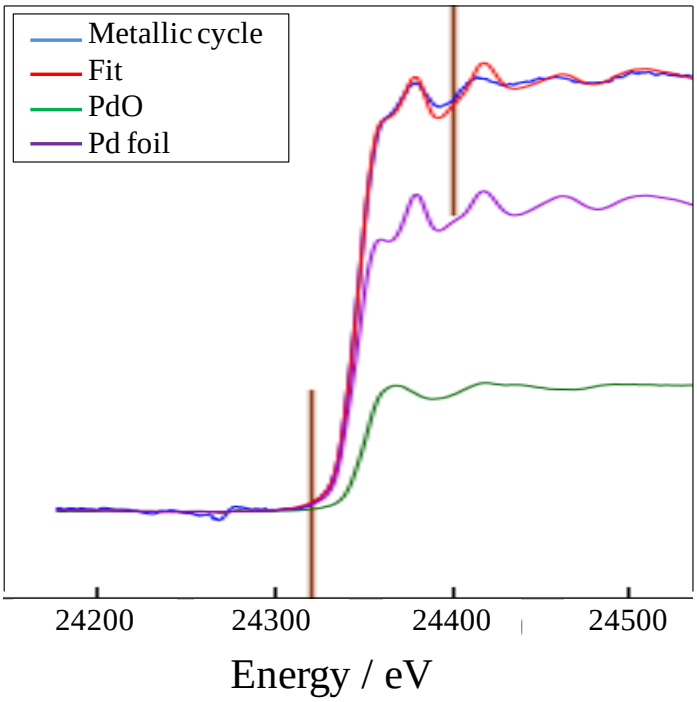


**Figure 4.5 – Linear combination fit to 1.03 wt% Pd/meso-$Al_2O_3$ at 180 °C under crotyl alcohol. Fit calculated between markers at -30 and +50 eV relative to a fixed $E_0$**

The redox capacity, defined as the observed change in white line absorbance (Δ) (oxidation state) relative to the maximum change possible during a $Pd^0/Pd^{2+}$ redox process ($\Delta_{max}$), was also calculated as shown in *Figure 4.6*.

$$\text{Redox capacity} = \left(\frac{\Delta}{\Delta_{max}}\right) \times 100$$

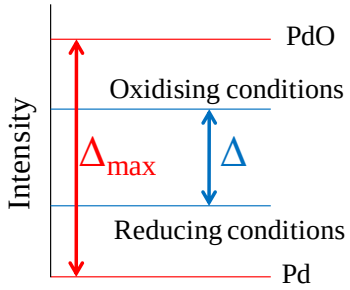


**Figure 4.6 – Redox capacity defined as the ratio of change in absorbance relative to the maximum change between PdO and Pd metal**

#### 4.2.1.3 Diffuse reflectance FTIR

Adsorbates were detected using DRIFTS under reaction conditions. Using this surface sensitive technique, the intensity of characteristic stretching frequencies for crotonaldehyde ($\nu_{c=o}$ = 1712 $cm^{-1}$ or $\nu_{c-H}$ = 2850 $cm^{-1}$), crotonic acid ($\nu_{c=o}$ = 1720 $cm^{-1}$) and CO ($\nu_{c=o}$ = 1915 $cm^{-1}$)[20-22] were followed with time and quantified. Extinction coefficients for the different adsorbates must also be considered, since the $\nu_{c=o}$ stretch in linearly-bound free CO is much greater than that in propionaldehyde ($\varepsilon$ = 4.95 mL $mg^{-1}$ $mm^{-1}$ versus 0.4 mL $mg^{-1}$ $mm^{-1}$) and that of the $\nu_{c=c}$ stretch in allyl alcohol ($\varepsilon$ = 0.026 mL $mg^{-1}$ $mm^{-1}$).[23, 24] Quantitative analysis of DRIFTS data was not possible due to lack of calibration standards at the synchrotron. Raw IR spectra were therefore compared against model spectra to identify the nature of adsorbed reaction intermediates/products. Density functional theory, using Gaussian 03 and a 6-311 Gdp basis set and the B3LYP functional, was employed by Adam Lee to calculate gas-phase model spectra for geometry optimised structures; these are displayed in *Figure 4.7* and *Figure 4.8*.

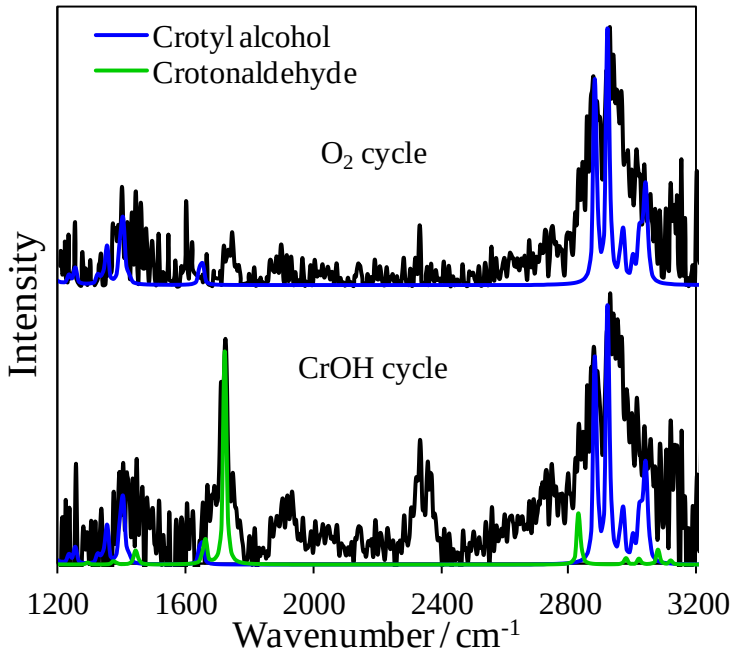


**Figure 4.7 – Calculated IR spectra of crotonaldehyde and crotyl alcohol and experimental spectra obtained under oxygen or crotyl alcohol cycles at 80 °C**

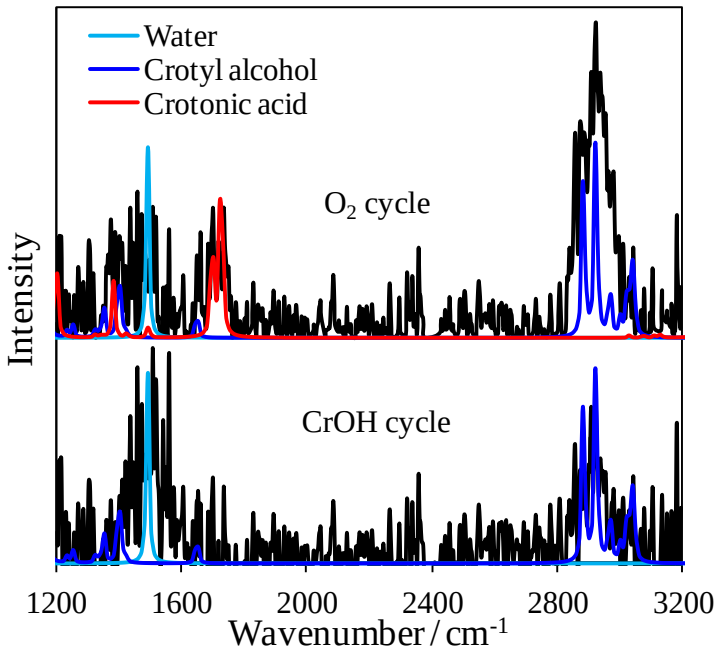


**Figure 4.8 – Calculated IR spectra of crotonic acid, crotyl alcohol and water and experimental spectra obtained under oxygen or crotyl alcohol cycles at 250 °C**

Before each experiment a reference interferogram was measured of the fresh catalyst in the absence of reactants. An interferogram of the catalyst under reaction conditions was then measured every 1.2 s. The raw interferograms were processed using OPUS 3D software. The reference and sample interferograms were converted into spectra, and an absorption spectrum was created using the software spectrum calculator and the equation based on the Beer-Lambert law given in *Equation 4.1*. This produced a 3D plot of intensity as a function of wavenumber along the x-axis and time along the y-axis. Intensity variations with time, normalised to the baseline in the z direction in order to account for fluctuations caused by movement of the sample bed, could then be deduced for selected wavenumbers in order to track specific adsorbates on the catalyst surface as a function of time/temperature.

$$absorption = -\ln\left(\frac{spectrum_{sample}}{spectrum_{reference}}\right)$$

**Equation 4.1 – Beer-Lambert law used for calculating absorption spectra in analysing DRIFTS data**

## 4.2.2 Catalytic reactivity

Employing the preceding methodologies, MS and DRIFTS profiles were constructed for a range of palladium catalysts. Focusing first on the 1 wt% Pd/meso-$Al_2O_3$ sample, representative DRIFTS and MS profiles for selective oxidation products are displayed in *Figure 4.9*.

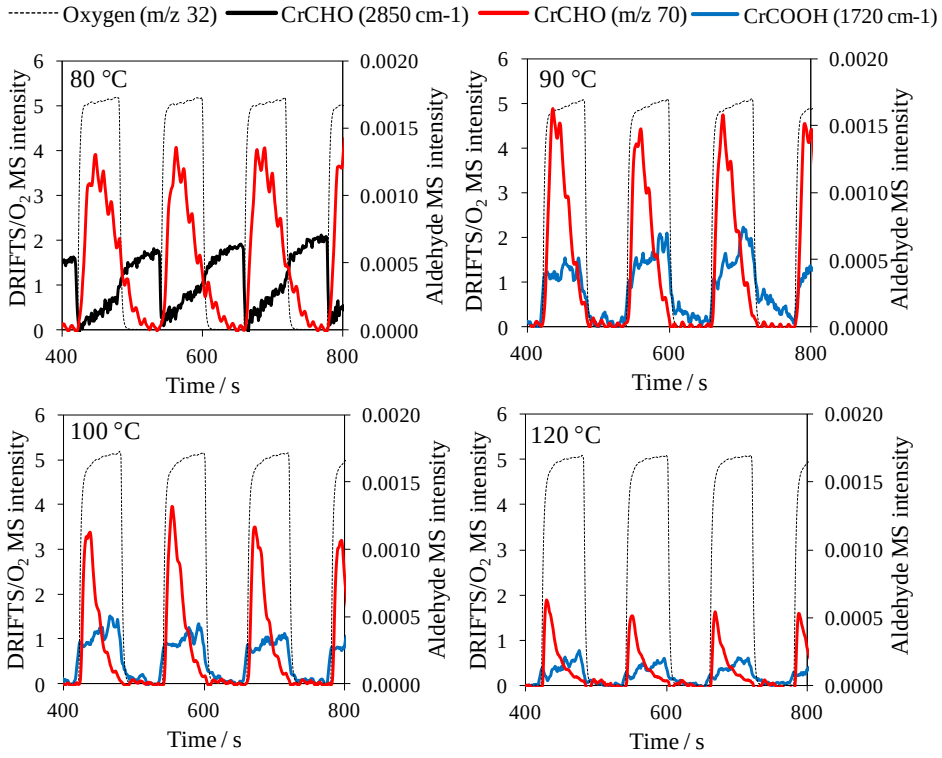


**Figure 4.9 –DRIFTS and MS profiles for selective oxidation products over 1 wt% Pd/meso-$Al_2O_3$**

At low temperatures (below 120 °C), exposure to crotyl alcohol resulted in significant crotonaldehyde formation, as evidenced by the rapid growth in the 2850 $cm^{-1}$ band in the DRIFTS, which equilibrated within 20 s. Switching to the oxygen feedstream resulted in the rapid loss of this crotonaldehyde signal, indicative of further reaction or desorption. The latter is confirmed by considering the simultaneous MS, from which gas phase crotonaldehyde desorption is observed, coincident with the introduction of oxygen.

These reaction profiles unequivocally demonstrate that oxidative dehydrogenation of crotyl alcohol to crotonaldehyde occurs under these reaction conditions, with the reactively-formed aldehyde released from the catalyst surface even at low temperatures. The anti-phase time-dependence of surface and gas phase

crotonaldehyde suggests an important role for co-adsorbed oxygen in weakening aldehyde adsorption, as previously observed over Pd(111) and Au/Pd(111) single crystal model catalysts.[25, 26] As the reaction temperature increases, the yield of gas phase crotonaldehyde progressively decreases, falling by a factor of 30 by 200 °C. Surface crotonic acid formation was also identified by DRIFTS over a narrow temperature range between 90-120 °C. Production was synchronous with gas phase oxygen, which indicates a higher oxygen demand than crotonaldehyde. This is to be expected given that generation of the former requires direct oxygen insertion. The absence of crotonic acid at 80 °C suggests that the selective oxidation of crotonaldehyde has a higher energy barrier than that of the corresponding alcohol: conjugation within the aldehyde may help stabilise it towards further over-oxidation.

Reaction profiles for the 2 wt% and 4 wt% Pd/SBA-15, 5 wt% Pd icosahedra and 5 wt% Pd nanorods/meso-alumina catalysts are shown at 80 °C and 100 °C in *Figures 4.10* and *4.11* respectively, and reveal qualitatively similar behaviour to the 1 wt% Pd/meso-$Al_2O_3$ sample, with selective oxidation predominant at low temperature.[*] Likewise crotonaldehyde was reactively formed on contacting samples with crotyl alcohol vapour, but only desorbed upon switching to an oxygen feedstream. There are some subtle differences between the DRIFTS spectra, although some of this can be attributed to differences in catalyst activity and the sensitivity towards detecting small amounts of surface species, as described in the following paragraphs.

[*] Due to the presence of hydroxyl attachment to the silica support in the two SBA-15 supported catalysts, the baseline around the aldehyde stretch at 2850 $cm^{-1}$ was too noisy for suitable analysis. Thus aldehyde was measured using the stretch at 1712 $cm^{-1}$, very close to the acid stretch at 1720 $cm^{-1}$, and so it is possible some surface acid or aldehyde has not been resolved from the spectra for these two catalysts.

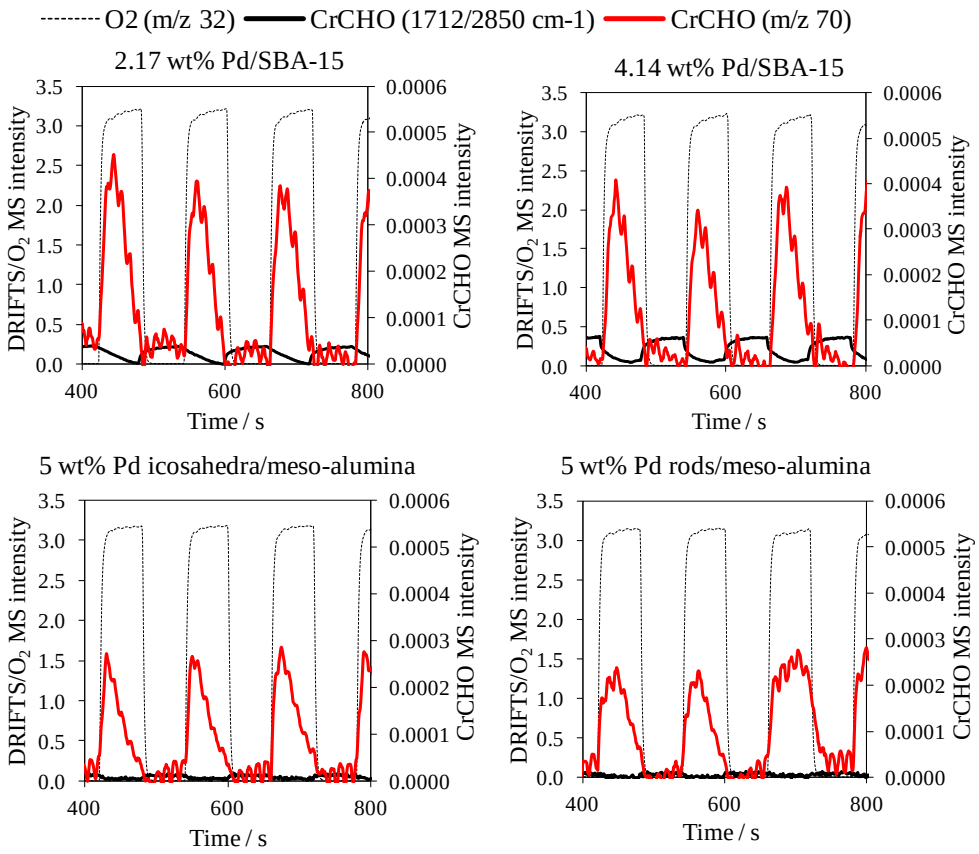


**Figure 4.10 – 80 °C reaction profiles showing adsorbed (DRIFTS) and desorbed (MS) crotonaldehyde**

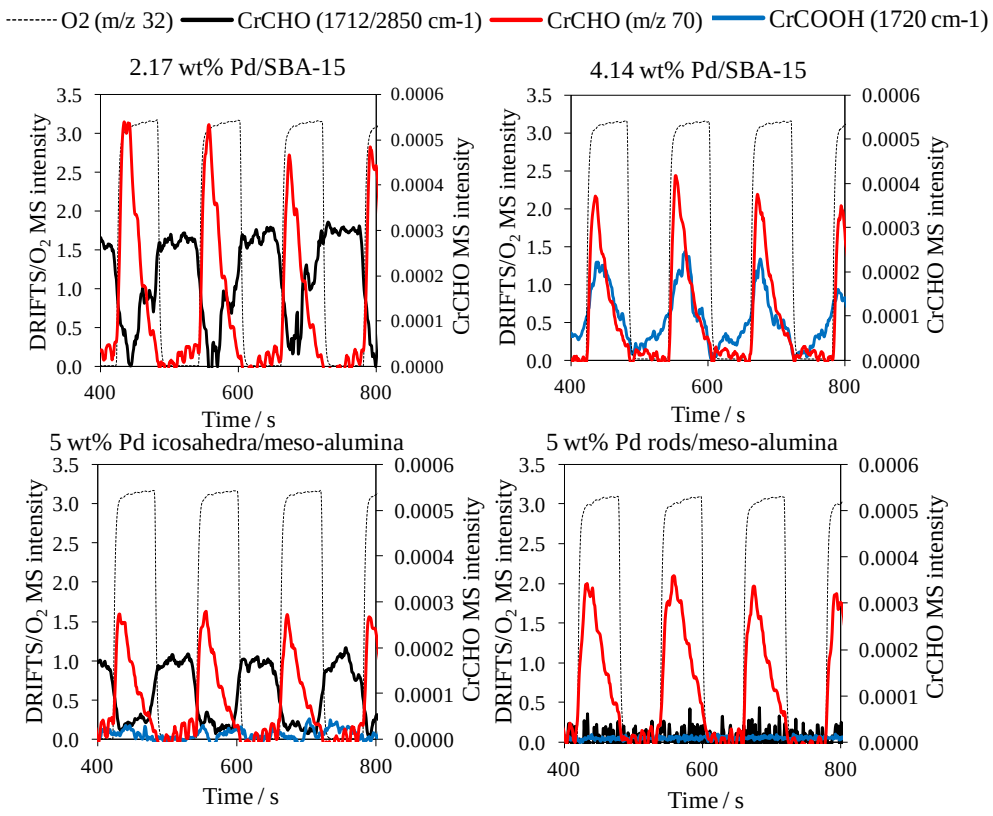


**Figure 4.11 – 100 °C reaction profiles showing adsorbed (DRIFTS) and desorbed (MS) products**

At 80 °C, aldehyde production is apparent, although very little surface aldehyde is detected by DRIFTS. It is shown later in this chapter that the activity for these catalysts is lower than the 1 wt% Pd/meso-alumina catalyst, thus detection of surface aldehyde may be more difficult. By 100 °C (*Figure 4.11*) surface aldehyde or acid is seen, showing a similar pattern of reactivity as before: aldehyde is reactively formed on the catalyst surface and desorbs once oxygen is introduced. Also comparable to the 1 wt% Pd/meso-alumina catalyst, above 80 °C aldehyde further oxidises to crotonic acid under a reactive oxygen atmosphere.

Only the Pd nanorods show no evidence of surface adsorbates. Although this may be interpreted as superior selectivity or a different mechanism for aldehyde formation, this cannot be deduced here: in the next section it is clear that the activity of this catalyst is very low, and species present on the surface may be more difficult to detect.

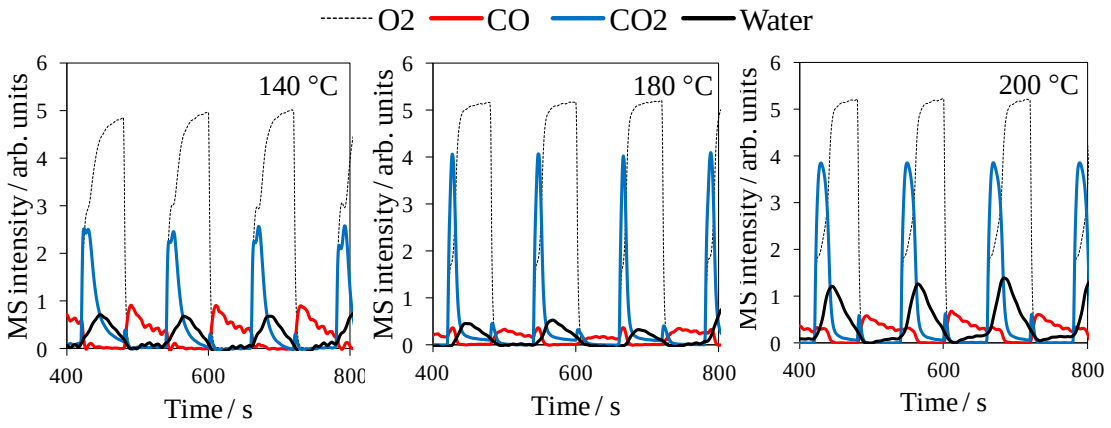


**Figure 4.12 –Non-selective products showing adsorbed (DRIFTS) and desorbed (MS) species for 1 wt% Pd/meso-$Al_2O_3$**

Higher reaction temperatures favour combustion products (*Figure 4.12*), with CO, $CO_2$, water and propene formation noted. There is a 20 fold increase in $CO_2$ yield between 100 °C and 200 °C, with significant production only observed by 140 °C. CO is formed and desorbs during the alcohol cycle, although there is no significant decrease in the desorbed product detected. Propene production has been excluded for clarity, with yields and trends directly comparable to CO shown later in *Figure 4.18*.

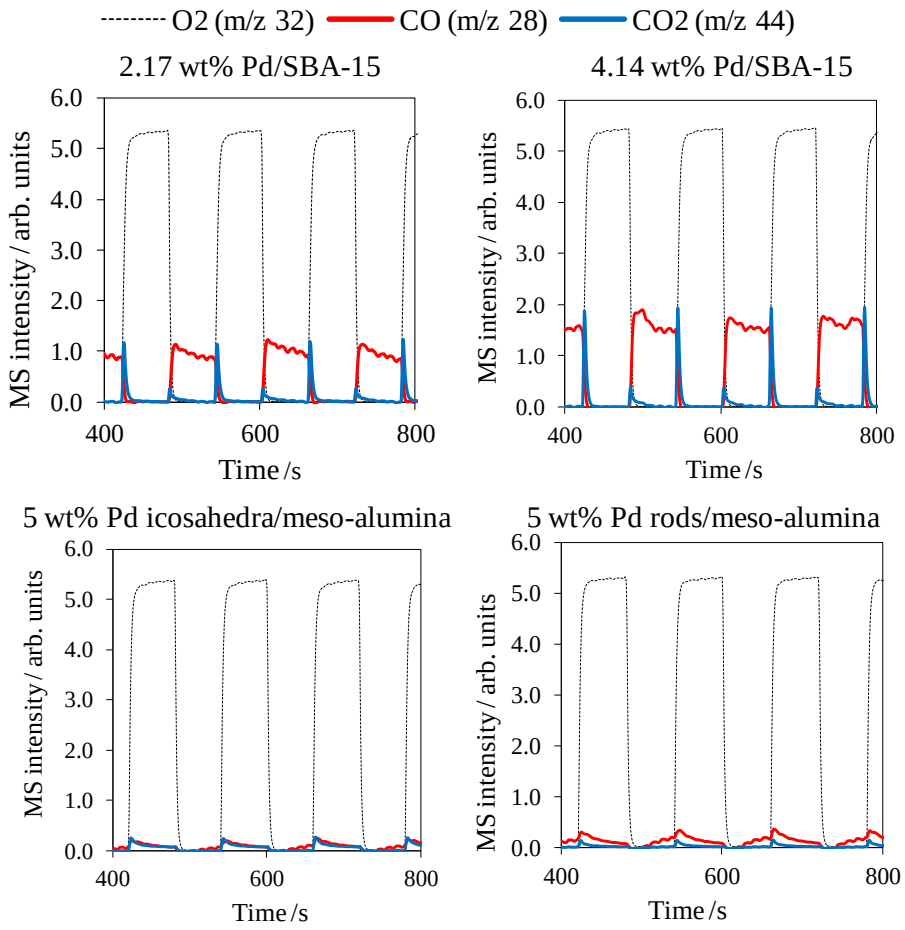


**Figure 4.13 – 180 °C reaction profiles showing CO and $CO_2$ products (MS)**

These decarbonylation and combustion products are also observed at higher temperature across the other four catalysts. By 180 °C the yields of combustion products are significant for the SBA-15 catalysts (*Figure 4.13*) and have increased by 25 times that observed at 100 °C (see appendix for figure). In light of their poor selectivity to crotonaldehyde, the low CO and $CO_2$ yields of the sol-immobilised Pd nanoparticles can be attributed to their lower activity, as shown in the following section.

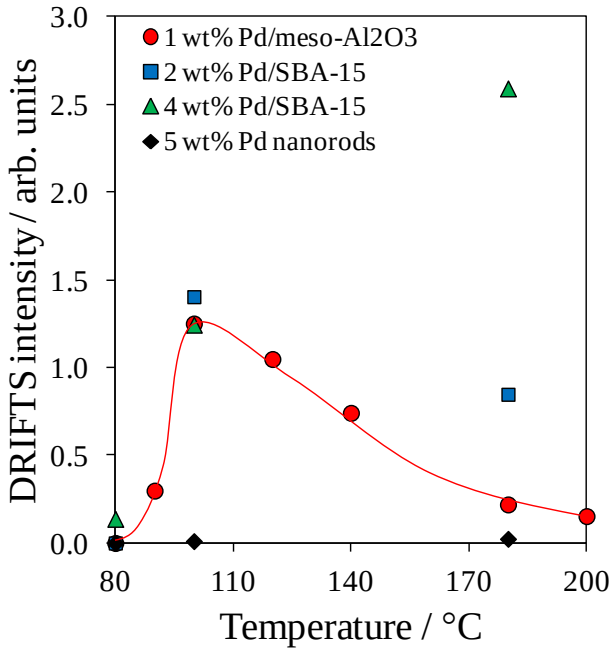


**Figure 4.14 – Variation in surface CO with temperature of 1 wt% Pd/meso-$Al_2O_3$, including a comparison with three other catalyst. Note it was not possible to calibrate the DRIFTS and so DRIFTS intensity has not been normalised**

Finally, it is worth considering the behaviour of adsorbed CO on the surface, detected by measuring the intensity of the 1915 $cm^{-1}$ stretch using DRIFTS (*Figure 4.14*).[27] First, for the 1 wt% Pd/meso-$Al_2O_3$ catalyst that has been considered in detail, CO formation is observed on the surface by 90 °C and yield peaks by 100 °C before steadily decreasing with temperature. It is interesting that there is no CO detected on the catalyst surface at 80 °C, contrary to single crystal studies over Pd(111) that show decarbonylation of crotonaldehyde to CO and propene occurs at room temperature.[28] Here is further evidence that the oxidic surface of these catalysts hinders the decarbonylation pathway. The subsequent decrease in surface yield of CO is not accompanied by an increase in desorbed CO from the MS profiles (*Figures 4.12* and *4.13*), although there is some increase in $CO_2$ production. This suggests that there is a partial switchover from incomplete oxidation to total oxidation.

The equivalent pattern of CO adsorption for the two SBA-15 supported catalysts and the Pd nanorods has also been included at 80 °C, 100 °C and 180 °C on *Figure 4.14* (not normalised). Note that it was not possible to measure surface-bound CO via DRIFTS in the icosahedra sample, due to interfering bands in this region (possibly due

to the presence of the organic stabiliser). Consistent with previous observation, no surface CO is detected on the Pd nanorods, which can once again be rationalised by their low activity. The behaviour of the 2 wt% Pd/SBA-15 catalyst mirrors that of the 1 wt% Pd/meso-$Al_2O_3$ catalyst already discussed. CO is only detected at 80 °C on the higher loading, more metallic 4 wt% Pd/SBA-15, further confirming that the more oxidic the catalyst surface, the more the decarbonylation pathway is obstructed. Significantly more CO is detected by 180 °C for this catalyst than at 100 °C. Unlike the 1 wt% Pd/meso-$Al_2O_3$ catalyst, this is accompanied by an increase in desorbed CO and in $CO_2$ formation, indicating that this can be in part accounted for by an increase in combustion for this catalyst at 180 °C. However, CO formation in particular is greater for this catalyst than the more oxidic 1 wt% Pd/meso-$Al_2O_3$ and 2 wt% Pd/SBA-15 catalysts. There is, thus, a subtle difference in behaviour of these catalysts. CO consumption may be reduced if further oxidation to $CO_2$ is less significant. Additionally, it is possible that the decarbonylation of crotonaldehyde to CO and propene is more prevalent over the more metallic 4 wt% Pd/SBA-15 catalyst, leading to increased CO formation.

### 4.2.3 Reversible catalyst restructuring

Having examined catalytic reactivity by MS and DRIFTS, the analogous catalyst structure was investigated through XANES analysis under these dynamic conditions. *Figure 4.15* compares the palladium oxidation state determined by XANES with select surface and gas phase reaction products over 1 wt% Pd/meso-$Al_2O_3$, 2 wt% Pd/SBA-15 and 5 wt% Pd icosahedra/meso-$Al_2O_3$ catalysts in a temperature regime in which all three are selective towards crotonaldehyde. At temperatures below 120 °C, the oxidation state of the three Pd catalysts was insensitive to changes in the reactant feedstream, with nanoparticles comprising between 20-60 % of PdO. It is important to recall that XAS is an averaging technique, hence the surface of the associated nanoparticles may be more heavily oxidised. However, the higher degree of oxidation observed for the larger icosahedra was unexpected. In *Chapter 3* the complex surface chemistry of the Pd icosahedra and Pd nanorods was examined in detail, and it was noted that particle morphology, in addition to size, may also be important in dictating selox performance. This chemical stability over the minute timescale (at mild

temperatures) mirrors that observed during a liquid phase, *in situ* XAS study of cinnamyl alcohol selox over Pd/C, for which partially oxidised palladium nanoparticles resisted reduction for over one hour at 60 °C.[29]

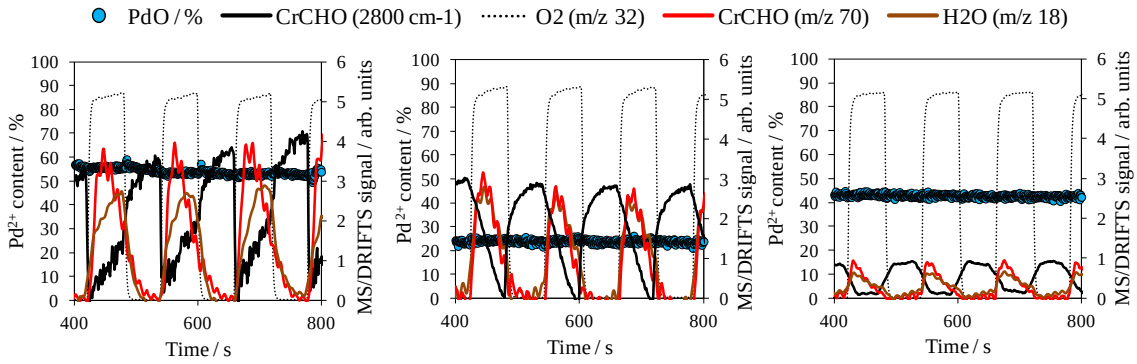


**Figure 4.15 – 80 °C reaction profiles for (left to right) 1 wt% Pd/meso-$Al_2O_3$, 2 wt% Pd/SBA-15 and Pd icosahedra showing principal products and oxidation state variability**

At higher temperatures above 180 °C, XANES analysis reveals oscillations in the palladium oxidation state in addition to this new combustion chemistry. *Figure 4.16* illustrates this new behaviour at 250 °C (200 °C for the 1 wt% Pd/meso-alumina catalyst), the highest temperatures we were able to study without physical movement of the catalyst bed that prevented DRIFTS and XAS acquisition. The introduction of alternating gas phase oxygen and crotyl alcohol cycles induced variations of up to 40 % in the proportion of PdO present in the 1 wt% Pd/meso-$Al_2O_3$ and 30 % in the 2 wt% Pd/SBA-15 catalysts, although the corresponding variation for the Pd icosahedra was orders of magnitude smaller and indeed could only be observed at 250 °C. It is proposed that this reflects slower oxygen penetration and abstraction through the capping layer present over these larger icosahedra.

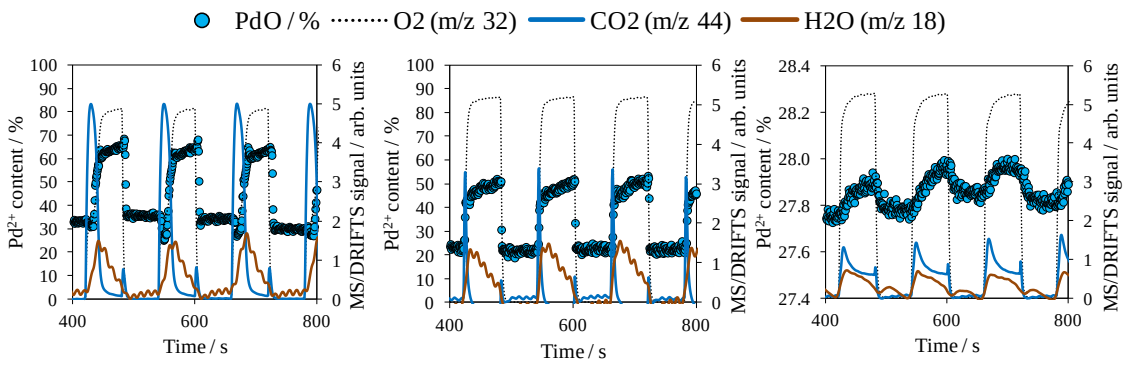


**Figure 4.16 –Reaction profile for (left to right) 200 °C 1 wt% Pd/meso-$Al_2O_3$, and 250 °C reaction profiles for 2 wt% Pd/SBA-15 and Pd icosahedra showing principal products and oxidation state variability**

Although the magnitude of these oxidation state changes was dependent on the catalyst formulation, in all cases restructuring occurred on a similar, extremely short, time scale (< 2 s) and in-phase, hence reaction-induced restructuring appears general to Pd catalysts, irrespective of size, morphology, support or preparation methods. Note that an arbitrary scale has been adopted for clarity in portraying the DRIFTS, MS and XAS spectra collectively, hence further quantitative analysis has been performed separately later in this section.

Further evidence for the universal dynamic behavior of Pd catalysts is seen in the comparable response of another mesoporous alumina benchmark catalyst. This was prepared under identical conditions to the 1 wt% Pd/meso-alumina sample, albeit reduced at 400 °C such that the as-prepared catalyst is less oxidic. The detailed response of this 2.4 wt% Pd/meso-alumina catalyst is noted in the following paragraphs, and further details of this catalyst are given in reference 20.[19, 20]

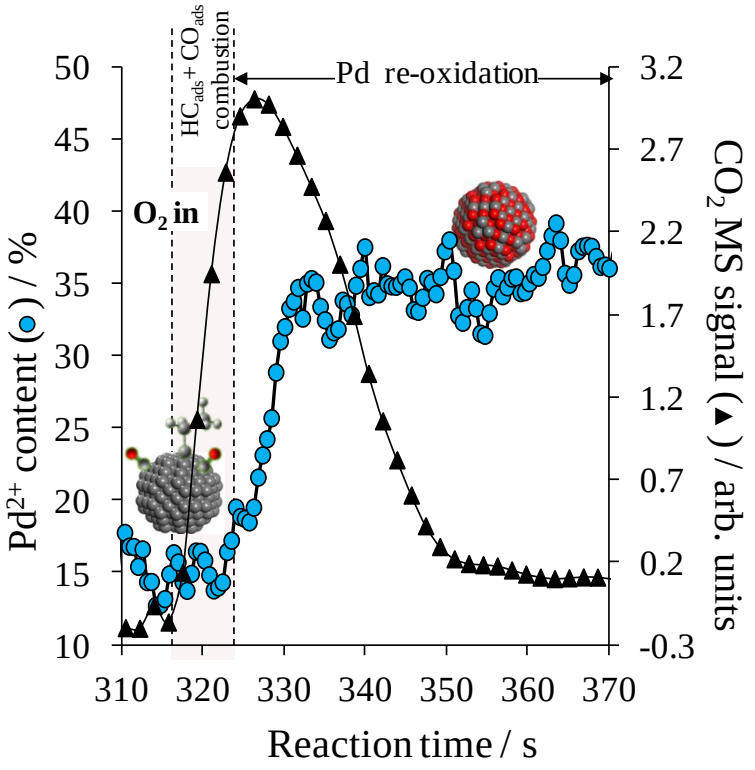


**Figure 4.17 – Evolving $CO_2$ yield and Pd oxidation state during switchover of crotyl alcohol/He →$O_2$/He reactant stream over 2.4 wt% Pd/meso-$Al_2O_3$ catalyst at 250 °C. Combustion occurs before re-oxidation of metal nanoparticles.**

*Figure 4.17* shows the evolution of reactively-formed $CO_2$ and the PdO concentration, which was recorded simultaneously, for the 2.4 wt% Pd/meso-alumina catalyst as it switches, from an initial crotyl alcohol feedstream to oxygen, at 315 s. Exposure to the reducing alcohol environment results in a highly reduced palladium state prior to the introduction of oxygen. Crotyl alcohol adsorption over Pd(111) at such temperatures undergoes extensive decomposition with ~50 % of a saturated adlayer remaining as propylidyne and carbonaceous residues in a single turnover.[25] Hence, the surface of such metallic nanoparticles is likely to accumulate significant residual hydrocarbon moieties during the crotyl alcohol cycle. Evidence for this prediction is apparent, due to the instantaneous $CO_2$ desorption peak on switching to an oxygen feedstream, implying rapid removal of hydrocarbon species. Combustion proceeds and attains a maximum rate over a 10 s window, during which palladium remains in a reduced form. It is clear from XANES that at approximately 325 s, the nanoparticles re-oxidise and there is a rapid drop in $CO_2$ production that occurs simultaneously, to a very low background rate, over the PdO shell. Approximately 73 % of the total $CO_2$ desorbs

prior to substantial catalyst re-oxidation. Hence, crotyl alcohol combustion is clearly favoured over Pd metal and not PdO. Conversely, 70 % more crotonaldehyde is released from the oxidic species than the metallic species for 1 wt% Pd/meso-$Al_2O_3$ at 200 °C, by comparing the amount of aldehyde detected by MS during an oxidic cycle and that formed during a reducing cycle.

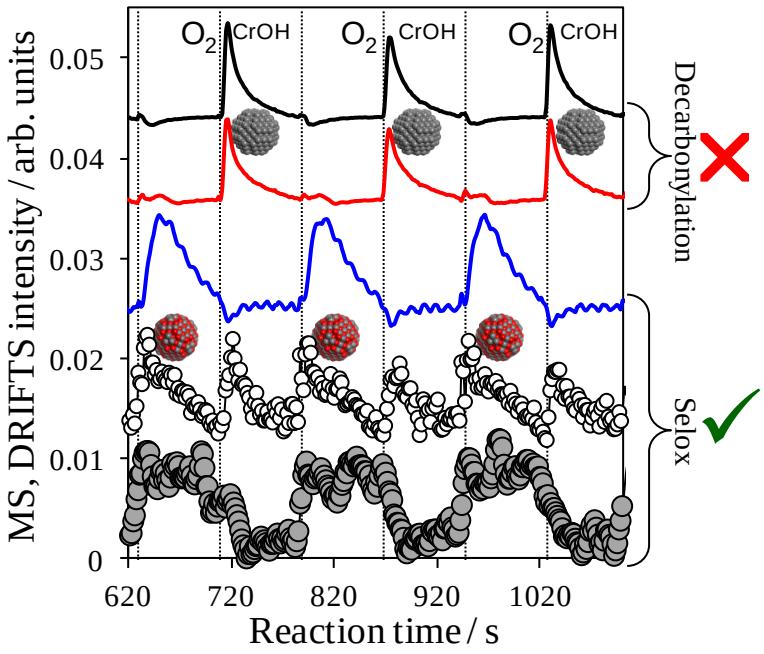


**Figure 4.18 – DRIFTS/MS intensities during alternating CrOH/$O_2$ cycles over 2.4 wt% Pd/meso-$Al_2O_3$ catalyst at 250 °C highlighting the predominance of selox chemistry over $PdO_x$ and decarbonylation over reduced Pd nanoparticles respectively: — (blue) $H_2O$ (m/z = 18), — (black) $C_3H_6$ (m/z = 41), — (red) CO (m/z = 28), ○ crotonaldehyde (m/z = 70), ● crotonic acid (1720 $cm^{-1}$ band).**

Further support for this conclusion is evident on comparing the time-resolved response of selective oxidation and decarbonylation products under crotyl alcohol versus $O_2$ cycling at high temperature (*Figure 4.18*). It was noted in *Section 4.2.2* that propene formation was directly comparable to CO production, and here it is apparent that production of these gases is favoured when the catalyst is reduced upon exposure to the alcohol reactant. The propensity of metallic Pd surfaces for decarbonylation was recently demonstrated for allyl alcohol over Pd(110)[30] and acetaldehyde over Pd(110), Pd(111) and Pd/$SiO_2$[30], with the latter dispersed catalyst exhibiting high selectivity to CO and methane at 250 °C. In this study, the rapid decay seen in *Figure 4.19* of both decarbonylation products under exposure to a continuous stream of crotyl alcohol, is

consistent with self-poisoning via blocking of surface metal sites by strongly-bound $CH_x$ fragments.

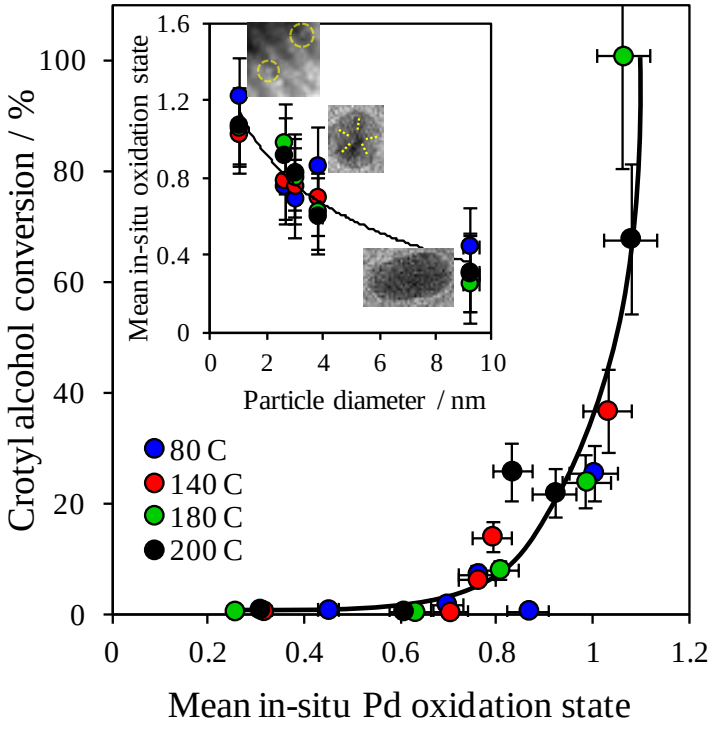


**Figure 4.19 – Crotyl alcohol conversion as a function of mean *in situ* oxidation state (particle size). Mean oxidation states are the average determined over four oxidising cycles**

*Figure 4.19* shows the relationship, independent of further physical properties such as pre-treatment history and support, between particle size, oxidation state and conversion. Average oxidation state under oxidising conditions, calculated using the least squares fitting method described in *Section 4.2.1.2* is considered here as the most representative when accounting differences in redox capacity. Mean *in situ* Pd oxidation state is represented here on a scale between 0 and 2 for pure metal and oxide standards respectively. As noted in *Section 4.2.1.1*, crotyl alcohol conversions were calculated relative to the baseline zero conversion level of that over Pd nanorods at 120 °C.

There is a clear correlation between Pd oxidation state and alcohol conversion that is universal across the different catalysts studied. Above a threshold of approximately 30 % oxide, conversion increases sharply and exhibits some temperature dependence, peaking at 180 °C. One particular physical property of the catalysts, which can be tailored to achieve these enhanced activities of crotyl alcohol selox, is the particle size. The insert to *Figure 4.19* depicts a clear inverse relationship between mean

*in situ* oxidation state and particle diameter: higher oxidation states are associated with decreasing size and the highest activities, irrespective of the other catalyst physical properties such as support and morphology. Thus, it is apparent from these results that PdO content plays a significant role in promoting catalyst activity, and in fact supports the hypothesis introduced by Lee and collaborators that PdO is the catalyst active site.[25, 31] The onset of catalytic activity above a threshold oxidation state is also consistent with this model, whereby the presence of sufficient levels of oxide significantly retard deactivation processes such as the formation of self-poisoning CO, and instead promotes the desorption of intact aldehyde, as proposed earlier in this chapter.

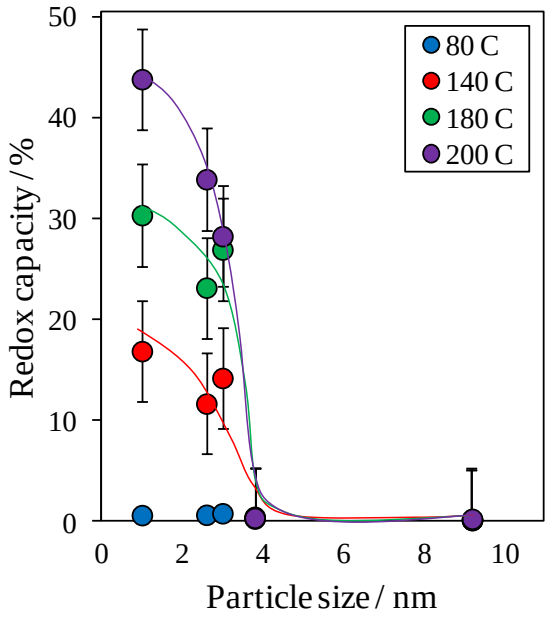


**Figure 4.20 – Inverse relationship exists between particle size and redox capacity which becomes more prominent with increasing temperature**

It is, however, important to note that the smallest (most active) nanoparticles are also the most unstable, as evidenced by their temperature-dependent redox capacity (*Figure 4.20*). Large particles exhibit extremely small redox capacities (tending to zero for the nanorods), and are insensitive to temperature. In contrast, Pd nanoparticles below 4 nm are highly susceptible to redox cycling, with their redox capacities increasing from around 10 % at 140 °C to up to 45 % by 200 °C, i.e. almost half of the palladium atoms in a 1 nm particle underwent full oxidation during the $O_2$ cycle at high temperature. To the author's knowledge, this represents the first demonstration of

operando XAS as a rapid and quantitative tool for the measurement of redox capacity in metal nanoparticles.

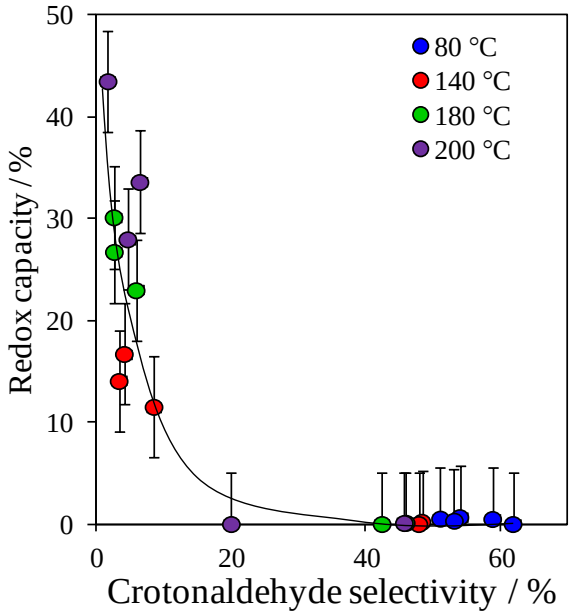


**Figure 4.21 – Crotonaldehyde is inversely proportional to redox capacity indicating that the more stable, larger catalysts are more selective**

A strong, inverse relationship between redox capacity and crotonaldehyde selectivity was also apparent, with small (highly active) particles more prone to reduction at higher temperatures, and concomitant loss in selectivity (*Figure 4.21*) via crotonaldehyde decarbonylation to undesired propene and CO by-products. This highlights the importance of stabilising Pd in a high oxidation state in order to achieve high crotonaldehyde yields.

## 4.2.4 Kinetics analysis

In order to further understand the flexible response of Pd nanoparticles to temperature and oxidising/reducing conditions discussed above, the redox kinetics of the catalysts were analysed at reaction bed temperatures from 80 to 200 °C. *Figure 4.22* illustrates the redox behaviour for all the catalysts considered in this chapter during a typical switching cycle from a crotyl alcohol to $O_2$ feed at 200 °C (250 °C for Pd nanoicosahedra – see earlier comment). We have already seen that the redox process is fully reversible for over 5 cycles, with a complete return to the initial oxidation state

attained on switching from crotyl alcohol to $O_2$ and back. Another common feature is the apparent non-linear oxidation process, which proceeds via rapid oxide formation and is followed by a slower, more gradual oxidation process, which does not reach a plateau throughout the remaining oxidation cycle. In contrast, reduction occurs in a single, rapid step.

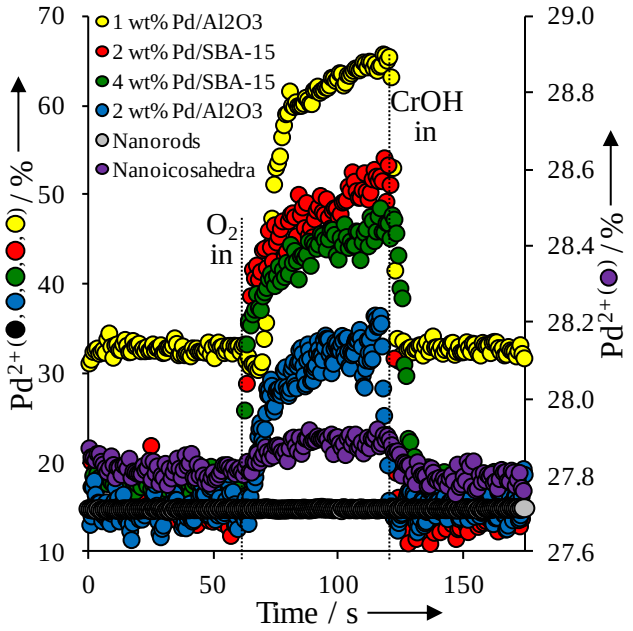


***Figure 4.22* – Pd nanoparticle redox response under crotyl alcohol/$O_2$ cycling at 200 °C (icosahedra at 250 °C)**

To better understand the oxidation kinetics of the redox active NPs, their correspondence to a Mott-Cabrera model for diffusion limited oxidation of thin films was explored.[32] This model describes the rapid oxidation of a metal, to form a thin film oxide layer, followed by slower diffusion through the oxide layer to form the metal oxide. Although this model was developed with regards to oxide films, it is applicable to other examples of ionic diffusion through an equivalent medium.[33] The assumption that electron transfer will occur more rapidly than the diffusion of metal cations or oxygen anions, results in the formation of an electric field between the adsorbed oxygen and metal surface. This lowers the energy barrier for diffusion through the oxide layer so that it can occur at lower temperature.[34, 35]

The formation of a potential difference between the adsorbed oxygen, oxide surface and metal is illustrated in *Figure 4.23*.[36] This is analogous to the formation of a

chemical gradient and the diffusion of ions across that gradient, which decreases as the system reaches equilibrium.

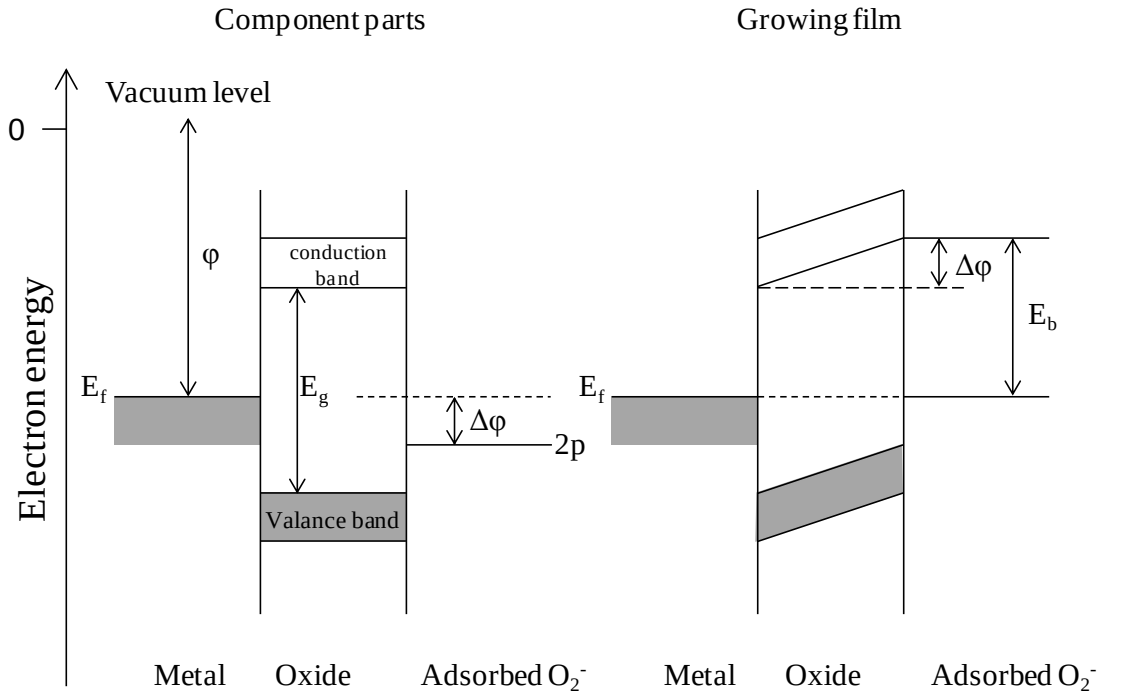


**Figure 4.23 – Band diagram modified from reference 19 showing the formation of the Mott potential $E_b$ on the interaction of an oxide film (band gap $E_g$) and metal (work function φ), with adsorbed oxygen: Δφ is the voltage across the film**

The resulting parabolic rate law is given in *Equation 4.2*:

$$-\frac{d[PdO]}{dt} = \frac{k}{[PdO]}$$

**Equation 4.2 – the parabolic rate law**

Using the linear integrated form of *Equation 4.2*, the parabolic rate constants can be calculated by plotting PdO concentration against $t^{½}$ (*Figure 4.24*) from *Equation 4.3*,

$$[PdO] = (2kt)^{½}$$

**Equation 4.3 – linear form of the parabolic rate law**

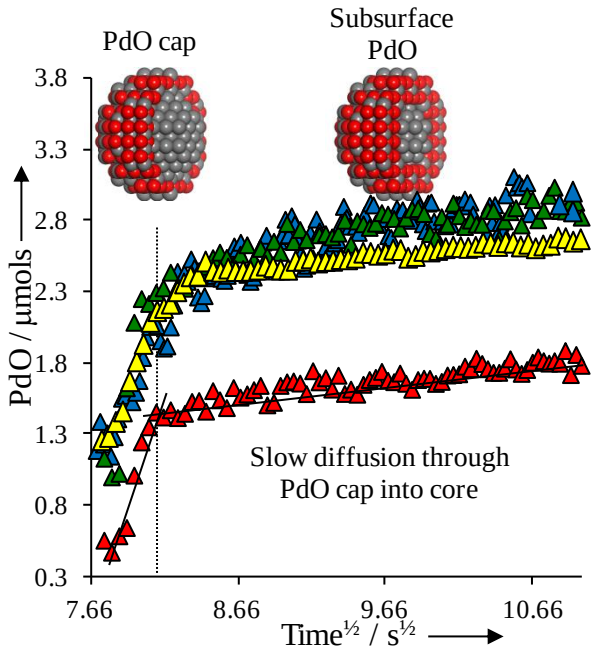


**Figure 4.24 – Correspondence to Mott-Cabrera diffusion-controlled oxidation of supported Pd NPs at 200 °C**

Excellent agreement was obtained to the resulting linear fits for all supported nanoparticles at 200 °C, confirming the existence of two distinct oxidation regimes. Rate constants for the 1st and 2nd oxidising regimes and the reduction process are shown in *Table 4.2*, and have been used to calculate activation energies for these three steps by applying the Arrhenius equation (*Equation 4.4*). It is apparent from these values that the two oxidising regimes have over an order of magnitude difference in rates.

| Catalyst | $k_{ox}^1$/µmol$^2$ s$^{-1}$ | $k_{ox}^2$/µmol$^2$ s$^{-1}$ | $k_{red}^1$/µmol$^2$ s$^{-1}$ |
|---|---|---|---|
| 1 wt% Pd/meso-$Al_2O_3$ | 61 | 4.6 | 195 |
| 2 wt% Pd/meso-$Al_2O_3$ | 48 | 5.2 | 193 |
| 2 wt% Pd/SBA-15 | 41 | 0.6 | 238 |
| 4 wt% Pd/SBA-15 | 136 | 0.7 | 228 |

**Table 4.2 – parabolic rate constants for Pd nanoparticles redox cycling processed at 200 °C**

$$k = A\exp\left(-\frac{E_a}{RT}\right)$$

**Equation 4.4 – Arrhenius equation**

The resulting activation energies, and their dependence on particle size for the 1 wt% Pd/meso-$Al_2O_3$, and 2 and 4 wt% Pd/SBA-15 catalysts are shown in *Figure 4.25*. As may be expected, if palladium oxidation indeed follows a Mott-Cabrera model involving rapid surface oxidation followed by slower oxygen permeation through a passivating oxide overlayer, the activation for the second oxidation process is systematically higher than that of the first by between 5-20 kJ $mol^{-1}$. These values compare favourably with those reported by M. Salmeron et al. from a high pressure XPS study of oxidation of a Pd(111) single crystal, and similar values of J. Han and co-workers, who report activation energies of 60-85 kJ $mol^{-1}$ for surface oxidation of clean Pd(111) and 111-116 kJ $mol^{-1}$ for oxygen penetration.[37, 38] E. D. German and collaborators calculated the energy barrier for oxygen penetration of an oxygen atom on a Pd(111) surface diffusing from a 3-fold hollow site to a subsurface site as 150 kJ $mol^{-1}$ using DFT.[39] In contrast, reduction of PdO nanoparticles appears facile, with activation energies ranging between 35-70 kJ $mol^{-1}$. Size dependence was also apparent, with larger particles exhibiting lower barriers towards both oxidation and reduction. This can be attributed to the lower degree of strain and atomic displacements necessary in incorporating and removing oxygen atoms from the surface of large metallic Pd nanoparticles in comparison with their smaller counterparts.

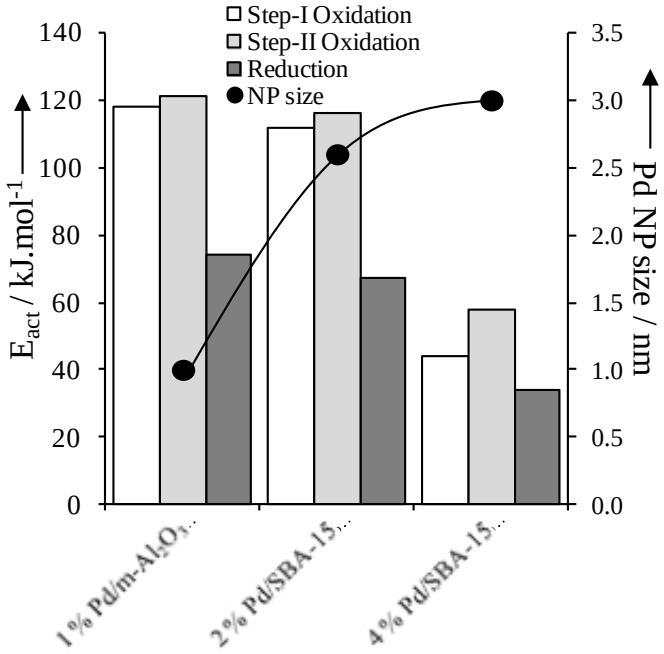


**Figure 4.25 -Variation in activation energies (averaged across 4 cycles) with particle size**

Finally, it is worth noting that the relationship between oxidation state and activation barrier is not linear across the three catalysts studied. It is possible that this is because an increase in particle size does not equate to a linear increase in the number of metal atoms, which may be a significant factor in atom displacement. There may also be a support effect that leads to a difference in the energy barrier, although further quantitative experimental data would be required to explore this hypothesis further.

## 4.3 Conclusions

The application of synchronous XAS/MS/DRIFTS on vapour phase catalysis is a unique experiment that demonstrates the possibility of analysing relevant reactions under operating conditions. In the introduction, the need to overcome the "black box" catalyst model was raised, and here catalyst dynamics are assessed *in situ*, whilst simultaneously monitoring reaction progression and catalyst response. The results indicate that particle size dependent fluctuations in oxidation state during reaction have an effect on catalyst activity and selectivity. *Scheme 4.2* shows the higher temperature dependence of catalyst oxidation state, reactant environment and surface chemistry. Starting with the oxidic catalyst (bottom right), the introduction of crotyl alcohol reduces the nanoparticle and crotonaldehyde forms on the surface. Decarbonylation occurs on the metallic surface leading to adsorbed $CH_x$ species. When the crotyl alcohol feed is switched to oxygen, the $CH_x$ species react with oxygen to form carbon dioxide. Additionally, at lower temperatures, when the surface is more oxidic, further oxidation of the aldehyde to acid will occur, and the surface will re-oxidise. Oxygen introduction on a catalyst that is not as reducible, such that decarbonylation does not occur, results in the release of aldehyde and water products.

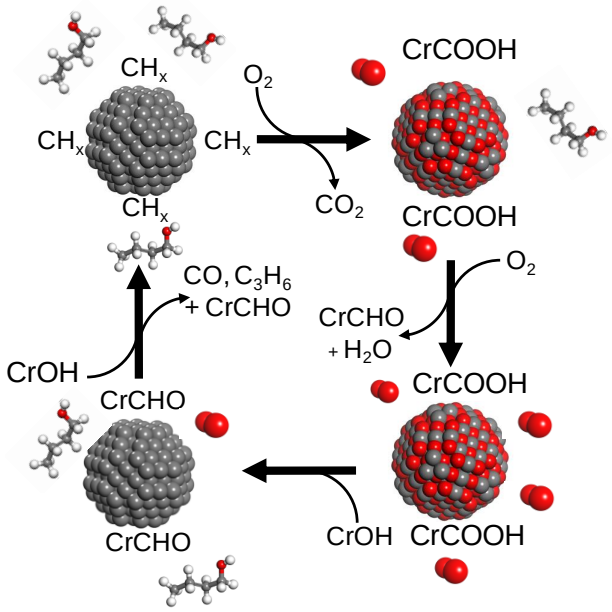


**Scheme 4.2 – Catalyst restructuring as a response to its reactive environment with associated selectivity towards crotyl alcohol oxidation above 150 °C**

In addition to these general observations, a number of specific conclusions can be stated. First of all, by isolating individual reactants during the reaction the role of oxygen in crotonaldehyde selective oxidation is clearly to release the product from the surface: aldehyde formation occurs before oxygen is introduced. Secondly, the metallic surface is significantly less reactive to selective chemistry: at low temperature activity is poorer and, at higher temperature, combustion chemistry is dominant. However, the oxidic surface is associated with smaller, less stable particles and a decrease in selectivity. Catalysts in which redox capacity is minimised, but high oxidation state is maintained are clearly desirable for crotonaldehyde formation and provide challenges in future catalyst design, particularly support development. Finally, kinetic analysis of the rate of oxidation state changes reveal diffusion limited redox cycling. Catalyst oxidation is more difficult than reduction with energy barriers as high as 120 kJ $mol^{-1}$ and is dependent on particle size and possibly is sensitive to the support. Confirmation of these latter relationships would require screening of further catalysts that display measureable redox cycling across a range of temperatures.

## 4.4 References


1. G. Rothenberg, *Catalysis: Concepts and Green Applications*, Wiley-VCH, Weinheim, 2008.
2. K. Tamaru, *Proc. Jpn. Acad. Ser. B-Phys. Biol. Sci.*, 2004, **80**, 119.
3. M. A. Newton, *Chem. Soc. Rev.*, 2008, **37**, 2644.
4. S. S. C. Chuang and F. Guzman, *Top. Catal.*, 2009, **52**, 1448.
5. B. M. Weckhuysen, *Chem. Commun.*, 2002, 97.
6. B. M. Weckhuysen, *Phys. Chem. Chem. Phys.*, 2003, **5**, VI.
7. C. O. Arean, B. M. Weckhuysen and A. Zecchina, *Phys. Chem. Chem. Phys.*, 2012, **14**, 2125.
8. M. A. Banares, *Adv. Mater.*, 2011, **23**, 5293.
9. P. Bazin, S. Thomas, O. Marie and M. Daturi, *Catal. Today*, 2012, **182**, 3.
10. J. Scalbert, F. C. Meunier, C. Daniel and Y. Schuurman, *Phys. Chem. Chem. Phys.*, 2012, **14**, 2159.
11. M. A. Newton, C. Belver-Coldeira, A. Martinez-Arias and M. Fernandez-Garcia, *Angew. Chem.-Int. Edit.*, 2007, **46**, 8629.
12. M. A. Newton, S. G. Fiddy, G. Guilera, B. Jyoti and J. Evans, *Chem. Commun.*, 2005, 118.
13. M. A. Newton, A. J. Dent, S. G. Fiddy, B. Jyoti and J. Evans, *Phys. Chem. Chem. Phys.*, 2007, **9**, 246.
14. S. F. J. Hackett, R. M. Brydson, M. H. Gass, I. Harvey, A. D. Newman, K. Wilson and A. F. Lee, *Angew. Chem. Int. Ed.*, 2007, **46**, 8593.
15. C. Keresszegi, T. Burgi, T. Mallat and A. Baiker, *J. Catal.*, 2002, **211**, 244.
16. A. F. Lee and K. Wilson, *Green Chem.*, 2004, **6**, 37.
17. J. D. Grunwaldt, M. Caravati and A. Baiker, *J. Phys. Chem. B*, 2006, **110**, 25586.
18. C. M. A. Parlett, D. W. Bruce, N. S. Hondow, A. F. Lee and K. Wilson, *ACS Catalysis*, 2011, **1**, 636.
19. S. F. J. Hackett, University of York (PhD), 2008.
20. A. F. Lee, C. V. Ellis, J. N. Naughton, M. A. Newton, C. M. A. Parlett and K. Wilson, *J. Am. Chem. Soc.*, 2011, **133**, 5724.
21. S. Devarajan, P. Bera and S. Sampath, *J. Colloid Interface Sci.*, 2005, **290**, 117.
22. NIST Mass Spec Data Centre and S. E. Stein (director), *Infrared Spectra in NIST Chemistry WebBook, NIST Standard Reference Database Number 69*, Eds. P. J. Linstrom and W. G. Mallard, National Institute of Standards and Technology, Gaithersburg, MD, 20899, http://webbook.nist.gov, (Retrieved 24/10/2011).
23. T. S. Chong, S. T. Tan and W. Y. Fan, *Chem.-Eur. J.*, 2006, **12**, 5128.
24. M. A. Vannice and S. Y. Wang, *J. Phys. Chem.*, 1981, **85**, 2543.
25. A. F. Lee, Z. Chang, P. Ellis, S. F. J. Hackett and K. Wilson, *J. Phys. Chem. C*, 2007, **111**, 18844.
26. A. F. Lee, S. F. J. Hackett, G. J. Hutchings, S. Lizzit, J. Naughton and K. Wilson, *Catal. Today*, 2009, **145**, 251.
27. A. Guerrero-Ruiz, S. W. Yang, Q. Xin, A. Maroto-Valiente, M. Benito-Gonzalez and I. Rodriguez-Ramos, *Langmuir*, 2000, **16**, 8100.
28. J. Naughton, A. F. Lee, S. Thompson, C. P. Vinod and K. Wilson, *Phys. Chem. Chem. Phys.*, 2010, **12**, 2670.
29. A. F. Lee and K. Wilson, *Green Chem.*, 2004, **6**, 37-42.

30. M. Bowker, L. Gilbert, J. Counsell and C. Morgan, *J. Phys. Chem. C*, 2010, **114**, 17142.
31. A. F. Lee, S. F. J. Hackett, J. S. J. Hargreaves and K. Wilson, *Green Chem.*, 2006, **8**, 549.
32. N. Cabrera and N. F. Mott, *Rep. Prog. Phys.*, 1949, **12**, 163.
33. D. B. Pedersen, S. L. Wang, E. J. S. Duncan and S. H. Liang, *J. Phys. Chem. C*, 2007, **111**, 13665.
34. Q. Fu and T. Wagner, *Surf. Sci. Rep.*, 2007, **62**, 431.
35. J. Han, D. Y. Zemlyanov and F. H. Ribeiro, *Surf. Sci.*, 2006, **600**, 2752.
36. A. Atkinson, *Rev. Mod. Phys.*, 1985, **57**, 437.
37. M. Salmeron and R. SchlÃ¶gl, *Surf. Sci. Rep.*, 2008, **63**, 169.
38. J. Y. Han, D. Y. Zemlyanov and F. H. Ribeiro, *Surf. Sci.*, 2006, **600**, 2752.
39. E. D. German, M. Sheintuch and A. M. Kuznetsov, *J. Phys. Chem. C*, 2009, **113**, 15326.

# Chapter 5

# Tuneable $TiO_2$ supported Au-shell Pd-core catalysts for liquid phase crotyl alcohol selective oxidation

## 5.1 Introduction

The impact of structure-reactivity relations of palladium nanoparticles as catalysts for selective oxidation was investigated in *Chapters 3* and *4*. Palladium is a promising catalyst for application in this area of fine chemical synthesis, but it is prone to deactivation and selectivities can be low.[1, 2] For example, the selectivity of $Pd/TiO_2$ towards benzaldehyde formation is as low as 55 % after one hour.[3] It has been shown here, and elsewhere, that palladium's catalytic performance can be improved by modifying particle size and morphology (and thus oxidation state and exposed facets).[4, 5] Superior reactivity can also be attained through the use of promoters[6-8]; in particular, a second metal component can influence both the electronic and geometric properties. For example, new adsorption sites can be exposed, the adsorption geometry may be modified or substrate binding at existing adsorption sites may be affected by charge transfer.[9]

Gold addition to palladium can enhance catalyst selectivity, activity and lifetime.[10-12] The catalytic activity of nanoparticulate gold, a surprising discovery noted independently by Hutchings and Haruta in the 1980s,[13, 14] has stimulated intense experimental and computational research in gold catalysis[15-18], as discussed in *Chapter 1*. Many groups have explored gold as a promoter in bimetallic Au/Pd alloy catalysts, wherein gold is proposed to enhance selectivity by suppressing product degradation (and thus self-poisoning)[19] and enhancing desired product desorption. These effects may manifest changes in the electronic structure of the active site, due to charge transfer, or create new surfaces, as implicated by model studies.[9, 20] The precise Au:Pd ratio is an important factor, but it is poorly understood, although single-crystal vacuum measurements have been successfully utilised in this area.[21]

This chapter addresses the impact of gold on Pd catalysed liquid phase selox of crotyl alcohol and builds upon the following two observations. The first of these observations comes from Enache and co-workers' comparison of gold, palladium and a gold-palladium bimetallic catalyst for allylic alcohol oxidation.[3] *Figure 5.1* shows the resulting conversions and selectivities towards benzyl alcohol oxidation. While gold initially exhibits high selectivity, this varies significantly over the course of reaction and it has a low turn over frequency (TOF). Palladium is more active, but deactivates after 2 hours, with selectivity towards benzaldehyde falling from 65 % to only 35 %. In contrast, gold-palladium displays a high TOF, with constant high benzaldehyde

selectivity, and does not deactivate, resulting in 100 % conversion of benzyl alcohol to benzaldehyde after 12 hours. The origin of this synergy, however, is poorly understood, reflecting limited synthetic control over the Au/Pd distribution (e.g. alloy composition, phase-separation and electronic properties of both elements).

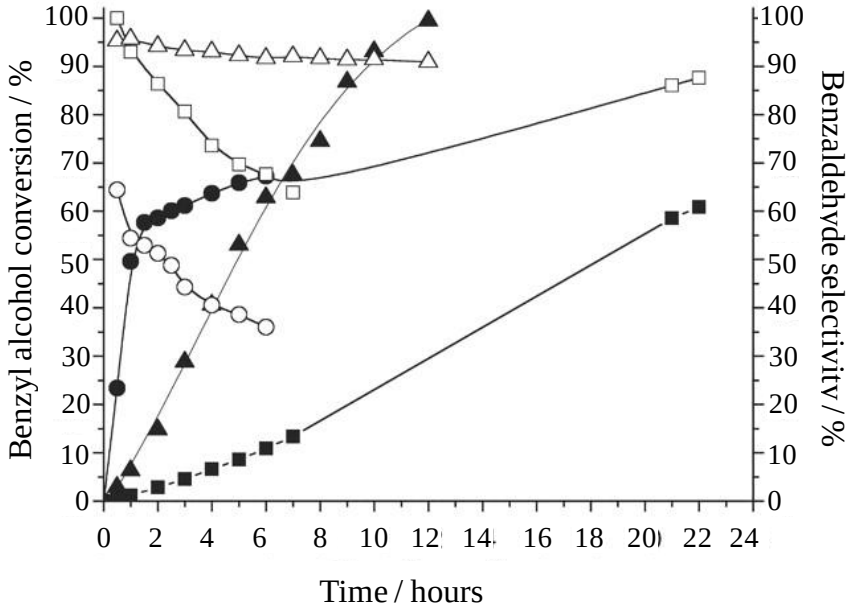


**Figure 5.1 – Benzyl alcohol conversion (filled shapes) and selectivity (hollow shapes) over Au (squares), Pd (circles) and Pd/Au (triangles). Reproduced from reference 3**

The second observation comes from single crystal studies under ultra-high vacuum (UHV), in which the surface chemistry of crotyl alcohol over Pd(111) and Pd/Au(111) model catalysts has been probed.[19] *Figure 5.2* shows the temperature programmed-desorption (TPD) traces from mass spectrometry of crotyl alcohol on the respective mono- and bi-metallic surfaces. At surface temperatures of 200 K, Pd(111) drives the oxidative dehydrogenation of crotyl alcohol to crotonaldehyde, accompanied by significant decarbonylation to form propene and CO. Higher reaction temperatures induce further decomposition and carbon deposition by 580 K. These may account for Pd deactivation and low aldehyde selectivity in dispersed Pd catalysts. Gold incorporation greatly lowers, and delays, the onset of decarbonylation (trace observed ~400 K), with a dramatic corresponding enhancement in surface and evolved crotonaldehyde. This may explain the observations of Enache et al. regarding higher selectivities and lifetimes for Pd/Au catalysts versus pure palladium. This surface science study predicted that a composition of $Au_{40}Pd_{60}$ would be optimal for crotyl

alcohol selox. It was noted in *Chapter 1* that catalyst composition will likely exert a powerful influence on product adsorption in selox chemistry, and thus secondary (undesired) reactions.[22]

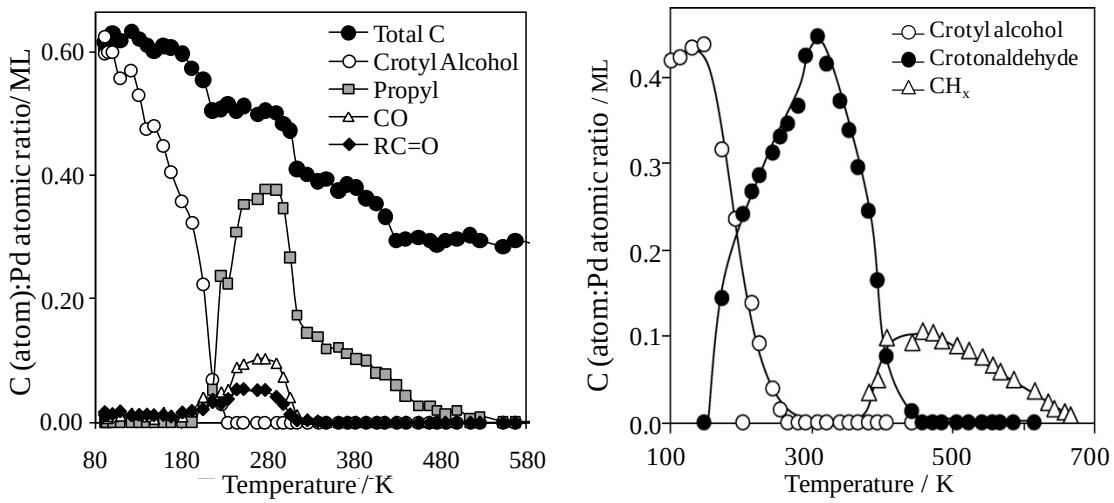


**Figure 5.2 – Temperature programmed desorption traces from the adsorption of crotyl alcohol on Pd(111) (left) and Au/Pd(111) (right). Reproduced from reference 19**

This chapter tests the preceding model predictions, via synthesis of titania-supported Au-shell/Pd-core nanoparticles for liquid phase crotyl alcohol selox, to identify the optimum alloy composition under 'real-world' conditions.[23] The surface metal composition is carefully tuned through controlled thermal processing, and the resulting nanoparticles extensively characterised for comparison against model single crystal UHV measurements. A comparable study, by A. F. Lee and co-workers, has been performed on analogous Pd-shell/Au-core colloidal nanoparticles for the cyclotrimerisation of acetylene to benzene. Alloying improved both activity and selectivity towards benzene, although surface compositions were not directly probed.[24]

## 5.2 Results and discussion

### 5.2.1 High resolution transmission electron microscopy and elemental analysis

The Au-shell/Pd-core nanoparticles were prepared by Prof. Adam Lee using a seeded growth method, similar to that used in the synthesis of Pd shapes from previous chapters and described in *Chapter 2*.[23, 25] The resulting colloid was then dispersed on

approximately 100 nm anatase crystals. It was necessary to support the nanocatalysts so that sufficiently large quantities of sample were available for analysis and to stabilise the particles on annealing. The formation of a core-shell structure was dependent on achieving fine control in the synthetic procedure, and thus required dilute conditions. Consequently, only milligram quantities of product were obtained. There would have been limited characterisation techniques that could be applied to confirm the core-shell structure if the nanoparticles had not then been supported. Additionally, intermixing of the Pd and Au was achieved through controlled annealing (see below). Unsupported nanoparticles would have exhibited significant sintering if annealed at these temperatures, particularly as a weakly-interacting citrate stabiliser was used in the synthesis. Further developments in the synthesis of stable, unsupported, core-shell nanoparticles, such as those used in *Chapter 3*, would help eliminate support effects. Furthermore, fine control of particle size, in order to account for size effects, is important for developing this work, although there is very limited success reported in the synthesis of monodisperse core-shell Au-Pd structures with diameters <10 nm.[26]

High resolution transmission electron microscopy (HRTEM) for the as-prepared supported nanoparticles, and those annealed at 300 °C and 700 °C, are given in *Figure 5.3*. The as-prepared catalyst has a mean particle size of 20 nm and approximate cuboctahedral morphology. High angle annular dark field scanning transmission electron microscopy (HAADF-STEM) was attempted in order to unequivocally identify the thin Au shell. The detector used in this technique minimises collection of Bragg scattered electrons by collecting electrons scattered by the nuclei at higher angle. Consequently, the intensity of features in the micrograph is proportional to their associated atomic number (intensity $\propto Z^2$) and this mode is also termed Z-contrast imaging.[27] In theory it is possible to distinguish between the Au shell and Pd core using this instrument, but this attempt was unsuccessful, probably because the Au shell is very thin. However, a number of additional techniques have been used to confirm the core-shell starting structure.

HRTEM permitted measurement of the lattice spacing at the edge of a (111) oriented facet, wherein contributions from the Au shell should dominate. This is shown in *Figure 5.3b* and was determined as 0.24 nm ±0.01 nm, in close agreement with the interlayer spacing of bulk gold (0.2355 nm compared with 0.2246 nm for bulk palladium) and consistent with that of Au overlayers of comparable thickness grown on a Pd(111) single crystal and alumina supported Pd core-shell nanoparticles.[28, 29]

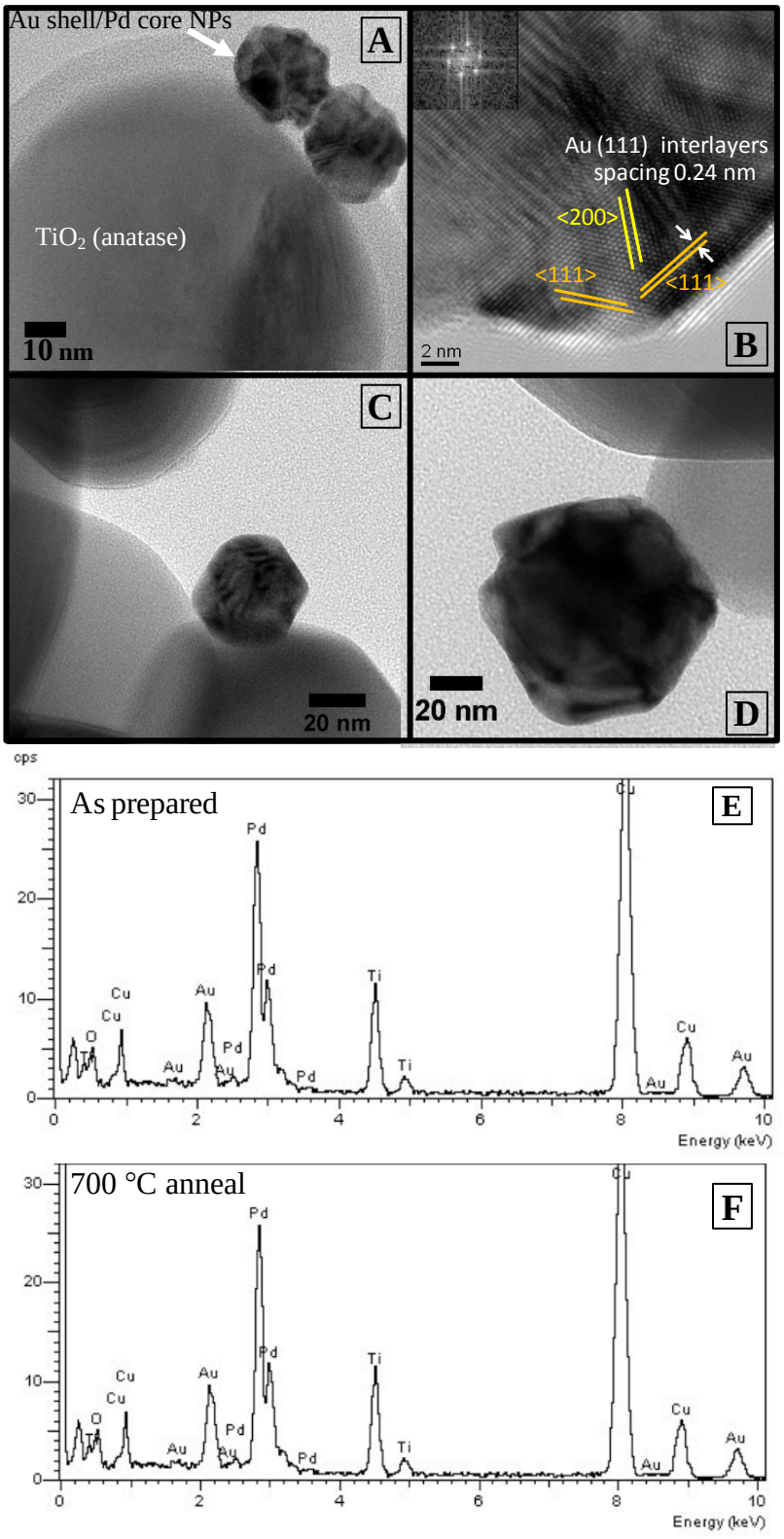


**Figure 5.3 – HRTEM of as-prepared Au-Pd/$TiO_2$ nanoparticles (A & B) and after annealing at 300 °C (C) and 700 °C (D). Example EDX spectra for the as-prepared (E) and 700 °C (F) samples**

Energy dispersive X-ray spectroscopy (EDX) confirmed that Pd and Au were present in individual nanoparticles, with an average composition of 70:30 Pd:Au.

Furthermore, inductively coupled plasma optical emission spectrometry (ICP-OES) analysis revealed metal loadings of 0.21 % Pd and 0.18 % Au with a bulk molar percentage of 65 % Pd. From this compositional data, and the particle size information, it is possible to construct a simple model to estimate the Au shell thickness. Assuming spherical particles, and due to the similar unit cell sizes of Pd and Au,[30] [*] the mol% of Pd in the fresh nanoparticles is related to the shell volume by *Equations 5.1* and *5.2* below.

$$Fresh\ Pd\ mol\% = \frac{Core\ volume}{(Core\ volume + Shell\ volume)}$$

**Equation 5.1 – Relationship between amount of Pd and Au shell volume**

$$Shell\ volume = \left[{}^{4}/_{3}\,\pi(r+w)^{3}\right] - \left[{}^{4}/_{3}\,\pi r^{3}\right]$$

**Equation 5.2 – Determination of Au shell volume based on the Pd core radius (*r*) and shell thickness (*w*) which is the product of the number of Au layers (n) and the Au interlayer spacing**

It is clear from *Table 5.1* below that the closest fit for an Au composition of 35 % is given by a particle with a core Pd diameter of 20 nm encapsulated by 5 atomic layers of gold. An interlayer spacing of 0.235 nm was used to calculate the Au shell thickness. The molar ratio of the two metals was determined using the molar density for gold and palladium (0.0979 $cm^{-3}$ and 0.1128 $cm^{-3}$ respectively).[†31] This model is in excellent agreement with the experimentally determined total Pd diameter of 20 nm.

[*] Reference data obtained from the Chemistry Database Service at Daresbury "The United Kingdom Chemical Database Service", Fletcher, D.A., McMeeking, R.F., Parkin, D., *J. Chem. Inf. Comput. Sci.* **1996**, 36, 746

[†] Calculated from the specific gravity and relative molecular mass of Au and Pd respectively

| Diameter Core / nm | Volume core / $nm^3$ | Number of shells | Shell thickness / nm | Total diameter / nm | Total volume / $nm^3$ | Shell volume / $nm^3$ | Ratio shell:core | Molar ratio |
|---|---|---|---|---|---|---|---|---|
| 18 | 3054 | 4 | 0.94 | 19.88 | 4114 | 1060 | 34.72 | 30.17 |
| 18 | 3054 | 5 | 1.175 | 20.35 | 4413 | 1359 | 44.50 | 38.67 |
| 18 | 3054 | 6 | 1.41 | 20.82 | 4725 | 1672 | 54.75 | 47.57 |
| 19 | 3591 | 4 | 0.94 | 20.88 | 4766 | 1175 | 32.72 | 28.43 |
| 19 | 3591 | 5 | 1.175 | 21.35 | 5096 | 1504 | 41.88 | 36.39 |
| 19 | 3591 | 6 | 1.41 | 21.82 | 5440 | 1848 | 51.46 | 44.71 |
| 20 | 4189 | 4 | 0.94 | 21.88 | 5485 | 1296 | 30.93 | 26.88 |
| 20 | 4189 | 5 | 1.175 | 22.35 | 5846 | 1657 | 39.55 | 34.37 |
| 20 | 4189 | 6 | 1.41 | 22.82 | 6222 | 2033 | 48.54 | 42.18 |
| 21 | 4849 | 4 | 0.94 | 22.88 | 6271 | 1422 | 29.33 | 25.49 |
| 21 | 4849 | 5 | 1.175 | 23.35 | 6666 | 1817 | 37.47 | 32.55 |
| 21 | 4849 | 6 | 1.41 | 23.82 | 7077 | 2228 | 45.94 | 39.91 |
| 21 | 4849 | 7 | 1.645 | 24.29 | 7504 | 2655 | 54.75 | 47.57 |

**Table 5.1– Theoretical Pd core diameters and Au shell thicknesses with the resulting core volume/shell volumes and hence Pd content. A 20 nm core and 5 layer thick shell results in the best fit to 35 % Au composition**

Mean particle sizes were also determined by TEM as a function of annealing temperature as shown in *Figure 5.4*. Particle sizes remained roughly constant at ~ 20 nm diameter up to 400 °C, above which significant particle growth is observed, with sizes up to ~70 nm attained by 700 °C. Further examples of images used for particle size analysis are given in the appendix.

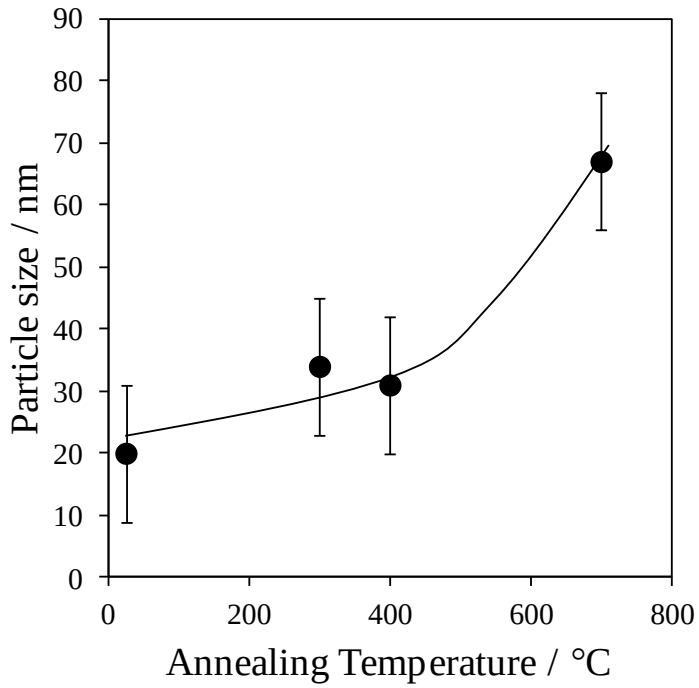


**Figure 5.4 – Variation in particle size with annealing temperature. Note that due to the very low metal loading these measurements are based on only ~50 particles, and so the error is likely to be larger than that indicated, particularly for the high temperature anneal**

## 5.2.2 *In situ* X-ray diffraction

*In situ* XRD of the as-prepared Au-Pd/$TiO_2$ material was also employed to investigate potential alloying. Powder patterns of the as-prepared sample, and those after thermal annealing in vacuo, are presented in *Figure 5.5*, in which reflections from the anatase support dominate. A weak shoulder due to the (111) reflection of a metallic Pd-containing phase is visible at approximately 39.8°, which sharpens and shifts to a lower angle with increasing temperature. No bulk Au features were detected, which is consistent with the presence of either small Au nanoparticles (< 2 nm), or a very thin Au shell.[32]

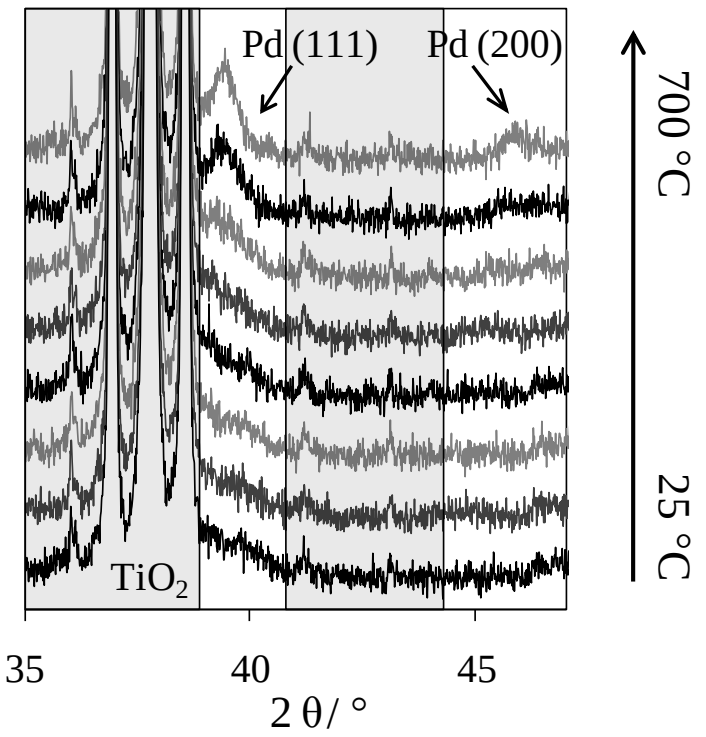


**Figure 5.5 – Powder XRD patterns for the as-prepared Au-Pd/$TiO_2$ catalyst and after subsequent in-vacuo annealing from 25 °C, 100 °C then in 100 °C intervals up to 700 °C**

Using Bragg's law (*Equation 5.3*) the shift in the Pd feature can be quantitatively related to expansion of the Pd fcc lattice parameter (*Equation 5.4*), as shown in *Figure 5.6*. The lattice parameter rises from 0.3917 nm in the fresh material to 0.3960 nm after a 700 °C anneal. Since Pd and Au are fully miscible in the solid state, the lattice parameter of their alloys can be used to directly derive an average composition, assuming a linear variance between bulk Pd and Au lattice parameters (0.39 nm and 0.4079 nm respectively).[28, 29*] The resulting calculation yields a limiting 700 °C composition of $Au_{35}Pd_{65}$, close to the stoichiometry predicted by EDX and ICP-OES bulk elemental analysis, indicating a homogeneous Au-Pd composition across all particles.

$$\lambda = 2d \sin\theta$$

**Equation 5.3 – The Bragg law**

[*] Structures were downloaded from the Chemistry Database Service at Daresbury "The United Kingdom Chemical Database Service", Fletcher, D.A., McMeeking, R.F., Parkin, D., *J. Chem. Inf. Comput. Sci.* **1996**, 36, 746

$$d = \frac{a}{\sqrt{h^2 + k^2 + l^2}}$$

**Equation 5.4 – Relationship between the distance between lattice planes and the lattice parameter for a cubic unit cell. h, k and l are Miller indices**

### 5.2.3 *In situ* X-ray photoelectron spectroscopy

The surface composition of Au-Pd nanoparticles was further assessed by XPS as a function of in-vacuo annealing. The resulting Pd:Au atomic ratios are shown in *Figure 5.6*, derived from quantifying the Pd $3d_{5/2}$ (335 eV) and Au $4f_{7/2}$ (84 eV) core-hole peak intensities, and are compared with the corresponding lattice parameters obtained from *in situ* XRD at analogous temperatures.

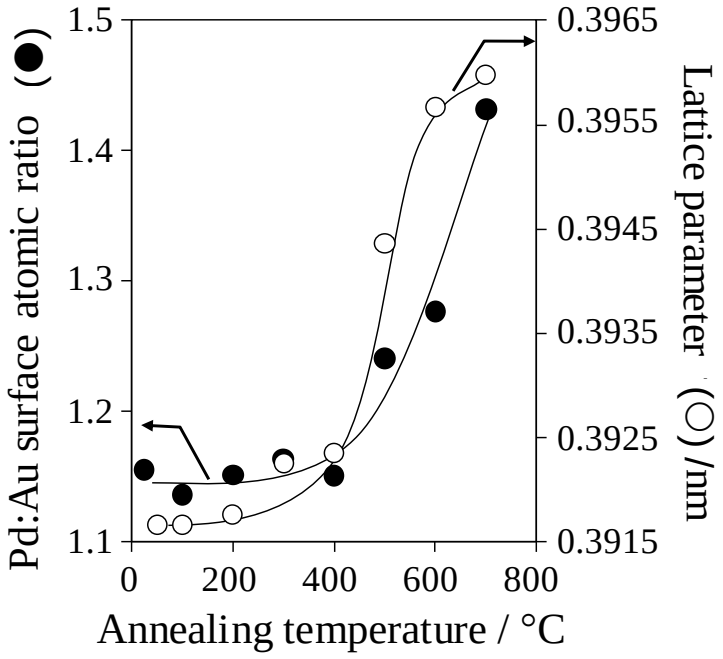


**Figure 5.6 – Pd:Au surface atomic ratios from XPS and Pd lattice parameter measurements from XRD for Au-Pd/$TiO_2$ catalyst on annealing**

Since the escape depth of palladium using conventional Mg or Al X-ray sources extends over several atomic layers, the potential exists to observe subsurface Pd from the targeted Au-shell Pd-core nanoparticles, and indeed a significant amount of Pd was

visible in the as-prepared sample. The relative Au:Pd intensities can be used to calculate the thickness of the postulated Au shell as will be described later. However, when first considering the thermal response of the Pd:Au surface atomic ratio, it is clear that the surface composition remains approximately stable until 400 °C, above which Pd surface segregation is apparent from the increased Pd:Au ratio. The onset for Pd diffusion to the nanoparticle surface coincides with the corresponding lattice expansion of the Pd nanocrystalline cores observed by XRD, consistent with Au-Pd intermixing to produce uniformly alloyed Au-Pd nanoparticles containing an estimate of 33 % Au in bulk and ~ 40 % Au in the surface. Compositions calculated using the lattice parameters shown and pure Pd and Au lattice parameters of 0.39 nm and 0.4079 nm respectively are shown in *Table 5.2*

| Temperature / °C | Lattice parameter / nm | Au bulk composition / % |
|---|---|---|
| 50 | 0.3917 | 9.3 |
| 100 | 0.3917 | 9.3 |
| 200 | 0.3918 | 9.8 |
| 300 | 0.3923 | 12.6 |
| 400 | 0.3924 | 13.2 |
| 500 | 0.3944 | 24.4 |
| 600 | 0.3957 | 31.7 |
| 700 | 0.3960 | 33.4 |

**Table 5.2 – bulk Au compositions deduced from the measured lattice parameters shown and pure Pd and Au lattice parameters of 0.39 nm and 0.4079 nm**

These structural changes are accompanied by corresponding electronic perturbation of the Au 4f (*Figure 5.7*) and Pd 3d (*Figure 5*.8) XP spectra. Previous studies of Au overlayers on Pd(111) by Goodman and co-workers reported a 0.45 eV shift in the Au 4f XP spectra to lower binding energy upon alloying, and a corresponding 0.15 eV shift to lower binding energy in the Pd 3d XP spectra.[33] E. Tysoe, although also noting a shift in the Au 4f XP spectra to lower binding energy of 0.5 eV, reported a shift to higher binding energy of 0.8 eV in the Pd 3d XP spectra.[34] It should be noted that these studies were performed on single crystals, and there are many factors that could affect the nature of this shift. Tysoe noted that complex final state effects make it very difficult to predict these shifts in binding energy on alloying. Earlier work by B. E. Koel et al. recorded little or no shift (<0.2 eV) for either metal

environment.[35] The Au 4f spectra of as-prepared Au-Pd/$TiO_2$ shown in *Figure 5.7* contain two distinct chemical environments. The dominant feature at 83.0 eV binding energy is attributed to the pure gold shell, while the weak feature at 85.6 eV likely arises from residual surface Cl from the precursor, and indeed a comparable Au 4f binding energy is observed for $HAuCl_4$ deposited on Si(100),[36] although the presence of trace $Au_2O_3$ cannot be discounted.[37] Chloride could not be detected by EDX, however it is anticipated that any such surface chloride would be at a very low concentration and more detailed XPS compositional analysis would be required to confirm its presence. Annealing induced a systematic increase in the binding energy of the majority peak component of 0.5 eV, associated with migration of gold atoms from within the pure gold shell into the Pd core and concomitant alloying. A small shift in the opposite direction to that reported by Tysoe and Goodman is seen; in this case an increase in binding energy is seen.[33, 34]

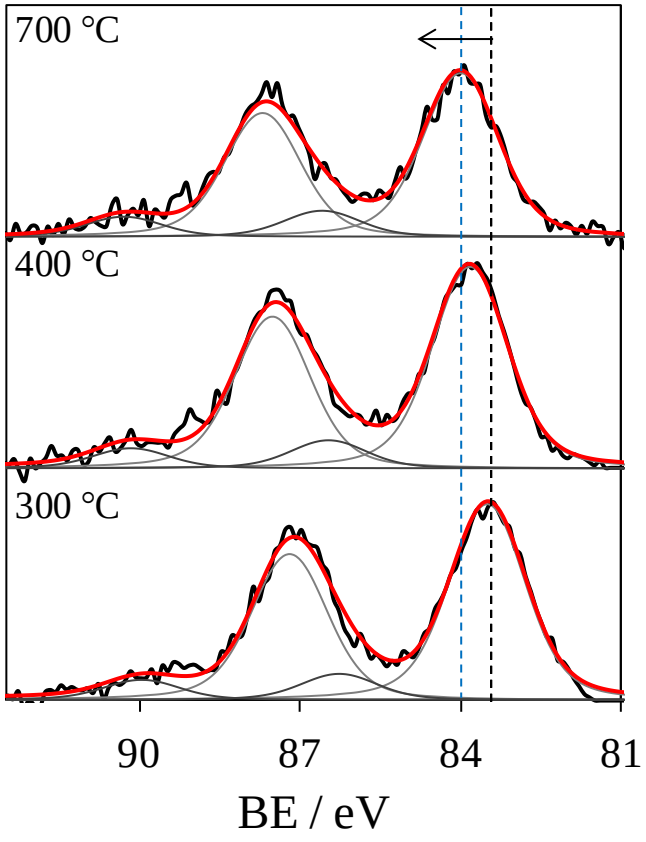


**Figure 5.7 – Au 4f XP spectra for the as-prepared Au-Pd/$TiO_2$ catalyst and subsequent annealing**

The Pd 3d XP spectra also exhibit two distinct states, the dominant feature at 334.5 eV is consistent with Pd metal,[38] while the weaker feature at 335.4 eV is most

likely attributable to electronically perturbed Pd atoms at the interface with the gold shell.[34] This second feature is unlikely to be because of PdO. The chemical shift from pure Pd metal of nearly 2 eV is between 0.5-1 eV larger than generally observed, and recorded in other chapters of this thesis. It is apparent from the evidence presented so far the Pd is likely to be encased in a thin Au-shell, and is thus not directly exposed to air for oxidation to occur. There is a shift in the Pd 3d XP spectra of 0.25 eV, to higher binding energy, after annealing the catalyst to 700 °C. In this case, Goodman has recorded a shift to lower binding energy, whereas Tysoe states that there was a shift to higher binding energy.[33, 34] It should be noted that the overlapping contribution from the Au $3d_{5/2}$ transition at ~328 eV has been removed in *Figure 5.8.* The area of the perturbed Pd component accounts for approximately 2 % of the total Pd content for the as-prepared catalyst. The contribution from this component increases upon annealing, and by 700 °C it accounts for nearly 20 %. If only 1-2 atomic layers of Pd from the 20 nm core are perturbed by the Au shell, an interlayer spacing of 0.225 nm amounts to approximately 90 atomic layers in total and thus a predicted intensity ratio of 1-2 %. On annealing, further Pd atoms are perturbed on intermixing, as would be expected.

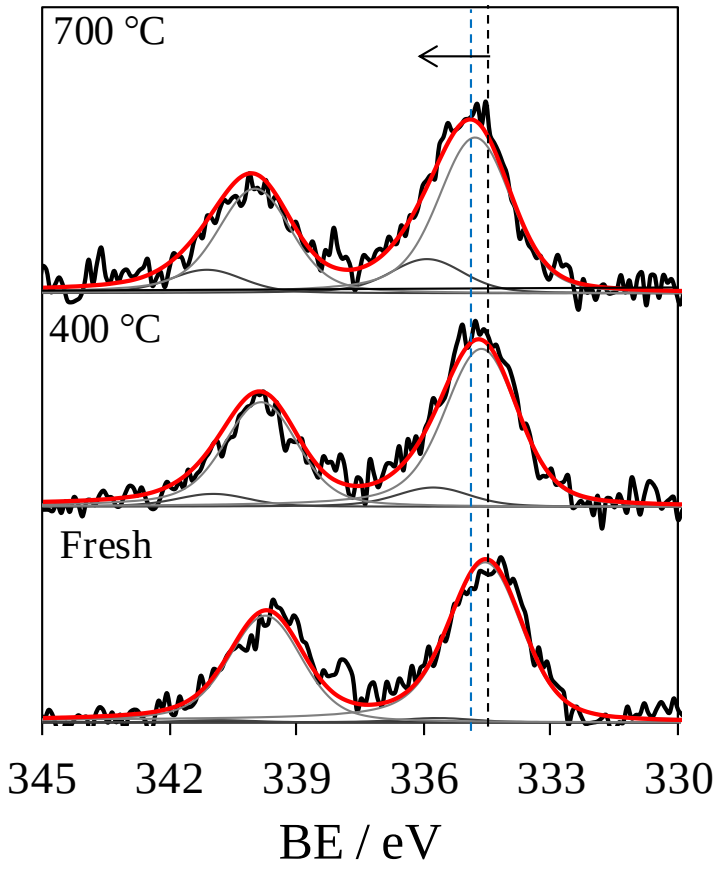


**Figure 5.8 – Pd 3d XP spectra for the as-prepared Au-Pd/$TiO_2$ catalyst and subsequent annealing**

In light of the preceding strong evidence for Au and Pd phase segregation in a core-shell structure within the as-prepared nanoparticles, the associated Au shell thickness was estimated by comparing the surface Au-Pd compositions obtained using Al $K_\alpha$ (1486.6 eV) versus Mg $K_\alpha$ (1253.6 eV) sources. The inelastic mean free path (IMFP) of photoelectrons (the distance they travel before collision) depends strongly on the energy of the exciting X-ray source due to the resultant change in photoelectron kinetic energy. This is illustrated by the universal IMFP curve in *Figure 5.9* below.[39]

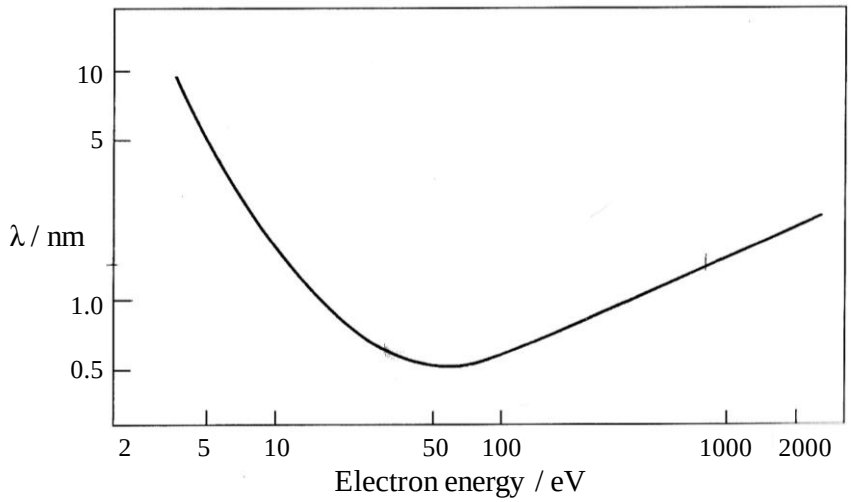


**Figure 5.9 – The relationship between the inelastic mean free path and kinetic energy of a scattered electron reproduced from reference 40**

Gold overlayers will attenuate the signal from the underlying Pd core according to the thickness of the Au layer, and the IMFP of the relevant Pd photoelectron, as described in *Equation 5.5*.

$$I_{Pd}^{Actual} = I_{Pd}^{Bulk}\, exp - \left[\frac{(n \times w)}{\lambda_{Pd} \times \cos 90}\right]$$

**Equation 5.5 – The absolute Pd 3d intensity $I_{Pd}$ for a palladium core buried beneath a capping gold film: λ is the IMFP of Pd 3d electrons, dependent on the X-ray source; n is the number of Au layers and w is the layer thickness. Cosθ = 1 because emission is normal to the surface**

In this case the intensity of bulk Pd (i.e. that expected in the absence of an Au shell) is unknown. However, it has been explained that the kinetic energy of the ejected photoelectron, and hence IMFP ($\lambda_{Pd}$), is dependent on the X-ray source. Therefore, if the Pd intensity is measured for two different photon energies then this unknown can be eliminated from the calculation. For Pd $3d_{5/2}$ photoelectrons, $\lambda_{Pd}$ was estimated at 1.12 nm from a Mg $K_\alpha$ source and the associated raw peak intensity was 53.6 cps, while $\lambda_{Pd}$ was estimated at 1.31 nm from an Al $K_\alpha$ source which gave rise to a measured intensity of 62.2 cps.[40] This information can be combined into the resulting *Equation 5.6*.

$$\frac{53.6}{62.2} = exp - \left[\frac{(n \times w)}{1.12} - \frac{(n \times w)}{1.31}\right]$$

**Equation 5.6 – Using two different X-ray sources a set of simultaneous equations can be created**

For a mean Au interlayer spacing of 0.235 nm, *Equation 5.5* can be rearranged to *Equation 5.7*:

$$\ln\frac{53.6}{62.2} = -n\left[\frac{(1.31\times 0.235)-(1.12\times 0.235)}{(1.12\times 1.31)}\right]$$

**Equation 5.7 – Assuming a Au interlayer spacing of 0.235 nm the number of Au layers can be determined**

This can be simplified as below (*Equation 5.8*) giving a value of n = 4.9. Hence the predicted Au overlayer thickness from XPS is in excellent agreement with the geometric model described in *Section 5.2.1* based upon TEM and XRD of an Au shell 5 layers thick.

$$\ln\left(\frac{53.6}{62.2}\right) = -n\frac{0.04465}{1.4672} \Rightarrow n = \frac{0.1488}{0.0304} = 4.89$$

**Equation 5.8 – The number of Au layers n is equated to be 5 layers thick**

Thermal properties of the citrate stabiliser can also be assessed by considering the *in situ* C 1s XP spectra. These are given in *Figure 5.10* and clearly show that surface citrate ligands characterised by the carboxylate component (~ 288 eV) decompose above 200 °C. Loss of citrate thus occurs below temperatures where Au-Pd intermixing commences, and so any changes in catalyst performance (discussed later), which correlate with these higher temperature structural modifications, cannot be associated with loss of the citrate stabiliser. This confirms the observations of previous literature studies which suggest that the nanoparticle stabilisers do not hinder catalyst reactivity.[24, 41, 42]

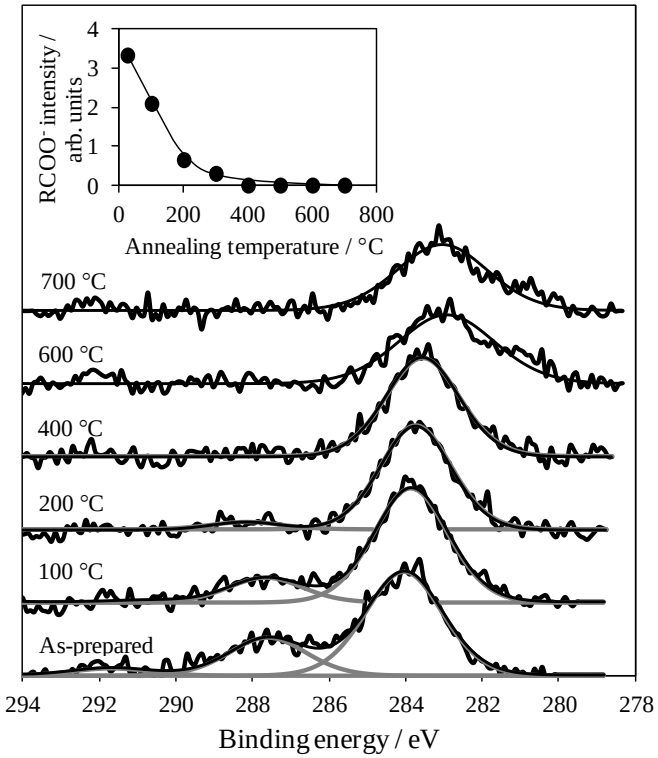


**Figure 5.10 – *In situ* temperature-programmed C 1s XP spectra of Au-Pd/$TiO_2$ catalysts as a function of annealing temperature. The integrated intensity of the carboxylate component from citrate stabiliser is shown in the inset**

## 5.2.4 *In situ* X-ray absorption spectroscopy

The structure of the $TiO_2$ supported Au-Pd nanoparticles was further probed using *in situ* X-ray absorption spectroscopy (XAS) by Prof. Adam Lee and Dr. Karen Wilson (Cardiff University) using the Daresbury SRS facility. Pd-K edge spectra were obtained for both the as-prepared particles and the particles after *in situ* annealing under inert conditions at 500 °C. Au $L_{III}$ edge measurements were acquired for the as-prepared sample only. For details on the collection of XAS data and subsequent analysis refer to *Chapter 2*.

EXAFS spectra of the as-prepared Au-Pd/$TiO_2$ are displayed in *Figure 5.11-13*.

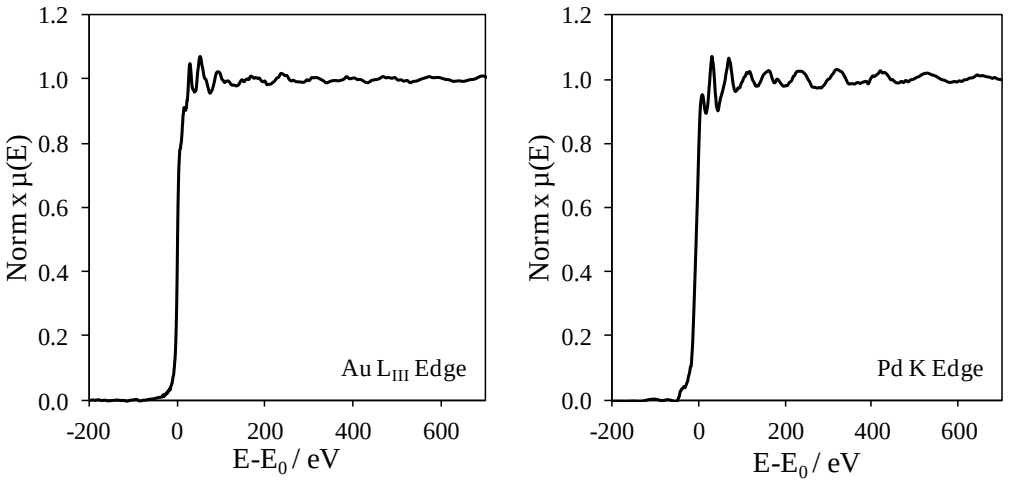


**Figure 5.11 – Au $L_{III}$ edge and Pd K Edge normalised EXAFS spectra for the as-prepared Au-Pd/$TiO_2$ nanoparticles**

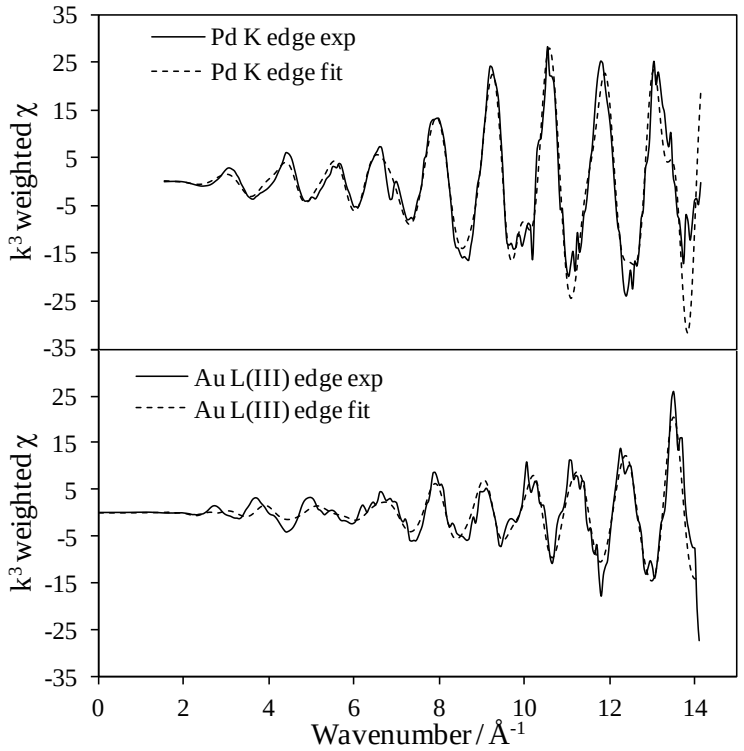


**Figure 5.12 – Au $L_{III}$ edge and Pd K Edge $k^3$ weighted $\chi$ data for the as-prepared Au-Pd/$TiO_2$ nanoparticles**

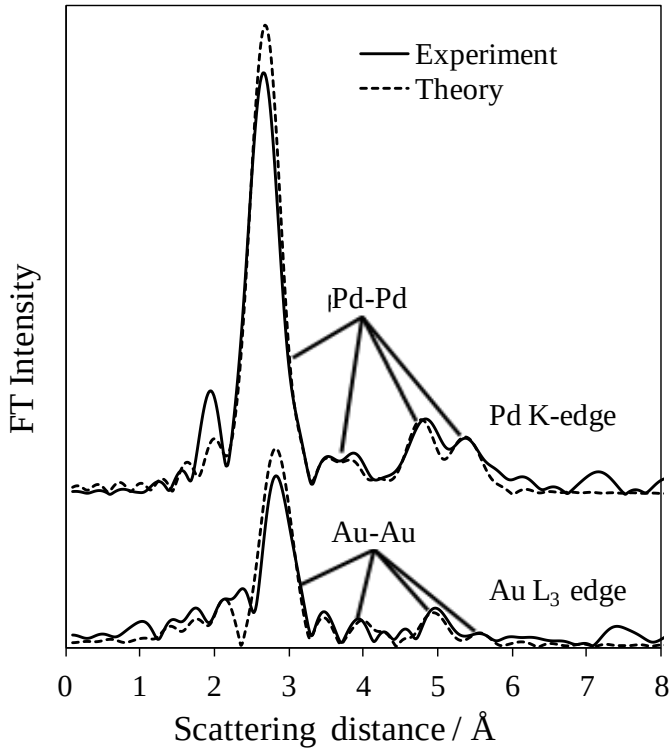


**Figure 5.13 – Fourier transform of the Au $L_{III}$ edge and Pd K Edge EXAFS data plotted in terms of the scattering distance R**

Au $L_{III}$ and Pd K-edge spectra can be fitted well to respective pure Pd and Au local environments, with the resulting parameters given in *Table 5.3*. The average Pd coordination number is consistent with a large continuous Pd core as it is comparable to the bulk Pd coordination number (12 for the first nearest neighbour). Additionally, the first nearest neighbour bond lengths, for both the Au and Pd data of 2.86 Å and 2.75 Å respectively, are in very good agreement with the monometallic species.[43-46] In a study on a Pd shell, Au core catalyst Adam Lee reported, for the as-prepared catalyst, a scattering distance of 2.86 Å for Au-Au and 2.79 Å for Pd-Pd. The latter expansion was accounted for as a consequence of a very thin Pd layer. No such perturbation has been observed for Au in the Au shell, Pd core catalyst considered here.[24]

The average Au coordination number of 8.4 is less than would be expected for continuous bulk gold. However, this observation is consistent with a high proportion of surface Au atoms, which have a lower coordination number than bulk gold, as a result of a thin Au layer. It is worth noting that, for a thin Au shell, only a small fraction of Au atoms will be coordinated to Pd. It is unsurprising, therefore, that for an averaging technique such as EXAFS this arrangement is invisible.

| Scatterers | CN1 | CN2 | CN3 | CN4 | R1 / Å | R2 / Å | R3 / Å | R4 / Å | $\sigma^2$ 1 | $\sigma^2$ 2 | $\sigma^2$ 3 | $\sigma^2$ 4 | $R^2$ |
|---|---|---|---|---|---|---|---|---|---|---|---|---|---|
| Au[a]-Au | 8.4 | 2.3 | 7.8 | 19.3 | 2.86 | 4.00 | 4.97 | 5.63 | 0.008 | 0.009 | 0.013 | 0.032 | 41 |
| Pd[a]-Pd | 12 | 6 | 24 | 12 | 2.75 | 3.86 | 4.80 | 5.41 | 0.010 | 0.020 | 0.021 | 0.012 | 30 |

**Table 5.3 – EXAFS parameters used to fit the Au $L_{III}$ edge and Pd K edge spectra for the as prepared Au-Pd/$TiO_2$ nanoparticles**

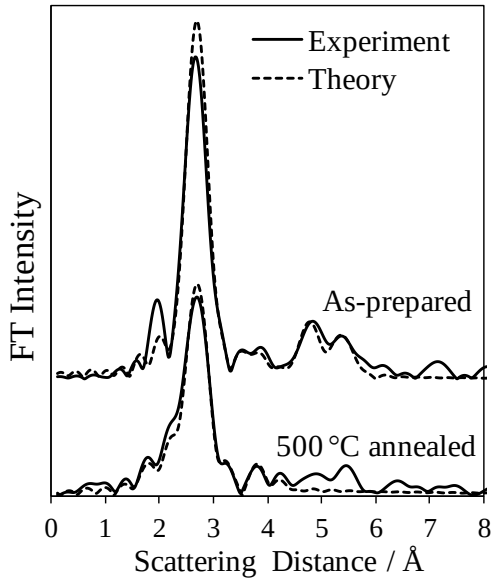


**Figure 5.14 – Comparison of the Fourier transform of the Pd K Edge EXAFS data plotted in terms of the scattering distance R for the as-prepared Au-Pd/$TiO_2$ nanoparticles and after *in situ* annealing**

These results are in agreement with the study on bimetallic Au/Pd catalysts by S. Marx et al. in which small $Au/Al_2O_3$ particles were measured and fit to a coordination number of 9.7, an Au-Au distance of 2.83 Å and a value for $\sigma^2$ of 0.0087.[47] The lower coordination number in this instance is a consequence of the small particle size of 4.4 nm, although it is worth noting that, despite this, the coordination number of Au for the bimetallic catalysts studied here is still lower. This further confirms the existence of a thin Au shell with few 'bulk' Au particles.

The Pd K-edge was measured after annealing the catalyst *in situ* under helium at 500 °C for 20 minutes. A comparison of the as-prepared and annealed spectra fit in R using a Pd fcc lattice is given in *Figure 5.14*, with the corresponding EXAFS parameters for the annealed sample shown in *Table 5.4*. The parameters for the Pd-Au pair were deduced using Daresbury Excurv98 packages by Prof. Adam Lee.

| Scatterers | CN1 | CN2 | R1 / Å | R2 / Å | $\sigma^2$ 1 | $\sigma^2$ 2 | $R^2$ |
|---|---|---|---|---|---|---|---|
| $Pd^a$-Pd | 7.4 | 4.5 | 2.77 | 3.88 | 0.012 | 0.025 | 29 |
| $Pd^a$-Au | 2.6 | 3 | 2.81 | 4.00 | 0.017 | 0.021 | 29 |

**Table 5.4– EXAFS parameters used to fit the Pd K edge spectra for the 500 °C *in situ* annealed Au-Pd/$TiO_2$ nanoparticles**

These parameters show that the average coordination number for Pd nearest neighbours is reduced upon heating, indicating that there is no longer a continuous Pd core, and is consistent with Pd-Au intermixing. In addition, the scattering distance between Pd and the first nearest neighbour Pd scatterer is 0.3 Å larger than in the as-prepared catalyst, consistent with a lattice expansion upon Au intermixing. Finally, the Pd-Au scattering pairs emerge on annealing for which the scattering distance is slightly less than that of the Au-Au pair, providing further evidence that alloying of the core-shell structure occurs after annealing at 500°C under inert conditions.

### 5.2.5 *In situ* carbon monoxide titrations

Carbon monoxide adsorbs strongly to the surfaces of metals such as palladium to such an extent that it is a common catalyst poison.[48] In fact, this is one of the sources of deactivation in the reaction considered here, as CO is a decarbonylation product of

crotonaldehyde. CO adsorption on gold is weaker,[19] which should improve catalyst performance. From UHV studies the desorption peak has been reported by Li et al. to be 120 K tailing to approximately 300 K for a 4 ML Au film on Pd (111) and 10 L CO.[34] They later also report a desorption peak value of 220 K, tailing to 320 K for an Au coverage over Pd (100) of $\theta = 0.81$.[49] Thus detection of CO adsorbed on Au at room temperature will be minimal, although very small amounts are still observed. Using CO as a titre, it is possible to identify the CO adsorption sites with *in situ* diffuse reflectance infra-red Fourier transform spectroscopy (DRIFTS).

| **ν / cm$^{-1}$** | **Site** | **Comments** | **Reference** |
|---|---|---|---|
| 2144 | Au atop | Modified by Pd | 34 |
| 2112 | | | 34 |
| 2109 | | Au/Pd alloy | 49 |
| 2092 | Pd atop | (111) terrace | 50 |
| 2086-2089 | | | 34 |
| 2085 | | | 51 |
| 2083 | | Observed at low pressure | 54 |
| 2074 | | Au/Pd alloy | 49 |
| 2069 | | | 53 |
| 2032 | | On Pd-Au | 52 |
| 1995 | Pd bridge | Pd (100) | 54 |
| 1960 | | Au/Pd alloy | 49 |
| 1955 | | | 54 |
| 1957 | | (111) terrace | 50 |
| 1951 | | | 51 |
| 1911-1934 | | | 34 |
| 1911 | | On Pd-Au | 52 |
| 1898 | | | 34 |
| < 1900 | Pd hollow | | 53 |
| 1895 | | 3-fold | 51 |
| 1875 | | (111) terrace hcp | 50 |
| 1830 | | | 53 |

**Table 5.5 – CO absorption bands and the corresponding adsorption mode on Pd, Au and Pd-Au bimetallic surfaces from experimental and model results in the literature**

Unlike XPS, this technique will probe only the topmost metal atomic layer, and as the CO vibration frequency is very sensitive to the adsorption environment (see *Table 5.5*), it will also allow the presence of Pd-Pd and $Pd_nAu$ sites to be identified. Thus, changes to the core-shell structure on annealing can be qualitatively determined.[34, 49-54]

*Figure 5.15* shows the DRIFT spectra for the as-prepared catalyst after CO exposure and also after subsequent annealing. Strong bands are present at 2015 $cm^{-1}$ and 2035 $cm^{-1}$ that have been identified as CO bound to atop palladium sites.[52] There are no features at lower wave number that are characteristic of bridged or multi-coordinate CO, which would be expected for larger palladium clusters, suggesting that these Pd atop features are likely to be associated with very small particles or isolated Pd atoms. CO adsorption on pure palladium is found to favour bridging sites over atop sites, where a more ordered, stable structure has been observed with only bridging sites occupied in some cases. The proportion of Pd atop sites that are occupied is found to vary with pressure, temperature and particle size, however.[50, 51] A weak feature observed at 2110 $cm^{-1}$ is consistent with CO adsorption on atop gold sites. CO only adsorbs atop on gold, and so it is unsurprising that no other features associated with gold are observed.[34, 55-59]

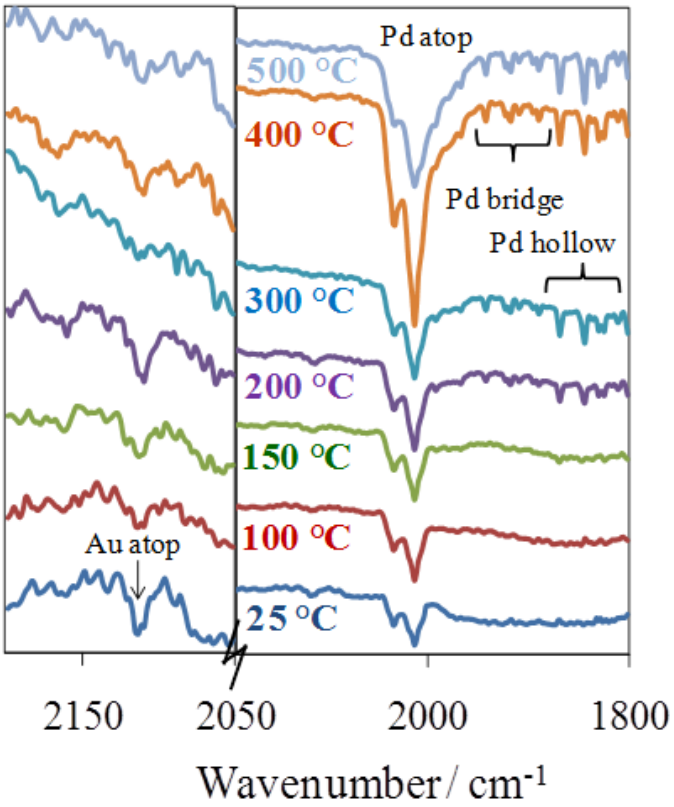


**Figure 5.15 – *In situ* DRIFTS spectra of Au-Pd/$TiO_2$ nanoparticles following exposure to room temperature CO**

Qualitative analyses of the CO features through peak area measurements observed are given in *Figure 5.16*. As the annealing temperature is increased, there is a general decrease observed for the CO atop Au feature, while the Pd atop feature increases. Additionally, Pd bridge and Pd hollow bands appear by 200 °C and increase with annealing temperature. This is in agreement with Pd intermixing with Au and also surface segregation of Pd since multi-coordinate sites become available above 200 °C. Clearly, CO DRIFTS titrations are more sensitive to the surface composition than the other techniques discussed. Changes in the surface composition are detected as low as 200 °C, although extensive alloying only occurs above 300 °C, which is consistent with predictions from single crystal studies, XPS and XRD data.[19]

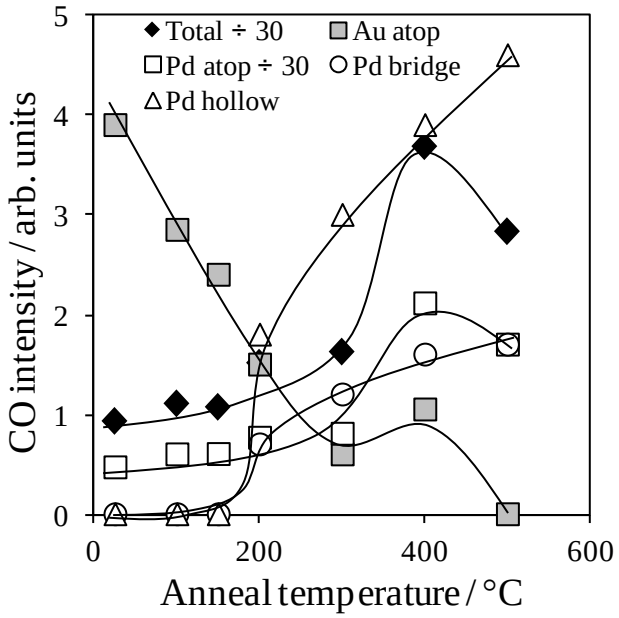


**Figure 5.16 – Qualitative plot of the intensity of CO features with annealing temperature for Au-Pd/$TiO_2$ nanoparticles associated with different adsorption sites**

The decrease in intensity observed at 500 °C for the Pd atop sites is most likely associated with the increase in particle size at this temperature (and therefore a decrease in surface area), since the total CO intensity also decreases at this temperature. This will be expanded on further below.

CO titrations using pulse chemisorption were also attempted on this catalyst *in situ*. The very low loadings and relatively large initial particle size made precise measurements difficult; however the uptake volume of CO was recorded and is given in *Table 5.6*. Up to 400 °C, at which point it has already been established that the particle

size is constant, there is an increase in CO uptake and "apparent" Pd surface area on annealing. The true surface area cannot be calculated in this way, since CO does adsorb to Au as well, albeit weakly, and the variability in the instrument measurements is sufficiently large that these results are not reliable. Nevertheless this study is consistent with an increase in surface Pd between 25 °C and 400 °C. At 600 °C and 700 °C, when there is an increase in particle size, the volume of CO uptake drops as the overall metal surface area has reduced. It is worth noting that this reduced CO uptake coincides with the decrease observed for the dominant atop feature in the DRIFTS experiment, emphasising a reduction in all types of Pd surface sites, probably due to an increase in particle size.

| Temperature / °C | Monolayer CO uptake / $x10^{-7}$ mol $g^{-1}$ |
|---|---|
| 25 | 2.12 |
| 300 | 2.24 |
| 400 | 2.67 |
| 600 | 1.92 |
| 700 | 2.54 |

**Table 5.6 – CO uptake from pulse chemisorption on Au-Pd/$TiO_2$ nanoparticles with *in situ* annealing**

## 5.2.6 Crotyl alcohol selox

The catalytic reactivity of the annealed series of core-shell nanoparticles was tested for the liquid phase selox of crotyl alcohol to crotonaldehyde. The key part of this study is to investigate the impact of catalyst surface composition on activity and selectivity. In particular, by controlled annealing of exactly the same well defined catalyst, any changes in reactivity can be directly related to the extent of intermixing of the two metals. All the reactivity data in this section has been normalised to surface catalyst weight. An additional geometric correction factor was applied using the TEM particle sizes to account for particle growth and associated decrease in metal surface area at higher annealing temperatures. Reaction profiles prior to normalisation are shown in the appendix. As discussed in *Chapter 1*, since quantum size effects are

generally observed in particles < 5 nm and these particles are > 15 nm, size is assumed not to have a significant effect on reactivity.

*Figure 5.17* reveals the correlation between initial rate and surface Au composition (annealing temperature) across the series. The gold rich surface is a poor catalyst for crotyl alcohol selective oxidation; the large particle size and Au shell exhibit bulk gold properties for which crotyl alcohol desorbs intact over single crystal studies of a 3.9 ML Au film over Pd(111).[19] Also, in accordance with the model experiments, it is apparent from *Figure 5.17* that catalyst activity increases as Pd diffuses to the surface. There is a sharp increase in both activity and selectivity above 300 °C, the temperature at which compositional changes have been detected. By 700 °C, when the surface composition is approximately $Au_{40}Pd_{60}$, the activity and aldehyde selectivity begins to plateau. These observations also coincide with the optimum Au-Pd composition determined from the model studies with more Pd rich surfaces, predicted to show lower activity.[19] It should be noted that, as the bulk composition of these nanoparticles is $Au_{40}Pd_{60,}$ by 700 °C the fully intermixed state has been reached so higher temperature anneals would not change the surface termination. Although it must be raised as a possibility, it is unlikely that the slight drop in activity is attributed to sintering for the reasons described in the previous paragraph. A study on the influence of size effects for >15 nm particles would be required to confirm this, nevertheless, the general trend of increased reactivity with increased alloying is still clear from these results.

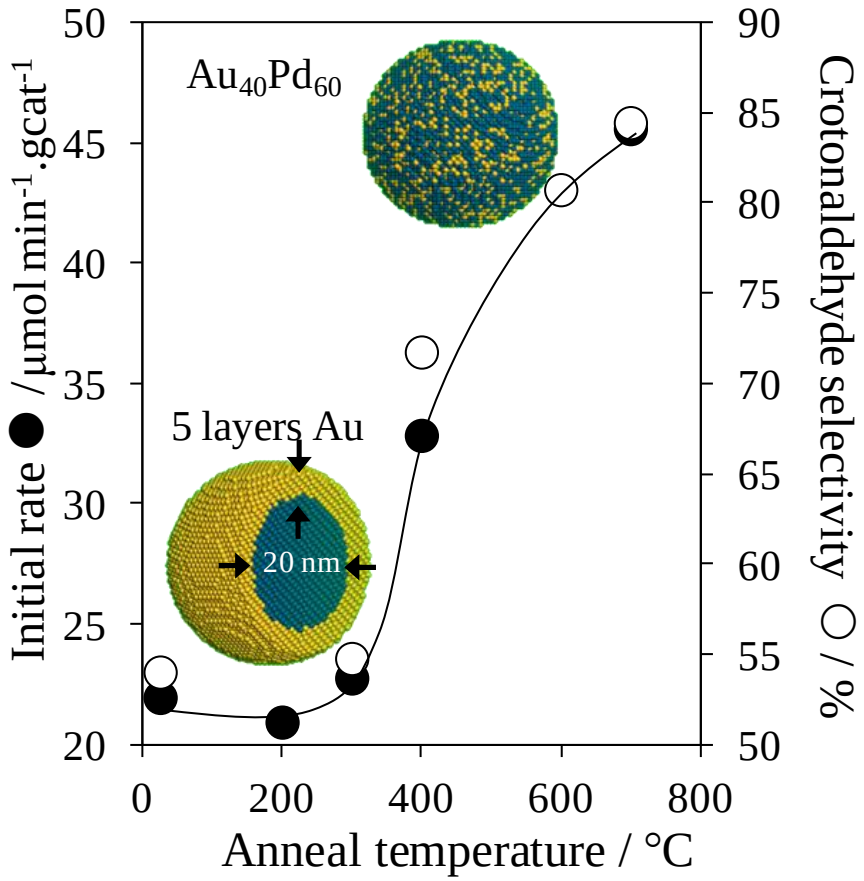


**Figure 5.17 – Surface area normalised initial rates and selectivities of crotyl alcohol aerobic selective oxidation over Au-Pd/$TiO_2$ nanoparticles as a function of annealing temperature**

The variation in selectivity towards crotonaldehyde formation shown in *Figure 5.17* can also be interpreted in terms of the alloying process. The only by-product in these reactions was butyraldehyde, with mass balances > 90 %. Catalysts with a primarily gold shell intact will essentially behave as bulk gold, since the particles are relatively large and the shell is about 5 layers thick. It is possible that these supported 'gold' films are able to catalyse the formation of crotonaldehyde, but not the dissociation of $O_2$ on the surface. It has previously been proposed that dissociated oxygen cleans the surface hydrogen formed during the reaction, preventing undesired hydrogenation of the C=C bond which results in the formation of butyraldehyde. On annealing, Au-Pd intermixing will facilitate dissociative adsorption of $O_2$ and thus selectivity to crotonaldehyde will increase by turning off C=C hydrogenation. In addition, surface oxygen has also been shown to play a key role in aiding aldehyde desorption[19] from Pd-Au alloys, which would thus prevent decarbonylation of the aldehyde as reported in *Chapter 4*.[2] The results reported here are also in line with

predictions from these model studies, where surface alloying and $O_2$ result in increased crotonaldehyde selectivity.

## 5.3 Conclusions

The focus of this chapter was to use tailored core shell Au/Pd nanoparticles to determine whether predictions from detailed UHV model investigations, which anticipated an optimum alloy composition of $Au_{40}Pd_{60}$ for crotyl alcohol selox, could be transferred to a real liquid phase catalysed process. Initially it was necessary to determine the exact composition of the catalyst series, in particular the surface composition, and subsequently assess the impact on crotyl alcohol selox.

The as-prepared catalyst has been characterised extensively and a palladium-core, gold-shell structure has been identified. Geometry calculations using HRTEM alongside elemental analysis from EDX and ICP-OES reveal a gold shell that is 5 atomic layers thick. This is further confirmed from XPS derived film thickness calculations. *In situ* XAS also confirms a core-shell structure, with the Au and Pd bond distances in the as-prepared catalyst comparable to the monometallic species. Pd coordination numbers are found to be close to bulk Pd, whereas the Au coordination number is reduced, which suggests the existence of a thin Au layer capping a Pd core.

Characterisation of catalysts annealed, under inert atmosphere to a range of temperatures up to 700 °C, confirm progressive alloying and Pd segregation. A lattice expansion was detected by *in situ* XRD, and the final lattice parameter was compared to the pure components to calculate an approximate bulk composition of 35 % Au. Further bulk analysis by XAS shows changes in coordination number and the emergence of a Pd-Au scattering pair on annealing indicative of alloying. CO titrations reveal monometallic Pd sites in the as-prepared catalyst and the onset of intermixing of the two metals at temperatures as low as 200 °C. XPS analysis shows the 700 °C annealed catalyst to have a composition of $Au_{40}Pd_{60}$, which is comparable to the surface composition predicted to be optimum for crotyl alcohol selox by model studies.

The selectivity and activity of crotyl alcohol selective oxidation is shown to increase progressively with increased alloying. As expected, activities are low on a predominantly gold surface. Selectivity to crotonaldehyde is also poor, possibly due to the build up of hydrogen on isolated Pd sites or sub-surface Pd, which could lead to

hydrogenation of the allyl bond. It would be interesting to test this composition effect further and see if activity and selectivity begin to decrease with an increasing surface palladium composition. Unfortunately, further annealing will not lead to a Pd-shell, Au-core structure, but will most likely result in more significant sintering. However, if an equivalent pre-synthesised Pd-shell, Au-core catalyst were annealed under the same conditions to similar temperatures it is proposed, from model studies, that activity and selectivity would be seen to increase with Au/Pd intermixing.[19, 22] The use of *in situ* spectroscopy to accurately characterise these core shell systems is critical to validating predictions of the optimum surface composition from model UHV studies. In summary, this work demonstrates how the rational development of catalysts with optimised performance can be achieved through tailored catalyst design and use of alloy systems.

## 5.4 References


1. C. Keresszegi, T. Burgi, T. Mallat and A. Baiker, *J. Catal.*, 2002, **211**, 244.
2. A. F. Lee, Z. Chang, P. Ellis, S. F. J. Hackett and K. Wilson, *J. Phys. Chem. C*, 2007, **111**, 18844.
3. D. I. Enache, J. K. Edwards, P. Landon, B. Solsona-Espriu, A. F. Carley, A. A. Herzing, M. Watanabe, C. J. Kiely, D. W. Knight and G. J. Hutchings, *Science*, 2006, **311**, 362.
4. A. X. Yin, X. Q. Min, Y. W. Zhang and C. H. Yan, *J. Am. Chem. Soc.*, 2011, **133**, 3816.
5. L. Piccolo, A. Valcarcel, M. Bausach, C. Thomazeau, D. Uziob and G. Berhault, *Physical Chemistry Chemical Physics*, 2008, **10**, 5504.
6. F. Wang and G. Lv, *Progress in Chemistry*, 2010, **22**, 1538.
7. A. F. Lee, J. J. Gee and H. J. Theyers, *Green Chem.*, 2000, **2**, 279.
8. C. P. Vinod, K. Wilson and A. F. Lee, *J. Chem. Technol. Biotechnol.*, 2011, **86**, 161.
9. M. Neurock and D. H. Mei, *Top. Catal.*, 2002, **20**, 5.
10. N. Dimitratos, A. Villa, D. Wang, F. Porta, D. S. Su and L. Prati, *J. Catal.*, 2006, **244**, 113.
11. G. J. Hutchings, *Chem. Commun.*, 2008, 1148.
12. P. Dash, T. Bond, C. Fowler, W. Hou, N. Coombs and R. W. J. Scott, *J. Phys. Chem. C*, 2009, **113**, 12719.
13. G. J. Hutchings, *J. Catal.*, 1985, **96**, 292.
14. M. Haruta, T. Kobayashi, H. Sano and N. Yamada, *Chem. Lett.*, 1987, 405.
15. A. S. K. Hashmi and G. J. Hutchings, *Angew. Chem.-Int. Edit.*, 2006, **45**, 7896.
16. A. Chiorino, M. Manzoli, F. Menegazzo, M. Signoretto, F. Vindigni, F. Pinna and F. Boccuzzi, *J. Catal.*, 2009, **262**, 169.
17. M. Boronat, P. Concepcion and A. Corma, *J. Phys. Chem. C*, 2009, **113**, 16772.
18. M. D. Hughes, Y. J. Xu, P. Jenkins, P. McMorn, P. Landon, D. I. Enache, A. F. Carley, G. A. Attard, G. J. Hutchings, F. King, E. H. Stitt, P. Johnston, K. Griffin and C. J. Kiely, *Nature*, 2005, **437**, 1132.

19. A. F. Lee, S. F. J. Hackett, G. J. Hutchings, S. Lizzit, J. Naughton and K. Wilson, *Catal. Today*, 2009, **145**, 251.
20. F. A. Al-Odail, A. Anastasopoulos and B. E. Hayden, *Phys. Chem. Chem. Phys.*, 2010, **12**, 11398.
21. D. I. Enache, D. Barker, J. K. Edwards, S. H. Taylor, D. W. Knight, A. F. Carley and G. J. Hutchings, *Catal. Today*, 2007, **122**, 407.
22. J. Naughton, A. F. Lee, S. Thompson, C. P. Vinod and K. Wilson, *Phys. Chem. Chem. Phys.*, 2010, **12**, 2670.
23. A. F. Lee, C. V. Ellis, K. Wilson and N. S. Hondow, *Catal. Today*, 2010, **157**, 243.
24. A. F. Lee, C. J. Baddeley, C. Hardacre, R. M. Ormerod, R. M. Lambert, G. Schmid and H. West, *J. Phys. Chem.*, 1995, **99**, 6096.
25. G. Schmid, A. Lehnert, J.-O. Malm and J.-O. Bovin, *Angew. Chem.-Int. Edit.*, 1991, **30**, 874.
26. C. J. Serpell, J. Cookson, D. Ozkaya and P. D. Beer, *Nat. Chem.*, 2011, **3**, 478.
27. R. J. Keyes, A. J. Garrett-Reed, P. J. Goodhew and G. W. Lorimer, *Intorduction to Scanning Transmission Electron Microscopy*, BIOS Scientific Publishers, Oxford, 1998.
28. H. E. Swanson and E. Tatge, *National Bureau of Standards*, 1953, **539**, 1-95.
29. J. Haglund, F. Fernandez Guillermet, G. Grimvall and M. Korling, *Physical Review, Series 3. B - Condensed Matter*, 1993, **48**, 11685.
30. X. S. Yan, P. Lin, X. Qi and L. Yang, *International Journal of Materials Research*, 2011, **102**, 381.
31. D. R. Lide, ed., *CRC Handbook of Chemistry and Physics*, 75th edn., The Chemical Rubber Publishing Company, 1994.
32. R. J. Matyi, L. H. Schwartz and J. B. Butt, *Catal. Rev.*, 1987, **29**, 41.
33. C. W. Yi, K. Luo, T. Wei and D. W. Goodman, *J. Phys. Chem. B*, 2005, **109**, 18535.
34. Z. J. Li, F. Gao, Y. L. Wang, F. Calaza, L. Burkholder and W. T. Tysoe, *Surface Science*, 2007, **601**, 1898.
35. B. E. Koel, A. Sellidj and M. T. Paffett, *Phys. Rev. B*, 1992, **46**, 7846.
36. M. Aizawa and J. M. Buriak, *J. Am. Chem. Soc.*, 2005, **127**, 8932.
37. W. A. Pireaux, M. Leihr, P. A. Thiry, J. P. Delrue and R. Caudano, *Surf. Sci.*, 1984, **141**, 221.
38. K. Noack, H. Zbinden and R. Schlogl, *Catal. Lett.*, 1990, **4**, 145.
39. E. M. McCash, *Surface Chemistry*, Oxford University Press, Oxford, 2001.
40. P. J. Cumpson and M. P. Seah, *Surface and Interface Analysis*, 1997, **25**, 430-446.
41. D. de Caro and J. S. Bradley, *New J. Chem.*, 1998, **22**, 1267.
42. P. J. Ellis, I. J. S. Fairlamb, S. F. J. Hackett, K. Wilson and A. F. Lee, *Angew. Chem.-Int. Edit.*, 2010, **49**, 1820.
43. S. H. Overbury, V. Schwartz, D. R. Mullim, W. F. Yan and S. Dai, *J. Catal.*, 2006, **241**, 56.
44. R. Zanella, S. Giorgio, C. H. Shin, C. R. Henry and C. Louis, *J. Catal.*, 2004, **222**, 357.
45. A. F. Lee, S. F. J. Hackett, J. S. J. Hargreaves and K. Wilson, *Green Chem.*, 2006, **8**, 549.
46. A. F. Lee and K. Wilson, *Green Chem.*, 2004, **6**, 37.
47. S. Marx, F. Krumeich and A. Baiker, *J. Phys. Chem. C*, 2011, **115**, 8195.

48. J. D. Grunwaldt, M. Caravati and A. Baiker, *J. Phys. Chem. B*, 2006, **110**, 25586.
49. Z. J. Li, F. Gao, O. Furlong and W. T. Tysoe, *Surf. Sci.*, 2010, **604**, 136.
50. I. V. Yudanov, R. Sahnoun, K. M. Neyman, N. Rosch, J. Hoffmann, S. Schauermann, V. Johanek, H. Unterhalt, G. Rupprechter, J. Libuda and H. J. Freund, *J. Phys. Chem. B*, 2003, **107**, 255.
51. E. Ozensoy, D. C. Meier and D. W. Goodman, *J. Phys. Chem. B*, 2002, **106**, 9367.
52. S. Devarajan, P. Bera and S. Sampath, *J. Colloid Interface Sci.*, 2005, **290**, 117.
53. D. Loffreda, D. Simon and P. Sautet, *Surf. Sci.*, 1999, **425**, 68.
54. B. Bourguinon, S. Carrez, B. Dragnea and H. Dubost, *Surf. Sci.*, 1998, **418**, 171.
55. J. D. Grunwaldt, M. Maciejewski, O. S. Becker, P. Fabrizioli and A. Baiker, *J. Catal.*, 1999, **186**, 458.
56. M. A. Bollinger and M. A. Vannice, *Appl. Catal., B*, 1996, **8**, 417.
57. F. Boccuzzi, A. Chiorino, M. Manzoli, P. Lu, T. Akita, S. Ichikawa and M. Haruta, *J. Catal.*, 2001, **202**, 256.
58. F. Boccuzzi, A. Chiorino, S. Tsubota and M. Haruta, *Journal of Physical Chemistry*, 1996, **100**, 3625.
59. Y. Denkwitz, B. Schumacher, G. Kucerova and R. J. Behm, *J. Catal.*, 2009, **267**, 78.

# Chapter 6

# The deactivation of industrial Pd/C catalysts for liquid phase selective nitrile hydrogenation

## 6.1 Introduction

In the previous three chapters, catalyst design and structure is considered as a means for improving the productivity of a relatively simple selective oxidation reaction. In this chapter, a more complex, problematic reaction will be explored over a single commercial Pd/C catalyst, which is used industrially for the hydrogenation of nitriles, but cannot be recycled due to significant deactivation. The aim of this chapter is to identify the source of deactivation and to consider how the approach of catalyst design could be employed to create a selective, recyclable catalyst.

The application of nitrile hydrogenation reactions and the production of primary amines are reviewed in *Chapter 1*. The reaction considered here, the selective hydrogenation of benzyl cyanide to 2-phenylethylamine (PEA), is a model for a reaction used by industry for which the Heraeus Pd/C catalyst deactivates after one cycle. Although PEA is the desired product, strong product adsorption to the catalyst surface is thought to lead to the formation of the secondary amine bis-(2-phenylethyl)amine (BPEA) and poisoning of the active site resulting in deactivation, as shown in the reaction scheme in *Scheme 6.1*.[1, 2] Another possible side reaction includes the cleavage of the C-N bond leading to the formation of ethyl benzene. One solution to the formation of the secondary amine, that will also minimise ethyl benzene formation, is the addition of acid to protonate the primary amine so that it can be removed as a salt. Data for reaction of the aromatic nitrile without acid, was provided by Rachel Donker at Syngenta, and shows only 17 % product conversion compared with complete conversion when the reaction is performed in the presence of sulphuric acid.[3, 4]

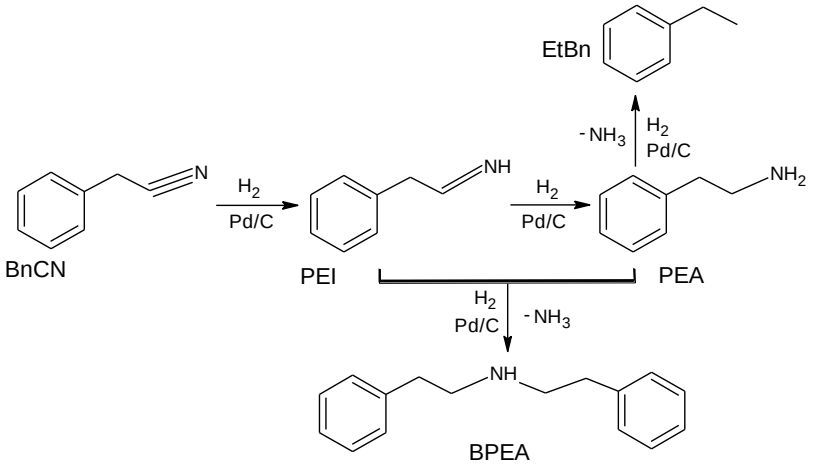


**Scheme 6.1 – Proposed reaction scheme of benzyl cyanide hydrogenation to phenylethylamine (PEA) via phenylethylimine (PEI) and dimerising to bis-(2-phenylethyl)amine (BPEA)**

Addition of stoichiometric quantities of sulphuric acid is commonly used in industry for the production of aromatic amines. However, even if potential poisoning by the primary amine has been eliminated, catalyst deactivation is still a significant problem, with only one reaction cycle possible. An equivalent reaction, used by Syngenta for the production of hydroxyl-functionalised aromatic amines from cyanohydrin hydrogenation in the presence of sulphuric acid, gave a product yield of 59.1 % using the fresh Pd/C catalyst, and only 39.7 % after reusing the catalyst.[*5] This chapter aims to identify the source of deactivation, and assess potential routes to enhance catalyst performance.

Deactivation due to chemical poisoning and changes to the physical structure are both potential problems.[6] There is literature evidence that suggests chemical poisoning due to adsorption of N and S species can be the origin of catalyst deactivation. Pd/C catalysts used for the synthesis of the compound N-(4-amino-2-methoxyphenyl)acetamide, were found to deactivate as a result of surface accumulation of this species, and not from poisoning by low concentration sulphur species, or structural changes to the Pd catalyst.[7] Detailed first principle calculations of the interaction of sulphur with Pd surfaces reveal that even a relatively low coverage of sulphur is sufficient to prevent hydrogen adsorption.[8] The application of bi- and tri-metallic catalysts, including Au, Co and Ni doped Pd-Pt catalysts and Rh-Pt or Rh-Pd, have been found to improve against sulphur poisoning.[9-11] The interaction of amine with the surfaces of bimetallic catalysts is clearly significant: Huang et al. record examples of

[*] Data courtesy of Syngenta

Ni and Cu catalysts, doped with Ru, Rh, Pd and Pt, both improving and retarding acetonitrile and butyronitrile reactivity. In particular they note the selectivity dependence of the catalyst ensemble towards secondary amine formation.[12] A thorough investigation of the catalyst physical structure and surface composition is therefore necessary in order to investigate sources of deactivation in nitrile hydrogenation.

Initially, the structural properties and composition of the fresh catalyst will be outlined, including analysis of the palladium particle size, support porosity and the catalyst surface composition. The reaction of benzyl cyanide hydrogenation in the absence of acid is then analysed to clearly identify all side reactions that may occur. The structural properties and surface composition of the spent catalyst is then extensively characterised. A series of acid pre-treatments on the catalyst are used to understand the impact of sulphuric acid on the catalyst physical properties and the surface composition. Finally, the conclusions drawn from this investigation are discussed in the light of the catalyst design work from the previous three chapters, and some improvements to the catalytic system investigated in this chapter are proposed.

## 6.2 Results and discussion

### 6.2.1 Fresh catalyst characterisation

#### 6.2.1.1 Microscopy and particle size analysis

The fresh Pd/C catalyst was analysed using transmission electron microscopy (TEM). *Figure 6.1* shows the low resolution and high resolution (insert) micrographs on the left and a particle size histogram on the right. It is clear from the images that particle morphology is irregular, thus it is likely that the particles comprise a combination of Pd(111) and Pd(100) low energy facets. Size analysis reveals a broad Gaussian distribution with a size range from 2-20 nm and a relatively large mean size of 6.3 nm and a mode of 4 nm.

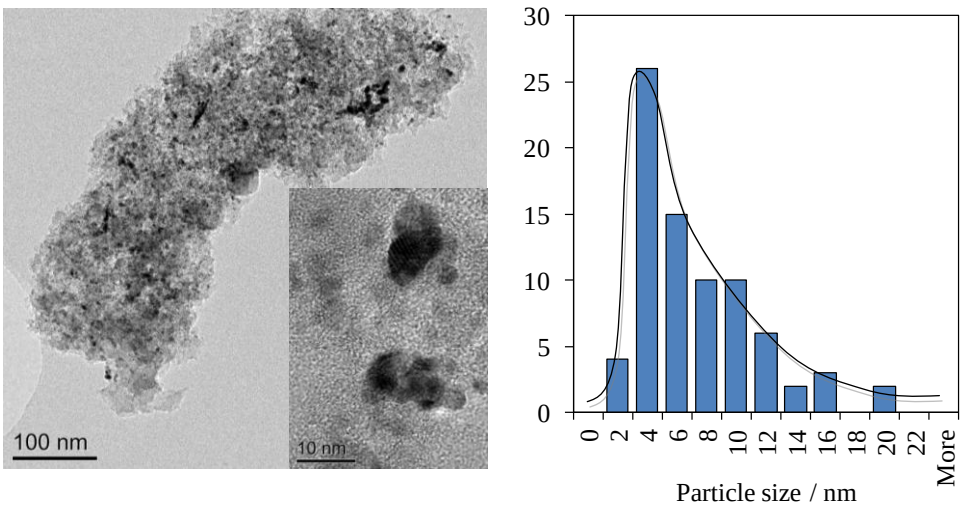


**Figure 6.1 – TEM and HRTEM (insert) of fresh 5 wt% Pd/C Heraeus catalyst (left) and particle size distribution (right)**

Since TEM is a localised technique, further size analysis was performed using X-ray diffraction (XRD) and CO chemisorption titrations. The powder pattern of the Pd/C fresh catalyst is given in *Figure 6.2*. The poor background is attributable to the amorphous carbon support. The Pd reflections for Pd(111) at 40.05° and Pd(200) at 46.6° are highlighted by *. It is possible the sharp reflection at 43.0° is due to graphite (expected graphite reflections indicated by †), although there is no reflection at 26.6°. This may be obscured by the background if there is only a small amount of graphite present. Neither this reflection, nor the remaining unidentified reflections (•) are due to PdO for which there should be reflections at 33.26°, 34.36° and 42.86°.

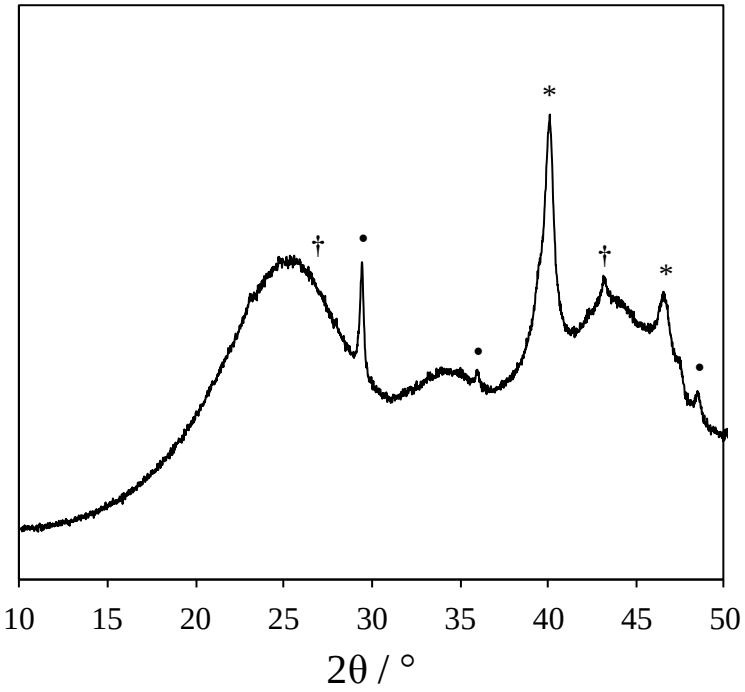


**Figure 6.2 – XRD pattern of fresh 5 wt% Pd/C Heraeus catalyst**

The Pd reflection is slightly asymmetric, which may reflect the broad size distribution, or this shoulder may be due to another peak. Scherrer analysis (see *Chapter 2* and *Chapter 3* for details) was used to determine particle size from the Pd(111) reflection at 40.05 °. This result is tabulated alongside chemisorption and TEM size analysis in *Table 6.1*. Considering the broad size distribution, the average particle size from the three techniques agree well. The results from XRD are unsurprisingly dominated by the larger particles. This may partly be due to the asymmetric peak shape, the irregular particle morphology and also the limits of the instrument to detect the smallest particles. The smallest particles will not be detected by powder XRD analysis.[13] Such a broad size distribution and relatively large particle size is undesirable for catalytic applications, particularly as it leads to inhomogeneity in the catalyst batch and thus a large variation in reactivity from batch to batch.

| Technique | Particle size / nm |
|---|---|
| CO Chemisorption | 8.6 |
| XRD | 12.3 |
| TEM | 6.4 |

**Table 6.1 – Particle size analysis using different techniques on 5 wt% Pd/C fresh Heraeus catalyst**

### 6.2.1.2 Nitrogen porosimetry

The surface of area of the catalyst and porosity of the carbon support was assessed using nitrogen porosimetry. Details of the total surface area, mesopore area and micropore area using the Brunauer, Emmett and Teller (BET) isotherm, Barrett, Joyner and Halenda (BJH) isotherm and t-plot micropore analysis respectively, alongside the average mesopore diameter, calculated using BJH theory, are listed in *Table 6.2*. The mesopore size distribution and pore volume from BJH theory are also shown in *Figure 6.3*. The adsorption/desorption isotherm is shown in the insert of *Figure 6.3*, and is type IV, typical for microporous and mesoporous solids.[14] Details of these isotherms are given in *Chapter 2*.

| | |
|---|---|
| BJH surface area | 187 $m^2$ $g^{-1}$ |
| t-plot micropore area | 392 $m^2$ $g^{-1}$ |
| BET surface area | 678 $m^2$ $g^{-1}$ |
| Pore diameter | 3.44 nm |

**Table 6.2 – Quantitative surface area analysis from nitrogen porosimetry on fresh 5 wt% Pd/C Heraeus catalyst**

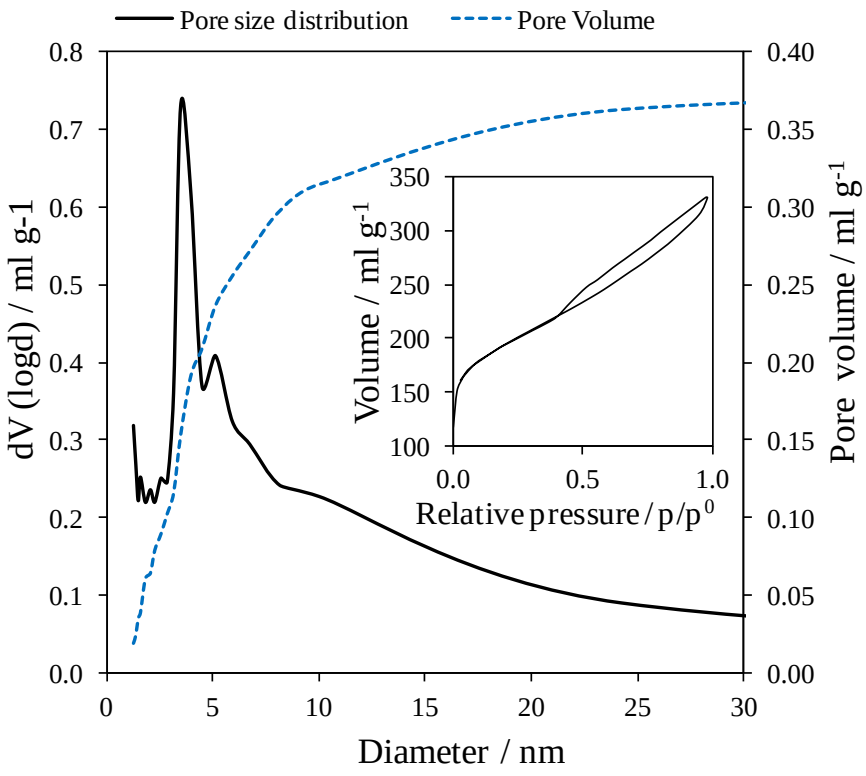


**Figure 6.3 – BJH isotherm mesopore size distribution for the fresh 5 wt% Pd/C Heraeus catalyst**

The majority of the porosity in this catalyst is due to the micropores. Additionally, an average mesopore diameter of 3.4 nm is small and also significantly less than the Pd particle size. This implies that Pd distribution will be poor and predominantly on the external surface of the catalyst support.[15, 16] Microporosity is also unfavourable for liquid phase reactions, due to limitations in mass transport and pore blocking from large molecules. The build up of molecules blocking pores in the carbon support may also affect the longevity of the catalyst.[14]

#### 6.2.1.3 Compositional analysis*

The catalyst composition was characterised using energy dispersive X-ray spectroscopy (EDX), inductively coupled plasma optical emissions spectroscopy (ICP-OES) and X-ray photoelectron spectroscopy (XPS). The bulk composition from EDX single point analysis was 3 ±1 wt% Pd, and from ICP-OES was 2.96 wt%. For a nominal weight loading of 5 wt% these results show that there is a large variation in the metal weight loading, reflecting poor dispersion and homogeneity. Surface compositions by XPS are given in *Table 6.3*. Clearly, there is twice as much palladium as predicted by the nominal weight loading. This may be due to a greater distribution of Pd on the surface of the support as indicated in the previous section, and is quite a common occurrence in Pd/C catalysts.[15-17]

| Oxygen / wt% | Carbon / wt% | Palladium / wt% |
|---|---|---|
| 4.71 | 84.03 | 11.26 |

**Table 6.3 – Surface compositions of fresh 5 wt% Pd/C Heraeus catalyst**

The C 1s and Pd 3d XP spectra are given in *Figure 6.4*. The carbon spectrum is dominated by a peak due to the amorphous carbon support, although a small amount of ether/alcohol functionality is visible. All spectra were charge corrected to adventitious carbon at 285 eV.[17] A significant amount of oxide is present in the Pd region assigned to

* Databases used throughout this section: *NIST X-ray Photoelectron Spectroscopy Database*, Version 3.5 (National Institute of Standards and Technology, Gaithersburg, 2003) http://srdata.nist.gov/xps, Accessed 13/03/2012; R. Benoit, *La Surface*, http://www.lasurface.com/accueil/index.php, Date accessed: 13/03/2012

the peak at 337.5 eV.[18] This equates to 25.8 wt% PdO. Since no PdO was detected by XRD this is most likely due to surface oxide.

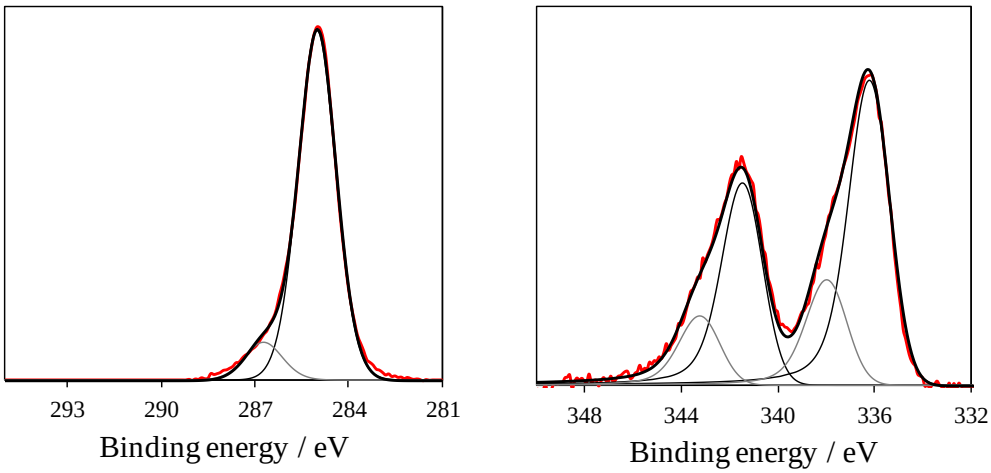


**Figure 6.4 – C 1s XP spectrum (left) and Pd 3d XP spectrum (right) of fresh 5 wt% Pd/C Heraeus catalyst**

## 6.2.2 Benzyl cyanide hydrogenation

The hydrogenation of 8.4 mmol benzyl cyanide with 200 mg of Pd/C catalyst was tested using methanol as a solvent at 1 – 2.5 bar hydrogen and 20 – 50 °C, to study the reaction products and kinetics by gas chromatography mass spectrometry (GCMS). The chromatographs of the initial solution and the reaction mixture after 6 hours are shown in *Figure 6.5*. The peak at 3.88 minutes is from mesitylene (structure indicated in the figure), used as an internal standard in this experiment. The peak at 5.09 minutes is from benzyl cyanide reactant. The principal product detected is ethyl benzene. This can be confirmed by comparing the mass spectra of the product indicated in the 6 hour chromatograph and that of ethyl benzene, shown in *Figure 6.6a*. Surprisingly, no BPEA formation is observed. From the insert in *Figure 6.5* it is apparent that a small amount of PEA is detected. Once again, the identity of this peak can be confirmed by comparing the mass spectra in *Figure 6.6b*. The identity of X, Y and Z has not been determined. X is an impurity present in the benzyl cyanide reagent, which is consumed or adsorbed after 10 minutes of reaction. It is possible Y and Z are products of this impurity, since the retention time of all three are very similar. The mass spectra, displayed in *Figure 6.7*, show a peak at 91 g $mol^{-1}$ for all three components, implying that the three species

are aromatic. It has been confirmed, by comparing with standards, that they are not phenylacetamide or phenyl ethanol. The prominent mass ion in X with m/z 117 g $mol^{-1}$ implies that this species contains nitrogen functionality, however further assignment cannot be determined from the information presented here.

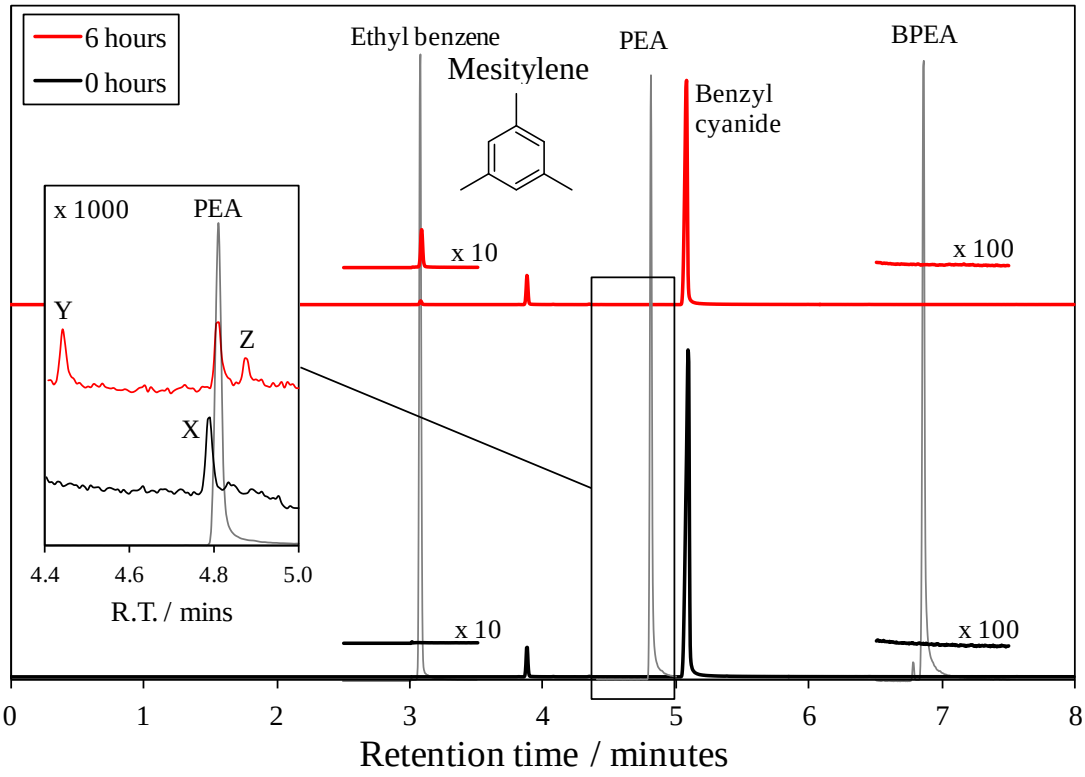


**Figure 6.5 – GCMS chromatographs for reaction of 8.4 mmol benzyl cyanide at 21 °C and 2 bar $H_2$ over 5 wt% Pd/C**

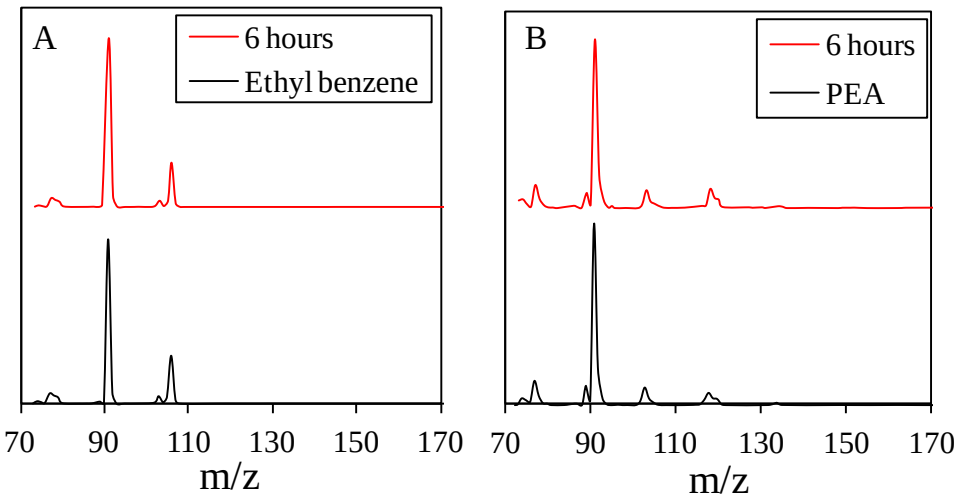


**Figure 6.6 – mass spectra for ethyl benzene standard and product peak at 3.08 minutes after 6 hours reaction (a) and PEA standard and product peak at 4.82 minutes after 6 hours reaction**

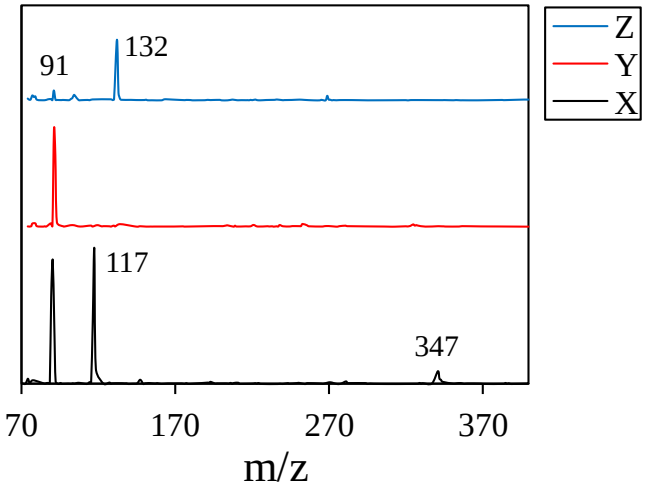


**Figure 6.7 – mass spectra for unknown impurity A (4.79 minutes) in initial reaction solution and unknown products B and C (4.44 minutes and 4.87 minutes respectively)**

The conversion of benzyl cyanide at 21 °C using a range of hydrogen pressures is displayed in *Figure 6.8*. Conversion after 6 hours equates to around 45 % and, under these conditions, is independent of hydrogen pressure.

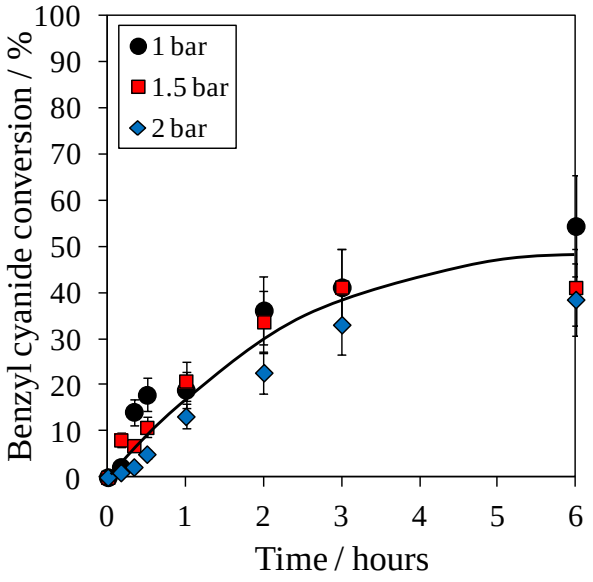


**Figure 6.8 – Reaction profiles for 8.4 mmol benzyl cyanide hydrogenation at 21 °C over 5 wt% Pd/C**

A pseudo first order reaction has therefore been assumed, in order to calculate the activation energy of benzyl cyanide hydrogenation over this catalyst under these conditions. Initial rates were measured over the first hour of reaction during the linear

part of the reaction profile for the reaction carried out at 21 °C, 30 °C, 40 °C and 50 °C. Reaction profiles for all four temperatures are displayed in *Figure 6.9* and the extracted rates are given in *Figure 6.10*. The Arrhenius plot is shown in *Figure 6.11*. The exclusion of the 30 °C data point, due to the poor quality of the data, merely changed the energy barrier value by 1 kJ $mol^{-1}$, which is less than the error determined from performing multiple reactions.

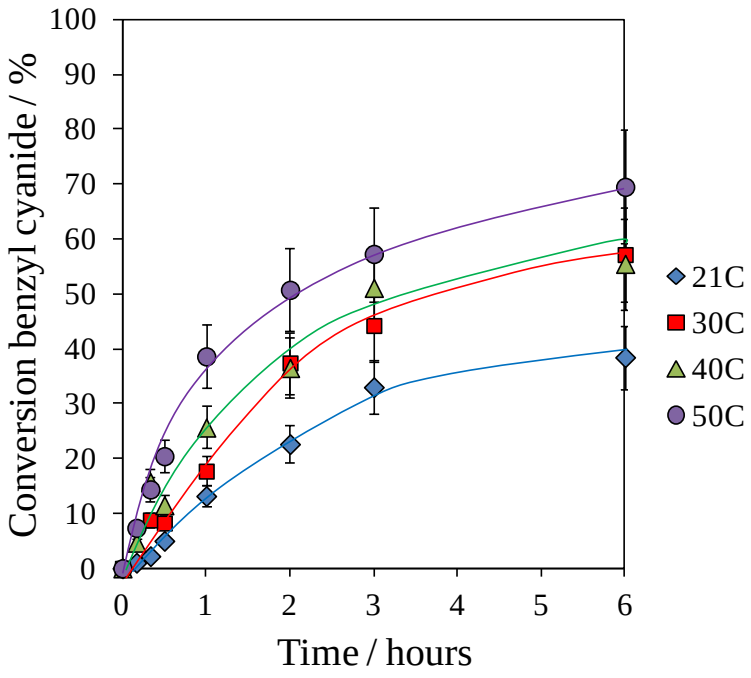


**Figure 6.9 – Reaction profiles showing the temperature dependence of benzyl cyanide conversion using 200 mg Pd/C under 2 bar $H_2$**

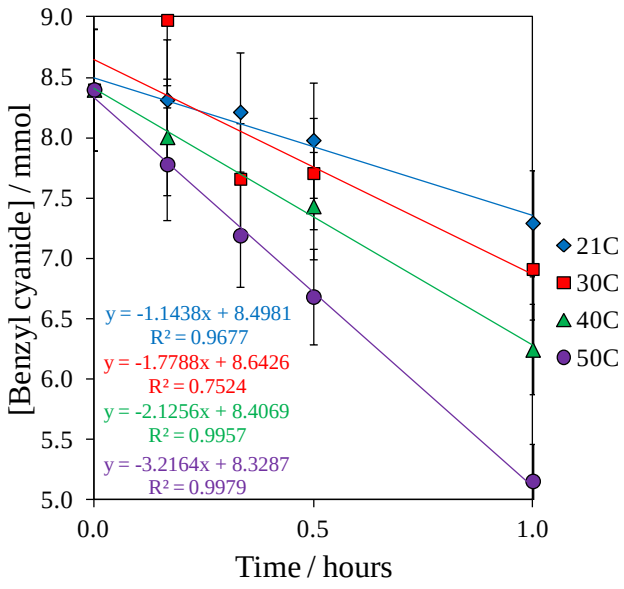


**Figure 6.10 – Initial rates measurements over the first hour of reaction of benzyl cyanide hydrogenation over 200 mg Pd/C at 2 bar $H_2$**

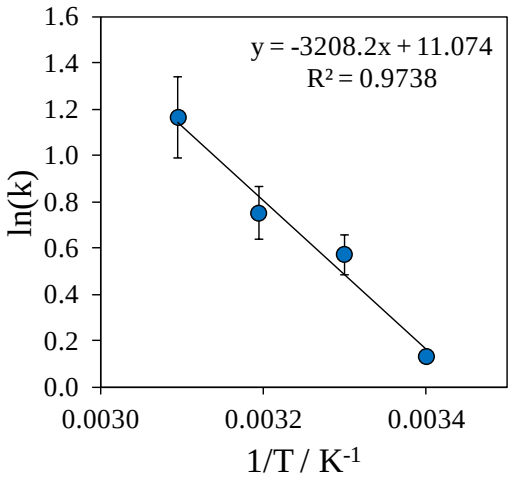


**Figure 6.11 – Arrhenius plot used to calculate activation energy of benzyl cyanide hydrogenation over Pd/C under 2 bar hydrogen**

An activation barrier of approximately 26 ±4 kJ $mol^{-1}$ was determined for benzyl cyanide hydrogenation in this reaction. This is lower than examples of activation barriers in the literature for nitrile hydrogenation over Ni and Co catalysts: S. P. Bawane et al. calculate an energy barrier of 60.27 kJ $mol^{-1}$ for benzonitrile hydrogenation over Raney© Nickel and B. Bigot and collaborators report an activation

energy of 46 kJ $mol^{-1}$ for acetonitrile hydrogenation over a boron doped Co catalyst.[19, 20] The lower energy barrier indicates that the benzyl cyanide reduction over Pd/C is easier than the two given examples, implying a more active catalyst, but also suggesting that the other reaction pathways outlined in *Scheme 6.1* are more facile, so the catalyst is potentially less selective. In fact, as discussed in *Chapter 1*, primary amine formation is favoured over Ni and Co catalysts, whereas the further dimerisation to secondary amines is preferred over Pd catalysts.[21]

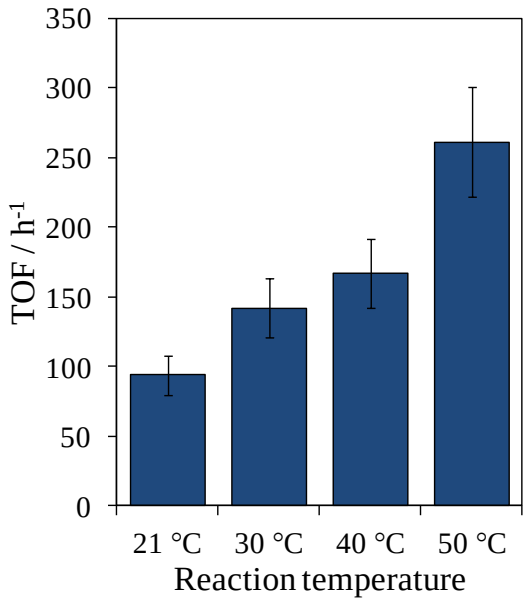


**Figure 6.12 – Turn over frequencies for 8.4 mmol benzyl cyanide hydrogenation at 2 bar $H_2$ pressure**

Turn over frequencies (TOFs) for the reaction at four temperatures are given in *Figure 6.12*. These were calculated based on dispersions of 13 % from CO chemisorption. These values are lower than what is generally found in the literature for nitrile hydrogenation reactions under a variety of conditions. G. D. Yadav et al. calculate a TOF of 8460 $h^{-1}$ for benzonitrile hydrogenation over $Ni/SiO_2$.[22] Benzonitrile hydrogenation was found to have a TOF of 5000 $h^{-1}$ and 46 % conversion over $Pd/SiO_2$ by O. Dominguez-Quintero and co-workers for reaction carried out at 145 °C and 120 psi.[23] Finally, a TOF of 1326 $h^{-1}$ has been reported for benzonitrile hydrogenation over $Pd/\gamma\text{-}Al_2O_3$ compared with 66 $h^{-1}$ over an equivalent iridium catalyst at 100 °C under 300 psi $H_2$.[24] Apart from the Ir catalyst, all these values are considerably higher than the results obtained here, although it is worth noting the high temperatures and hydrogen pressures. In addition, the authors do not report dispersion measurements and calculate

TOF in terms of moles of metal. It must also be noted that metal surface area and mass transport effects could significantly alter the values reported here.

In order to further explore the kinetics of this reaction and confirm these results it would be necessary to consider the effect of changing benzyl cyanide concentration; the catalyst:substrate ratio; the molar quantity of hydrogen, where it can be confirmed that the system is not saturated with $H_2$; and mass transport limitations. This work is beyond the scope of this study on the catalyst deactivation, but may provide more insight into the catalyst mechanism for this reaction and the observed selectivity.

## 6.2.3 Catalyst deactivation

### 6.2.3.1 Product formation

Having characterised the catalyst and considered the reaction scenario, it is now possible to investigate the sources of catalyst deactivation including structural changes and chemical poisoning. The identity and fate of the reaction products will be considered first. *Figure 6.13* shows the consumption of benzyl cyanide and formation of ethyl benzene and PEA at 21 °C and at 50 °C.[*]

[*] It is important to note at this point that these were the products detected and confirmed by GCMS. Later in the chapter the possibility of toluene formation is considered. The reaction chromatograph reveals that ethyl benzene is detected immediately after electron ionisation is turned on at 3 minutes. Before this the detector is saturated by the solvent, thus, although toluene may form, this could not be confirmed by GCMS.

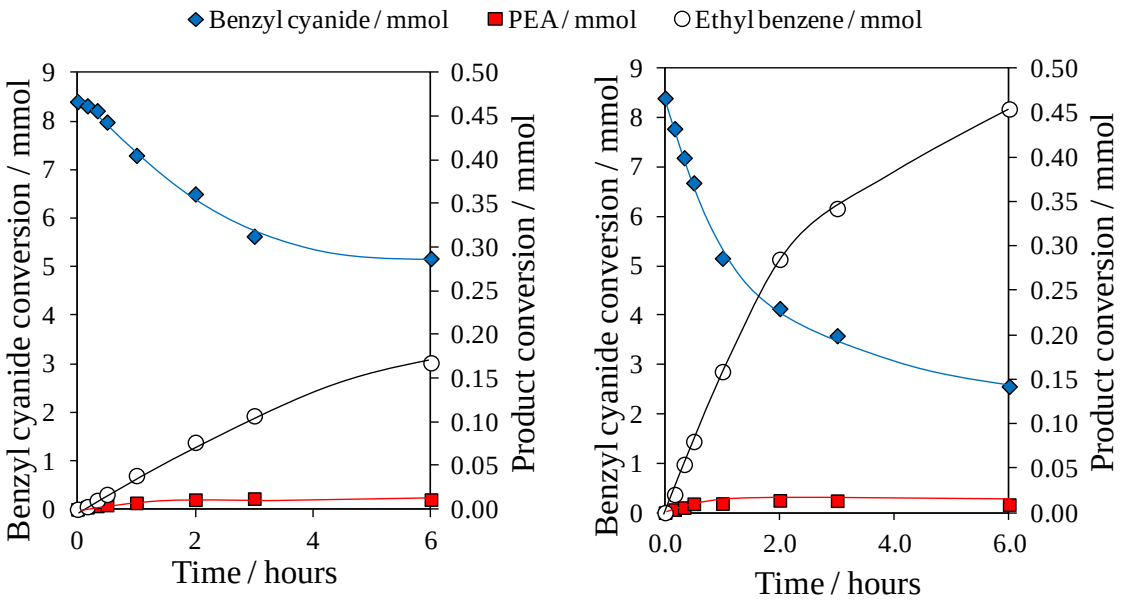


**Figure 6.13 – Benzyl cyanide consumption and product formation for 8.4 mmol benzyl cyanide hydrogenation under 2 bar $H_2$ over 200 mg of 5 wt% Pd/C at 21 °C (left) and 50 °C (right),**

Conversion by 50 °C has increased by about 20 %, there is over 2.5 times more ethyl benzene formed, however the same amount of PEA is detected, only 0.01 mmol. This variation in selectivity is also illustrated in *Figure 6.14*. Selectivity was calculated as a percentage of the amount of conversion of benzyl cyanide since the poor mass balance (see below) indicates that not all the products have been accounted for. This calculation shows that, not only is there an increase in activity of the catalyst by 50 °C, resulting in increased ethyl benzene yield, but the selectivity of the reaction towards ethyl benzene formation also increases with temperature. There is no change in PEA selectivity with temperature. The increase in selectivity towards ethyl benzene must also be at the expense of the selectivity of other products, even if these are not detected by GCMS, such as adsorbed primary and secondary amine.

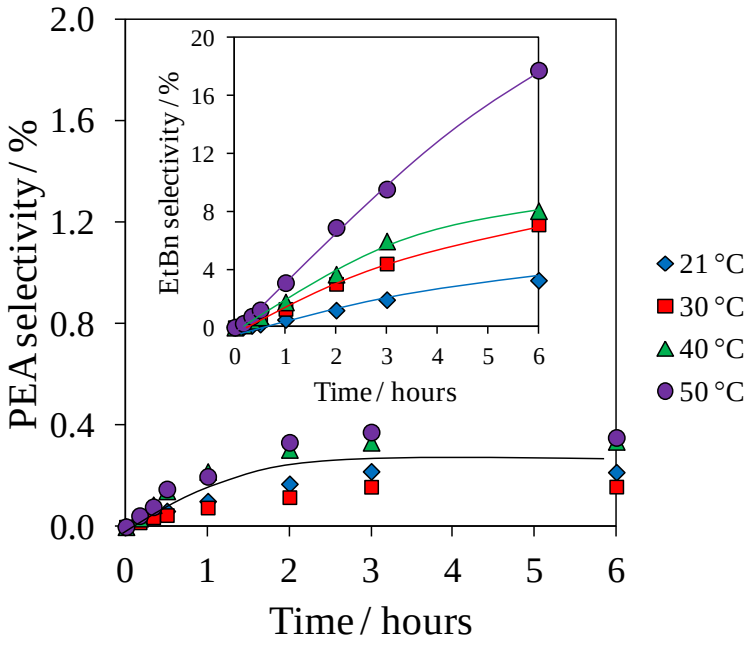


**Figure 6.14 – Estimated PEA and ethyl benzene (EtBn) selectivities calculated from the ratio of each species to benzyl cyanide**

Additionally, the mass balance of the reaction at 21 °C after 6 hours was only 63 %. By 50 °C the mass balance was as low as 36 %. Some of this drop in mass balance with temperature may be due to evaporation, but since all the identified species in the reaction have boiling points > 100 °C, it is unlikely that evaporation accounts for a 50 % reduction in the mass balance over 30 °C. The substrate:Pd ratio is low at approximately 180:1, thus there is a large catalyst surface area available for adsorption. Characterisation of the spent catalyst surface is therefore employed to determine the identity and fate of the remaining products.

### 6.2.3.2 Transmission electron microscopy

The spent catalyst after reaction at 40 °C has been analysed by TEM for size analysis. An example micrograph is shown in *Figure 6.15* and the particle size histogram is given, alongside that of the fresh catalyst in *Figure 6.16.*

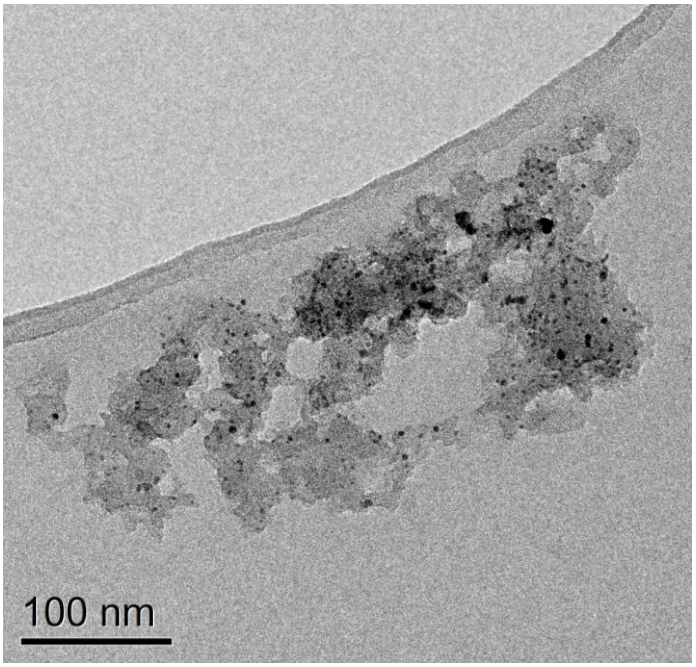


**Figure 6.15 – TEM image of spent 5 wt% Pd/C after reaction with 8.4 mmol benzyl cyanide at 40 °C under 2 bar $H_2$**

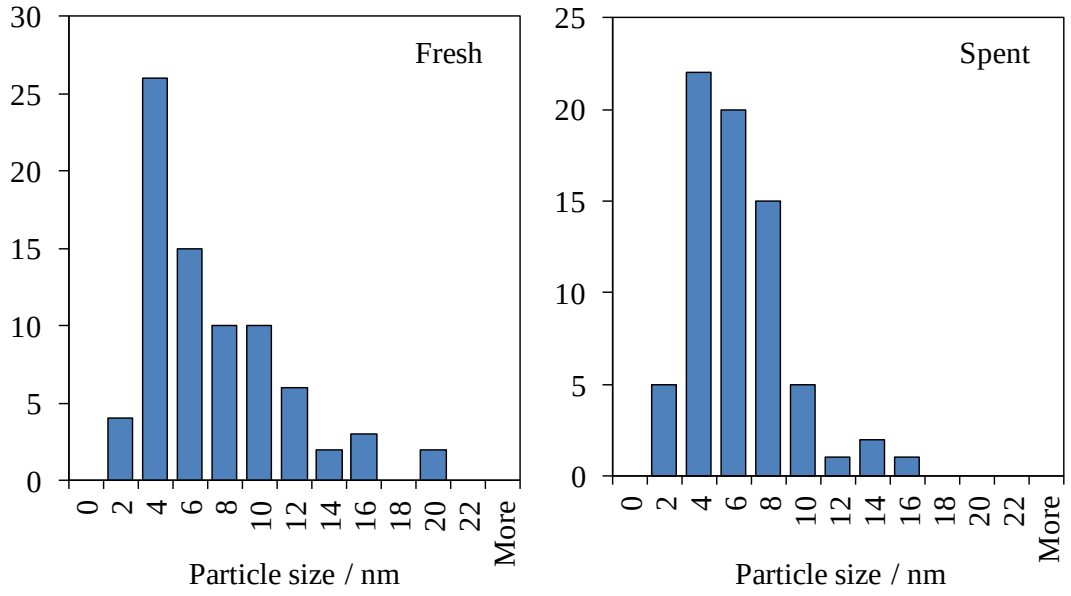


**Figure 6.16 – Size histograms of 5 wt% Pd/C before (left) and after (right) reaction with 8.4 mmol benzyl cyanide at 40 °C under 2 bar $H_2$**

Mean particle size for the spent catalyst was determined to be 5.3 nm, with a mode of 4 nm. There has been no change to particle size after reaction, which is to be expected under such mild reaction conditions. Further discussion of the effects of acid treatment on particle size is considered in *Section 6.2.4*.

### 6.2.3.3 Diffuse reflectance infra-red Fourier transform spectroscopy

The spent catalysts were probed using diffuse reflectance infra-red Fourier transform spectroscopy (DRIFTS). Spectra of the catalyst after reaction at 21 °C, 40 °C and 50 °C subtracted from the fresh catalyst spectrum are shown in *Figure 6.17* (left) and the spent catalyst compared with adsorbed products and standards is also shown (right).

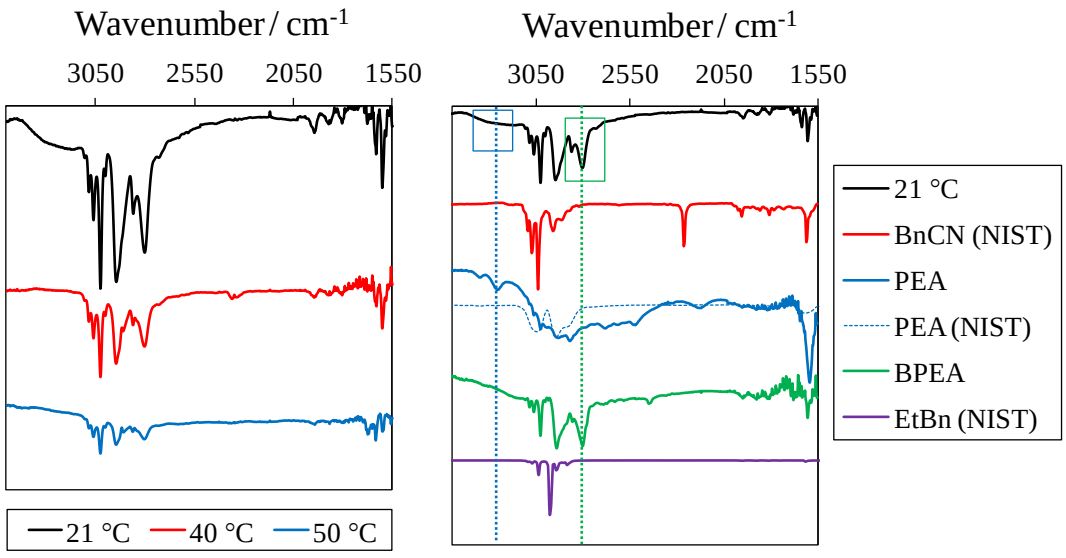


**Figure 6.17 – DRIFT spectra for spent 5 wt% Pd/C catalyst after reaction with 8.4 mmol benzyl cyanide at 2 bar pressure and specified temperature (left) and spent catalyst from 21 °C reaction compared with standards adsorbed on the fresh catalyst or obtained from NIST database (right). Each spectrum has been subtracted from the fresh catalyst spectrum to show the adsorbed functionality.**

The region around 3050 $cm^{-1}$ can be assigned to the aromatic structure and is identical to all the standards in this region, although the resolution of the PEA spectrum is unfortunately poor. A number of further observations can be drawn from these spectra. Comparing benzyl cyanide starting material with the spent catalyst spectrum, the C≡N stretch at 2264 $cm^{-1}$ is not present in the spent catalyst. The distinctive feature at 2809 $cm^{-1}$ in the BPEA spectrum is clear in the spent catalyst spectrum and in fact these two spectra are almost identical (highlighted in green). Additionally, there is no clear feature relating to the NH stretch expected in PEA in the spent catalyst spectrum around 3260 $cm^{-1}$ (highlighted in blue), although the curve in the baseline may obscure any small vibrations attributable to this. There is a small feature in the spent catalyst

spectrum at 1633 $cm^{-1}$ that is consistent with the C=N stretch from an imine, so the co-adsorption of some primary amine and some imine cannot be ruled out from the information in these spectra.[25]

Thus, it can be confirmed that surface adsorbates are dominated by the secondary amine. It is interesting to recall that this was the expected product from the reaction and it was not detected in the liquid phase by GCMS. The possibility of Pd-CN formation is worth noting here, although the C=N stretch is expected to be detected around 1525 $cm^{-1}$, and would thus be impossible to distinguish from the other species, which have strong features in this region (this is not included in the figure for clarity, but the spectra are given in the appendix).[26]

#### 6.2.3.4 X-ray photoelectron spectroscopy

Further quantitative analysis of the adsorbed species is possible using XPS. Due to the small amounts of spent catalyst that were recovered, the sample was run on carbon tape and so direct elemental analysis was not possible. The C 1s spectra for the fresh catalyst, the catalyst after reaction at room temperature, after reaction at 50 °C and after heating the room temperature spent catalyst to 500 °C under inert are shown in *Figure 6.18*. There is little change between the spectra for these species.

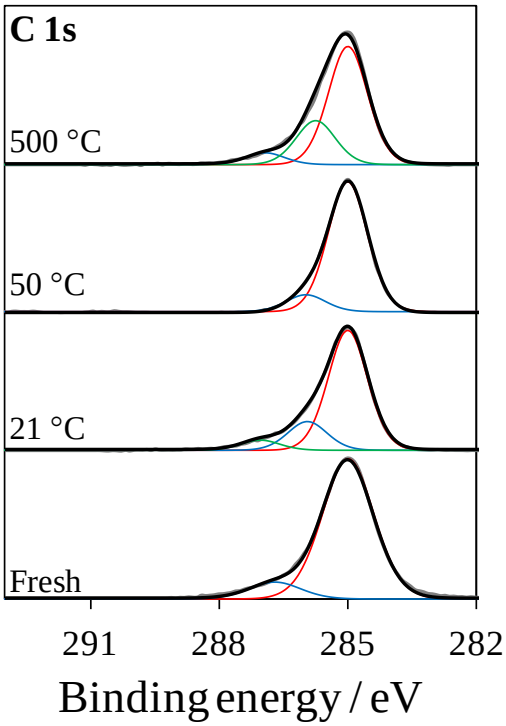


**Figure 6.18 – C 1s XP spectra of fresh 5 wt% Pd/C and spent catalyst after reaction with benzyl cyanide at 2 bar $H_2$ at 21 °C and 50 °C. The top spectrum is of the spent catalyst from reaction at 21 °C heated under inert to 500 °C**

The nitrogen:palladium ratio calculated by weight is given in *Table 6.4*. There is an increase in the N:Pd ratio after reaction, and particularly at higher reaction temperature. Since there is no surface nitrogen in the fresh catalyst, it is clear that there is adsorption of some nitrogen species on the surface. The high N:Pd ratio observed at 50 °C is possible if there has been a loss in Pd surface area, the adsorption of aromatic amines occurs end on and the amines stack closely together to reduce the footprint of these species, or the adsorbed nitrogen species is a small molecule such as $NH_2$ or CN. It is possible that there has been a loss in Pd surface area, either through sintering or leaching, although it is reasonable to assume the loss in Pd surface area is minimal, as size analysis in *Section 6.2.3.2* would suggest. The latter observation, however, is significant on consideration of the Pd 3d XP spectra later in this section.

| Sample | Pd 3d / wt% | N 1s / wt% | N:Pd |
|---|---|---|---|
| Fresh | 100 | 0 | 0.00 |
| 21 °C | 69.63 | 30.37 | 0.44 |
| 50 °C | 22.08 | 77.91 | 3.53 |
| 500 °C | 73.16 | 26.84 | 0.37 |

**Table 6.4 – Ratio of N: Pd surface composition by weight from XPS analysis for 5 wt% Pd/C fresh and spent catalysts**

Based on the nominal weight loading of Pd in the catalyst, and the catalyst mass used in reaction, it is possible to estimate the amount of this species on the surface and compare it with the missing mass balance from the product and reactant reaction profiles. 5 wt% of Pd in 200 mg of catalyst equates to 0.094 mmol of Pd. 30.37 % of the total Pd and N content at 21 °C is attributable to N species, or 0.029 mmol. By 50 °C this has increased to 77.91 %, or 0.073 mmol. Assuming 1 equivalent nitrogen containing product, the remainder of the mass balance, from *Section 6.2.3.1* at 21 °C is 3.1 mmol and at 50 °C is 5.4 mmol. Either the missing product has been lost due to evaporation, or these results indicate that significant quantities of product are adsorbed on the support surface or within the carbon micropores.

After heating the room temperature spent catalyst to 500 °C there is some decrease in N, but surprisingly not all the N has been removed. Literature studies generally report thermal decomposition of amines and amine derived molecules to occur between 400 °C – 550 °C. Due to the short duration at which the spent catalyst was exposed to these temperatures (ramp rate 10 K $min^{-1}$ followed by immediate cooling), it is therefore likely that there has been minimal decomposition of amine species on the surface.[27-29]

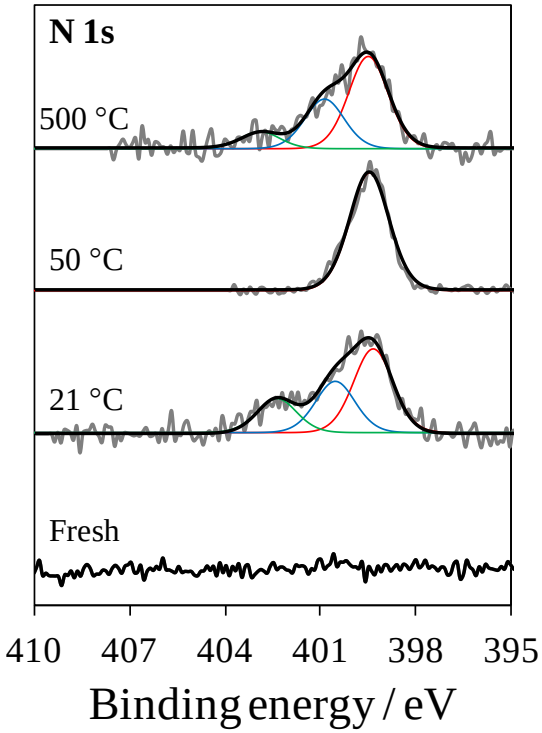


**Figure 6.19 – N 1s XP spectra for fresh and spent 5 wt% Pd/C**

The N 1s spectra for the four catalysts are displayed in *Figure 6.19*, which shows that the spent catalyst, following reaction at 21°C, has three N components. These components are retained even after heating to 500 °C under inert. After reaction at 50 °C only one species dominates. This may reflect the differences noted in the catalyst selectivity between 21 °C and 50 °C. N 1s binding energies of 399.4 eV are consistent with CN functionality (KCN 398.1 eV, PhCN 399.0 eV) although amine functionality cannot be differentiated from these results alone ($PhNH_2$ 399.1 eV).[30-32] It is therefore possible the peak at 400 eV is due to primary amine. The peaks at slightly higher binding energy (402.4 eV) are consistent with nitrogen in the $NH_4^+$ species, if formation of the quaternary cation of phenylethylamine has occured.[33]

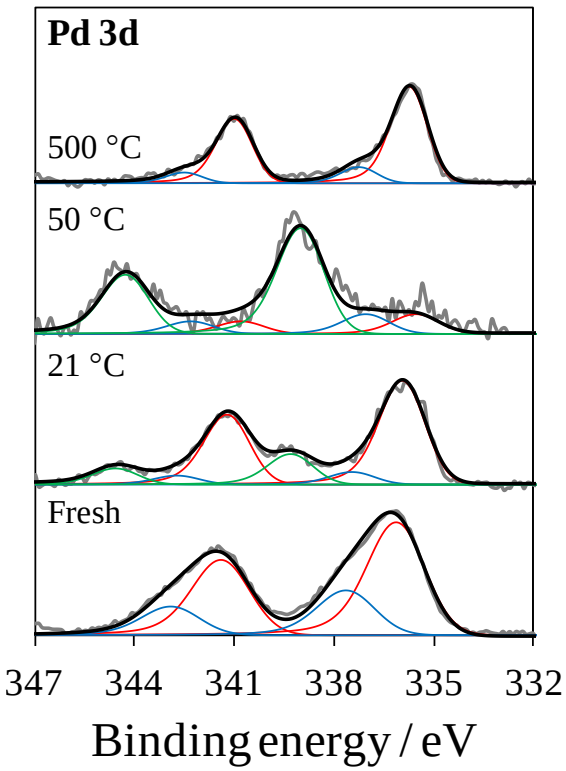


**Figure 6.20 – Pd 3d XP spectra for fresh and spent 5 wt% Pd/C catalysts**

Finally, the Pd 3d XP spectra are given in *Figure 6.20*. These results show striking changes following the reaction. Pd and PdO are highlighted for each catalyst in the figure, and as would be expected, there is a reduction in the amount of PdO in all three spent catalysts. There is a third peak, however, with a binding energy of 339 eV present after reaction at 21 °C, dominating after reaction at 50 °C and removed after heating the room temperature catalyst to 500 °C. The large shift in this species (ΔBE = 3.5 eV) signifies that it must be strongly bound and electron withdrawing. Chemical shifts of this magnitude are not reported in the literature examples of Pd interaction with amine or hydroxyl species.[34-37] The high N:Pd ratio indicates that this species may be small. Literature assignments for Pd XP spectra with a binding energy of 339.1 eV are assigned to $Pd(CN)_2$ species.[38] This large shift to higher binding energy is possible due to electron transfer from Pd through the π-π* interaction. The $CN^-$ species is isoelectronic with CO, thus the same back-donation is observed here, as described in *Chapter 3* regarding CO adsorption.[39] There is thus strong evidence for the assignment of a $Pd(CN)_2$ species, although the formation of this species could not be confirmed by DRIFTS (due to conflicting vibrational modes) or the detection of toluene by GCMS (see footnote *Section 6.2.3.1*).

Thus, these results suggest that, in addition to the formation of primary amine and the reduction of amine to ethyl benzene, C-C bond cleavage of the benzyl cyanide molecule is directly possible, leading to the accumulation of CN species on the catalyst surface. This accumulation is significant by a reaction temperature of 50 °C, but still occurs at room temperature, although there is more evidence of amine adsorption at lower temperature. The strong adsorption of CN is a likely source of catalyst deactivation, and may not be prevented by introduction of acid, as this route occurs before the formation of amine which the acid is used to protonate and remove.

#### 6.2.3.5 Nitrogen porosimetry[*]

In characterising the fresh catalyst it was suggested that the microporosity of the support could affect catalyst performance. Thus, the effect of systematic adsorption of PEA on the porosity of the catalyst will now be examined. A series of pre-treatments using 8.4 mmol PEA under reaction conditions with 2.5 g of catalyst (a 15 fold decrease in substrate:Pd ratio) were conducted and the treated catalyst was assessed using porosimetry.[†]

The BJH pore size distribution is displayed in *Figure 6.21*. Apart from a reduction in intensity, there is no change in the distribution indicating that pores are not selectively blocked. Surface area analyses using the BET, BJH and t-plot isotherms are given in *Table 6.5*. There is an increase in surface area after treating the catalyst in methanol under hydrogen, but in the absence of any adsorbates, implying that residual adsorbates, most likely carbonaceous from XPS, were cleaned during this procedure. There is a significant reduction in surface area after treating with PEA and microporosity is lost entirely. There is also a slight increase in pore diameter, consistent with the selective blocking of micropores. This confirms the hypothesis that the micropores become blocked and that a microporous support structure is inadvisable for this reaction.

[*] Experimental work for this section was carried out by Amy Kidner under the supervision of the author.
[†] The quantity of spent catalyst recovered from the reactions was not sufficient for analysis by porosimetry. Catalyst was lost through filtration, and was thus collected after centrifugation and multiple washing steps.

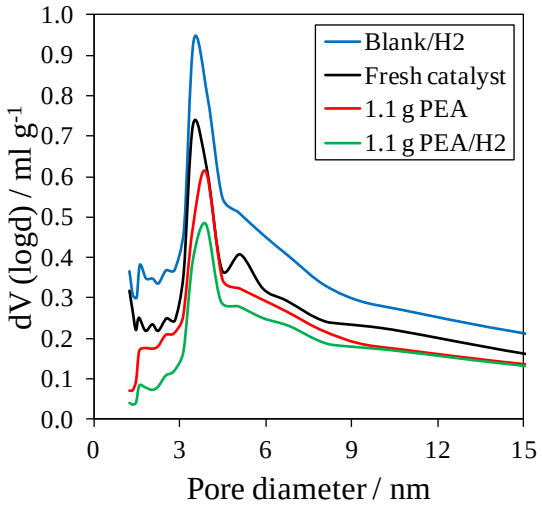


**Figure 6.21 – BJH isotherm mesopore size distributions for 5 wt% Pd/C catalyst treated with 8.4 mmol phenylethylamine**

| Sample | BJH S.A. / $m^2$ $g^{-1}$ | t-plot micropore area / $m^2$ $g^{-1}$ | BET S.A. / $m^2$ $g^{-1}$ | Pore diameter (peak max) / nm |
|---|---|---|---|---|
| Fresh | 187 | 392 | 678 | 3.44 |
| Blank/H2 | 249 | 469 | 872 | 3.44 |
| 1.1g PEA | 156 | 0 | 223 | 3.87 |
| 1.1g PEA/H2 | 129 | 0 | 138 | 3.83 |

**Table 6.5 – Quantitative porosimetry surface area analysis for 5 wt% Pd/C catalyst treated with 8.4 mmol phenylethylamine**

## 6.2.4 Promoter effects: the addition of sulphuric acid

### 6.2.4.1 Nitrogen porosimetry

At this point the effect of acid on the catalyst properties were considered. Once again, nitrogen porosimetry was used to see the effect of acid on the support porosity. The pore size distributions from the BJH isotherm are shown in *Figure 6.22* for increased concentrations of acid. Although there is a decrease in intensity there is no change in the pore size distribution. *Table 6.7* shows the surface area measurements from the different isotherms. Acid does not affect the catalyst porosity until 0.5 M concentrations. From this concentration of acid, the mesopore surface area is reduced, although the microporosity is not as significantly affected.

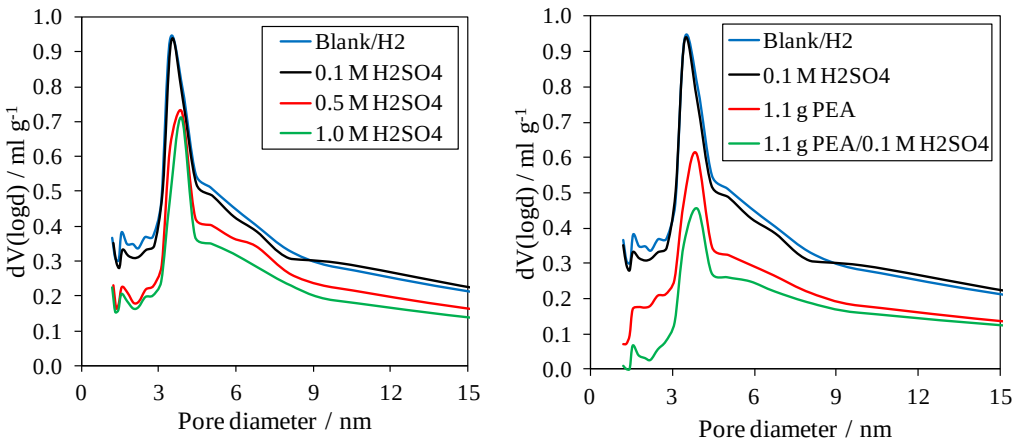


**Figure 6.22 – BJH isotherm mesopore size distributions for 5 wt% Pd/C treated with $H_2SO_4$ (left) and effect of 0.1 M $H_2SO_4$ and phenylethylamine adsorption (right)**

The catalysts were then treated with a combination of 0.1 M $H_2SO_4$ (1 mmol) and 8.4 mmol PEA. These results are also given in *Table 6.6*. Addition of this quantity of acid does not make any impact in improving the catalyst porosity. In order for the acid to remove PEA as a salt, equivalent quantities are required, thus for this method to be of use, acid concentrations that will affect the catalyst structure are required.

| Sample | BJH S.A. / $m^2$ $g^{-1}$ | t-plot micropore area / $m^2$ $g^{-1}$ | BET S.A. / $m^2$ $g^{-1}$ | Pore diameter (peak max) / nm |
|---|---|---|---|---|
| Fresh | 187 | 392 | 678 | 3.44 |
| Blank/$H_2$ | 249 | 469 | 872 | 3.44 |
| 0.1 M $H_2SO_4$ | 238 | 466 | 854 | 3.45 |
| 0.5 M $H_2SO_4$ | 192 | 389 | 677 | 3.89 |
| 1 M $H_2SO_4$ | 164 | 304 | 559 | 3.91 |
| 8.4 mmol PEA/0.1 M $H_2SO_4$ | 123.1 | 0 | 131.4 | 3.94 |

**Table 6.6 – Quantitative porosimetry surface area analysis for 5 wt% Pd/C catalyst treated with $H_2SO_4$ and effect of 0.1 M $H_2SO_4$ on phenylethylamine adsorption**

### 6.2.4.2 Transmission electron microscopy

The acid treated catalysts were analysed using TEM and a particle size distribution was measured. The results for catalysts treated in 0.1 M and 0.5 M acid are shown in *Figure 6.23*.

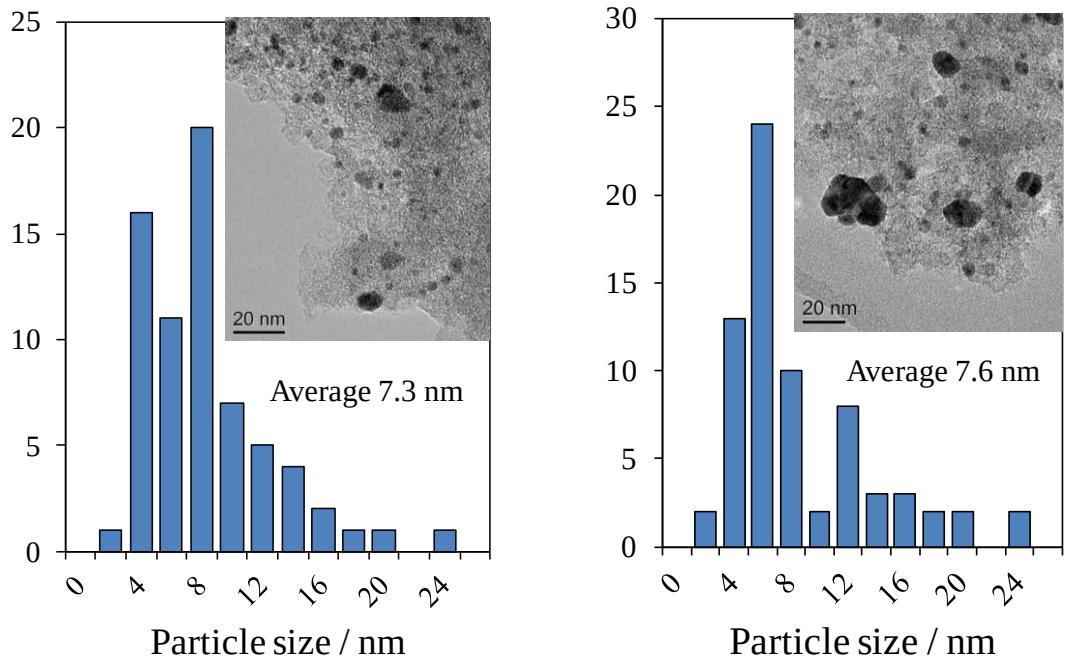


**Figure 6.23 – TEM analysis and particle size histograms for 5 wt% Pd/C treated with 0.1 M $H_2SO_4$ (left) and 0.5 M $H_2SO_4$ (right)**

The mean particle size by TEM for the 0.1 M acid treated catalyst is 7.3 nm, an increase of 1 nm from the fresh catalyst. There is a further increase in mean size to 7.6 nm for the 0.5 M treated catalyst. This increase is very small and there is no dramatic sintering of the particles. These data alone would not be sufficient, within the error of the technique, to determine a loss in surface area, although this may be signified. However, it is also possible that there has been some loss in surface area due to leaching. Elemental analysis on the acid treated catalyst was inconclusive with ICP-OES results giving a Pd loading of 4 wt%, a higher loading than observed for the fresh catalyst. It is likely that the metal distribution is too poor to conclude whether there has been a loss in overall metal content. Nevertheless, on consideration of changes in the distribution histogram, and further evidence in the next section from XPS, the possibility of leaching cannot be ruled out. There is a change in the particle size distribution for both acid treated catalysts, more so by 0.5 M $H_2SO_4$. Whereas for the

fresh catalyst there was a clear peak in particle size around 4 nm, after treating with acid the distribution is dominated more by particles in the range 6-8 nm and the largest particles are 4 nm bigger (24 nm) than those in the fresh catalyst sample.

#### 6.2.4.3 X-ray photoelectron spectroscopy

As with the spent catalysts, XPS can be used to quantitatively assess the surface composition of the catalyst and reveals possible sources of catalyst deactivation. *Table 6.7* lists the catalyst compositions by weight. There is a general decrease in Pd and C content and an increase in sulphur content. The amount of oxygen increases significantly on the introduction of acid. So, acid clearly has an effect on the catalyst surface composition. The S:Pd and Pd:C ratios are plotted in *Figure 6.24*. These confirm that on increasing acid concentration the sulphur content increases proportionally. Also, there is a loss in the amount of Pd with increased acid concentration. This latter observation implies the possibility of leaching or sintering: a 25 % reduction in surface Pd by 0.1 M acid is significant. As described in the previous section, the inhomogeneity of the catalyst makes it difficult to assess if leaching has occurred. It was outlined at the start of this chapter that the large Pd concentration by XPS compared with bulk analysis would suggest that Pd was distributed favourably over the external catalyst surface, thus a reduction in surface Pd may be more significant and noticeable than a reduction in total Pd from leaching.

| $[H_2SO_4]$ / M | O / wt% | Pd / wt% | C / wt% | S / wt% |
|---|---|---|---|---|
| 0.00 | 4.71 | 11.26 | 83.81 | 0 |
| 0.05 | 10.27 | 8.24 | 81.45 | 0.05 |
| 0.10 | 9.79 | 8.07 | 81.94 | 0.21 |
| 0.50 | 11.32 | 8.21 | 79.44 | 1.03 |
| 1.00 | 13.48 | 7.85 | 77.11 | 1.56 |

**Table 6.7 – Surface compositions of 5 wt% Pd/C treated with $H_2SO_4$ determined by XPS analysis**

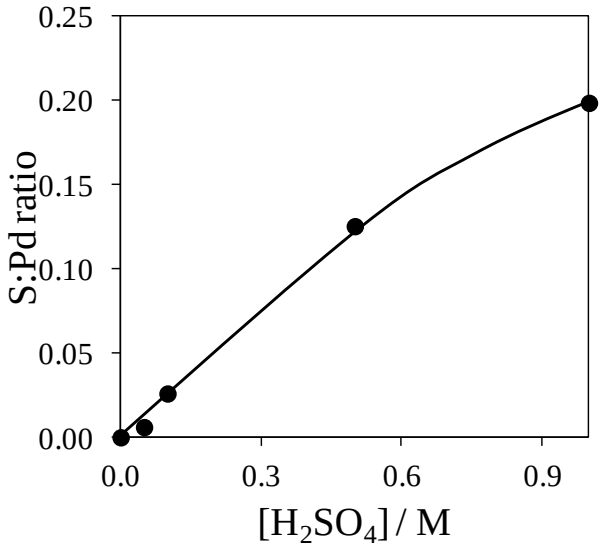


| $[H_2SO_4]$ / M | Pd (normalised to C) / % |
|---|---|
| 0.00 | 11.26 |
| 0.05 | 8.48 |
| 0.10 | 8.25 |
| 0.50 | 8.66 |
| 1.00 | 8.53 |

**Figure 6.24 – Effect of sulphuric acid concentration (total fixed volume 10 ml) on S content normalised to surface Pd and surface metal concentration normalised to C content with respect to the fresh catalyst**

The C 1s and S 2p XP spectra are given in *Figure 6.25* and Pd 3d XP spectra are displayed in *Figure 6.26*. There is no change in the composition of carbon components on the addition of acid. The surface S $2p_{3/2}$ species binding energy of 168.7 eV can be assigned to sulphate species. In fact, on inspection of the Pd 3d XP spectra, the peak shifted to 338.7 eV can be assigned to $PdSO_4$.[40, 41]

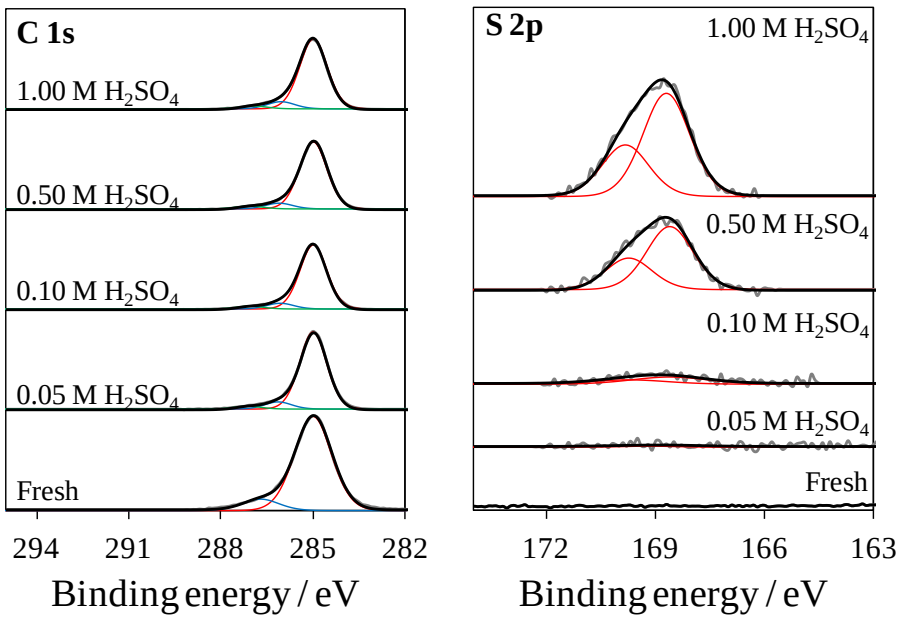


**Figure 6.25 – C 1s XP spectra (left) and S 2p XP spectra for 5 wt% Pd/C treated with $H_2SO_4$**

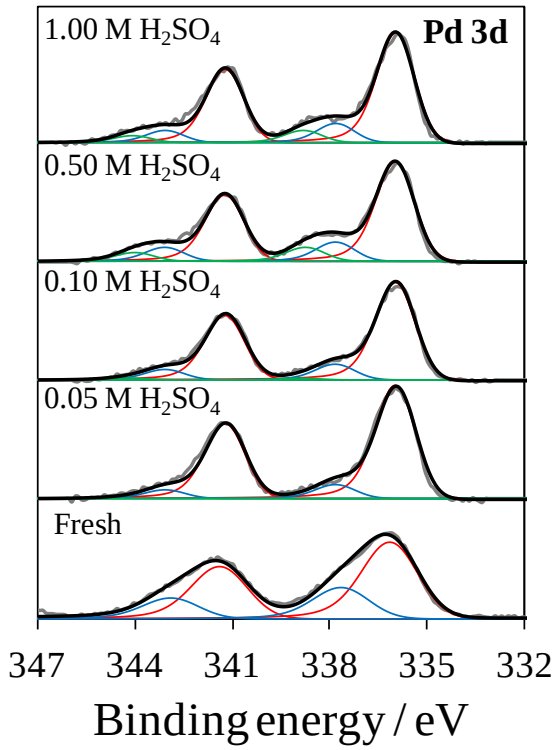


**Figure 6.26 – Pd 3d XP spectra for 5 wt% Pd/C treated with $H_2SO_4$**

Plotting the $PdSO_4$ component by weight with acid concentration reveals a dramatic increase in surface sulphate at concentrations of 0.5 M acid and above (*Figure 6.27*). The accumulation of adsorbed sulphates on the catalyst surface and formation of Pd salts may contribute significantly towards catalyst poisoning.

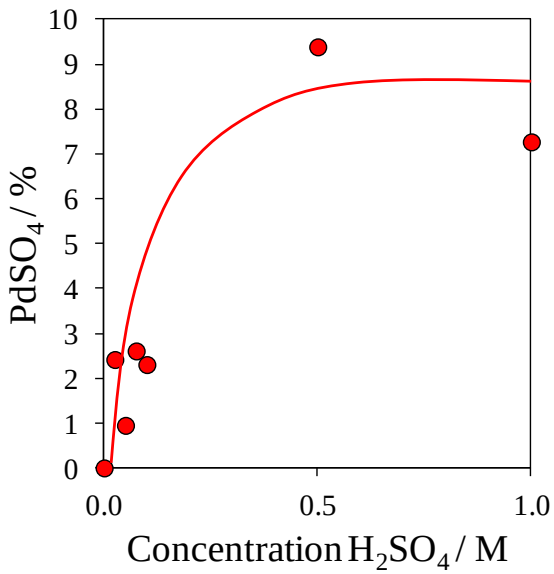


**Figure 6.27 – Effect of sulphuric acid concentration on the amount of sulphate formation in the absence of amine**

## 6.3 Conclusions

In this chapter, the deactivation of an industrial Pd/C catalyst employed in a problematic and useful reaction is investigated and a number of sources of deactivation have been identified. Structural changes in the catalyst are minimal, and although these may affect catalyst performance it is unlikely that they alone account for the significant deactivation reported by industry.

Firstly, the catalyst support is not ideal for a liquid phase reaction due to its microporosity and subsequent pore blocking, limiting mass transport. Although this will contribute to the accumulation of species on the catalyst surface as the pores become blocked, the most significant effect will be on reduced turnover frequencies due to mass transport limitations and poor metal dispersion, as the metal particles are larger than the catalyst pores. A mesoporous support is recommended here to improve the catalyst performance.

Pd particle size and size distributions are relatively large. Again, this will not have a significant impact on catalyst deactivation, although smaller particles and an increased surface area may improve the catalyst reactivity. Addition of acid does reveal a decrease in Pd surface area, possibly due to leaching, and a slight increase in particle

size. Further investigation into the catalyst support used to stabilise the metal particles here would be worthwhile in order to minimise these structural changes.

There are three clear sources of chemical poisoning in this system. The formation of BPEA was predicted in the introduction, and although no BPEA was detected by GCMS, it has been identified using DRIFTS and is found to adsorb strongly to the catalyst surface. In the absence of acid it is likely this is blocking catalyst active sites. In addition to product adsorption after the formation of amine, which acid should remove, CN accumulates through the fission of the benzyl cyanide C-C bond. This is less significant at lower reaction temperatures, but the strong Pd-CN bond will result in poisoning of the catalyst active site and cause deactivation. This reaction step could occur regardless of the removal of amine by the addition of acid. On treating the catalyst with $H_2SO_4$, sulphate accumulates on the surface. Again, the Pd-$SO_4$ bond is strong and the catalyst active sites will be blocked.

These sources of poisoning are a result of poor selectivity. If the catalyst was designed such that PEA was formed selectively, and acid was not required, it is very likely that the catalyst recyclability would improve. There are two points to consider here, using the investigations from *Chapter 3* and *Chapter 5*.

Breaking the C-C bond is a more energetically expensive process than hydrogenating the nitrile, so it is possible that the Pd (111) surface is selective to amine formation as a lower energy facet. Thus, designing a catalyst where the higher energy facets are minimised may improve the catalyst performance and reduce the accumulation of CN species on the surface. Testing this reaction using Pd (111) enclosed icosahedra in comparison with Pd (100) enclosed cubes could be used to test this hypothesis.

Secondly, in *Chapter 5*, the addition of Au to a Pd catalyst is outlined as a means for improving catalyst selectivity. Au softens the adsorption properties of the catalyst surface, so strongly bound species such as CN, amine and sulphates may desorb more easily. As above, the catalyst surface may be more selective to amine formation, but additionally hydrogenation to higher order amines, or the formation of ethyl benzene may be minimised using such a bimetallic catalyst.

## 6.4 References


1. L. Hegedus, T. Mathe and T. Karpati, *Appl. Catal., A.*, 2008, **349**, 40.
2. L. McMillan, D. Lennon and C. Brennan, *Abstracts of Papers of the American Chemical Society*, 2011, **241**.
3. W. H. Hartung, *J. Am. Chem. Soc.*, 1928, **50**, 3370
4. L. Hegedus and T. Mathe, *Appl. Catal., A.*, 2005, **296**, 209
5. M. W. Duch and A. M. Allgeier, *Appl. Catal. A-Gen.*, 2007, **318**, 190.
6. P. Albers, J. Pietsch and S. F. Parker, *J. Mol. Catal. A: Chem.*, 2001, **173**, 275.
7. Q. Zhang, L. Ma, C. Lu, J. Lv, W. Liu, H. Wang and X. Li, *Rare Met. Mater. Eng.*, 2010, **39**, 526
8. P. A. Gravil and H. Toulhoat, *Surf. Sci.*, 1999, **430**, 176
9. J. L. Aluha, G. Pattrick and E. van der Lingen, *Top. Catal.*, 2009, **52**, 1977.
10. P. Castano, D. van Herk, M. T. Kreutzer, J. A. Moulijn and M. Makkee, *Appl. Catal. B.,*, 2009, **88**, 213.
11. S. Cimino, L. Lisi, G. Russo and R. Torbati, *Catal. Today*, 2010, **154**, 283
12. Y. Y. Huang and W. M. H. Sachtler, *J. Catal.*, 1999, **188**, 215
13. G. Fagherazzi, P. Canton, P. Riello, F. Pinna and N. Pernicone, *Catal. Lett.*, 2000, **64**, 119.
14. F. Rouquerol, J. Rouquerol and K. Sing, *Adsorption by Powders and Porous Solids: Principles, Methodology and Applications*, Academic Press, London, 1999.
15. R. Pellegrini, G. Agostini, E. Groppo, A. Piovano, G. Leofanti and C. Lamberti, *J. Catal.*, 2011, **280**, 150.
16. N. Pernicone, M. Cerboni, G. Prelazzi, F. Pinna and G. Fagherazzi, *Catal. Today*, 1998, **44**, 129
17. A. L. D. Ramos, P. D. Alves, D. A. G. Aranda and M. Schmal, *Appl. Catal., A.*, 2004, **277**, 71.
18. V. I. Simagina, O. V. Netskina, E. S. Tayban, O. V. Komova, E. D. Grayfer, A. V. Ischenko and E. M. Pazhetnov, *Appl. Catal., A.*, 2010, **379**, 87
19. S. P. Bawane and S. B. Sawant, *Chem. Eng. J.*, 2004, **103**, 13
20. B. Bigot, F. Delbecq, A. Milet and V. H. Peuch, *J. Catal.*, 1996, **159**, 383
21. Y. Y. Huang and W. M. H. Sachtler, *Appl. Catal. A-Gen.*, 1999, **182**, 365.
22. G. D. Yadav and M. R. Kharkara, *Appl. Catal., A.*, 1995, **126**, 115
23. O. Dominguez-Quintero, S. Martinez, Y. Henriquez, L. D'Ornelas, H. Krentzien and J. Osuna, *J. Mol. Catal. A: Chem.*, 2003, **197**, 185
24. Y. M. Lopez-De Jesus, C. E. Johnson, J. R. Monnier and C. T. Williams, *Top. Catal.*, 2010, **53**, 1132
25. H. Gunzler and H.-U. Gremlich, *IR Spectroscopy: An Introduction*, Wiley-VCH, Weinheim, 2002.
26. M. E. Kordesch, W. Stenzel and H. Conrad, *Surf. Sci.*, 1988, **205**, 100
27. C. P. A. Mulcahy, A. J. Carman and S. M. Casey, *Surf. Sci.*, 2000, **459**, 1.
28. J. Cho and C. H. Choi, *J. Chem. Phys.*, **134**, 8.
29. R. Helbing, W. S. Kuhn and O. Gorochov, in *Materials Science Forum*, eds. H. Heinrich and J. B. Mullin, Zurich-Uetikon, Editon edn., 1995, vol. 182-, pp. 47-50.
30. Folkesso.B, *Acta Chem. Scand.*, 1973, **27**, 287
31. C. D. Wagner, W. M. Riggs, L. E. Davis, J. F. Moulder and G. E. Muilenberg, *Handbook of X-Ray Photoelectron Spectroscopy*, Perkin-Elmer Corporation, Physical Electronics Division, Eden Prairie, Minn. 55344, 1979.

32. C. Jones and E. Sammann, *Carbon*, 1990, **28**, 509
33. A. S. Vanini, J. P. Audouard and P. Marcus, *Corrosion Sci.*, 1994, **36**, 1825
34. L. Q. Jing, D. J. Wang, B. Q. Wang, S. D. Li, B. F. Xin, H. G. Fu and J. Z. Sun, *J. Mol. Catal. A: Chem.*, 2006, **244**, 193.
35. Z. Li, J. Gao, X. Xing, S. Wu, S. Shuang, C. Dong, M. C. Paau and M. M. F. Choi, *J. Phys. Chem. C*, 2010, **114**, 723.
36. A. V. Marikutsa, M. N. Rumyantseva, L. V. Yashina and A. M. Gaskov, *J. Solid State Chem.*, 2010, **183**, 2389.
37. L. M. Neal, M. L. Everett, G. B. Hoflund and H. E. Hagelin-Weaver, *J. Mol. Catal. A: Chem.*, 2011, **335**, 210.
38. G. Kumar, Blackbur.Jr, R. G. Aldridge, W. E. Moddeman and M. M. Jones, *Inorg. Chem.*, 1972, **11**, 296
39. D. F. Shriver and P. W. Atkins, *Inorganic Chemistry*, 3rd edn., Oxford University Press, Oxford, 1999.
40. B. Stypula and J. Stoch, *Corrosion Sci.*, 1994, **36**, 2159
41. T. L. Barr, *J. Vac. Sci. Technol. A*, 1991, **9**, 1793.

# Chapter 7

# Conclusions

## 7.1 Conclusions

One of the principal aims of this project is to consider catalyst design as a means of engineering suitable materials for a particular reaction. To this end, it is important to identify certain properties of the active site. Surface science studies have provided significant fundamental information, but as was noted in *Chapter 1*, these studies have their limitations.[1, 2] In this thesis, examples of techniques and methodologies that can be applied to the rational design of heterogeneous catalysts has been given, using the specific example of the selective oxidation of crotyl alcohol to crotonaldehyde as a well understood model reaction.

Several different approaches were adopted towards both developing tailored catalysts and assessing catalyst performance. The morphology of nanoparticulate Pd was controlled in order to investigate the sensitivity of the reaction towards catalyst shape.[3-7] Composition was tuned and so catalytic reactivity could be correlated with Pd promotion by Au.[8] The *in situ* structure-reactivity relationship of Pd catalysts and their reactive environment was explored in detail using a unique procedure, providing valuable mechanistic insight and revealing the role of both Pd oxidation state and reactive oxygen.[9] Finally, the source of deactivation in an industrial Pd catalyst was investigated through systematic characterisation. Potential solutions to the poor catalyst performance are then proposed using the knowledge acquired through this research.

In *Chapter 3*, Pd nanoparticles of three different morphologies have been successfully synthesised and their reactivity compared. Differences in activity, selectivity and longevity was observed: Pd(111) terminated icosahedra were found to be three times more active than Pd(100) encapsulated nanocubes and ten times faster than the nanorods exposing Pd(110) facets, although they exhibited the lowest selectivity. Rapid deactivation was observed over Pd nanorods and surface impurities did make it difficult to determine the source of variability in catalyst performance for the different shapes. Nevertheless, through detailed analysis of the surface chemistry differences in oxide stability, CO adsorption and residual halide were proposed as potentially affecting reactivity as a result of the synthetic procedure.[10-15] It is clear that further work is required in shape controlled synthesis that minimise surface impurities and improve monodispersity and size control on a larger scale.

The vital role of oxidation state in controlling selectivity and activity was highlighted in *Chapter 4*, and clearly illustrated in *Figure 7.1* (from this chapter).[2, 16] At

elevated temperatures, fluctuations in oxidation state led to the formation of metallic surfaces over which decarbonylation of the aldehyde occurs and the build up of $CH_x$ species. The extent of these fluctuations was defined as the redox capacity. Once an oxygen feedstream is introduced, the $CH_x$ species combust before subsequent nanoparticle re-oxidation in the reactive oxygen atmosphere. Thus, it can be concluded that combustion takes place over metallic surfaces. At lower temperatures the oxide surface is more stable and aldehyde remains intact on the surface until oxygen is introduced. Some aldehyde, at slightly raised temperatures, is then further oxidised to acid, but it is oxygen that promotes the release of aldehyde product from the surface. Redox capacity was found to be dependent on particle size and oxidation state: larger particles were more stable to redox cycling. However, these particles were also more metallic and exhibited poor activity and selectivity to crotonaldehyde at lower temperatures. Up to 70 % more aldehyde formation over the oxidic surface during redox cycling was noted. Hence, selective aldehyde formation takes place predominantly over oxidic surfaces. It was also shown that oxidation state fluctuations were fully reversible and followed the Mott-Cabrera model for diffusion limited thin film oxidation.[17]

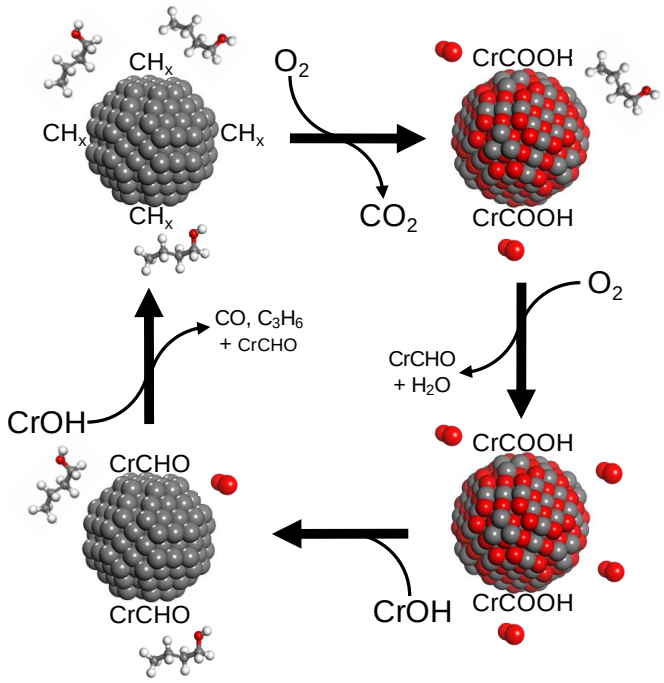


**Figure 7.1 – Crotyl alcohol selective oxidation over Pd/meso-alumina at 150 °C: the catalyst restructures in response to its environment, which then influences reaction selectivity**

Au promotion to Pd catalysts has previously been shown to be effective in improving performance,[18, 19] and in *Chapter 5*, an Au-shell, Pd-core $TiO_2$ supported catalyst with a 5 atomic layer thick shell and bulk composition of ~35 % Au was used to determine optimum surface composition for crotyl alcohol selox in the liquid phase. Progressive alloying on annealing was confirmed through extensive characterisation and it was shown that variation in surface composition correlates with improved activity and selectivity. Maximum performance was obtained at the predicted model composition of $Au_{40}Pd_{60}$.[19] This is shown in *Figure 7.2*. It is expected that if this study were replicated for an identical Pd-shell, Au-core catalyst, performance would decrease on further increased surface Pd composition.

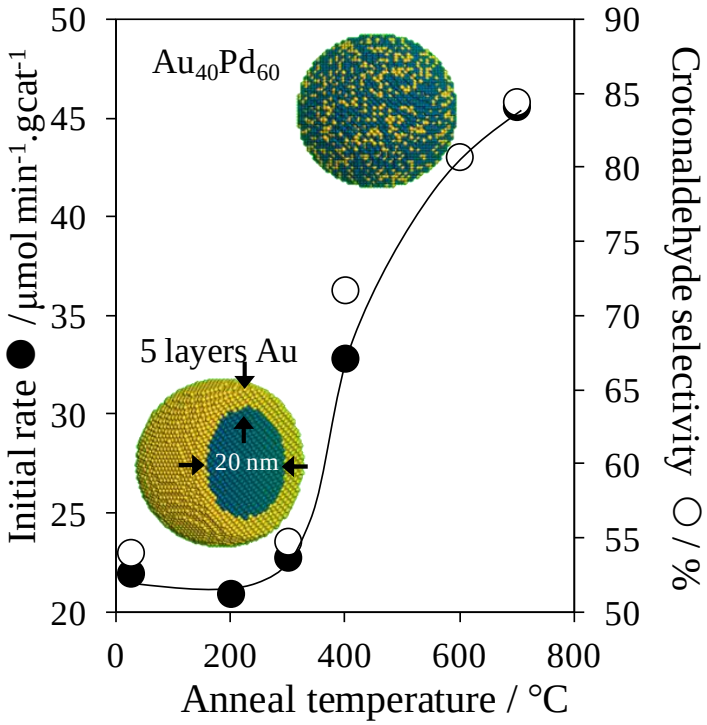


**Figure 7.2 – Activity and selectivity towards crotonaldehyde formation over Au-Pd/$TiO_2$. As annealing temperature is increased, surface Pd composition increases due to intermixing of the original core-shell structure**

In *Chapter 6*, the application of an industrial Pd/C catalyst in the synthesis of primary amines through nitrile hydrogenation is investigated in detail. It was noted that structural changes are not significant, although a mesoporous oxide support may improve mass transport and minimise particle growth, thus enhancing performance.[16, 20] The adsorption properties of the surface are found to be the predominant source of

deactivation in this system. In the absence of acid, strongly bound secondary amine formation was confirmed and identified as a catalyst poison (see *Scheme 7.1*).[21] Pd-CN formation and adsorption was observed and is a previously unknown source of deactivation. The implications of this are important, as accumulation of adsorbed cyanide could occur regardless of acid promotion. Additionally, the use of $H_2SO_4$ to remove primary amine and prevent secondary amine formation led to blocking of active sites by the formation of $PdSO_4$ species.

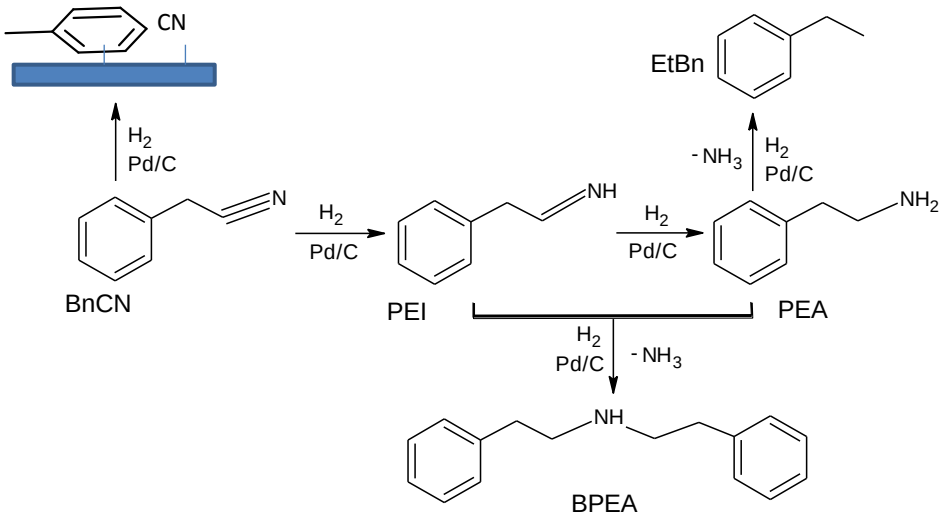


**Scheme 7.1 – Non-selective pathways in benzyl cyanide hydrogenation over Pd/C leading to the accumulation of surface poisons and subsequent catalyst deactivation**

It is clear from these results that the surface chemistry of the Pd catalyst must somehow be softened to prevent the formation and accumulation of strongly bound non-selective products, whilst still maintaining high activities for primary amine formation. Evidence from the previous three chapters in this thesis implies that Pd morphology, oxidation state and Au promotion can all be used to tune the adsorption properties. Hence, it is proposed that these tailored catalysts could be used here to achieve superior catalyst performance for benzyl cyanide hydrogenation, thus leading to the successful application of rational catalyst design in an industrially relevant, problematic system.

## 7.2 References


1. G. A. Somorjai and C. J. Kliewer, *React. Kinet. Catal. Lett.*, 2009, **96**, 191.
2. A. F. Lee, Z. Chang, P. Ellis, S. F. J. Hackett and K. Wilson, *J. Phys. Chem. C*, 2007, **111**, 18844.
3. Y. Li, Q. Liu and W. Shen, *Dalton Trans.*, 2011, **40**, 5811.
4. F. R. Fan, A. Attia, U. K. Sur, J. B. Chen, Z. X. Xie, J. F. Li, B. Ren and Z. Q. Tian, *Cryst. Growth Des.*, 2009, **9**, 2335.
5. Y. Xia, Y. J. Xiong, B. Lim and S. E. Skrabalak, *Angew. Chem.-Int. Edit.*, 2009, **48**, 60.
6. Y. J. Xiong, H. Cal, B. J. Wiley, J. Wang, M. J. Kim and Y. N. Xia, *J. Am. Chem. Soc.*, 2007, **129**, 3665.
7. Y. J. Xiong, J. M. McLellan, Y. D. Yin and Y. N. Xia, *Angew. Chem.-Int. Edit.*, 2007, **46**, 790.
8. A. F. Lee, C. V. Ellis, K. Wilson and N. S. Hondow, *Catal. Today*, 2010, **157**, 243.
9. A. F. Lee, C. V. Ellis, J. N. Naughton, M. A. Newton, C. M. A. Parlett and K. Wilson, *J. Am. Chem. Soc.*, 2011, **133**, 5724.
10. H. Conrad, G. Ertl, J. Koch and E. E. Latta, *Surf. Sci.*, 1974, **43**, 462.
11. B. Fu, W. Liu and Z. Li, *Appl. Surf. Sci.*, 2010, **256**, 6899.
12. J. Y. Park, C. Aliaga, J. R. Renzas, H. Lee and G. A. Somorjai, *Catal. Lett.*, 2009, **129**, 1.
13. N. Seriani, J. Harl, F. Mittendorfer and G. Kresse, *J. Chem. Phys.*, 2009, **131**.
14. R. Westerstrom, C. J. Weststrate, J. Gustafson, A. Mikkelsen, J. Schnadt, J. N. Andersen, E. Lundgren, N. Seriani, F. Mittendorfer, G. Kresse and A. Stierle, *Phys. Rev. B*, 2009, **80**, 125431.
15. G. Zheng and E. I. Altman, *Surf. Sci.*, 2002, **504**, 253
16. S. F. J. Hackett, R. M. Brydson, M. H. Gass, I. Harvey, A. D. Newman, K. Wilson and A. F. Lee, *Angew. Chem.-Int. Edit.*, 2007, **46**, 8593.
17. N. Cabrera and N. F. Mott, *Rep. Prog. Phys.*, 1949, **12**, 163.
18. D. I. Enache, J. K. Edwards, P. Landon, B. Solsona-Espriu, A. F. Carley, A. A. Herzing, M. Watanabe, C. J. Kiely, D. W. Knight and G. J. Hutchings, *Science*, 2006, **311**, 362.
19. A. F. Lee, S. F. J. Hackett, G. J. Hutchings, S. Lizzit, J. Naughton and K. Wilson, *Catal. Today*, 2009, **145**, 251.
20. C. M. A. Parlett, D. W. Bruce, N. S. Hondow, A. F. Lee and K. Wilson, *ACS Catalysis*, 2011, **1**, 636.
21. L. Hegedus, T. Mathe and T. Karpati, *Appl. Catal., A.*, 2008, **349**, 40.

# Appendix

## (i) Analysis of tailored nanoparticles by XRD (*Section 3.2.4.3)*

*In situ* XRD on Pd icosahedra was unsuccessful. A broad unsymmetrical peak was observed between 35° and 43° which could be attributed to Pd(111). However, these results were considered unreliable due to the asymmetric shape of the peak, which distorts increasingly at higher temperature, and the absence of any other Pd feature. The particles are small and detection is already at the limits of the instrument for ex-situ XRD. Also, on heating, the sample texture roughened, which will also have affected XRD measurements.

The Pd cubes sample were immobilised on an alumina support. This was because the minimum sample required for the *in situ* XRD cell was too large to allow analysis of the unsupported Pd cubes. This procedure was successful for Pd cubes, but not for Pd nanorods or Pd icosahedra. In order to achieve the desired shape in the synthesis of these two samples it is necessary to add a significant quantity of PVP, such that the maximum weight loading of the unsupported nanoparticles is only about 7 %. Consequentially, there is an upper limit for how much Pd can be loaded on the alumina support. As a result of this, and the smaller particle size, the Pd reflection was too small to detect when compared to the alumina background, thus only the larger and more concentrated Pd cubes/alumina could be characterised in this way.

**(ii) Reaction profile of combustion products from crotyl alcohol selox over Pd catalysts at 100 °C as discussed in *Chapter 4***

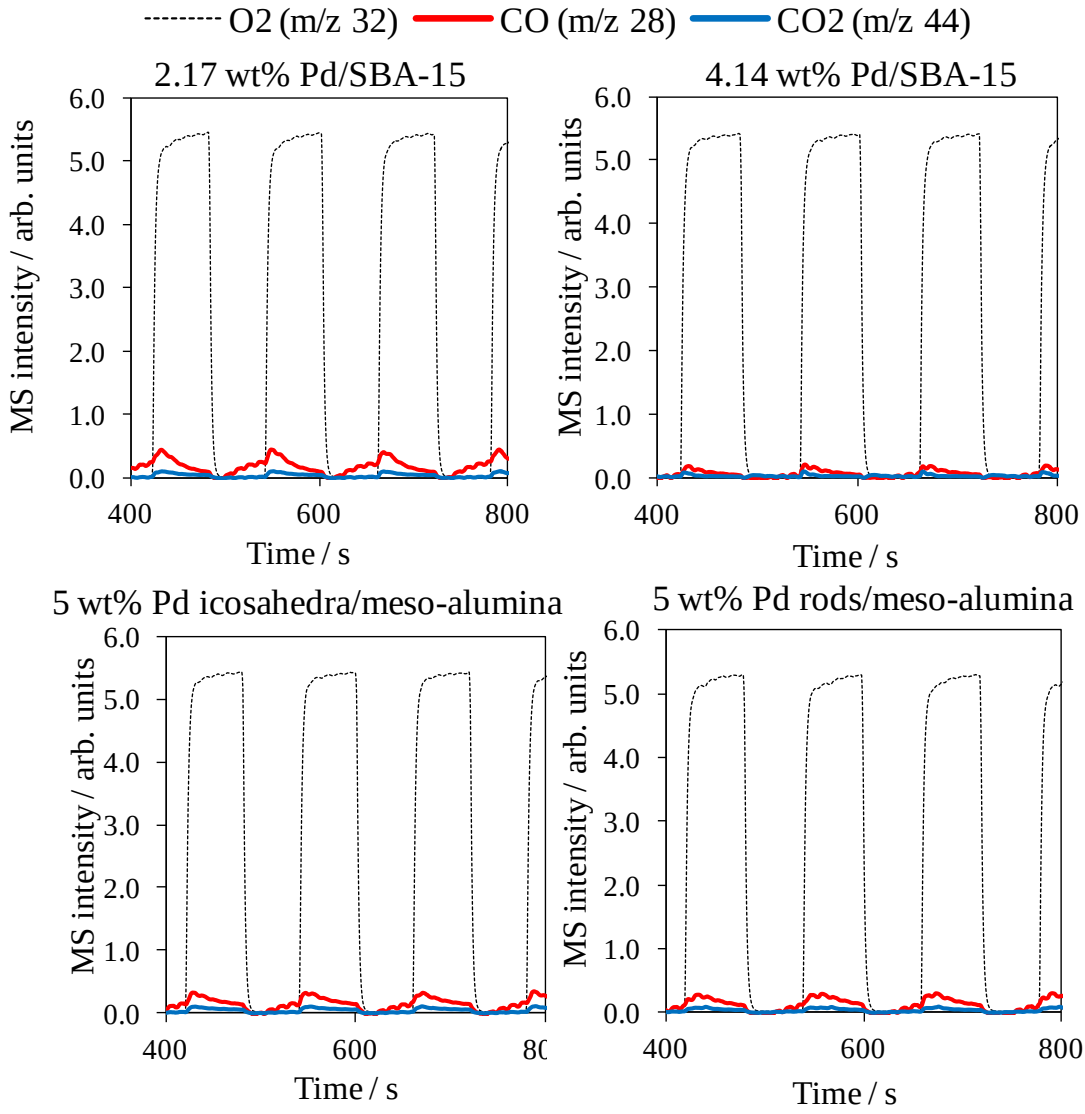


**Figure 1 – 100 °C reaction profiles for the non-selective pathway of crotyl alcohol oxidation over 2 and 4 wt% Pd/SBA-15 and 5 wt% Pd icosahedra and Pd nanorods/meso-alumina. Low levels of combustion products are seen in all cases**

## (iii) Example TEM images used for size analysis in *Chapter 5*

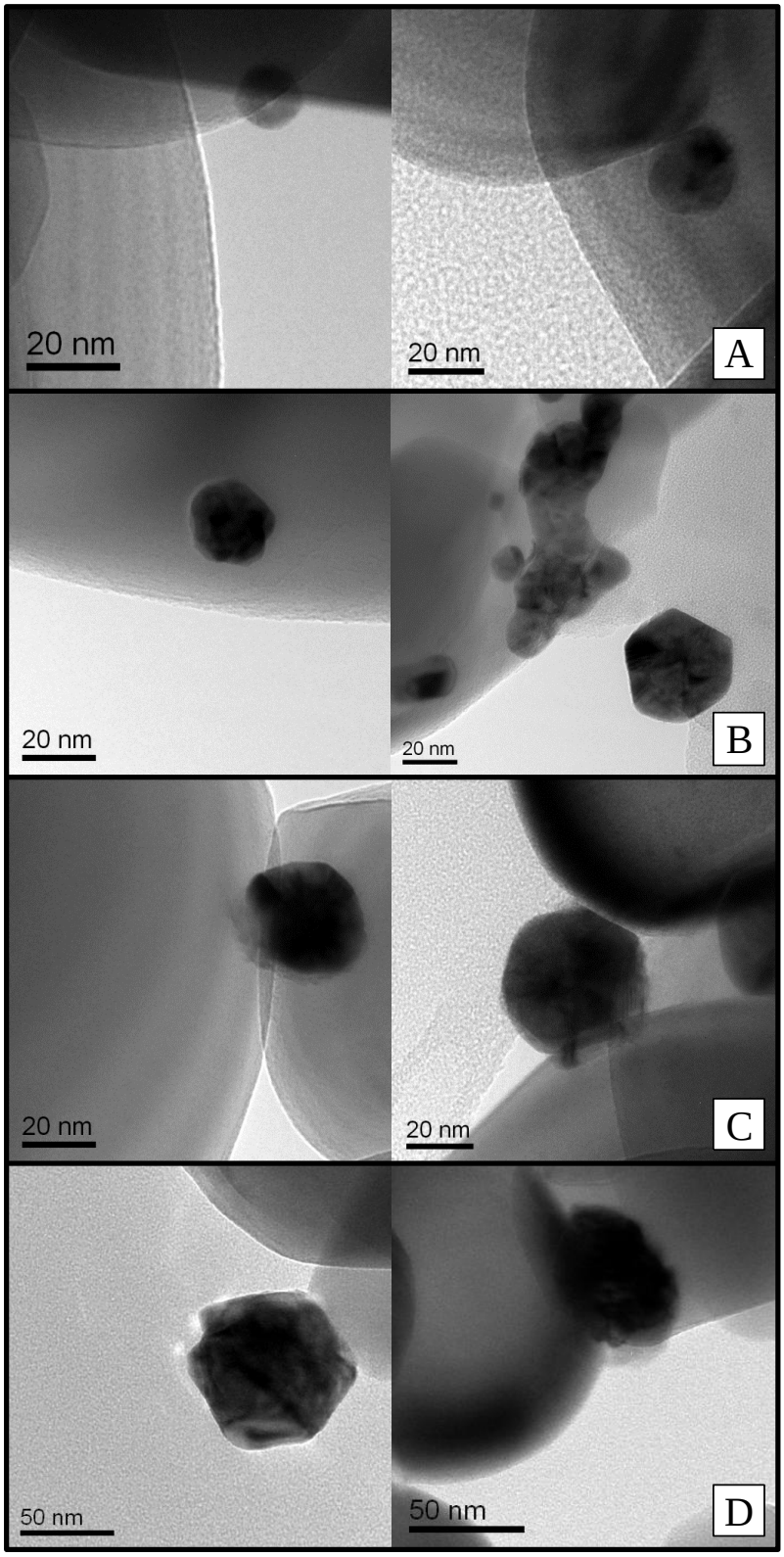


**Figure 2 – Selection of TEM images used for particle size analysis given in *Figure 5.4* for the as-prepared catalyst (A) and after annealing at 300 °C (B), 400 °C (C) and 700 °C (D)**

**(iv) Reaction profiles for Pd-Au/$TiO_2$ core-shell catalysts prior to normalisation to surface metal content and particle size from *Chapter 5***

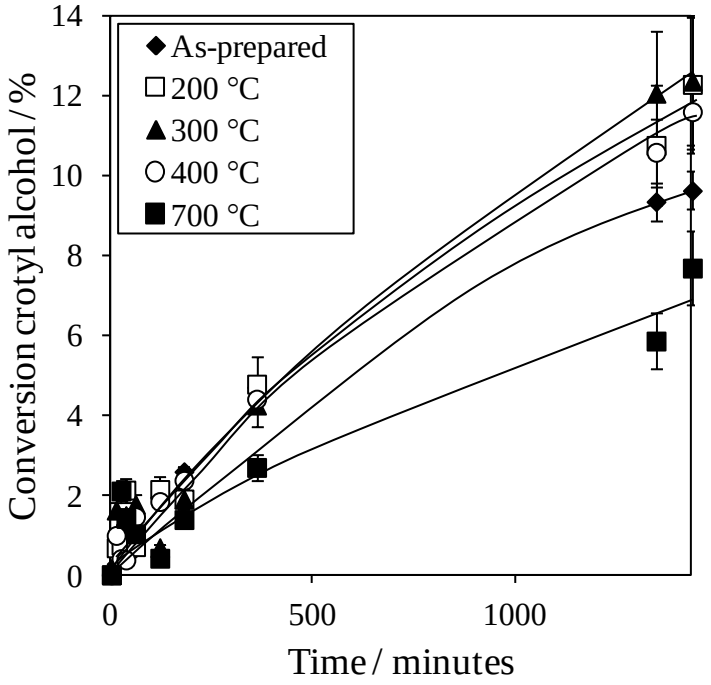


**Figure 3 – Reaction profiles showing % crotyl alcohol conversions prior to normalisation of the as-prepared and annealed Pd-Au/$TiO_2$ core shell catalysts**

## (v) DRIFTS analysis below 1550 $cm^{-1}$ for benzyl cyanide hydrogenation (*Chapter 6*)

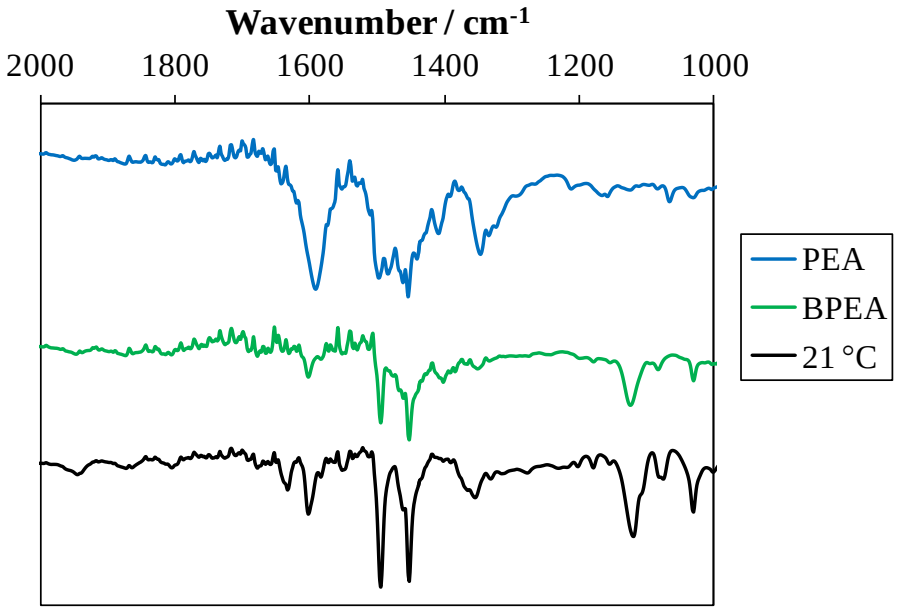


**Figure 4 – DRIFT spectra between 1000 $cm^{-1}$ and 2000 $cm^{-1}$ of 5 wt% Pd/C treated with phenylethylamine (blue), bis-(2-phenylethyl)amine (green) and after reaction at 21 °C under 2 bar hydrogen with benzyl cyanide (black)**